UNSTEADY HEAT CONDUCTION AND FRACTURE MECHANICS IN MULTILAYER ENGINE COATINGS

by

Georgios Koutsakis

A dissertation submitted in partial fulfillment of
the requirements for the degree of

Doctor of Philosophy

(Mechanical Engineering)

at the

UNIVERSITY OF WISCONSIN–MADISON

2022

Date of final oral examination: July 6th, 2022

The dissertation is approved by the following members of the Final Oral Committee:
Jaal B. Ghandhi, Professor, Mechanical Engineering
Gregory F. Nellis, Professor, Mechanical Engineering
David A. Rothamer, Professor, Mechanical Engineering
Sage L. Kokjohn, Associate Professor, Mechanical Engineering
John H. Perepezko, Professor, Materials Science and Engineering
Dimitrios Kyritsis, Professor, Mechanical Engineering, Khalifa University
Matthew R. Begley, Professor, Materials, University of California – Santa Barbara
John W. Hutchinson, Professor of Engineering Emeritus, Harvard University

to my family, including those who unconditionally supported me.

ABSTRACT

Unsteady heat transfer and fracture mechanics analytical techniques were developed to allow optimization of multilayer coatings for reciprocating internal combustion engines. The analytical heat conduction solution handles time-varying heat flux and temperature boundary conditions. The mathematical formulation was derived using the matrix method coupled with complex analysis residue-calculus Laplace transform inversion techniques. As compared to finite difference heat conduction schemes, the analytical nature of the solution requires no spatial discretization and the accuracy is guaranteed. The method to predict the surface temperature of multilayer engine walls was integrated with a commercial system-level simulation software package. Full simulations were performed using experimental boundary condition and with calibration data for a production multi-cylinder diesel engine to demonstrate thermal efficiency benefits of coating over extended drive cycles.

The fracture-based framework was developed using well-established techniques. The method evaluated the transient elastic energy release rates assuming equi-biaxial stress followed by plane strain after delamination. The peak energy release rate location was predicted to lie within the coating, suggesting that the coating may begin to fail via spalling rather than pealing off the substrate. This analysis was validated against several coated pistons tested in a high-output, single-cylinder diesel engine. The model was found to provide good trendwise comparison with the post-run coating integrity observations. Coatings with maximum energy release rate that significantly exceeded the toughness failed.

A high-throughput computational optimization was performed to maximize efficiency by minimizing heat transfer while obeying a structural integrity constraint for a production diesel engine using a multilayer-coated piston. The output uncovered the optimum coating material, thickness and thermomechanical properties for a real-world driving scenario. Over eight hundred real materials were investigated, and the optimization required more than one million drive cycle evaluations. This elucidated the importance of including mechanical considerations in the design of thermal barrier coatings for improved engine performance.

ACKNOWLEDGMENTS

In the years [1] I spent at the Engine Research Center (ERC), numerous individuals contributed to the experience and education I received. When I first joined the ERC, my lab and office colleagues were Ryan Walker, Austin Nawrocki, Noah Breneman, Flavio Chuahy, and John Roberts. They were great resources for getting me up to speed on the details of the ERC and the engine test cell. In addition, their comments and advice while rebuilding the single cylinder of B127 lab were particularly insightful. Thanks to all other students, staff and faculty of the ERC for providing me with invaluable life experience and wonderful memories. Good times.

I am grateful to my committee members for taking the time to read and digest this material. My advisor Prof. Jaal Ghandhi, who was suggested to me as "the best active engine advisor in the world", deserves a special acknowledgment for fully supporting me to solve the problems I was interested in. Were I able to go back in time, I would *again* pursue the same path to go even further. I am thankful to Prof. Greg Nellis, who not only taught me heat transfer in class, but for his immediate responses and willingness to support towards the first steps formulating the conduction heat transfer solution. Thanks to Prof. Emeritus John Hutchinson and Prof. Matthew Begley for conceptualizing together the fracture mechanics framework and for being my "mechanics co-advisors". Thanks to Prof. Dimitrios Kyritsis for his invaluable support during my graduate program and to Prof. David Rothamer and Prof. Sage Kokjohn for their engine related discussions about coatings. Lastly, I am indebted to my undergraduate advisor Harry Lefakis, retired from the University of Western Macedonia – Greece, for his support which started from the early years of my undergraduate program. Prof. Harry flew from Thessaloniki to Madison for attending my PhD defense.

I would like to acknowledge the funding support for this project from John Deere, as well as the expertise and advice provided by our contacts Scott Miles,

[1] May 2017 through August 2022

Dou Danan, and the rest of engine development group, who joined us in monthly teleconferences and in-person visits. Scott's input was especially valuable when implementing our conduction heat transfer solution to the full powertrain model of the commercial system-level simulation software package.

Madison, WI was the ideal location for me because not only did I receive the academic skills to help me succeed professionally, but also life-skills and lifelong memories. I will always be grateful for the amazing hospitality I received from Mike Kahl and the Hoffman family. The myriads of Wisconsin activities and the Greek Easter festivals will always be remembered.

The deepest gratitude I feel is toward my family in Greece. My parents, Vana and Stavros, my sister Maria and my grandmother Marika (Mutuyia). They continually support me while I pursue my dreams, no matter the circumstances, and I am forever grateful. Their trip to the US to attend my commencement in-person will always be remembered. Eleni, my significant other and best friend. We have always been supportive of each other, but her part was definitely harder than mine. I would like to thank her for always being understanding and supporting me during my worst failures and my greatest achievements. Her packed lunches and late-night dinner deliveries kept me alive. As this chapter of my life closes, I look forward writing many more with her.

CONTENTS

LIST OF TABLES

LIST OF FIGURES

NOMENCLATURE

Unless otherwise specified

Abbreviations

1-D – One dimensional
2-D – Two dimensional
AFR – Air-Fuel Ratio
AHRR – Apparent Heat Release Rate
APS – Atmospheric Plasma Spray
(a)TDC – (after) Top Dead Center
BDC – Bottom Dead Center
BMEP – Brake Mean Effective Pressure
CMAS – Calcium-Magnesium Alumino-Silicates
CPU – Central Processing Unit
CTE – Coefficient of Thermal Expansion
ECU – Electronic Control Unit
EGR – Exhaust Gas Recirculation
EPA – Environmental Protection Agency
ERR – Energy Release Rate
EU – European Union
EVC – Exhaust Valve Close
EVO – Exhaust Valve Open
f() – function of
FFT – Fast Fourier Transform
FGM – Functionally Graded Material
FIR – Finite Impulse Response
GdZr – Gadolinium Zirconate
IC – Internal Combustion
IMEPg – Indicated Mean Effective Pressure gross
IVC – Intake Valve Close
IVO – Intake Valve Open

NRTC – Non Road Transient Cycle
Ra – absolute profile height arithmetic average over length
RMS – Root Mean Square
SENB – Single Edge Notch Bend
SiRPA – Silica-Reinforced Porous Anodized Aluminum
SOI – Start of Injection
TBC – Thermal Barrier Coating
TGO – Thermal Grown Oxide
TS – Temperature Swing
US – United States
WHTC – World Harmonized Transient Cycle
YSZ – Yttria Stabilized Zirconia

Heat Transfer Symbols
A,B,C,D – Matrix coefficients
c – Specific Heat Capacity [$\mathrm{Jkg^{-1}K^{-1}}$]
C – Capacitance per unit area [$\mathrm{Jm^{-2}K^{-1}}$]
h – Convective heat transfer coefficient [$\mathrm{Wm^{-2}K}$]
k – Thermal Conductivity [$\mathrm{Wm^{-1}K^{-1}}$]
L – Length [m]
n_x, n_y – Summation terms [–]
N – Number of layers [-]
$\dot{q}''$ – Heat Flux [$\mathrm{W\ m^{-2}}$]
$\bar{q}''$ – Mean heat flux [$\mathrm{Wm^{-2}}$]
Q'' – Integrated Heat Transfer Rate [J]
Q_p – Pumped heat [$\mathrm{W/m^{-2}}$]
r – Magnitude of complex function
s – Laplace, frequency variable [Hz]
R – Thermal resistance [$\mathrm{m^2KW^{-1}}$]
t – Temperature [K]
x – Distance [m]

X – Combustion chamber response function subject to heat flux pulses [K-m^2 W^{-1}]
Y – Coolant surface response function subject to backside temperature pulses [–]

β - Positive real number and simple root of D(s) [Hz]
Δ – Time step [s]
θ – Time [s]
ρ – Density [kgm^{-3}]
ρc – Volumetric heat capacity [Jm^{-3}K^{-1}]
ψ – Generalized residue parameter
Ψ – Generalized residue
Ω – Root dependent ratio [–]

Fracture mechanics symbols
a_{ij}, b_{ij} – Deformation analysis coefficients [–]
$\bar{c}$ – θ coefficient [–]
E – Young's Modulus [GPa]
$\bar{E}$ – Effective moduli [GPa]
G – Energy Release Rate [Jm^{-2}]
G_c – Toughness [Jm^{-2}]
H_b – Bottom sub-multilayer height [m]
ℓ_i – Element thickness [m]
N – Number of nodes [–]
U – Strain energy [Jm^{-2}]
x – Position x [m]
y – Position y [m]

α – Coefficient of Thermal Expansion [K^{-1}]
ϵ – Total strain [–]
ϑ – Thermal strain [–]
κ – Curvature [m^{-1}]
ν – Poisson Ratio [–]

σ – Stress [Pa]

Sub/Super-scripts

b – bottom
c – coolant
conv – convection
d – downstream
g – gas
i – surface/interface index
ini – initial
j, n – time index
m – root index
N – coolant-side surface
o – combustion chamber surface
rad – radiation
ref – reference
t – top
u – upstream
w – wall
w – whole
x – x-direction
y – y-direction
z – z-direction

Other symbols

$\circledast$ – Convolution symbol
$\mathcal{F}$ – Fast Fourier transform operation
$\mathcal{F}^{-1}$ – Inverse fast Fourier transform operation $\mathcal{O}$ - Complexity

1 INTRODUCTION

1.1 Motivation

The issues associated with greenhouse gases and climate change will likely incentivize new mobile powertrain solutions in the future. Because reciprocating internal combustion engines are currently the most cost-effective powertrain option available, improvements in their combustion, aftertreatment strategies, and thermal management are necessary in the short term. With proper design, an optimized engine is a difficult target to overtake. One potential pathway to increase thermal efficiency is to reduce heat loss to the cylinder walls.

The choice of optimal in-cylinder coating materials for internal combustion engines is not clear. Engines can be used over a wide range of speeds and loads, thus the optimum material for one application may not be the most favorable for another. Furthermore, a coating material that optimizes one performance parameter may adversely affect another performance parameter. For instance, if a coated engine is operated at high loads, *i.e.*, higher wall surface temperatures, the heat transfer during combustion and the power stroke might be lower compared to the baseline, but the higher surface temperatures reduce air mass flow and consequently lower engine power output.

Research on the insulation of reciprocating engine chamber surfaces with coatings has been ongoing for almost 45 years, however, such technology has not been widely commercialized yet. The primary concerns are: *i*) the engine breathing penalty, and *ii*) durability and reliability of such coating systems. The newest generation of coatings largely eliminates the breathing penalty, but durability issues remain.

Since internal combustion engines are not heat engines, heat transfer is not a fundamental requirement. Only under certain circumstances, such as cooling the intake air after turbocharging or heating up exhaust after-treatment, is heat transfer desirable in engine operation. Otherwise it increases cooling requirements, and decreases efficiency and power output. The ultimate goal is to reduce the

instantaneous rate of heat transfer at the gas-wall interface to zero and, in turn, the time-averaged heat transfer will also be reduced to zero. Different heat flow rates and directions exist in almost every stroke of an engine cycle. The heat transfer characteristics in reciprocating engines are significantly different than aerospace propulsion systems, suggesting that advanced coatings used in aerospace cannot be directly used in combustion engines. Unlike gas turbines, reciprocating engine heat transfer is highly unsteady. Three distinct frequency ranges can be identified. The lowest frequency range ($\sim 10^{-3} - 10^{-2}$ Hz) occurs during the engine start-up or shutdown, where a slow heating or cooling process occurs. The intermediate range ($\sim 10^{-1}$ Hz) corresponds to sudden load/speed changes during operation. The highest frequency range ($\sim 1 - 10^{2}$ Hz) involves the heat transfer changes that occur during the engine cycle itself [1].

During the intake stroke, heat often flows *from* the hot combustion chamber surfaces *to* the fresh charge; this heating leads to a decrease in volumetric efficiency, *i.e.*, how much air can be inducted, which limits power output. On the compression stroke, the gas is compressed and its temperature increases at a faster rate than the wall. Heat flows *from* the gas *to* wall for the rest of the cycle, resulting in a reduced gas temperature and pressure. Close to the combustion event, the temperature and pressure are maximized. The peak intra-cycle heat flux in a diesel engine can reach 10-15 MW/m^2 [2, 3] and the minimum value is near zero. The exhaust gas exits past the exhaust valves, and through the ports, manifolds, turbochargers and after-treatment devices all of which play an important role in the overall system thermal management. Depending on the operating condition, 20-40 % of the fuel energy could be lost due to heat transfer [4].

The in-cylinder heat transfer is only a part of the total energy balance of a cycle simulation but its accuracy has significant bearing on the validity of the overall simulation. Knowledge of the in-cylinder conduction heat transfer mechanism, *i.e.*, wall surface temperature and heat flux, is essential for the development of thermal-barrier-coated engines. The ability to predict rejection of in-cylinder heat has to be evaluated in terms of both materials technology and insulation strategy. Existing approaches to evaluate coated engine performance lack computational efficiency,

stability, and depend on high spatial discretization for achieving accuracy.

The trade-off between in-cylinder heat transfer and durability – the crack driving force (discussed in detail later) – is depicted in Fig. 1.1. The heat transfer reduction, Γ_{net}, is calculated over a full drive cycle and the crack driving force is given as ratio of maximum energy release rate, $G_{\max}$, to the material toughness, G_c; when $G_{\max}/G_c \geq 1$ coating failure is predicted. As the coating thickness increases the heat transfer decreases but $G_{\max}/G_c$ increases rapidly, indicating the likelihood of a coating failure. The optimum heat transfer reduction scenario would be according to the path defined by the dashed lines in Fig. 1.1; the maximum thickness is reached to get the "Best Performance" when $G_{\max}/G_c$=1, which is defined as the "Crack Limit". Details will be provided later in the thesis.

During the research and development process of a thermally insulated engine, cycle simulation has been used to assess performance and heat transfer characteristics for different insulation strategies. The ability to predict rejection of in-cylinder heat and coating structural integrity has to be evaluated in terms of both materials technology and insulation strategy.

1.2 Objectives

There are three primary objectives of this research, all of which focus on thermal barrier coating design in reciprocating internal combustion engines:

i) Develop an analytical solution of the unsteady heat conduction problem of multilayer engine walls.

ii) Develop a framework for predicting coating failure and driving forces for delamination.

iii) Demonstrate an optimization procedure for selecting thermal barrier coatings that includes both thermal and durability performance considerations.

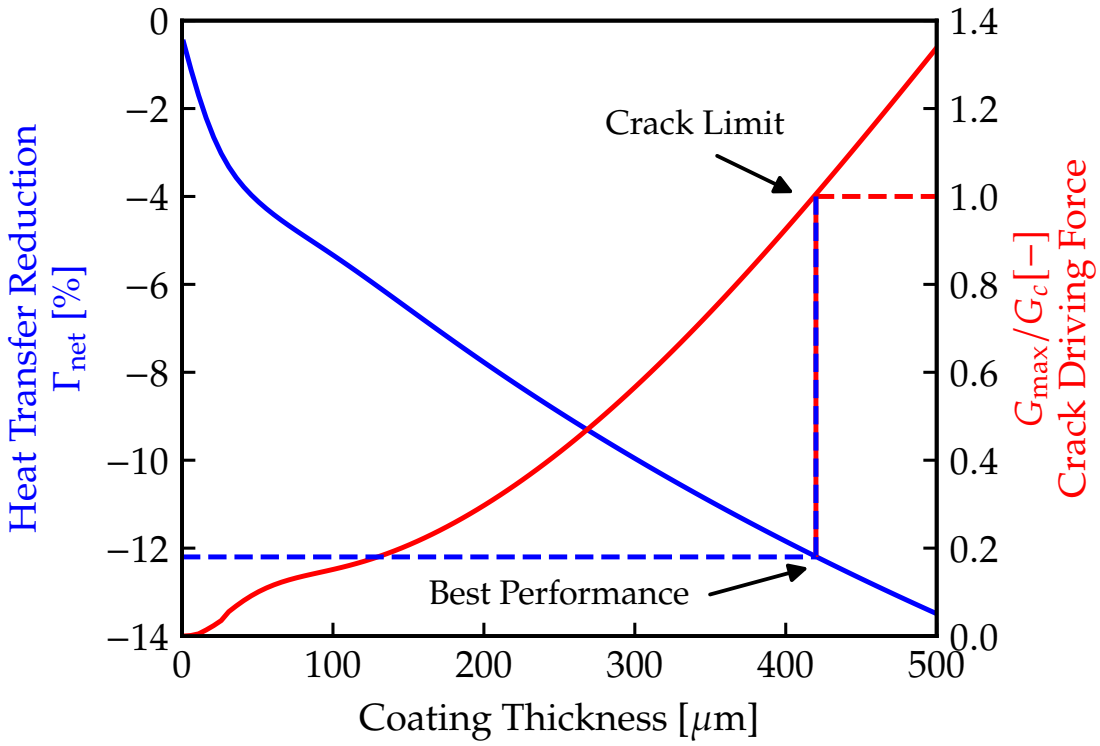

Figure 1.1: Trade-off between in-cylinder heat transfer reduction and crack-driving force for various coating thicknesses during a full vehicle drive cycle. Boundary conditions, wall architecture, and thermomechanical properties can be found in Chapter 7.

1.3 Outline

This dissertation is divided into eight Chapters. Chapter 2 contains a literature review of existing approaches to coating performance and durability in reciprocating engines. Chapter 3 provides an analytical solution for the surface temperature of a multi-layer system subject to time-varying heat flux on the combustion surface and temperature on the backside coolant surface. Chapter 4 develops a framework for predicting coating failure that combines a rigorous analysis of thermal transients during an engine cycle with a thermomechanical analysis of coating stress and the driving forces for delamination. Chapter 5 applies the fundamental heat transfer

solution of Chapter 3 to system-level engine simulation to predict performance. Chapter 6 validates the general delamination framework of Chapter 4 by comparing with experimental data. Chapter 7 utilizes the knowledge of all aforementioned Chapters to set-up a high-throughput optimization routine using a real-world driving scenario to identify the trade-off between engine performance and coating structural integrity of nearly one thousand materials with real properties. Chapter 8 provides the summary of the work performed and recommendations for future work.

2 LITERATURE REVIEW

2.1 Background on Insulated Engines

Climate change and human health concerns drive government environmental agencies to set stringent emission regulations for engine manufacturers, making the design process more challenging due to the trade-off between pollutant emissions and engine efficiency. A separate pathway to achieve higher efficiency is to reduce the heat transfer losses to the combustion chamber walls. Depositing insulating coatings on the combustion chamber surfaces is a relatively old concept, but recent materials having low thermal conductivity and low volumetric heat capacity have renewed the interest of the engine community.

Many of the early coatings applied to the power cylinder components *i.e.*, piston, intake/exhaust valves, cylinder head and liner, were identical of those used in the gas turbine industry. Foundational insights on the subject were generated during the "adiabatic" engine program [5, 6, 7], which sought to reduce or even completely remove cooling systems by using high-temperature ceramics. These early coatings were thick, on the order of a millimeter, with "long" thermal conduction time scales that resulted in substantially higher surface temperatures during all strokes of the thermodynamic cycle. The lack of adequate coating design [8, 9] led to negligible performance gains, which, in turn, suppressed research in the area.

Researchers [10, 11, 12] suggested that thin coatings, on the order of one hundred micrometers, with "short" time scales could *instantaneously* reduce the gas-wall temperature difference that drives convective heat transfer. Such "short" time scales were conceptualized by using thin, highly porous coatings.

2.1.1 Performance

In-cylinder thermal insulation has a long history for internal combustion engines. A recent state-of-the-art literature review [13], provides a historical evolution of thermal barrier coating technology starting from 1970s up to the current day. It focuses on the conflicting nature of the engine performance and emission results with respect to the thermal barrier coating characteristics, *e.g.* material (thermal/radiative) properties, thickness, porosity and surface roughness. Apart from the coating material properties, it discusses how the gas-wall interface characteristics (*e.g.* velocity gradient, flame distribution, local near wall air-fuel mixture composition and radiative heat transfer) affected the earlier engine performance studies.

The thermodynamic performance and pollutant emissions results of coated engines varied widely. Researchers have investigated the effect of yttria-stabilized zirconia (YSZ) as a coating material deposited onto metal engine wall components in various thicknesses and different engine operating conditions/configurations. Improved fuel economy [14, 15, 16, 17] was observed by some researchers while others reported inferior performance results [9, 17, 18, 19, 20] with thermal barrier coatings. Experimental and modeling work by Morel *et al.* [21] found reduced fuel consumption for every coated case tested compared to an uncoated baseline. Dickey *et al.* [20], however, found efficiency gain from simulation results, but their experimental studies showed a decrease in thermal efficiency due, in part, to a lack of re-optimization of combustion after the coating addition.

To get the full benefit out of a coated engine, combustion system re-optimization [19, 21, 22, 23], *e.g.* fuel injection timing, injection rates and pressures, air intake temperature and exhaust pressure, is necessary when compared to the baseline. A number of previous experiments (without any combustion parameter re-optimization) have shown degraded combustion [20, 9, 8, 24] for diesel engines with thermal barrier coatings. This deterioration may be ascribed to slower combustion, *i.e.*, less premixed burn fraction and increased diffusion burn duration for the insulated engine, reducing thermal efficiency [20]. Additionally, direct substitution of coated components without re-optimization leads to excess soot deposits on piston surface [9],

fuel injector malfunctioning in hotter combustion chamber temperatures [23] and thermal boundary layer thinning due to elevated wall temperatures [8]. In the latter, Woschni *et al.* [8] argued that the local heat transfer coefficient increased substantially and counter-balanced any heat transfer benefit that would have occurred with in-cylinder coatings. On the other hand, promising results in fuel economy were presented after re-optimizing the combustion system [19, 21, 22], but some authors suggested more fundamental redesign is required [9].

The potential of the heat loss reduction to increase brake work is not realized for every coating and engine configuration. Some studies have found [14, 20, 9, 24, 25] that the majority of the heat ends up in the exhaust as sensible enthalpy while others [15, 16, 26] observed lower exhaust temperatures. Depending on the application, an increase in exhaust enthalpy might favor the overall system efficiency, for example, additional work might be produced by turbo-compounding the engine, additional fueling needed for cold-start after-treatment heating time may be reduced [27], the enthalpy may be used by waste heat recovery systems [28], or high residual temperatures may enable low temperature combustion strategies at low load conditions [29, 30].

Thermal-swing coatings having low thermal conductivity and low volumetric heat capacity (mainly driven by high porosity), were recently proposed for in-cylinder heat insulation [31]. This combination of properties, allows the surface wall temperature to track the gas temperature closer, reducing the wall heat transfer throughout the cycle. Toyota Central Research Labs [31, 32, 33, 34] designed and demonstrated a thin, low thermal conductivity and low volumetric heat capacity coating for reciprocating internal combustion engine surfaces. The low volumetric heat capacity requirement was achieved via a 100μm highly porous aluminum structure impregnated with silica [32], termed SiRPA (Silica-Reinforced Porous Anodized Aluminum). This strategy enabled the surface to quickly respond to transient gas temperature fluctuations induced by the combustion event, *i.e.* at the highest frequency discussed above in Section 1.1. Durrett *et al.* [35] developed a coating with similar thermal properties made of sintered hollow nickel-alloy micro-spheres to achieve higher porosity. Reliable operation in a spark-ignited

engine environment was demonstrated by Andrie *et al.* [36] using a high volume low pressure (HVLP) method; two coatings with outstanding coating properties were developed. An upgraded version of the previous coating was utilized for compression ignition engine testing. The coating successfully demonstrated over 25 hours of testing without signs of failure. Results indicated about 1 % improvement in gross indicated efficiency at high-load conditions, higher exhaust gas temperature across all engine conditions and no penalty on engine-out emissions. The new generation of thermal-swing coatings typically have thermal conductivity about one quarter of zirconia and volumetric heat capacity around one third of zirconia. More recent formulations have shown positive thermal efficiency results across the few steady state conditions tested, ranging from 0.5 to 1 % gain [37, 38, 39, 36]. A 5% fuel consumption benefit [33, 34] was reported (based on experiments) after 1 minute of cold start operation.

Researchers have studied the effects of soot deposits, surface roughness, and heat transfer coefficient on coated combustion chambers. Coated walls have shown reduced combustion chamber soot deposits on the piston periphery [40], while homogeneous charge compression ignition (HCCI) operational range has been extended to lower loads [29].

Surface roughness may play an important role in the combustion chamber heat transfer. There is evidence that roughness influences near-wall air-fuel mixing and combustion, which may explain results that differ from what would have been expected by smooth higher temperature metal walls [41, 42, 43, 44, 45]. Increased surface roughness provides more effective area and can increase near-wall turbulence. Additionally, the air-fuel mixing process can be affected, which in turn, affects chemistry [46]. Machined metal combustion chamber walls have surface roughness in the order of Ra of 1 μm. The SiRPA coating was reported to have surface roughness Ra 3-5 μm, which was due to the uneven alumina growth of the anodizing process [47]. Traditional thermal barrier coatings deposited via atmospheric plasma spray techniques can have Ra more than 10 μm [48, 49]. Minor efficiency improvements [42, 43, 44] have been shown for polished [49] thermal barrier coatings at high loads compared to the as-sprayed condition.

A number of researchers claimed that the nature of the heat transfer process remained unchanged throughout the cycle due to the coating addition, and the lower difference between gas and the wall temperature reduces heat flux, $\dot{q}'' \equiv h(t_g - t_w)$, where h is the convection coefficient, and t_g and t_w are the gas and wall temperatures. Several studies [14, 9, 22, 50] agreed with this hypothesis. Conversely, a handful of others [26, 8, 24, 51] state that although increased cylinder wall temperature is a benefit, the convection coefficient becomes large enough to overcome the temperature difference benefit and, thus, the heat flux actually rises. The lack of quantitative information on the effect of surface roughness on heat transfer prevents it from being included in the calculations that are undertaken in this dissertation.

Combustion regimes such as conventional diesel combustion (CDC) and low-temperature-combustion (LTC) may have substantial spatial variations of heat flux over the cycle. An experimental investigation by Hendricks *et al.* [52] showed that CDC heat flux has higher spatial non-uniformity than dual-fuel reactivity-controlled compression ignition (RCCI) [53, 54], since the latter combustion occurs at a more uniform equivalence ratio and lower peak local combustion temperatures. Optical measurements from Kokjohn *et al.* [55] demonstrated that RCCI heat-release rate spatial variations fall between CDC and that of a fully premixed combustion strategy, *e.g.* HCCI.

A major concern for exhaust aftertreatment is the transient thermal behavior of catalytic devices during cold start operation [56, 57, 58]. Recently, the effect of thermal insulation on various aftertreatments components has been demonstrated over a WLTC (Worldwide harmonized Light vehicles Test Cycle) [59]. In this study, there were no improvements in fuel consumption, however, the insulation increased the exhaust enthalpy and lowered the cummulative pollutant emissions. This behavior can be explained by the complicated non-linear coupling between the multiple effects at play. In order to eliminate this behavior and provide a comprehensive comparison between a coated and an uncoated engine, a transient drive cycle needs to be considered.

2.1.2 Durability

Propulsion systems and spacecraft reentry vehicles often use protective coatings for components exposed to extreme thermal conditions because most structural materials can not withstand high temperatures, and vice versa. Multilayer architectures allow an appropriate balance, specific to the application, between mechanical and thermal properties, stored strain energy arising from thermal misfit, and adhesion. Arguably, thermal barrier coatings in gas turbines represent the most advanced coating systems, and have enabled dramatic gains in efficiency by allowing higher turbine inlet temperatures.

In reciprocating combustion engines, the durability and reliability of such coatings has been the primary issue preventing their widespread implementation. There are multiple reports in the literature of delaminated coatings, spallation, and cracks in the coating following diesel [60, 61, 62, 63, 64, 65, 66, 67] and homogeneous charge compression ignition (HCCI) [42, 43] engine testing. Rapid heating and cooling of the surface leads to coating delamination (debonding).

Beardsley [68, 69] showed a cross section of a coating applied on a Caterpillar heavy duty engine piston, see Fig. 2.1. The engine was operated at 14 bar BMEP, 1800 rpm speed and 160 bar peak cylinder pressure using three modifications: water cooled baseline, an unsealed thick thermal barrier coating and a sealed thick thermal barrier coating approximately 3.5 mm thick. The sealed coating was an attempt to reduce the influence of the porosity in the ceramic coating to interact with the combustion process. It was assumed that the air/fuel mixture for combustion was forced into the pore structure of the coating during compression and would consequently not be directly available for combustion, thereby lengthening the combustion duration and decreasing the overall efficiency of the engine [70]. Indeed, the sealed coating showed better performance than the baseline and unsealed coating. Results indicated almost 5 % decrease in specific fuel consumption despite a similar decrease in volumetric efficiency. However, the durability of both coatings was limited to approximately 100 hours. Figure 2.2 shows the top view of the glass composite sealed piston. Cracking was observed across the entire circumference of

the squish area, however, only one large spallation region was observed between 8 and 9 o'clock.

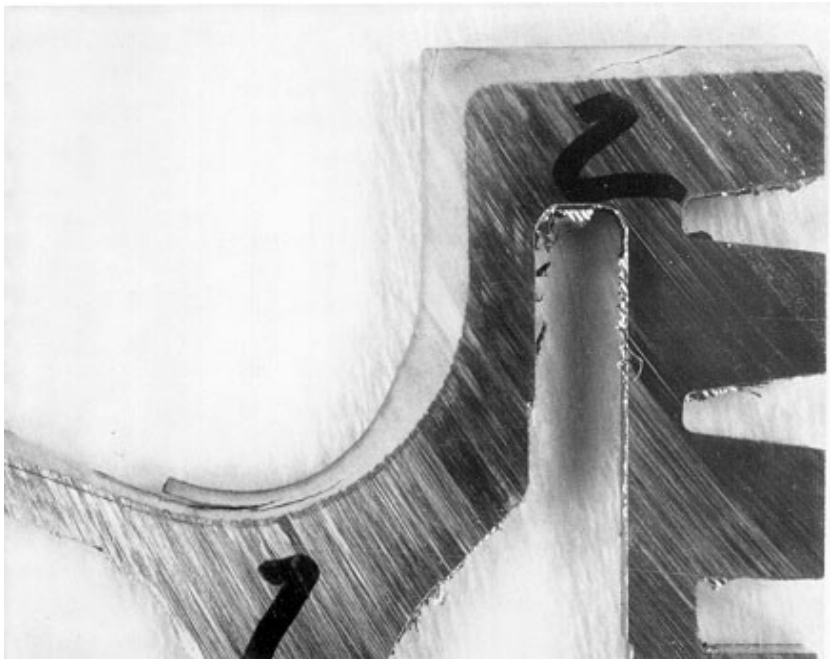

Figure 2.1: Cross section of a Caterpillar heavy duty piston showing coating delamination near the bowl wall and in the squish area. Taken from Beardsley [68, 70].

Andruskiewicz *et al.* [65] numerically and experimentally investigated the engine performance of an anisotropic Barium–Neodymium–Titanate (BNT) coating on a direct-injected single-cylinder gasoline spark-ignition engine. Experimental results suggested that any potential benefit of coatings was dominated by increased heat losses due to porosity, fuel absorption losses, and a reduction in compression ratio, emphasizing the need to maintain a sealed coating surface. The main scope of this work was to obtain the largest performance benefit by maximizing the heat transfer reduction, thus targeting thicker configurations. Durability analysis was omitted in this study, resulting in significant mechanical failures especially for the thickest (1000 μm) coating, see Fig. 2.3.

Figure 2.4 shows examples of large spallation coating failures in heavy-duty compression ignition diesel engines. Figure 2.4 a) shows an example of a delami-

Figure 2.2: Top view of a Caterpillar heavy-duty piston showing spallations and cracks of a glass sealed coating at the squish area. Taken from Beardsley [68, 70].

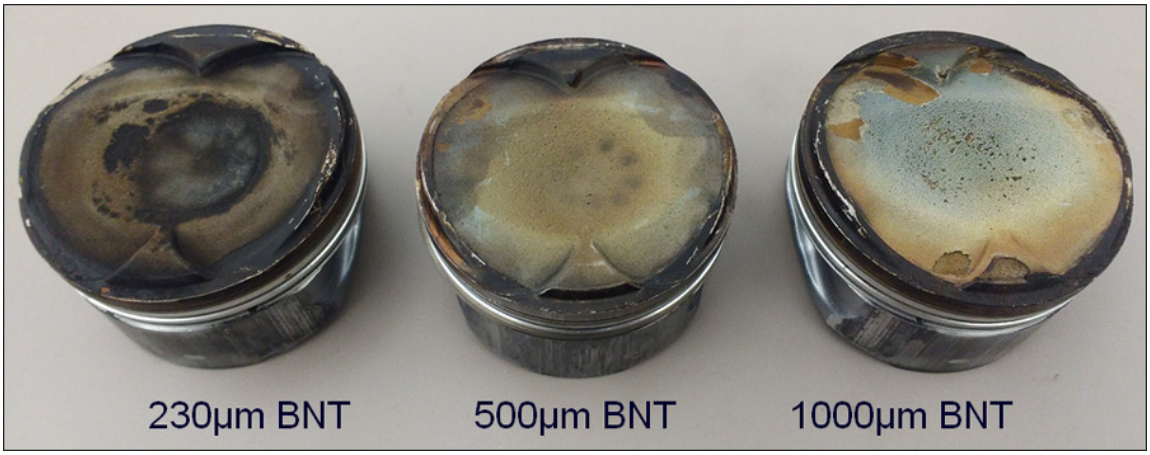

Figure 2.3: Post-testing observations from left to right: 230 μm, 500 μm and 1000 μm of a Barium–Neodymium–Titanate (BNT) coating applied on a spark-ignited engine. The thickest coating suffered severe degradation throughout testing; spallation regions were observed in multiple locations. Taken from Andruskiewicz *et al.* [65, 66].

nated piston (# 5) that was tested on a single-cylinder diesel engine by Cummins under a DOE/NASA research program [60]. A 2.54 mm thick zirconia-based coating was deposited on a ductile iron piston. The objective of this test was to assess coating structural integrity at 13.8 bar BMEP under steady state conditions. After holding several hours at this condition, the fuel consumption became inconsistent with prior measurements. When noticed, the engine test was stopped to allow for inspection. Indeed, the coating had delaminated in the entire central portion of the piston, as shown in Fig. 2.4 a). In a similar study, Adiabatics Inc. and U.S. Army TACOM modified a six-cylinder Cummins diesel engine using multiple insulation coatings on various components of the power-cylinder assembly. Figure 2.4 b) shows an unsuccessful attempt to maintain coating structural integrity of a 200 μm ceramic-based coating at 390 kW and 2900 rpm. The entire bowl wall and the central part completely chipped-off revealing the metal substrate. This engine test included 3 hours at full load and 50 hours at various speed and load combination across the engine map. Figure 2.4 c) shows another failed attempt of a novel multilayer piston insulation concept that was evaluated in a single-cylinder diesel engine at 8 bar BMEP and 1200 rpm. The multilayer had at a total thickness of 300 μm and consisted of four layers: a steel piston substrate, a bond coat, a high porosity layer and a thin dense layer on top to decrease roughness and close the open pores. It was believed that the excess porosity of 60 %, which was higher than the design specifications, resulted in inferior durability characteristics and led to failure.

Moser [71] performed a coupled thermomechanical analysis to design a Gadolinium Zirconate (GdZr) coating in a Daimler diesel engine. The analysis was undertaken using 3-D computational fluid dynamics and finite element analysis. The mechanical part of this study was evaluated using a stress-based approach; the William Warnke yield model [72]. The validity of this approach is questionable since it involves a large number of assumptions including that failure occurs during the peak stress condition. This yield criterion has been shown to provide a qualitative sense of failure risk mainly for concrete-like materials. Thus, the model is unable to be used as a general durability design tool, *e.g.* optimize the thickness of any coating material while ensuring structural integrity. Although the model

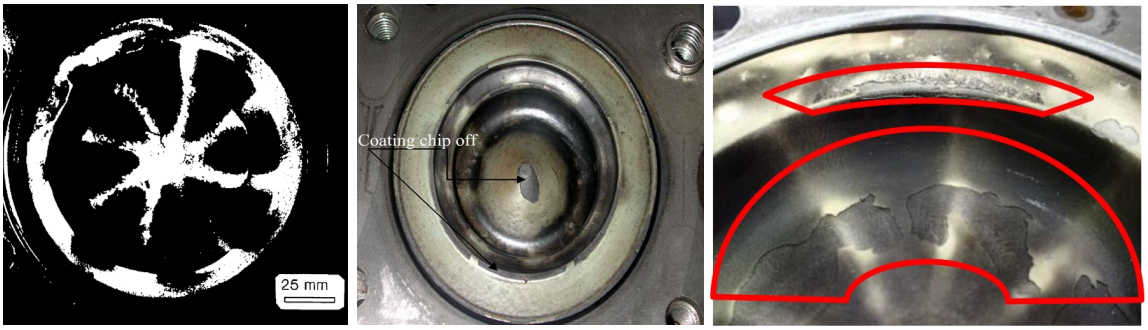

a) b) c)

Figure 2.4: Various piston coating failures tested on heavy-duty diesel engines taken from the literature: a) 2.54 mm zirconia on a single-cylinder Cummins [60], b) 200 μm ceramic-based coating on six-cylinder Cummins [61], c) 300 μm multilayer coating on a single-cylinder [63].

indicated in a qualitative manner the locations of high risk, it did not predict the optimum thickness to prevent failure. Figure 2.5 presents the top view of a cracked GdZr piston at a) the concave radius between the squish region and the bowl lip and b) localized spallation regions indicated with the red arrow [71].

Powell *et al.* [42, 43] experimentally demonstrated a YSZ thermal barrier coating with structural porosity (Gen 1 YSZ-SP) in a HCCI engine. This architecture provided 1.2 % and 2.5 % increase in combustion efficiency and net indicated efficiency under fuel matched condition [73]. However, extensive operation under several other engine conditions resulted in coating failure near the bowl, as shown in Fig. 2.5 c).

Thibblin and Olofsson [67] performed experiments on a heavy-duty diesel engine using a YSZ-coated piston manufactured via suspension plasma-spraying. They performed an SEM analysis of the coating after testing, and reported a unique finding, shown in Fig. 2.6: the coating showed evidence of delamination within the layer, not at the piston-coating interface.

Although structural integrity has been a long-standing problem and many studies have been conducted, limited fundamental work on the mechanics of thermal barrier coating system failure has been performed for reciprocating internal com-

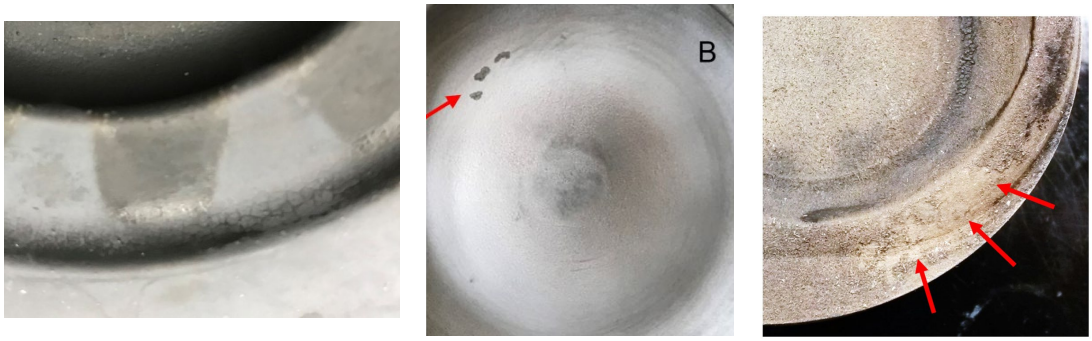

a) b) c)

Figure 2.5: Piston top view post-testing showing: a) cracks of a sealed Gadolinium Zirconate coating at the concave radius between the squish region and the bowl lip [71] and b) localized spallations of a) near the bowl wall [71], and c) spallation of a Yttria Stabilized Zirconia coating with structural porosity near the bowl wall, exposing the bond coat material [42, 43].

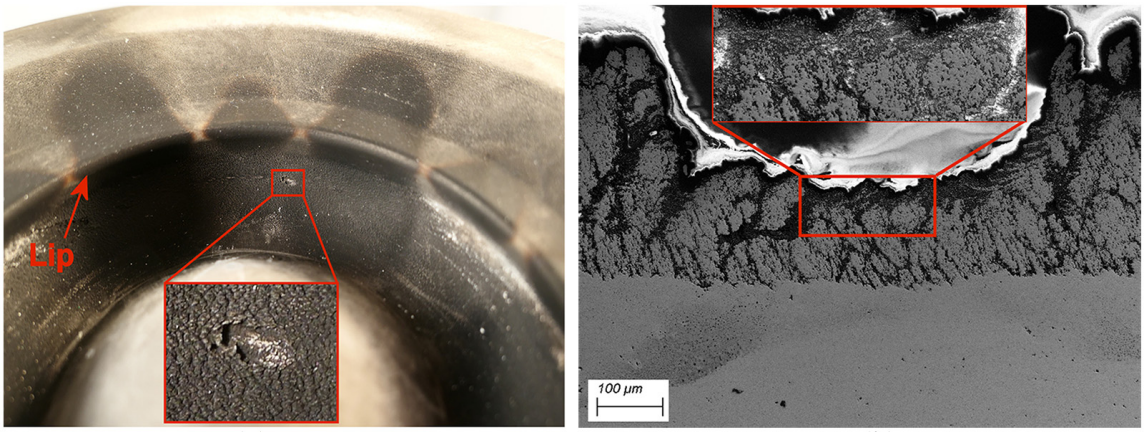

(a) (b)

Figure 2.6: (a) Spallation regions found in the YSZ suspension-plasma sprayed coating below the piston lip after the engine test and (b) cross section of one of the pits in (a) showing delamination within the layer, not at the piston-coating interface. Taken from [67].

bustion engines. A methodology to predict coating failure at the design stage considering all the aforementioned frequency ranges, discussed in Section 1.1, does not exist. Previous studies have been limited to time-averaged conditions, neglecting the transient intra-cycle temperature fluctuations of the coating [74, 75, 76, 77]. Zhu and Miller [78] highlighted the importance of the low and high frequency engine thermal transients for a thick ("long" time scale) YSZ coating. The study presented mechanisms of fatigue crack initiation and propagation as well as creep and fatigue interaction supported by numerical and experimental evidence simulating engine-like conditions. Experiments showed that the combined low- and high-frequency cycle fatigue tests induced more severe coating surface cracking, microspallation and accelerated crack growth than pure low-cycle fatigue tests. Recently, Baldissera and Delprete [79] analyzed the temperature, stress, and displacement distributions of a coated diesel piston. Steady-state thermo-mechanical analysis was performed at a single instant during the cycle, *i.e.* top dead center (TDC). The stress analysis revealed higher peak stresses at the coated surface relative to the uncoated baseline.

Existing approaches to durability of reciprocating engine coatings have been predominantly stress-based [80, 81, 69, 71]. However, because the coatings are loaded with pre-existing microcracks and flaws, delamination and spalling are not controlled by crack initiation events, which might be susceptible to a stress-based analysis. Rather, it is controlled by conditions were an initiated crack can advance multiple coating thicknesses (*e.g.*, delamination). Fracture-based approaches are more appropriate to assess the durability of coatings and its sensitivity to design parameters however, they are non-existent for reciprocating engine applications to the author's knowledge.

2.1.3 Optimization

There have been a large number of experimental and numerical studies of thermal barrier coatings as illustrated in a recent state-of-the-art literature review [13]. However, the existence of parametric or optimization investigations in the literature is limited. Existing studies have been performed: i) for a steady state operation;

ii) with only a few coatings; and *iii*) optimized only based on the engine thermal performance neglecting coating structural integrity [31, 37, 33, 39, 82, 83, 43, 84, 38, 85]. A more comprehensive approach to material and thickness optimization of the thermal barrier coatings will be required to achieve targeted brake thermal efficiencies beyond 55% [86, 87, 88].

2.2 Background on Heat Conduction

The First Law of Thermodynamics reveals that the rate of temperature change is proportional to the heat flow crossing a control volume. In the absence of convective motion, chemical reaction and phase change, and with the assumption of negligible radiation

$$\frac{\partial t}{\partial \theta} \propto \sum \dot{q}'' \tag{2.1}$$

where t is temperature [K] and θ is time [s]; an undesirable amount of heat is transferred through the walls of a piston internal combustion engine at two distinct time periods of the cycle. Heat is extracted from the gases to the wall during the most essential time for power generation, *i.e.* at top dead center, and heat flows to the gas at low temperatures during the intake stroke, biasing volumetric efficiency.

The objective of applying coatings to the surface of engine power cylinder components is to reduce in-cylinder heat flux. To a first approximation, the candidate material needs to have low thermal conductivity. Figure 2.7 shows a comparison of thermal conductivity and volumetric heat capacity for nearly a thousand different materials including ceramics, glasses, metals and polymers. Conventional engine walls are steel and aluminum alloys with properties near the upper righthand corner of Fig. 2.7. Assuming the existing power-cylinder components need to be maintained for structural reasons, additional layers should be deposited on the metal substrate. To consider the coating in the engine design, a heat conduction solution should be employed. Thermal resistance-based approaches are meant solely for steady-state conditions, unlike the current problem under consideration. The time-varying boundary conditions due to combustion in conjunction with the

large difference in volumetric heat capacity between the existing engine metal walls and potential material candidates with lower thermal conductivity, as suggested in Fig. 2.7, defines a clear need for transient heat conduction solution.

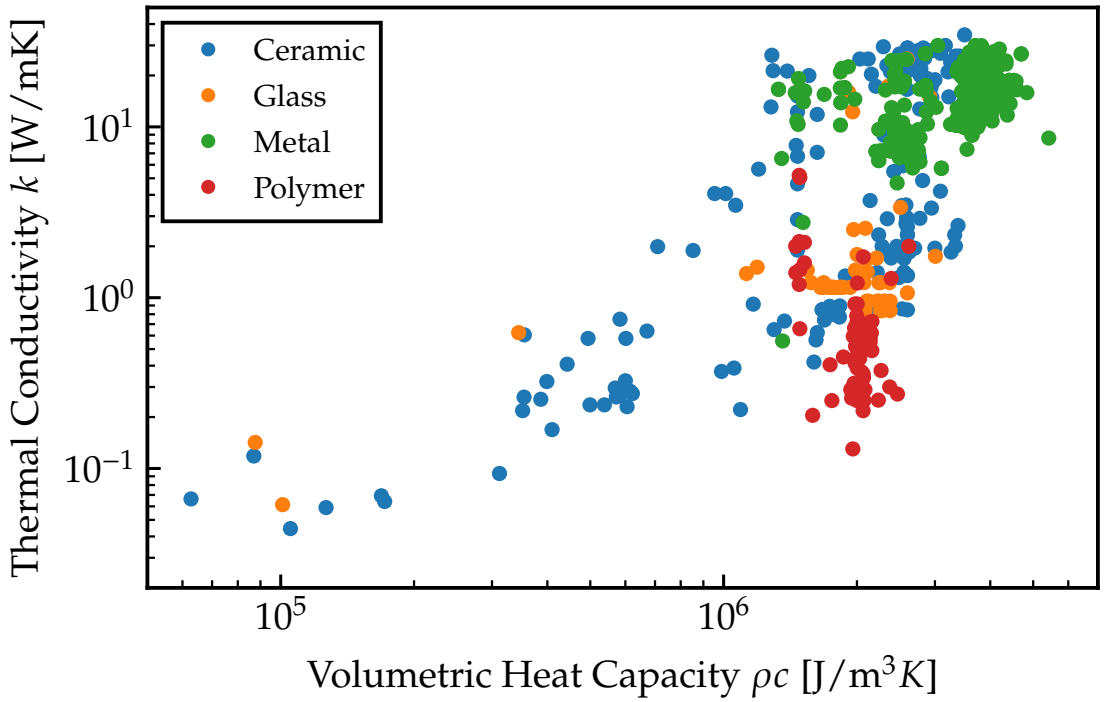

Figure 2.7: Comparison thermal conductivity k and volumetric heat capacity ρc for a wide range of materials (ceramics, glasses, metals and polymers).

Morel [10] defined the term "pumped heat" per unit area as: $Q_p = \frac{1}{2}\left(\overline{|q|} - \bar{q}\right)$, which represents the difference between the integral of the absolute heat flux and the net heat flux for the duration of an engine cycle, as illustrated in Fig. 2.8. The effect of coating material properties on the pumped heat is clearly shown in Figure 2.9. It is interesting to note that for decreasing thermal conductivity, the pumped heat is not monotonic across the range of interest. When $k\rho c = 0$, the pumped heat reaches zero. Pumped heat needs to be considered together with the net heat transfer when system-level optimization of a optimum coating architecture is

investigated.

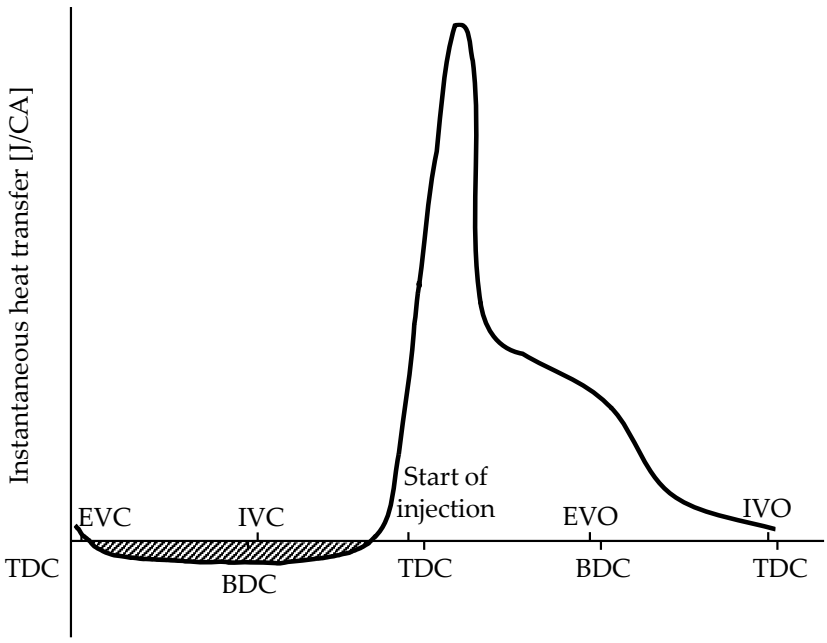

Figure 2.8: Rates and directions of instantaneous heat transfer rate during a four-stroke engine cycle. The shaded area represents the "pumped heat".

2.2.1 Finite Difference Techniques

Finite difference methods are the conventional approach employed to determine the coating surface dynamic temperature. Explicit schemes [89, 90] are simple and computationally efficient, but, they become unstable above a critical time step.

Assanis [89] utilized an Euler finite difference scheme to solve the conduction problem. The boundary condition on the combustion surface was convection while the boundary condition on the coolant side was temperature or prescribed heat flux. The time step taken was about 1°CA and approximately evenly-spaced 15 nodes were introduced in the insulating layer to satisfy the Courant condition. Miyairi [90] introduced 100 elements in the first 1 mm of the wall, assuming temperature swing

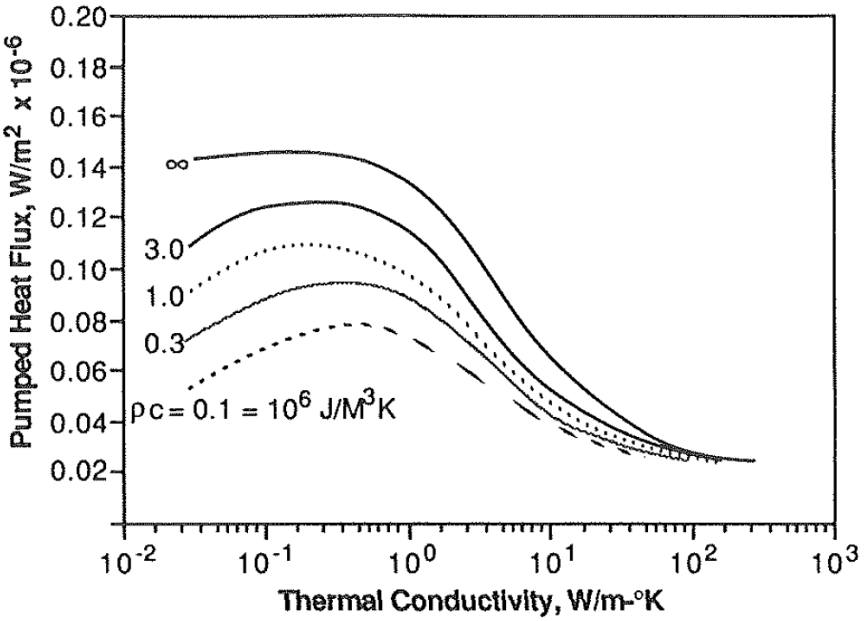

Figure 2.9: Pumped heat flux as function of coating thermal conductivity for different volumetric heat capacities. Taken from [1].

amplitude was negligible below this depth; the time step was set from 0.01°CA to 0.2°CA. Convective boundary conditions were used for both surfaces.

The relatively short thermal conduction time scale of the coating together with high temporal gradients of heat flux at the surface require high nodal density near the coating surface to guarantee numerical stability and accuracy. Implicit schemes [10, 66, 91, 92] are unconditionally stable and handle non-uniform grid spacing, but, can require large matrix inversions, which may become computationally costly when such calculations are coupled with combustion engine simulations. Guaranteed stability, however, does not eliminate the possibility of oscillations, so there are still limits on the time step size. A number of surrogate procedures have been used to compensate for computational cost.

Andruskiewicz [66] used a backwards-difference implicit method to couple the conduction problem with the engine thermodynamic model. The conduction solver was down-sampled from 0.5°CA to 4°CA to increase computational efficiency while sacrificing accuracy. The finite difference mesh was optimized using the

depth$_{1\%}$ approach [93]. Figure 2.10 shows the nodes were clustered close to the surface until the location where 99 % of the surface temperature swing has decayed. Only one single element was assigned from the depth$_{1\%}$ to the backside surface to reduce computational overhead. The non-uniform spacing approach aimed to capture the transient heat sources close to the surface sacrificing detail in the deeper part of the structure. A similar approach has to be performed in cases where the backside surface experiences transients, *e.g.* transient drive cycles or exhaust valve experiencing backside transients.

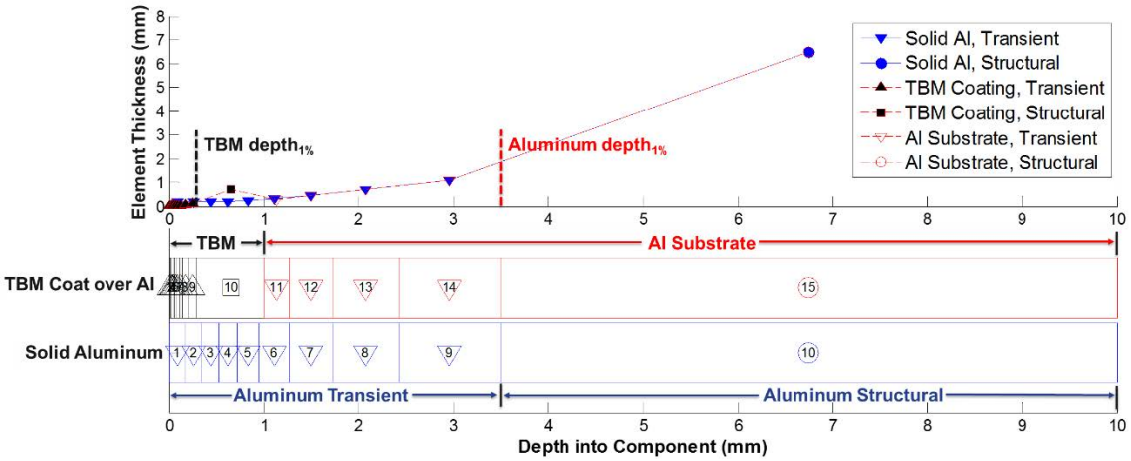

Figure 2.10: Optimized 1-D finite element mesh for a two- and one-layer engine wall using the depth$_{1\%}$ approach. Taken from Andruskiewicz [66].

The current version of GT-Power (v2020 b2) [91], a system-level simulation commercial software, accounts for thermal barrier coatings only via the 3-D finite element analysis template, *i.e.* "EngCylTWallSoln". The 3-D finite element of the metal engine is evaluated once per cycle, based on cycle-averaged conditions. When a coating layer is requested, a transient 1-D finite difference code is employed to resolve the transient surface temperature calculated over one engine cycle based on the varying combustion gas temperature and heat transfer coefficient. It is important to highlight that the coating-substrate interface remains at constant temperature over one cycle. This temperature value was updated from the finite element solution

at the end of every cycle. This treatment may not conserve energy for cases where the temperature at that location fluctuates.

Some researchers have attempted to couple 3-D CFD simulations and low spatial resolution heat conduction calculations, where the material properties near the surface were chosen to minimize errors in the dynamics of the system [94, 95, 96]. Lastly, the finite difference schemes require the entire temperature distribution to be evaluated at every time step; quite often the surface temperature is the only output of interest, *i.e.*, for providing boundary conditions to an engine simulation.

Existing approaches to conjugate heat transfer with combustion solvers are computationally expensive. However, because coating optimization may require evaluation over a wide range of material architectures and engine conditions, computational efficiency is critical. The coating effectiveness varies based on operating condition due to the non-linear coupling in an engine. In order to provide a comprehensive comparison between different coating designs, one needs to consider extended operation periods, *i.e.* drive cycles. An analytical solution is more appropriate to evaluate heat conduction because *i*) it is exact, *ii*) does not depend on spatial discretization; *iii*) it is computationally efficient since it solves for the only output of interest.

2.3 Background on Fracture Mechanics

Failure could be driven by a wide variety of different reasons [97], however one of the largest contributors is the layers' likelihood to expand at different rates with regards to thermal and mechanical conditions. Each layer would expand in a different manner if left alone, but it is bonded into a multilayer component. In turn, the constrained layers experience conformal deformation generating thermal stresses (compressive/tensile) and stored elastic energy that drives the system failure. To a first approximation, the layers would be happiest in their lowest energy state as individual pieces and consequently they pursue returning there; even if it requires splitting themselves into pieces and leaving part of themselves stuck to

another layer. A short description of layered systems used in semiconductors and gas-turbine engines follows.

Semiconductor and integrated circuit packages are composite structures that generally consist of many different layers with different thermo-mechanical properties. The interface between two different materials is usually the weak link due to the imperfect adhesion and the stress concentration. The initiation and growth of interface cracks determines the reliability and performance of the electronic packages. Interfacial delamination is one of major failure modes observed from encapsulated flip-chips in electronic packaging. This failure is usually due to sufficiently large thermo-mechanical stresses built up along the interfaces during the on/off procedure.

Gas-turbine engines use refractory-oxide ceramic coatings on the surfaces of the hottest metallic parts, allowing them to operate at substantially higher gas temperatures than the melting points of the metallic blades. Since the gas turbines are based on the Brayton cycle, higher gas turbine inlet temperature gives higher thermal efficiency and power output.

Initially, ceramic materials were introduced to extend the useful life of the stationary components, *e.g.* engine combustor. Thermal barrier coatings were applied to rotating turbine blades during the 1980s, and, their heat transfer capabilities were neglected during the engine design phase. Today, coatings are crucial engine components and any mechanical failure can endanger the engine [98].

The coating design criteria for the gas-turbine engines are: provide thermal insulation to prevent melting of the superalloy substrates, prevent oxygen diffusion to avoid substrate oxidation and environmental degradation from chemical attacks, and ensure structural integrity. Furthermore, such characteristics must be maintained for prolonged service times and thermal cycles. Typically, these times are 1000s and 10,000s of hours for jet engines and power-generation engines, respectively. The former are being cycled numerous times between a maximum temperature of ≈1300°C (for existing thermal barrier coatings systems) or ≈1500°C (for imminent environmental barrier coatings systems [99, 100]) and room temperature (takeoff/landing and on-ground). Although power-generation systems are increas-

ingly being employed to stabilize the electric grid with the addition of renewable sources, they require significantly fewer thermal cycles (maintenance/shut-downs).

At least four constituents comprise a traditional thermal barrier structure for a gas turbine, similar to Fig. 2.11. The top coat (1) serves as the thermal insulator, the substrate (2), bond coat (3), which acts as a strain compliance buffer and ensures proper adhesion between the top and bond coat. Lastly, a thermal grown oxide (TGO) layer (4) a reaction product that is formed (after long operation) between the top and bond coat, prohibiting oxygen diffusion. Each of these elements dynamically interact to control the performance and durability characteristics of the gas-turbine engine.

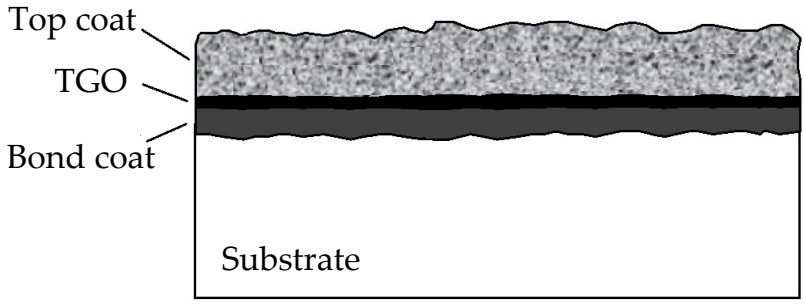

Figure 2.11: A traditional thermal barrier coating architecture

A major failure mechanism of interest in the aerospace applications arises from siliceous debris (airborne dust, sand or volcanic ash) that form glassy molten deposits on the turbine-blade coating surfaces. During peak temperature operating conditions, *e.g.* take-off or landing, these materials melt to yield calcium-magnesium alumino-silicates (CMAS) [101]. This glass wets the top surface and penetrates through and chemically dissolves the coating. When the CMAS solidifies upon rapid cooling (power cut during landing), the penetrated layer develops high modulus leading to cracking. Fracture mechanics approaches can predict coating failure and assess various failure mechanisms [102] due to CMAS penetration depending on the material thermomechanical properties and gas turbine engine conditions [103, 104, 97].

The identified, to date, failure mechanisms are categorized as intrinsic and extrinsic [101], as shown in Fig. 2.12. The former group mainly consists of mechanisms that are associated with thermal misfits between coating/substrate and usually are insensitive to thermal gradients. The latter are impossible to reproduced in lab experiments.

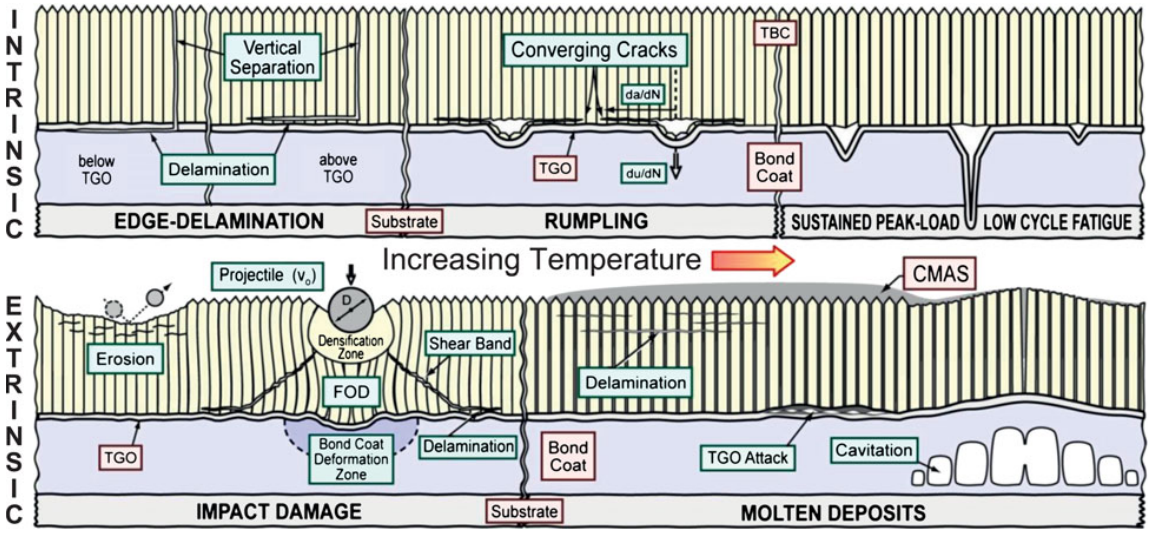

Figure 2.12: Extended menu of failure mechanisms in thermal barrier coating gas-turbine applications. Three general modes of CMAS damage (lower right), characteristic of higher temperature operation, have been identified so far. One involves delamination cracks propagating through the TBC, another leads to chemical attack of the thermally grown oxide (TGO) with concomitant loss of adherence, and a third results from creep cavitation of the bond coat below a heavily penetrated TBC. FOD, foreign object damage; da/dN, crack growth per cycle; du/dN, inward displacement of TGO per cycle. Taken from [101]

Thermal stresses that in turn result in strain energy have been found to be the key for thermomechanical coating evaluation. Strain energy plays the central role in fracture mechanics since it creates the driving force for failure; the only possible

mechanism to release this energy is crack advance. Strain energy is given by

$$U = \frac{E_c h_c (1+\nu_c)}{2(1-\nu_c)} \left\{ (\Delta\alpha_c \Delta T_{\text{sub}})^2 - (\Delta\alpha_c \Delta T_{\text{sub}})(\alpha_c \Delta T_{\text{sur/sub}}) + \frac{1}{3}(\alpha_c \Delta T_{\text{sur/sub}})^2 \right\} \tag{2.2}$$

for an equi-biaxial in-plane stress condition for a linear temperature distribution in a two-layer wall during the cooling phase of a gas-turbine engine. The product of Young Modulus, E_c, and coating thickness, h_c, normalize the elastic strain energy, which is useful for qualitative comparison between different materials or engine conditions. The bracketed term of Eq. (2.2) includes thermal expansion coefficient mismatch $\Delta\alpha_c$, substrate temperature difference with respect to a reference condition ΔT_{sub} and the coating temperature drop relative to the substrate $\Delta T_{\text{sur/sub}}$. The physical interpretation of the product $(\Delta\alpha_c \Delta T_{\text{sub}})(\alpha_c \Delta T_{\text{sur/sub}})$ is important. The compressive stress driven by cooling of the substrate, ΔT_{sub} can be offset by tensile stress associated with the top surface cooling relative to the substrate, $\Delta T_{\text{sur/sub}}$ [101].

An isothermal slow-cooling and a rapid-cooling operating event can be envisioned based on the steady-state elastic energy strain of a coating deposited on a gas-turbine blade in Fig. 2.13.

The isothermal slow-cooling event represents a furnace cycle test where the coating and substrate have a uniform temperature both in the hot state and while cooled, *i.e.* ΔT_{sub} increases while $\Delta T_{\text{sur/sub}}$=0. It is illustrated that for relatively thick and completely penetrated CMAS coatings the likelihood of crack is increasing dramatically. However, a failure depends on the coating toughness under the pertinent crack propagation mode [101].

The rapid-cooling event considers the coating surface temperature to drop rapidly relative to the substrate, *i.e.* $\Delta T_{\text{sur/sub}} > 0$, and the substrate temperature to remain relatively unaffected, *i.e.* $\Delta T_{\text{sub}} \simeq 0$. Such scenario could mimic cold air impinging on the coating surface due to sudden engine flame-out event. Equation (2.2) suggests that the term $\alpha_c \Delta T_{\text{sur/sub}}$ scales proportionally to thermal stress and it develops primarily from self-constraint of the coating to thermal contraction as

its surface cools faster than the region closer to the substrate. Finally, Fig. 2.13 suggests that a synergy between both ΔT_{sub} and $\Delta T_{\text{sur/sub}}$ could define a path along the valley in $U/E_c h_c$ surface for lower strain energy buildup.

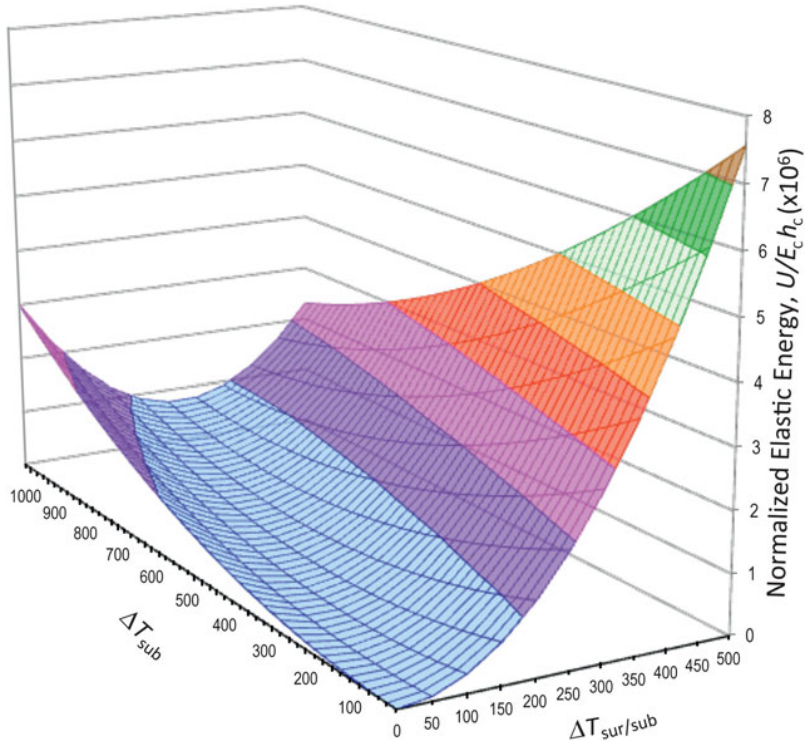

Figure 2.13: Normalized elastic energy/area in the coating $(U/E_c h_c)$ available for release under plane strain conditions due to steady state thermal stress induced by cooling from an initially high temperature. Note that cooling paths wherein $\Delta T_{\text{sur/sub}}$ and ΔT_{sub} change simultaneously may result in much lower strain energy buildup. Taken from [101]

One objective of this work is to develop a framework that could predict system failure due to thermomechanical loads in an internal combustion engine environment. The model is to be reduced to capture the essential fracture mechanics physics, while ignoring the negligible effects on the behavior of interest.

3 DIRECT HEAT CONDUCTION

An analytical solution of the unsteady heat conduction problem in multilayer walls was developed and applied to study thermal barrier coatings for reciprocating internal combustion engines. The method allows paramount computational efficiencies, enabling it to be used in combustion simulation software to correctly calculate wall heat transfer, which is important for engine applications. The mathematical solution was derived using the matrix method and complex analysis / residue-calculus Laplace transform inversion techniques. Section 3.1 develops the analytical approach to determine surface temperature subject to a time-varying heat flux. The applied heat flux was approximated as a series of step-changes; the backside temperature was held constant. A special case solution of the two-layer wall (coating and substrate) problem was determined and provided the foundation for defining a set of non-dimensional parameters that uniquely characterize the surface temperature swing for arbitrary periodic heat flux. The non-dimensional parameters have been exploited to identify thermodynamically equivalent materials suitable for conjugate heat transfer applications.

Section 3.2 expands on this solution by simulating the boundary conditions as the superposition of two adjacent triangular, unit-magnitude pulses, which gives a piece-wise linear representation of the applied flux or temperature history, *and* adds a time-varying temperature to the backside surface. The temperature at any location of interest was also solved. The solution is found as the convolution of a transfer function, which results from the inversion, with the discrete-time heat flux or backside temperature history. The transfer functions describe the exact response and only depend on the multilayer architecture, therefore, they can be computed *a priori*. This method computes only the output of interest ,*i.e.*, wall surface temperature, as opposed to the finite difference method that must evaluate the entire wall temperature distribution and progresses one step at a time. The triangular-pulse method provides a more than two order of magnitude reduction in computation time compared to a finite difference solution at the same level

of accuracy. A 10^4-fold speed increase relative to a finite difference solution was realized when using the Overlap-add convolution technique for a full drive cycle simulation, *i.e.*, a long time record. The transfer function acts like a finite impulse response and can be viewed in the frequency domain to reveal complementary information about coating performance.

The analysis is based on the heat diffusion equation. Consider 1-D heat flow in a multilayer engine wall, as shown in Fig. 3.1, with overall thickness L and constant thermophysical properties within each layer. The governing heat diffusion equation is

$$k\frac{\partial^2 t}{\partial x^2} = \rho c\frac{\partial t}{\partial \theta} \tag{3.1}$$

where t is temperature, θ is time, x is location, k and ρc are thermal conductivity and volumetric heat capacity, respectively. The $x = 0$ location represents the combustion chamber surface where a time-varying heat flux, $\dot{q}''_o(\theta)$, is imposed

$$-k\frac{\partial t}{\partial x}\Big|_{x=0} = \dot{q}''_o(\theta) = f(\theta) \tag{3.2}$$

The applied heat flux is unsteady and can be aperiodic during transient operation of a reciprocating engine. A heat flux boundary condition is used instead of a convective boundary because both the gas temperature and heat transfer coefficient change with time in an engine. The unsteady part of this problem, which will be dealt with in subsequent sections, has an initial wall temperature that is uniform and taken as zero.

$$t_{\theta=0} = 0 \tag{3.3}$$

For simplicity, the step-change solution in Section 3.1 assumed assume constant backside wall temperature as

$$t_{x=L,\theta\to\infty} = t_c \tag{3.4}$$

On the other hand, during startup or engine load changes the back side of the wall may show significant temperature changes due to, for example, the coolant heating. The backside condition at $x = L$, *i.e.*, the coolant or oil surface, is therefore

also allowed to vary as a prescribed function of time for the triangular-pulse solution discussed in Section 3.2

$$t_N(\theta) = f(\theta) \tag{3.5}$$

The transient heat conduction problem is formulated with linear and homogeneous boundary conditions. The thermophysical properties vary only with spatial domain. The wall temperature distribution oscillates about a steady-state distribution, which is found trivially from the mean (over the cycle) surface heat flux, $\bar{q}''$ and the backside temperature. In practice, in order to more rapidly reach the converged periodic condition, the steady-state temperature distribution is used as an initial state as will be discussed below.

The problem is divided into four sub-problems and their superposition comprises the general solution [105]. The first and second problems are the time-varying heat flux at the combustion surface and the time-varying backside temperature at the coolant/oil surface, respectively, as shown in Fig. 3.1. The third and fourth sub-problems address the initial conditions associated with the prior combustion chamber heat flux and coolant-side surface temperature, respectively.

3.1 Step-change Solution

In this formulation, the problem relies only on the prescribed heat flux, including data from the past to solve for the gas-side wall surface temperature. The time-dependent wall temperature can then be used in the gas-side convective cooling model, as compared to assuming a constant wall temperature, to more accurately predict heat flow to the wall.

3.1.1 Superposition Concept

For the proposed problem with constant layer thermophysical properties, the governing partial differential equation is linear and homogeneous. Thus, the solution can be found using the principle of superposition. The surface temperature of

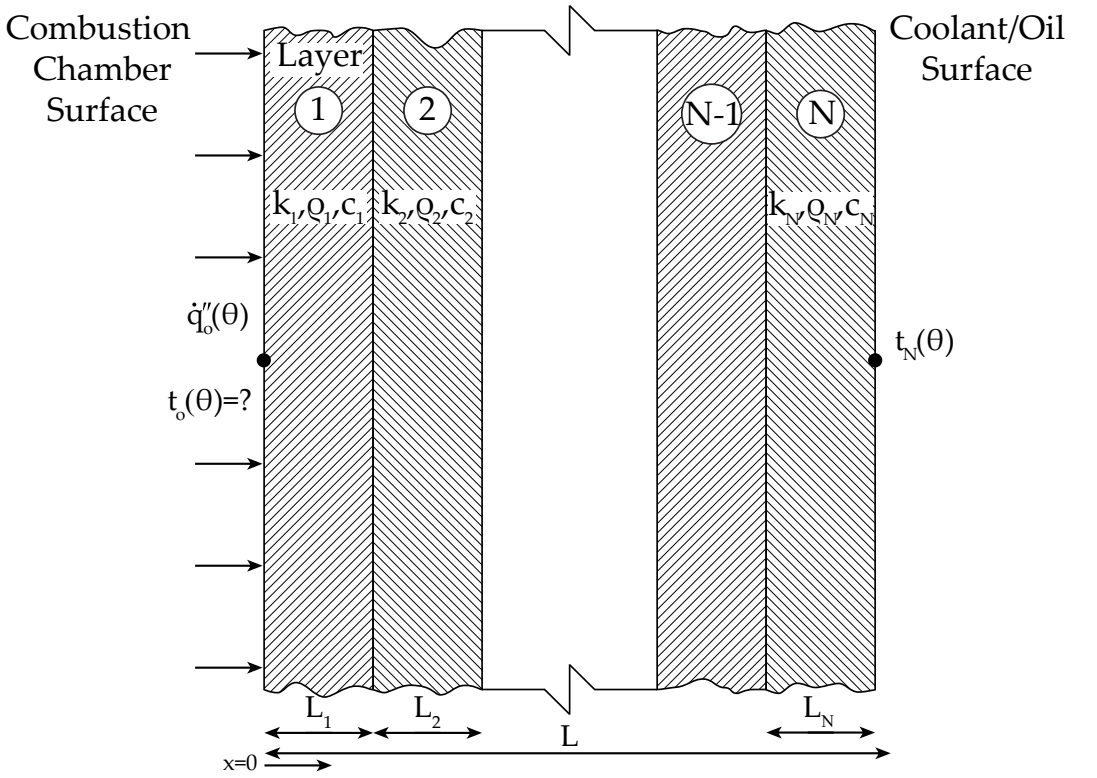

Figure 3.1: Illustration of an 1-D multilayer engine wall. Both boundary conditions, *i.e.* heat flux on the combustion chamber gas-side and temperature on the coolant side, are prescribed functions of time.

a wall subjected to $\dot{q}''(\theta)$ can be found as the summation of the responses to a series of step changes in surface heat flux taking place at successive times. Figure 3.2 illustrates this concept for an arbitrary applied heat flux. For example, the temperature at θ_5 is found by first discretizing the heat flux into a sequence of step changes in heat flux (see Fig. 3.2). The surface temperature response to each heat flux step is found from the solution of the heat diffusion equation. The surface temperature is then the sum of the step responses before θ_5, then θ_5 $t_{x=0}(\theta_5) = t_{o,1}(\theta_5 - \theta_1) + t_{o,2}(\theta_5 - \theta_2) + ... + t_{o,4}(\theta_5 - \theta_4)$, where $t_{o,j}$ for $j = 1..n-1$ with $n = 5$ is the temperature of the previous timesteps j.

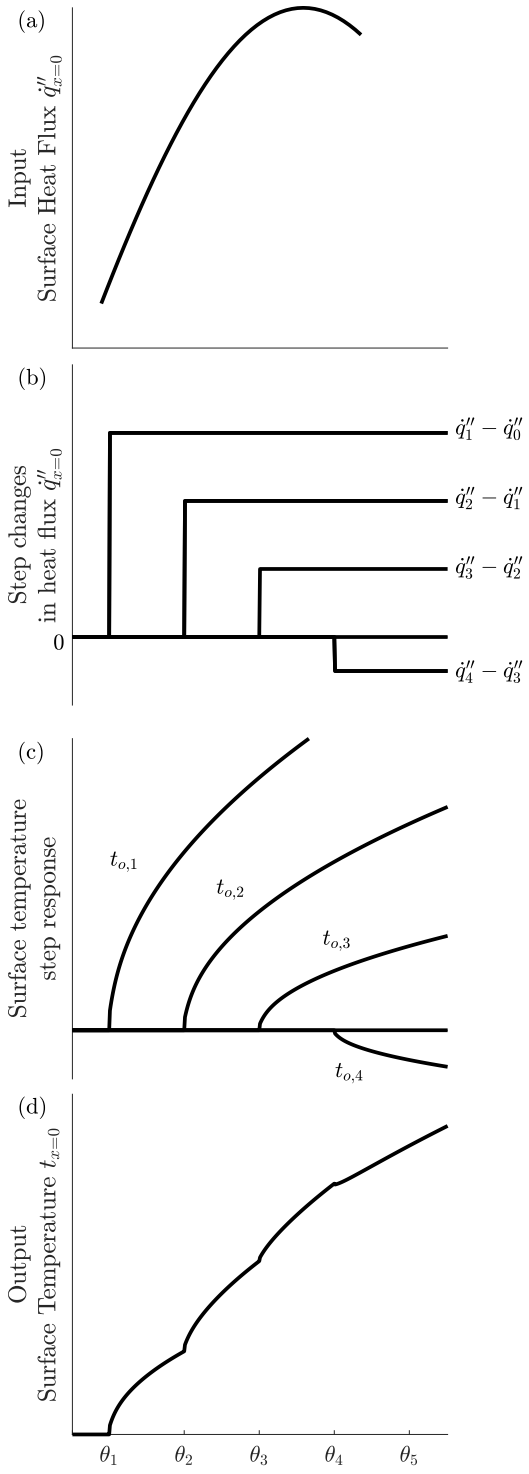

Figure 3.2: (a) Input continuous surface heat flux as a function of time approximated by (b) a series of step changes. (c) Output individual surface temperature step responses and (d) Total surface temperature is the sum of these step responses.

3.1.2 Initial Condition

By posing the problem with the boundary conditions (3.2) and (3.3) there will be a very long starting transient, that is it will take a large number of cycles to reach the periodic converged solution. For example, the imposition of a step change of heat flux $\bar{q}''$ to the surface will result (for a homogeneous wall) in an increase of surface temperature with a square root dependence on time [106]. This issue can be mitigated using the superposition framework. One can envision that for $\theta < 0$, there is a steady heat flux $\bar{q}''$ into the wall that establishes a steady, piece-wise linear temperature distribution. At time $\theta = 0$, the steady state heat flux will turn off, and it is replaced by the successive incremental step changes as discussed above. The net effect is the same as solving the problem with the initial temperature distribution of a steady state case.

3.1.3 Solution

The solution to the coated wall problem subject to a step change in heat flux can be found using the methodology established initially by Pipes [107] and later by Carslaw and Jaeger [105] based on taking the Laplace transform of Eq. (3.1). Using the notation $\hat{t}$ is the Laplace transform of surface temperature, and likewise $\hat{q}$ is the transform of surface heat flux, one can write for layer 1 the transformed general solution of the differential equation as

$$\hat{t}(x,s) = K_1 \cosh\left(x\sqrt{\frac{s}{\alpha}}\right) + K_2 \sinh\left(x\sqrt{\frac{s}{\alpha}}\right) \tag{3.6}$$

where K_1, K_2 are constants and α is thermal diffusivity. By differentiating equation (3.6) the general form of the heat flux becomes

$$\hat{q}(x,s) = -kK_1\sqrt{\frac{s}{\alpha}} \sinh\left(x\sqrt{\frac{s}{\alpha}}\right) - kK_2\sqrt{\frac{s}{\alpha}} \cosh\left(x\sqrt{\frac{s}{\alpha}}\right) \tag{3.7}$$

By evaluating $\hat{t}$ and $\hat{q}$ at $x = 0$ and $x = L_1$, and rearranging to eliminate constants K_1 and K_2 one gets

$$\hat{t}(0,s) = \underbrace{\left[\cosh\left(L_1\sqrt{\frac{s}{\alpha}}\right)\right]}_{A_1(s)}\hat{t}(L_1,s) + \underbrace{\left[\frac{\sinh\left(L_1\sqrt{\frac{s}{\alpha}}\right)}{k\sqrt{\frac{s}{\alpha}}}\right]}_{B_1(s)}\hat{q}(L_1,s) \tag{3.8}$$

$$\hat{q}(0,s) = \underbrace{\left[k\sqrt{\frac{s}{\alpha}}\sinh\left(L_1\sqrt{\frac{s}{\alpha}}\right)\right]}_{C_1(s)}\hat{t}(L_1,s) + \underbrace{\left[\cosh\left(L_1\sqrt{\frac{s}{\alpha}}\right)\right]}_{D_1(s)}\hat{q}(L_1,s) \tag{3.9}$$

Using the notation $\hat{t}_o(s) = \hat{t}(0,s)$ and $\hat{t}_1(s) = \hat{t}(L,s)$, and similarly for $\hat{q}$ one finds

$$\hat{t}_o(s) = A_1(s)\cdot\hat{t}_1(s) + B_1(s)\cdot\hat{q}_1(s) \tag{3.10}$$

$$\hat{q}_o(s) = C_1(s)\cdot\hat{t}_1(s) + D_1(s)\cdot\hat{q}_1(s) \tag{3.11}$$

or in matrix form:

$$\begin{bmatrix}\hat{t}_o\\ \hat{q}_o\end{bmatrix} = \begin{bmatrix}A_1(s) & B_1(s)\\ C_1(s) & D_1(s)\end{bmatrix}\begin{bmatrix}\hat{t}_1\\ \hat{q}_1\end{bmatrix} \tag{3.12}$$

The coefficients of the matrix in (3.12) can be written as

$$\begin{bmatrix}A_1(s) & B_1(s)\\ C_1(s) & D_1(s)\end{bmatrix} = \begin{bmatrix}\cosh\sqrt{sR_1C_1} & \frac{R_1}{\sqrt{sR_1C_1}}\sinh\sqrt{sR_1C_1}\\ \frac{\sqrt{sR_1C_1}}{R_1}\sinh\sqrt{sR_1C_1} & \cosh\sqrt{sR_1C_1}\end{bmatrix} \tag{3.13}$$

where $R_1 = \frac{L_1}{k_1}$ is the thermal resistance per unit area and $C_1 = L_1\rho_1 c_1$ is the volumetric heat capacity per unit area. The above relation (3.12) may also be written in the following form to take advantage of the known boundary conditions

$\hat{t}_1$ (ultimately at $x = L$) and $\hat{q}_o$

$$\begin{bmatrix} \hat{t}_o \\ \hat{q}_1 \end{bmatrix} = \begin{bmatrix} \frac{A_1D_1 - B_1C_1}{D_1} & \frac{B_1}{D_1} \\ -\frac{C_1}{D_1} & \frac{1}{D_1} \end{bmatrix} \begin{bmatrix} \hat{t}_1 \\ \hat{q}_o \end{bmatrix} \tag{3.14}$$

The first element of the transfer matrix can be simplified to

$$A_1D_1 - B_1C_1 = \cosh^2\sqrt{sR_1C_1} - \sinh^2\sqrt{sR_1C_1} = 1 \tag{3.15}$$

and in general $A_iD_i - B_iC_i = 1$ is the determinant of the matrix (3.13) for $i = 1..N$ layers. This approach can be extended to any number of layers

$$\begin{bmatrix} A(s) & B(s) \\ C(s) & D(s) \end{bmatrix} = \begin{bmatrix} A_1(s) & B_1(s) \\ C_1(s) & D_1(s) \end{bmatrix} \cdot \begin{bmatrix} A_2(s) & B_2(s) \\ C_2(s) & D_2(s) \end{bmatrix} \cdots \begin{bmatrix} A_N(s) & B_N(s) \\ C_N(s) & D_N(s) \end{bmatrix} \tag{3.16}$$

3.1.3.1 Methodology

The two-layer problem, which has been the physical model employed in the past for a coated wall, will be used to demonstrate the solution methodology. Later it will be extended to any number of layers. For a two-layer problem having a relatively thin coating and the metal wall as the second layer, the analogous form of Eq. (3.14) using the overall transfer matrix is

$$\begin{bmatrix} \hat{t}_o \\ \hat{q}_2 \end{bmatrix} = \begin{bmatrix} \frac{1}{C_1B_2 + D_1D_2} & \frac{A_1B_2 + B_1D_2}{C_1B_2 + D_1D_2} \\ -\frac{C_1A_2 + D_1C_2}{C_1B_2 + D_1D_2} & \frac{1}{C_1B_2 + D_1D_2} \end{bmatrix} \begin{bmatrix} \hat{t}_2 \\ \hat{q}_0 \end{bmatrix} \tag{3.17}$$

From matrix algebra the *transform* of surface temperature, $\hat{t}_o$, can be determined using Eq. (3.17). From Eq. (3.3), $\hat{t}_2 = 0$ and the Laplace transform of the Heaviside function of unity magnitude, *i.e.*, $\hat{q}_o$ (the magnitude of the heat flux step will be added later) is $\frac{1}{s}$. The surface temperature in the time domain is then found from

the *inverse transform* of $\hat{t}_o$, which can be written as

$$t_o(\theta) = \mathbf{1} \cdot \mathcal{L}^{-1} \left\{ \frac{1}{s} \frac{\frac{R_1}{\sqrt{sR_1C_1}} \sinh\sqrt{sR_1C_1} \cosh\sqrt{sR_2C_2} + \frac{R_2}{\sqrt{sR_2C_2}} \cosh\sqrt{sR_1C_1} \sinh\sqrt{sR_2C_2}}{\Lambda \sinh\sqrt{sR_1C_1} \sinh\sqrt{sR_2C_2} + \cosh\sqrt{sR_1C_1} \cosh\sqrt{sR_2C_2}} \right\} \tag{3.18}$$

where $\Lambda = \sqrt{\frac{R_2C_1}{R_1C_2}} = \sqrt{\frac{k_1\rho_1c_1}{k_2\rho_2c_2}}$ is the ratio of thermal inertia of the coating to the thermal inertia of the metal wall.

The inverse Laplace transform for the equation above is not readily available in transform tables. Problems of this kind can be approached in two different ways. The first is by applying multiple geometric series expansions to bring the transform into a form that is included in Laplace transform tables. This approach requires significant algebra and the result does not necessarily lend itself to engineering applications [105]. The second approach is to utilize the general Heaviside function of the inverse Laplace transform

$$t_o(\theta) = \mathbf{1} \cdot \frac{1}{2\pi j} \int_{\Omega - j\infty}^{\Omega + j\infty} \hat{t}(s) e^{s\theta} ds \tag{3.19}$$

where $j = \sqrt{-1}$ and the constant Ω is a large positive real number approaching infinity. The Cauchy residue theorem states that the above integral is equal $2\pi j$ times the sum of the residues of $\hat{t}(s)$ at the poles of $\hat{t}(s)e^{s\theta}$. Also, it has been shown that the branch cut of $\sqrt{sRC}$ does not include the negative real axis [108].

3.1.3.2 Two-layer Problem, $\Lambda \to 0$

The use of thin, low thermal conductivity, low-volumetric heat capacity coating materials is of high interest. The thermal inertia of thermal-swing coatings described above is quite low, and the resulting thermal inertia ratio for a typical metal wall is correspondingly small ($\Lambda \simeq 0.015 - 0.025$). This observation allows the assumption

of $\Lambda \to 0$ which in turn allows a simplification of Eq. (3.18) to

$$t_o(\theta) = \mathbf{1} \cdot \left[R_1 \cdot \mathcal{L}^{-1} \left\{ \frac{\sinh \sqrt{sR_1C_1}}{s\sqrt{sR_1C_1}\cosh \sqrt{sR_1C_1}} \right\} + R_2 \cdot \mathcal{L}^{-1} \left\{ \frac{\sinh \sqrt{sR_2C_2}}{s\sqrt{sR_2C_2}\cosh \sqrt{sR_2C_2}} \right\} \right] \tag{3.20}$$

Consider the function:

$$\Phi_i(s) = \frac{\sinh \sqrt{sR_iC_i}}{s\sqrt{sR_iC_i}\cosh \sqrt{sR_iC_i}} \tag{3.21}$$

where $i = 1, 2$. The function $\Phi(s)$ has poles at $s_o = 0$, and at $\sqrt{s_\nu R_i C_i} = \frac{2\nu-1}{2}\pi j$ where $\nu = 1, 2....$ The latter can also be written as $s_\nu = -\frac{(2\nu-1)^2}{4R_iC_i}\pi^2$. The simple pole at $s_o = 0$ for the function $\Phi_i(s)$ gives residue

$$\begin{aligned} \text{Res}\,(\Phi_i; s_o) &= \lim_{s\to s_o} \left[s \frac{\sinh \sqrt{sR_iC_i}}{s\sqrt{sR_iC_i}\cosh \sqrt{sR_iC_i}} e^{s\theta} \right] \\ &= \lim_{s\to 0} \left[\frac{\left(\sqrt{sR_iC_i}\right) + \frac{\left(\sqrt{sR_iC_i}\right)^3}{3!} + \ldots}{\sqrt{sR_iC_i}\left[1 + \frac{\left(\sqrt{sR_iC_i}\right)^2}{2!} + \ldots\right]} e^{s\theta} \right] \\ &= \lim_{s\to 0} \left[\frac{1 + \frac{\left(\sqrt{sR_iC_i}\right)^2}{3!} + \ldots}{1 + \frac{\left(\sqrt{sR_iC_i}\right)^2}{2!} + \ldots} e^{s\theta} \right] \\ &= 1 \end{aligned} \tag{3.22}$$

For the singularities at $s_\nu = -\frac{(2\nu-1)^2}{4R_iC_i}\pi^2$, one can write $\Phi(s) = \frac{f(s)}{g(s)}$, with $f(s) = \sinh \sqrt{sR_iC_i}$ and $g(s) = s\sqrt{sR_iC_i}\cosh \sqrt{sR_iC_i}$. The residue can then be found

as [108]

$$\begin{aligned}
\text{Res}\left(\Phi; s_\nu\right) &= \frac{f(s_\nu)}{\frac{dg}{ds}|_{s_\nu}} e^{s_\nu \theta} \\
&= \frac{\sinh \sqrt{sR_iC_i}}{\frac{3}{2}\sqrt{sR_iC_i}\cosh\sqrt{sR_iC_i} + \frac{sR_iC_i}{2}\sinh\sqrt{sR_iC_i}} e^{s_\nu \theta} \\
&= \frac{1}{\frac{1}{2}\left[\frac{2\nu-1}{2}\pi j\right]^2} e^{-\frac{(2\nu-1)^2}{4R_iC_i}\pi^2\theta} \\
&= -\frac{8}{\pi^2\left(2\nu-1\right)^2} e^{-\frac{(2\nu-1)^2}{4R_iC_i}\pi^2\theta}
\end{aligned} \tag{3.23}$$

Using the values of the residues predicted by Eq. (3.23) in Eq. (3.20), the surface temperature as a function of time for the two-layer problem with negligible thermal inertia ratio subjected to a unit step change of heat flux on the surface is obtained

$$\begin{aligned}
t_o(\theta) = \mathbf{1} \cdot \Bigg[& R_1 \left(1 - \frac{8}{\pi^2}\sum_{\nu=1}^{\infty} \frac{1}{\left(2\nu-1\right)^2} e^{-\frac{(2\nu-1)^2}{4R_1C_1}\pi^2\theta}\right) \\
& + R_2 \left(1 - \frac{8}{\pi^2}\sum_{\nu=1}^{\infty} \frac{1}{\left(2\nu-1\right)^2} e^{-\frac{(2\nu-1)^2}{4R_2C_2}\pi^2\theta}\right) \Bigg]
\end{aligned} \tag{3.24}$$

3.1.3.3 Multi-layer Problem

The overall transfer matrix of the multi-layer wall was given by (3.16) and recasting the problem in the manner that takes advantage of the known boundary conditions, Eq. (3.14), one gets

$$\begin{bmatrix} \hat{t}_o \\ \hat{q}_N \end{bmatrix} = \frac{1}{D}\begin{bmatrix} 1 & B \\ -C & 1 \end{bmatrix}\begin{bmatrix} \hat{t}_N \\ \hat{q}_o \end{bmatrix} \tag{3.25}$$

where, similar to the case of a single layer, the determinant $AD - BC$ is found to be unity. Using the fact that $\hat{t}_N = 0$, the above formula becomes $\hat{t}_o = \frac{B}{D} \cdot \hat{q}_o$. By applying a step impulse of heat flux with unity magnitude such that $\hat{q}_o = \mathbf{1} \cdot \frac{1}{s}$, the

corresponding function, Ψ, that needs to be inverse transformed is

$$\Psi = \frac{1}{s}\frac{B(s)}{D(s)} \tag{3.26}$$

There is a simple pole at $s_0 = 0$, but finding the roots of $D(s) = 0$ is non-trivial, especially as the number of layers gets large. Carslaw and Jaeger, however, have shown in a two-layer wall problem with different boundary conditions and unknowns that all of the roots lie on the negative real axis and are simple [105]. Therefore, numerical techniques can be employed to find and tabulate the roots unless other simplifying assumptions can be made.

The roots of $D(s) = 0$ can be found as $s = -\beta_m$ where $m = 1, 2...\infty$. Applying the residue theorem

$$\begin{aligned}
\mathcal{L}^{-1}\{\Psi\} &= \text{Res}(\Psi; 0) + \sum_{m=1}^{\infty} \text{Res}(\Psi; -\beta_m) \\
&= \lim_{s\to 0}\left[s\frac{1}{s}\frac{B(s)}{D(s)}e^{s\theta}\right] + \sum_{m=1}^{\infty}\left[\frac{B(-\beta_m)}{-\beta_m \frac{dD}{ds}|_{-\beta_m}}e^{-\beta_m\theta}\right] \\
&= \lim_{s\to 0}\left[\frac{B(s)}{D(s)}e^{s\theta}\right] - \sum_{m=1}^{\infty}\left[\frac{B(-\beta_m)}{\beta_m \frac{dD}{ds}|_{-\beta_m}}e^{-\beta_m\theta}\right] \\
&= \frac{B(0^+)}{D(0^+)} - \sum_{m=1}^{\infty}\left[\frac{B(-\beta_m)}{\beta_m \frac{dD}{ds}|_{-\beta_m}}e^{-\beta_m\theta}\right]
\end{aligned} \tag{3.27}$$

Additionally, it has been verified that for any number of layers the $\lim_{s\to 0^+} B(s) = B(0^+) = R_{\text{total}}$ and $\lim_{s\to 0^+} D(s) = D(0^+) = 1$. Finally, the surface temperature history as a function of time for a step impulse of heat flux is given by

$$t_o(\theta) = \mathbf{1}\cdot\left[R_{\text{total}} - \sum_{m=1}^{\infty}\frac{B(-\beta_m)}{\beta_m \frac{dD}{ds}\Big|_{-\beta_m}}e^{-\beta_m\theta}\right] \tag{3.28}$$

3.1.3.4 Step-change Comparison

A 1-D Crank-Nicolson finite difference code was used to verify the two-layer solution of (3.28) and to evaluate the limitations of the $\Lambda \to 0$ solution in (3.24) for a step-change in surface heat flux and a two-layer wall. At time $\theta = 0$, a 1 MW/m^2 step change of heat flux was imposed at $x = 0$. The finite difference code included 400 nodes in the coating and 601 nodes in the metal substrate, including the interface node. The simulation was performed up to a time equal to $2R_1C_1$, *i.e.,* twice the coating characteristic time scale using 5000 time steps.

Two test cases will be illustrated by way of example. The coating and wall materials for both cases are shown in Table 3.1 and they represent (1) a state-of-the-art thermal-swing (TS) coating, and (2) a traditional 8% YSZ coating [36]; in both cases the base material was aluminum and the total domain length was 5 mm. The TS coating was evaluated with a 100 μm thickness that gives a characteristic time scale of 11.4 ms. The YSZ coating was evaluated with a 100 μm thickness resulting in a characteristic time scale of 19.2 ms. Figure 3.3 shows the surface temperature as a function of time for the two coatings. For each case the finite difference, full inversion solution Eq. (3.28), and the low-Λ limit solution Eq. (3.24), curves are shown, with the former taken as the reference.

Figure 3.3 shows that the full inversion solution, which was calculated using just the first 100 roots, tracks the finite difference solution very closely. The low-Λ solution also shows reasonable agreement for the two cases, albeit with some error. This difference is expected given the finite values of Λ seen in Table 3.1. The YSZ coating, which has the larger value of Λ, shows worse agreement.

In order to evaluate the limits of the proposed low-Λ approximate solution, the RMS error - using the finite difference code as a reference - was calculated for a wide range of coating properties but fixed substrate properties (Aluminum, see Table 3.1). More specifically, for every Λ ranging from 0.01-0.05 the product of $k_1\rho_1c_1$ was held fixed. The time scale of the hypothetical coating was varied from 1-100 ms using the coating thickness. Figure 3.4 shows that Λ alone does not control the observed error, the coating time scale, R_1C_1 also affects the results. At a given

coating time scale, the error increases monotonically with Λ, as expected. However, for a constant value of Λ the error can be seen to decrease as the coating timescale increases. There appears to be a counter acting effect of R_1C_1 in Eq. (3.18); a similar effect may also be observed for R_2C_2, but that is of less practical interest. For all cases, the error is below 3.5% when Λ is less than 0.05.

Table 3.1: Properties of coating and engine wall materials.

	k $[W/(mK)]$	ρc $[J/(m^3K)]$	L $[\mu m]$	$\sqrt{k\rho c}\times 10^{-6}$ $[J/(m^2Ks^{0.5})]$	Λ [-]	RC $[ms]$
TS	0.35	0.4	100	0.374	0.015	11.4
YSZ	1.3	2.5	100	1.803	0.075	19.2
Aluminum	213	2.4	4900	23.85	-	-

3.1.4 Superposition

As discussed above in Section 3.1.1, the step-change solution can be used in conjunction with the principle of superposition in order to find the wall surface temperature given an arbitrary heat flux history. The surface temperature found using the full solution and low-Λ approximation are given, respectively, as

$$t_o(\theta_n) = \sum_{i=0}^{n} \left\{ \Delta\dot{q}_i'' \left[R_{\text{total}} - \sum_{m=1}^{\infty} \frac{B(-\beta_m)}{\beta_m \frac{dD(s)}{ds}\Big|_{-\beta_m}} e^{-\beta_m(\theta_n-\theta_i)} \right] \right\} \tag{3.29}$$

and

$$\begin{aligned} t_o(\theta_n) = \sum_{i=0}^{n} \Bigg\{ \Delta\dot{q}_i'' \cdot \Bigg[& R_1 \left(1 - \frac{8}{\pi^2} \sum_{\nu=1}^{\infty} \frac{1}{(2\nu-1)^2} e^{-\frac{(2\nu-1)^2}{4R_1C_1}\pi^2(\theta_n-\theta_i)} \right) \\ & + R_2 \left(1 - \frac{8}{\pi^2} \sum_{\nu=1}^{\infty} \frac{1}{(2\nu-1)^2} e^{-\frac{(2\nu-1)^2}{4R_2C_2}\pi^2(\theta_n-\theta_i)} \right) \Bigg] \Bigg\} \end{aligned} \tag{3.30}$$

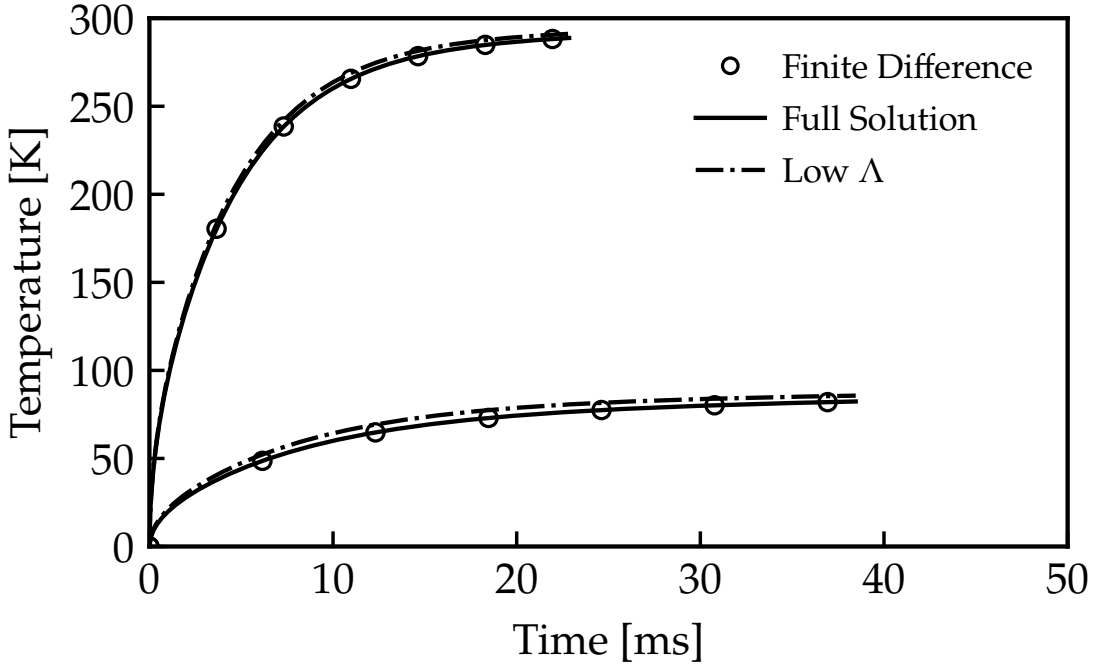

Figure 3.3: Transient surface temperature predicted by the full (solid) and approximate (dashdot) two-layer solution, and the finite difference code (circles) for a uniform initial temperature subjected to 1 MW/m^2 step-change in surface heat flux for TS and YSZ coatings.

where $\Delta\dot{q}''_i \equiv \left(\dot{q}''_i - \dot{q}''_{i-1}\right)$. In both cases, the heat flux history is discretized and the incremental step change in heat flux is multiplied by a response (shown in the square brackets) and summed over all previous times. Particular attention should be paid to the time summation (index i). At time $\theta_o = 0$, $\Delta q''_o = -\bar{q}'' + \dot{q}''_o$ as discussed in section 3.1.2. In the limit of long times in the past, the exponential terms go to zero and the response tends towards the total resistance, *i.e.* R_{total} in (3.29) and $R_1 + R_2$ in (3.30). This is related to the fact that after a certain amount of time has passed, the response to an earlier heat flux change has reached a steady state value.

Computationally, there are a few issues that one needs to address to maintain the desired efficiency. First, the number of roots to include in the solution needs to

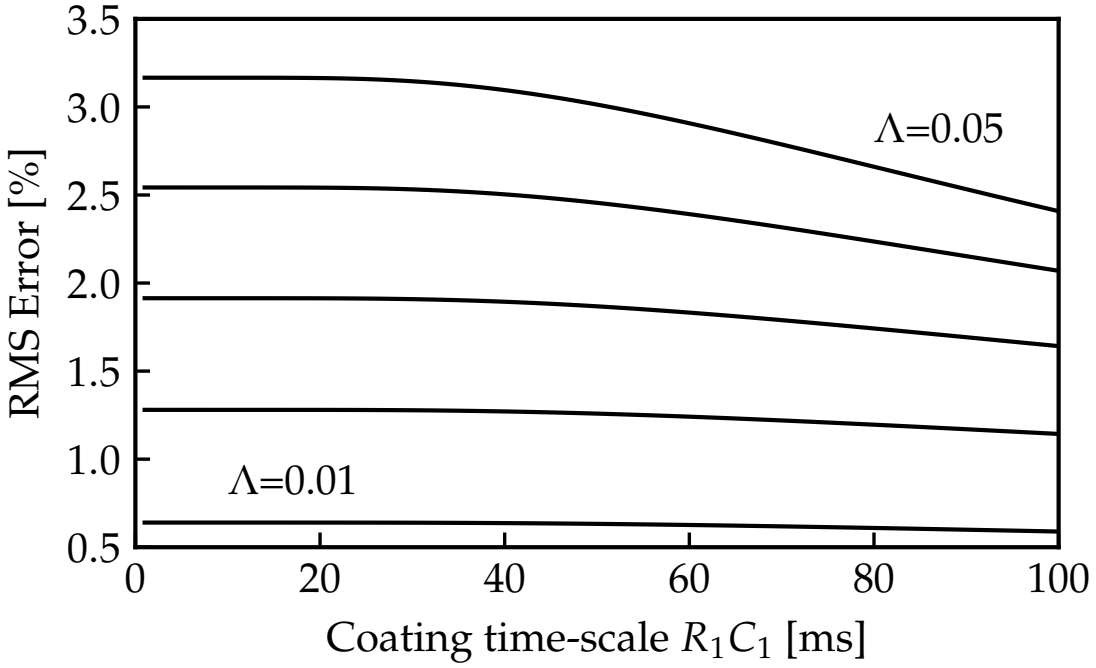

Figure 3.4: Validation of two-layer approximate solution. RMS error as a function of coating time scale RC for different thermal inertia ratios Λ

be limited to those that are necessary to ensure accuracy. For practical applications, the maximum root can be found to ensure a precision of ϵ for the smallest timestep so that: $e^{-\beta_{\max}\Delta\theta_{\min}} < \epsilon$. Second, the summation over time (index i) only needs to be performed until the response function has reached its steady state value. Since the numerical analysis and tolerance handling is identical between the step-change and the triangular-pulse method, the reader is encouraged to see Section 3.2 for further details.

After some manipulation and application of the superposition principle, the wall surface temperature at time θ_n is given, as

$$t_o(\theta_n) = t_c + \left(\bar{q}'' + \sum_{i=0}^{n} \Delta\dot{q}_i''\right) R_{\text{total}} - \sum_{i=0}^{n} \Delta\dot{q}_i'' \cdot X_{\text{step}}\left(\theta_n - \theta_i\right) \tag{3.31}$$

where the response, $X_{\text{step}}(\theta_n - \theta_i)$, describes the decay of the effect of the step change in heat flux that occurred from time i to time n and is given by

$$X_{\text{step}}(\theta_n - \theta_i) = \sum_{m=1}^{\infty} \frac{B(s)\big|_{s=-\beta_m}}{\beta_m \frac{dD(s)}{ds}\Big|_{s=-\beta_m}} e^{-\beta_m(\theta_n - \theta_i)} \tag{3.32}$$

The first term of Eq. (3.31) imposes the backside wall temperature boundary condition, and the second provides an initial condition that takes into account the converged steady solution of the wall subjected to a periodic condition having a net mean heat flux $\bar{q}''$. This considerably shortens the time needed to reach steady state, and is widely employed in finite difference solutions. In addition, the summation for the last term of (3.31) starts at zero even though this would require knowing heat flux at negative time. This is done to account for the transient effect of effectively removing the mean heat flux that led to the second term in (3.31), see above for details. Thus, the zeroth element of $\Delta\dot{q}''$ needs to be set as $\Delta\dot{q}''_o = -\bar{q}'' + \dot{q}''_o$. In the limit of long times in the past, the response factor X_{step} converges to zero - as this will be evident later, so the net effect is that the second and third terms becomes zero.

By way of example, a simulated in-cylinder heat flux was constructed as the sum of a sinusoidal function and a Gaussian as shown in Fig. 3.5. The positive portion of the sinusoid represents the compression and expansion, and the negative portion represents the heat flux reversal that occurs during the intake stroke. The Gaussian term simulates the effect of combustion, and the Gaussian was phased so that it would peak at the same time as the positive sinusoid. Figure 3.5 shows one cycle of the simulated heat flux for a case with a peak Gaussian heat flux of 3 MW/m^2, a sinusoid magnitude of 0.25 MW/m^2, an equivalent of 1500 rpm engine speed, and a Gaussian full-width at half-maximum value of 5.9 ms. A three-layer wall was considered. Layer 1 was a 100 μm TS coating, layer 2 was a YSZ coating of 150 μm, and layer 3, the remainder of the domain, was aluminum. The total domain length was 5mm. The surface temperature was calculated using both (3.29) and the finite difference code mentioned above.

The full and finite difference solution for the three-layer problem is shown in Fig. 3.6. Two different cycles are shown. The first cycle was shown in a dashed line with the symbols being the finite difference solution. Excellent agreement is seen between the two solutions. The first cycle is shown to highlight the treatment of the initial condition. The finite difference temperature domain was initialized using the steady solution derived from the cycle-mean heat flux, $\bar{q}''$ which is known in this case. The full inversion solution starts at time zero with a heat flux step of $-\bar{q}''$ as discussed in Section 3.1.2. It can be seen that virtually identical results are observed. The converged cycle shown in Fig. 3.6 is only shown for the full solution, but the agreement with the finite difference solution was excellent. Convergence was obtained in just a few cycles.

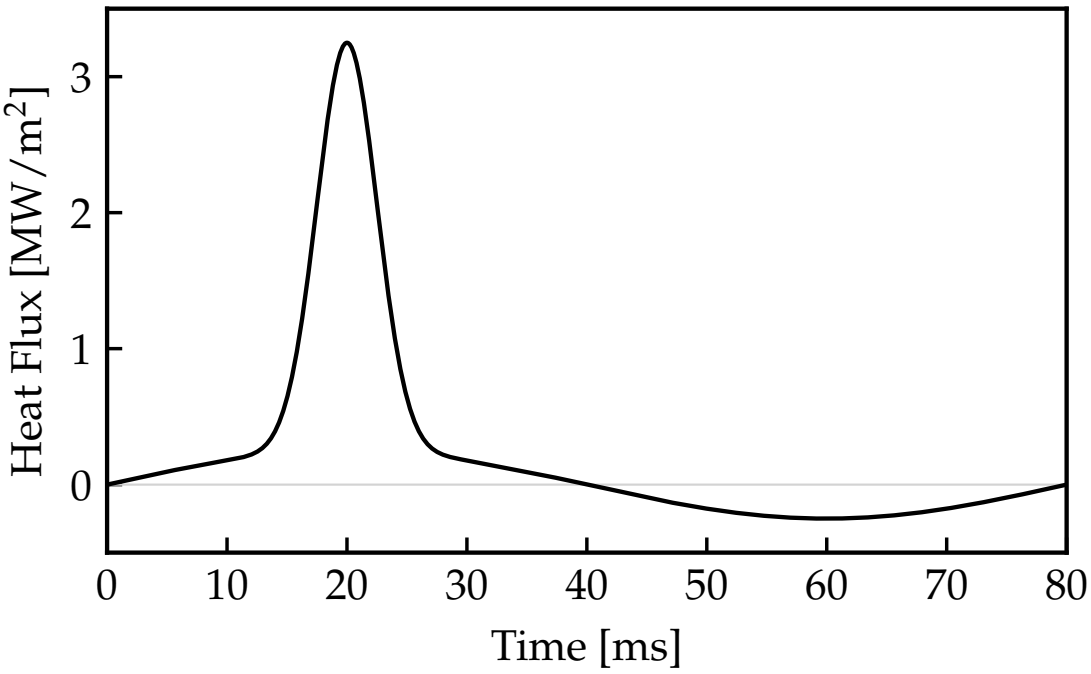

Figure 3.5: Gaussian added to a sinusoidal surface heat flux input

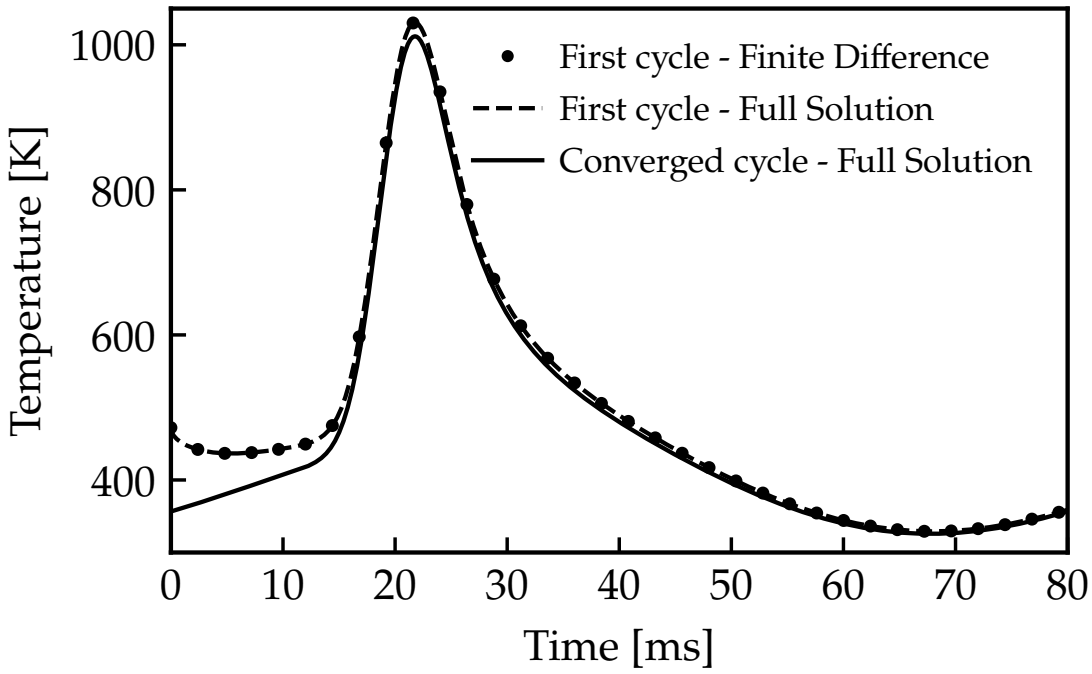

Figure 3.6: Surface temperature as a function of time for a three-layer problem (for material properties, see text) subjected to a prescribed surface heat flux

3.1.5 Step Response

The step response, X_{step}, shown in Eq. (3.32), is the summation of the product of a fraction that is purely material/structure dependent and an exponential term that depends on both structure and the lapsed time interval. The roots or poles, β_m, which are the locations where $D(s) = 0$, have the same nature as eigenvalues, therefore it is important that none are missed. In practice, the step response can be pre-calculated and tabulated *a priori* provided that the time step of the simulation is known.

Two test cases will be shown by way of demonstration. The first case represents a state-of-the-art thermal-swing coating [36] referred to hereafter as the TS case. The second case represents a four-layer wall that consisted of a traditional yttria-stabilized zirconia (YSZ) coating, a gradient layer, and a bond coat [49]. The

thermophysical properties and coating thicknesses are shown in Table 3.2. In both cases the engine wall was aluminum [109] and the total domain length remained fixed at 5 mm.

The first 15 roots were calculated for both coating structures. Figure 3.7 (top), shows the corresponding function $D(s)$ for the TS coating, with the roots of the equation marked on the x axis. Likewise, Fig. 3.7 (bottom), shows the results for the YSZ coating. It is seen that the roots of $D(s) = 0$ (indexed as m) are sequentially (and substantially) more negative as m increases - note that Fig. 3.7 uses the square root of β_m on the abscissa. Therefore the terms of the summation over m diminish in importance due to the exponential term at large m. Additionally, $D(s)$ is seen to oscillate and some roots are located very close to one another. For the two test cases illustrated above, the first 15 roots of $D(s) = 0$ are given in Table 3.3.

Table 3.2: Material properties of coatings and engine wall.

Layer	k [W/m-K]	$\rho c \times 10^{-6}$ [J/m^3-K]	L [μm]
TS	0.35	0.4	100
YSZ	0.77	1.8	210
Gradient	0.85	1.5	70
Bond	4.07	0.9	70
Aluminum	123	2.8	(bal. for 5mm)

The number of roots required for accuracy depends on many factors, but in general the goal is to find the minimum number to save computational cost (again, this is pre-computed so computational time is not too important). The fraction in the summation is useful for assessing whether one has found all of the roots, *i.e.*, roots have not been missed if they are close together, such as the 4^{th} and 5^{th} root in Fig. 3.7 for both the two- and four-layer wall. It is required that

$$\sum_{m=1}^{\infty} \frac{B(s)\big|_{s=-\beta_m}}{\beta_m \frac{dD(s)}{ds}\Big|_{s=-\beta_m}} \simeq R_{\text{total}} \tag{3.33}$$

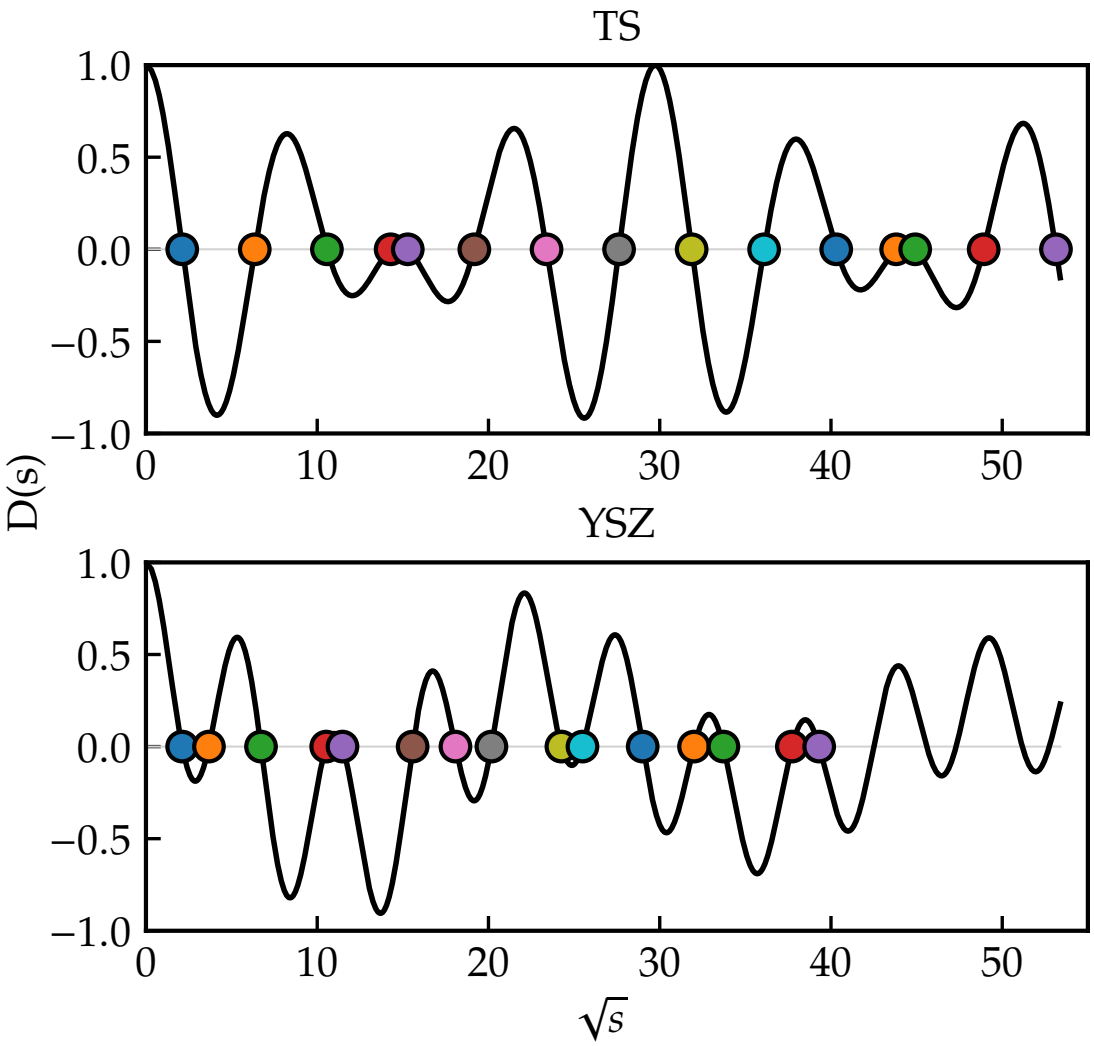

Figure 3.7: $D(s)$ with zeros identified for a two-layer coating (top) and four-layer coating (bottom) on cylinder engine wall. See Table 3.2 for material properties.

Table 3.3: First fifteen roots $-\beta_m$ of the two- and four-layer test cases

	Two-layer			Four-layer		
m	$-\beta_m$	$B\big\|_{s=-\beta_m}$	$\frac{dD(s)}{ds}\Big\|_{-\beta_m}$	$-\beta_m$	$B\big\|_{s=-\beta_m}$	$\frac{dD(s)}{ds}\Big\|_{-\beta_m}$
1	-4.49	$+2.610 \times 10^{-5}$	$+1.70 \times 10^{-2}$	-4.47	$+4.222 \times 10^{-5}$	$+11.13 \times 10^{-2}$
2	-40.35	-1.090×10^{-5}	-0.45×10^{-2}	-13.53	-19.688×10^{-5}	-5.77×10^{-2}
3	-111.64	$+1.190 \times 10^{-5}$	$+0.15 \times 10^{-2}$	-45.13	$+0.816 \times 10^{-5}$	$+5.36 \times 10^{-2}$
4	-204.10	-7.870×10^{-5}	-0.03×10^{-2}	-110.77	-3.521×10^{-5}	-1.38×10^{-2}
5	-233.72	$+5.290 \times 10^{-5}$	$+0.03 \times 10^{-2}$	-131.70	$+1.678 \times 10^{-5}$	$+1.28 \times 10^{-2}$
6	-367.67	-0.609×10^{-5}	-0.09×10^{-2}	-242.47	-0.406×10^{-5}	-2.03×10^{-2}
7	-547.19	$+0.287 \times 10^{-5}$	$+0.13 \times 10^{-2}$	-326.58	$+4.284 \times 10^{-5}$	$+1.23 \times 10^{-2}$
8	-763.21	-0.198×10^{-5}	-0.13×10^{-2}	-406.94	-0.381×10^{-5}	-1.31×10^{-2}
9	-1015.26	$+0.175 \times 10^{-5}$	$+0.11 \times 10^{-2}$	-588.51	$+0.643 \times 10^{-5}$	$+0.67 \times 10^{-2}$
10	-1302.93	-0.198×10^{-5}	-0.08×10^{-2}	-649.72	-1.648×10^{-5}	-0.61×10^{-2}
11	-1624.53	$+0.340 \times 10^{-5}$	$+0.04 \times 10^{-2}$	-841.33	$+0.248 \times 10^{-5}$	$+0.97 \times 10^{-2}$
12	-1918.92	-3.450×10^{-5}	-0.01×10^{-2}	-1024.23	-1.677×10^{-5}	-0.56×10^{-2}
13	-2017.59	$+1.310 \times 10^{-5}$	$+0.01 \times 10^{-2}$	-1136.92	$+0.342 \times 10^{-5}$	$+0.57 \times 10^{-2}$
14	-2392.78	-0.223×10^{-5}	-0.04×10^{-2}	-1422.39	-0.360×10^{-5}	-0.47×10^{-2}
15	-2823.46	$+0.123 \times 10^{-5}$	$+0.06 \times 10^{-2}$	-1545.29	$+1.139 \times 10^{-5}$	$+0.41 \times 10^{-2}$

in a steady-state limiting case. By defining a suitable error criterion, one can assess whether all of the roots have been found.

Assuming that all of the roots have been found, then this term can also be used to assess how many roots are required for maintaining sufficient accuracy. There is an infinite set of β_m's and all of them should be included for complete accuracy. For practical purposes, the question that arises is how large a root β_m must be before it can be neglected (due to the vanishing nature of the exponential term). For a cut-off root, $\beta_{\max}$ the contribution of $\beta_{\max}$ is at most $e^{-\beta_{\max}\Delta\theta}$ where $\Delta\theta$ is the timestep. To ensure a precision of 5×10^{-5} one can neglect contribution from those roots for which

$$e^{-\beta_{\max}\Delta\theta} < 5 \times 10^{-5} \simeq e^{-10} \tag{3.34}$$

or

$$\beta_{\max} \cdot \Delta\theta > 10 \tag{3.35}$$

Note, small time steps require additional roots for the response function calculation.

The response functions for the TS and YSZ coating are shown in Fig. 3.8. The plot abscissa was chosen to emphasize the fact that the response represents the importance of *previous* heat flux events on the *current* surface temperature. The response was calculated using 100 roots and a time step of 0.128 ms, which corresponds to 1 crank angle at 1300 rpm. Under these conditions, for the TS coating $\beta_{100} \cdot \Delta\theta$=17.33, suggesting excellent accuracy. The response curves for the two cases are both seen to monotonically decrease with lapsed time, which indicates that the effect of a heat flux event dies out in time. The two curves start at a different point on the ordinate because the first value corresponds to R_{total}, which is different for the two coating structures.

The major difference between the two curves is the rapid initial change of the TS coating response followed by a more slowly decreasing tail, whereas the YSZ coating has a more sustained decaying response. This behavior is driven by the large difference in time scales for the TS coating and base wall; for the YSZ coating the time scales are much closer. The overall time required to achieve an attenuation of the response function that is 10 % of the initial value is equivalent to slightly less than 0.5 cycles at 1300 rpm for the TS coating and 2.5 cycles for the YSZ coating.

Figure 3.8 embodies all of the conduction physics of the problem, and it should be used as a guide when coating design in engines is undertaken. Consider the steady operating case where the heat flux is the same every cycle as an example. The contribution of the last cycle on the surface temperature for the TS coating has attenuated by $\simeq$ 90%, see the circle in Fig. 3.8. In comparison, for the YSZ coating, the attenuation is much less, only $\simeq$ 60% as denoted by the square. In order to achieve a similar attenuation between the TS coating at one cycle, one needs to wait 3.5 cycles with the YSZ coating, shown by the triangle in Fig. 3.8. Alternatively, the TS coating *forgets* the majority of the contribution of a heat flux event within one cycle at 1300 rpm, but it takes the YSZ coating 3.5 cycles to forget the same heat flux event.

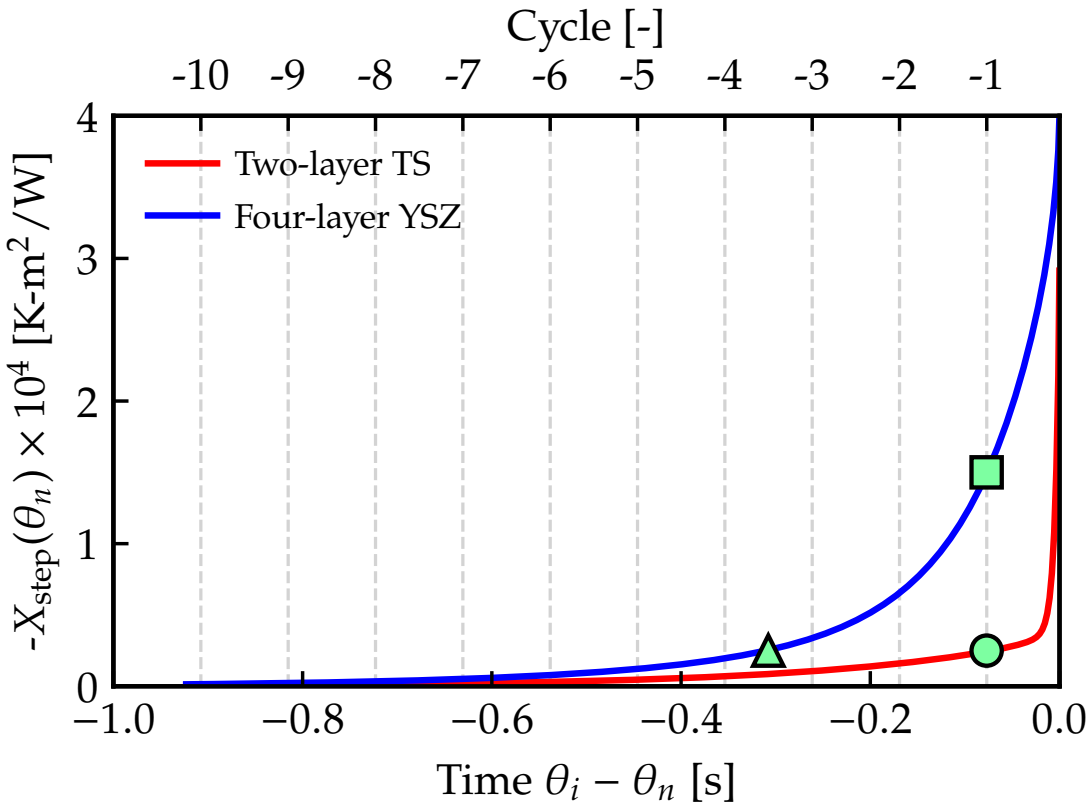

Figure 3.8: Step response X_{step} as a function of negative time for a two-layer TS and a four-layer YSZ coating. The total time shown corresponds to 10 cycles at 1300 rpm.

3.1.6 Dimensional Analysis

The mathematical form of Eq. (3.30) suggests a way to non-dimensionalize the two-layer problem of interest subjected to periodic heat fluxes, similar to those found in internal combustion engines. The amplitude of the surface temperature swing over a cycle should be normalized by the maximum heat flux swing and total resistance, $R_{total} = R_1 + R_2$, to give a non-dimensional temperature swing, Θ, as

$$\Theta = \frac{t_{\max} - t_{\min}}{\left(\dot{q}''_{\max} - \dot{q}''_{\min}\right) R_{\text{total}}} \tag{3.36}$$

The maximum heat flux swing was chosen to bound the value to unity. There are three independent parameters that arise from (3.30): Ξ, Ω_1, and Ω_2, given by

$$\Xi \equiv \frac{R_1}{R_2} \tag{3.37}$$

$$\Omega_1 \equiv f R_1 C_1 \tag{3.38}$$

$$\Omega_2 \equiv f R_2 C_2 \tag{3.39}$$

where f is the frequency corresponding to the periodic excitation. It has been verified that over a wide range of R_i, C_i, and f, chosen in a way that Ξ, Ω_1, and Ω_2 are held constant, the dependent parameter Θ is also constant for both the full inversion and low-Λ solutions.

The utility of this approach will be demonstrated by assuming a sinusoidally varying heat flux imposed at x=0. The fact that there are three independent parameters makes visualization difficult. In practice, one wants to know the ability of the surface temperature to swing to follow the imposed heat flux as the frequency of oscillation and coating properties change. A series of two-layer simulations were performed using the full solution where Ξ and Ω_1 were varied while Ω_2 was held constant. This approach was taken to allow simple visualization of the results. The substrate material properties (R_2 and C_2) are normally fixed while the coating properties are adjusted in the design phase; note Ω_2 can still change via f.

Figure 3.9 shows results for Ω_2=28.5 (left) Ω_2=142 (right). The first thing to notice is that the effect of Ω_2 is very small for the range of conditions tested. The conditions were chosen to be representative of internal combustion engines with thermal-swing coatings, *i.e.*, $R_1 > R_2$ and $R_1 C_1 << R_2 C_2$. Therefore, the effect of excitation frequency change can be, more or less, isolated to Ω_1. Either graph in Fig. 3.9 can then be taken to give the general solution to this problem.

Consider first the case of increasing the coating thickness by a factor of four

with all other geometric and material properties held fixed. The response to this change is complicated. The value of Ξ increases by four; Ω_1 increases by a factor of 16; and Ω_2 remains constant. For the situation where the initial case has Ξ=5, Ω_1=0.1, and Ω_2=28.5, shown as the open circle in Fig. 3.9, the modified state has Ξ=20, Ω_1=1.6, and Ω_2=28.5, shown as the star in Fig. 3.9. For this change, Θ would decrease from 0.81 to 0.30. The actual temperature swing, however, would *increase* by about 50% due to the increase in R_1. The coating is less efficient, but gives the desired effect of higher temperature swings.

Another typical case is the response of a fixed system to changes in frequency of the input, which corresponds to a change in the engine speed. Starting from the same initial point as the previous example, an increase in speed by a factor of five would result in Ξ=5, Ω_1=0.5, and Ω_2=142, shown as the triangle in Fig. 3.9. In this scenario, Θ decreases from 0.81 to 0.53, which gives a corresponding *decrease* in temperature swing. This underscores that thermal-swing coatings reduce their effectiveness at higher frequency.

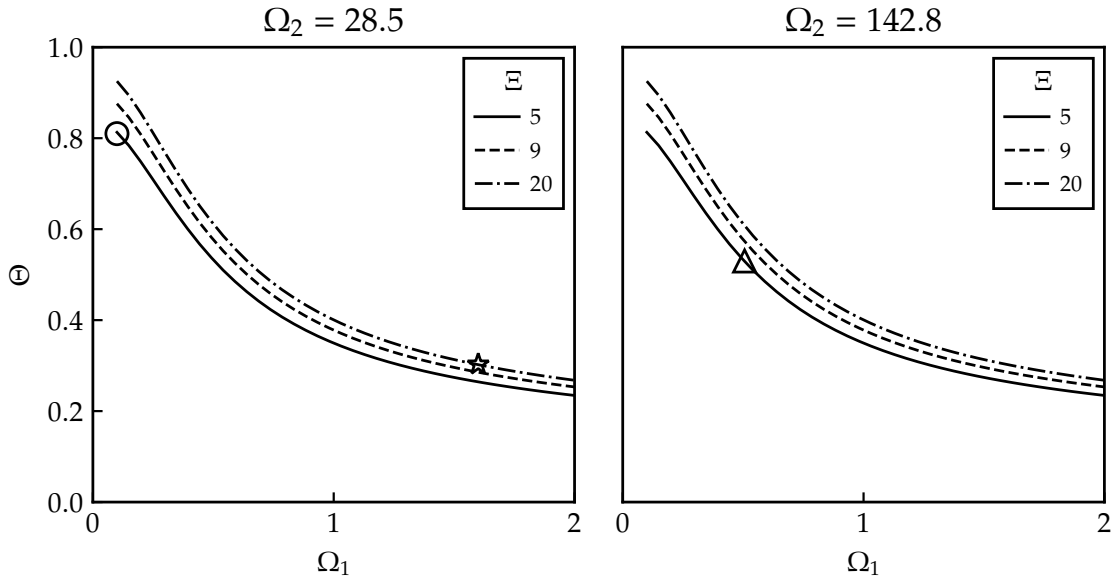

Figure 3.9: Dimensionless response of two-layer wall subjected to a sinusoidal heat flux.

3.1.6.1 Equivalant Pseudo-materials with Dynamic Similarity

In the recent paper "Numerical approach to define a thermodynamically equivalent material for the conjugate heat transfer simulation of very thin coating layers" by P. Olmeda, X. Margot, P. Quintero, J. Escalona, Int. J. Heat Mass Transfer 162 (2020) 120377 the authors develop a procedure to identify a thicker pseudo-material to mimic the dynamic response of a thin thermal barrier coating. A thicker layer is desired to allow efficient conjugate heat transfer analysis. They employ an *ad hoc* procedure for defining the thermal properties of the material to approximate dynamic similarity with low grid resolution. The analytical solution discussed above for this same problem allows the pseudo-material's thermal properties to be directly determined without a trial-and-error approach. The approach is elucidated and the effects of numerical resolution are explored.

Using the solution shown in this section with minimal assumptions the thermal properties of two pseudo-materials that provide full dynamic similarity can be directly obtained for coatings like those of interest for engines, and explore the effects of numerical resolution.

In Section 3.1.3.2 a multi-layer wall is considered, but a special-case analytical solution is given for a two-layer (one coating layer and the metal substrate) problem in the limit of $\Lambda \equiv \sqrt{\frac{R_2 C_1}{R_1 C_2}} \rightarrow 0$, where $R \equiv \frac{L}{k}$ is the resistance, $C \equiv \rho c L$ is the capacitance, L is the layer thickness, and the subscript 1 and 2 refer to the coating and substrate, respectively. For the conditions of Olmeda *et al.*, listed as the baseline case in Table 3.4, $\Lambda = 0.0055$, easily satisfying the constraint.

Following the analysis given previously, full dynamic similarity is achieved when the independent dimensionless parameters Ξ, Ω_1, and Ω_2 are matched between the baseline and scaled cases, which will be referred to using superscripts A and B, respectively, and f is the forcing frequency, which does not affect the results. Because the desire is to match the *dimensional* temperature at the surface, there is also a constraint that the total resistance, $R_1 + R_2$ needs to be matched. The last (fifth) mathematical constraint is that the total length of the wall, $L = L_1 + L_2$, should not change. The (six) unknown values are: $k_1^B, k_2^B, (\rho c)_1^B, (\rho c)_2^B, L_1^B, L_2^B$. The

Table 3.4: Baseline material properties, pseudo-material properties, and scaled pseudo-material properties from this work.

	Baseline [1]	Proposed	Scaled
k_1 [W/m-K]	0.1	1.546	1.0
k_2 [W/m-K]	144	-	75.8
$(\rho c)_1$ [J/m^3-K]	10^5	3769	10^4
$(\rho c)_2$ [J/m^3-K]	2.3×10^6	-	4.37×10^6
L_1 [mm]	0.1	2.0	1.0
L_2 [mm]	1.9	-	1.0

[1] k_2 and $(\rho c)_2$ based on other published work by same group [110]

problem is solved by the *a priori* selection of L_1^B to be a value suitable for the conjugate heat transfer analysis, as discussed more fully below. After some simple algebra, one finds

$$k_1^B = \frac{L_1^B}{L_1^A} k_1^A \tag{3.40}$$

$$k_2^B = \frac{L_2^B}{L_2^A} k_2^A \tag{3.41}$$

$$(\rho c)_1^B = \frac{L_1^A}{L_1^B} (\rho c)_1^A \tag{3.42}$$

$$(\rho c)_2^B = \frac{L_2^A}{L_2^B} (\rho c)_2^A \tag{3.43}$$

There are two ways to apply this analysis to the problem for the application of Olmeda *et al*. The first method, which is not favored, is to assume a single characteristic length for the conduction path through the piston (L_2^A) and a value of L_1^B that provides the desired grid resolution. The procedure above would then give the pseudo-coating and pseudo-piston properties. The piston is, however, three dimensional and defining a single characteristic length will add error.

The second approach, which will be demonstrated below and follows the example of Olmeda *et al.*, just replaces the piston material near the surface with

pseudo-materials 1 and 2 and leaves the remainder of the piston as its original material. In accordance with [94], a 2 mm zone will be replaced; they deemed that 2 mm was large enough to provide reasonably shaped finite element nodes but small enough to not adversely affect the prediction of the energy flow through the piston in the CHT solution. Further, to enable the most efficient possible meshing, the two pseudo-materials are chosen to have the same thickness. Table 3.4 shows the properties of the pseudo-materials resulting from the dimensional analysis, termed *Scaled*, and the values proposed by Olmeda *et al.*, termed *Proposed*.

A simple 1D example is used to illustrate the differences in these approaches. The domain length was 2.0 mm with one edge of the domain held at 430 K and the other subjected to a periodic (in time) Gaussian heat flux pulse

$$\frac{q''}{q''_{\max}} = \exp\left[-\left(\frac{t-\tau/2}{\tau/\alpha}\right)\right] \tag{3.44}$$

where τ is the cycle time, taken as 80 ms to match [94], and the width parameter, α, was included to allow frequency content of the forcing function to be varied. The fully resolved cases utilized 1024 nodes in material 1 and 512 nodes in material 2 (when present). Under-resolved cases will be described in terms of dx_1/L and dx_2/L, where dx_i is the node size in material i. For example, dx_1/L=0.125 and dx_2/L=0.25 corresponds to four nodes in material 1 and two nodes in material 2. In order to achieve a converged result, the cycle was repeated until the maximum difference in surface temperature relative to the prior cycle was less than 10^{-6} K. Unless otherwise stated, $q''_{\max} = 10^6$ W/m^2 and $\alpha = 16$.

Figure 3.10 shows the fully resolved surface temperature for the baseline, scaled and proposed cases from Table 3.4. It can be seen in Fig. 3.10 that the baseline and scaled cases match perfectly. The proposed case, however, shows substantial differences; the dynamic response of the wall is incorrectly predicted. This is a result of the incomplete dynamic similitude provided by the proposed solution. The principal argument of Olmeda *et al.* is that at lower spatial resolution the numerical errors will compensate for this mismatch in the physics.

Figure 3.11 shows the surface temperature error, relative to the fully resolved

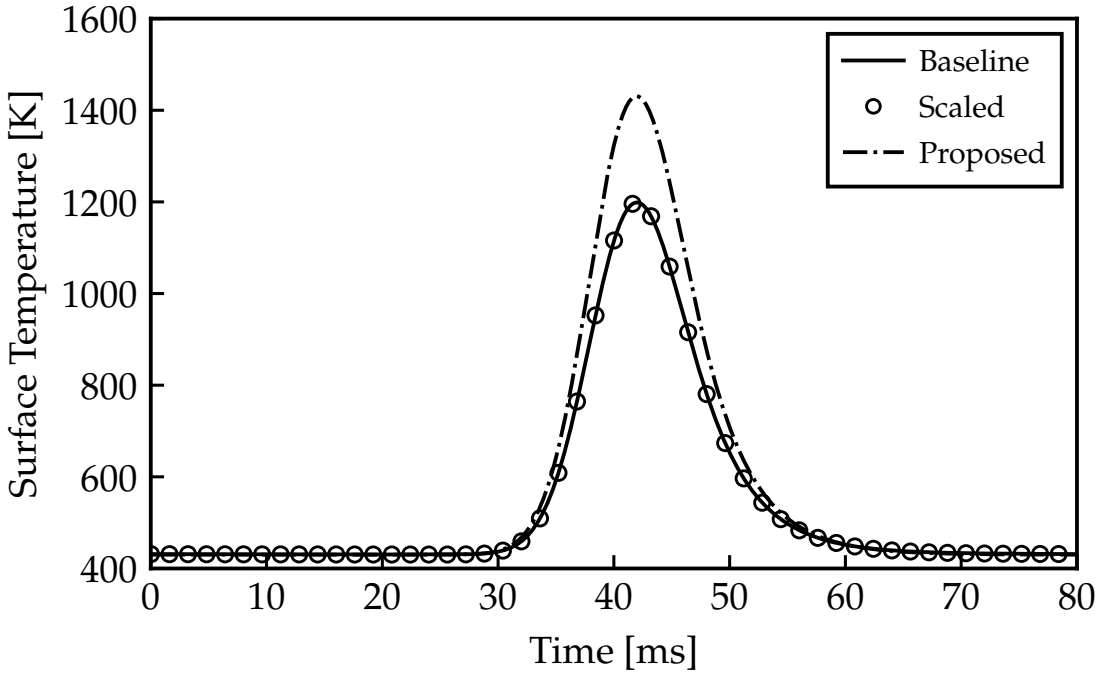

Figure 3.10: Comparison of fully resolved results for baseline coating, scaled solution, and proposed single pseudo-material.

baseline case, for the scaled properties. These cases were run with dx_2/L=0.25, *i.e.*, 0.5 mm node size, which represents a worst case. As seen from the very low error for dx_1/L=0.03125, the material 2 spatial resolution has a very small effect on the results. Figure 3.11 shows that better than 1% accuracy can be achieved with a resolution of just dx_1/L=0.125, which corresponds to just six nodes across the two materials. The same results for the proposed material (recall that there is only a single material for this case) are shown in Fig. 3.12. The error is significantly larger, which is consistent with Figure 3.10, but does not show a strong sensitivity to numerical resolution. There is a delay in the peak as the resolution decreases, which will feed back error when a prescribed gas temperature and heat transfer coefficient boundary condition are used.

The effect of the frequency content of the applied heat flux is demonstrated

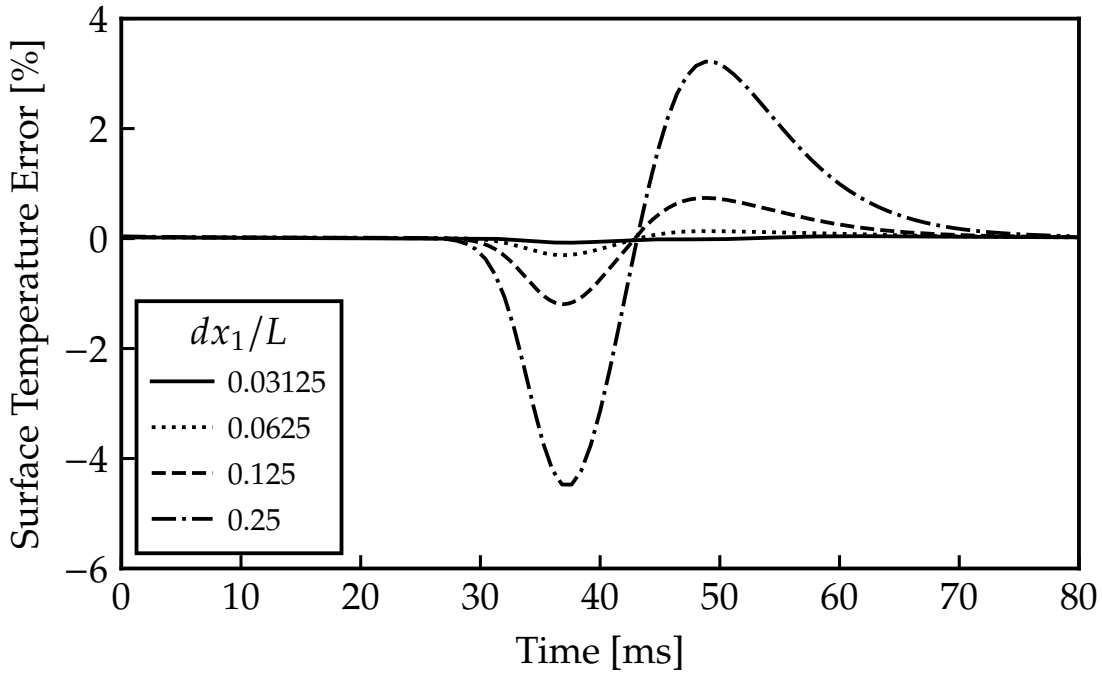

Figure 3.11: Surface temperature error for the scaled properties at the given nodal resolutions. All data have dx_2/L=0.25.

in Figure 3.13 where the parameter α was adjusted while τ was held constant. It should be noted that the highest value of α in Fig. 3.13 corresponds to a Gaussian pulse of 65 μs full width at half maximum, which is much faster than standard engine conditions. The scaled results were all performed with dx_2/L=0.25. The scaled results show an expected pattern of increased error as the forcing frequency increased, and that this error is mitigated by increasing the grid resolution. Based on these results, one would say that excellent results could be obtained for all practical engine conditions with dx_1/L=0.0625, which corresponds to 10 total nodes in the 2 mm nearest the surface. The single-layer proposed method of Olmeda *et al.* shows a beneficial response of reducing error with increasing forcing frequency, but the results are not improved with increasing spatial resolution. In fact, Olmeda *et al.* define different material properties as the grid resolution is changed [94].

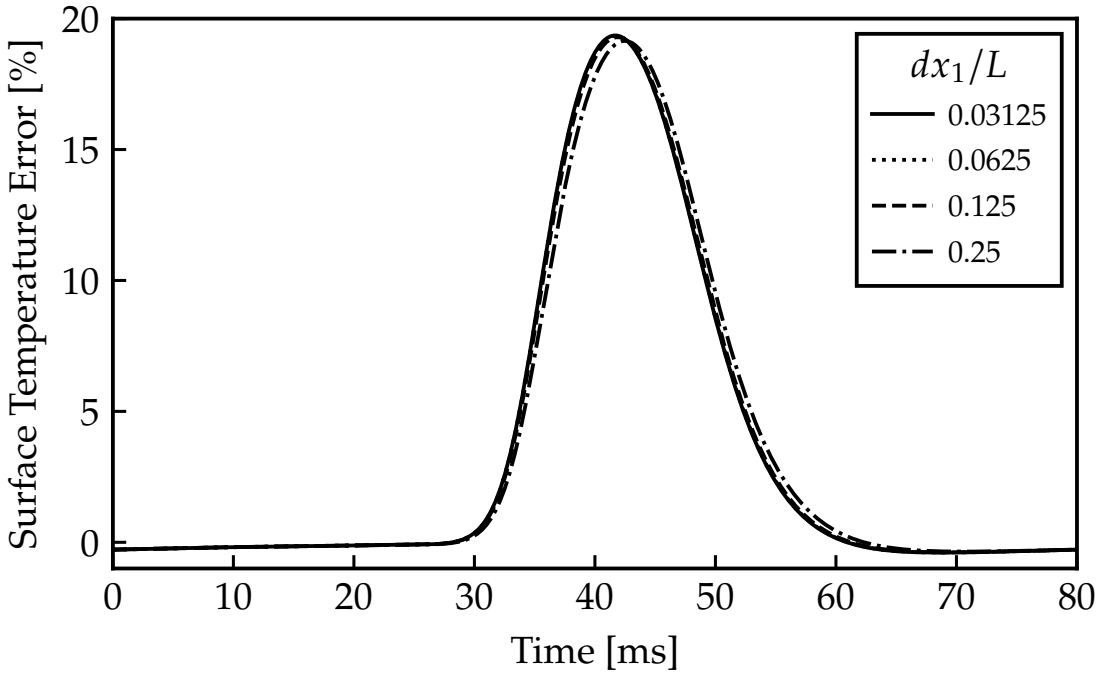

Figure 3.12: Surface temperature error for the proposed properties at the given nodal resolutions.

Overall, the method described herein is an improvement on that of Olmeda *et al.* because: its application only involves applying Eqs. (3.40) thru (3.43); it is based on the fundamental physics of the problem as compared to an *ad hoc* optimization procedure; and it performs better over all conditions tested.

3.1.7 Summary and Conclusions

The problem of a plane, coated wall with a time-varying heat flux applied to one surface and the other held at a constant temperature was investigated analytically under the assumption of one-dimensional heat flow in a plane wall with constant thermo-physical properties. The problem is linear, and superposition was used to determine the input surface temperature. The applied heat flux was discretized into a series of step changes, and surface temperature was found by combining

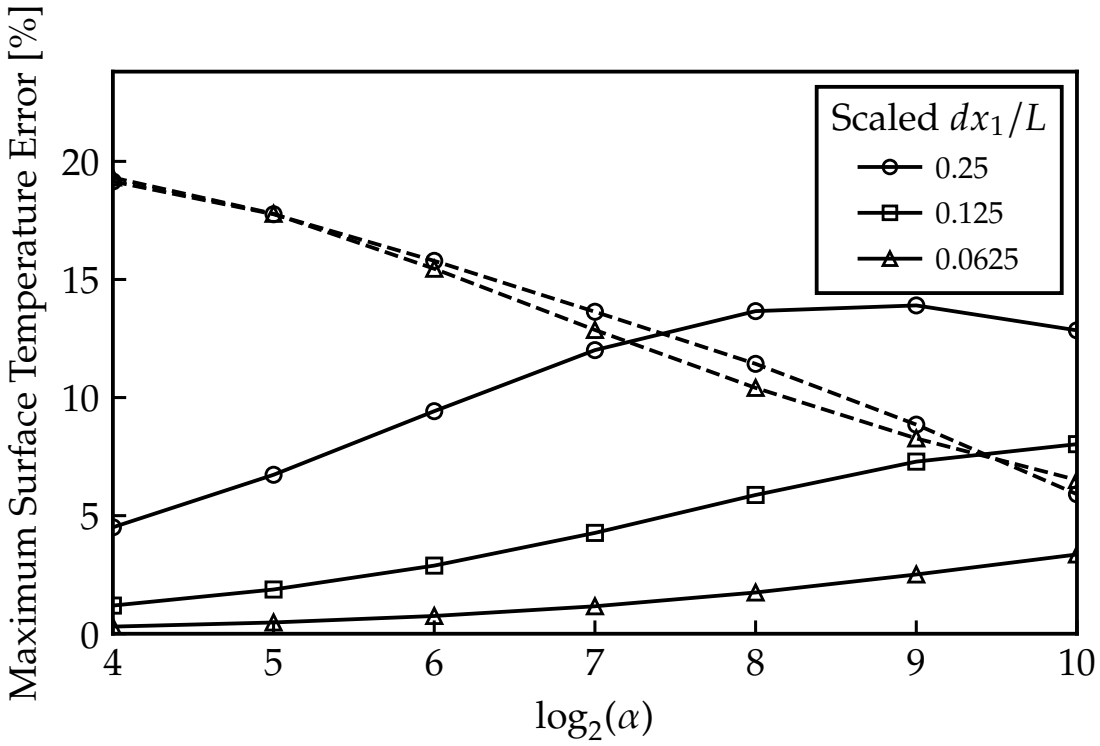

Figure 3.13: Maximum surface temperature error as a function of forcing frequency for different spatial resolution, denoted by symbol shape. The scaled results are shown in solid lines and the proposed results are in dashed lines.

the solutions for a single step change of heat flux. Two solutions were obtained to the step-change problem, the full solution and one found under the additional assumption that the coating's thermal inertia $\sqrt{k\rho c}$ was much less than that of the substrate, which is valid for thermal-swing coatings. The solutions were obtained using the matrix method in conjunction with the 1-D Laplace transformed heat diffusion equation. The full solution method, which is extendable to any number of layers, relies on the numerical evaluation of roots to invert to the time domain. The low-Λ solution is fully analytical, but is limited to a single coating layer.

The low-Λ analytical solution served as the basis of a non-dimensionalization of the general problem of a two-layer wall subjected to a periodic heat flux. Three

independent dimensionless parameters were derived; for thermal-swing type coatings only two were practically relevant. The dependent parameter was the surface temperature swing, which was normalized by the total wall resistance and the maximum swing in the surface heat flux. The dimensionless system was demonstrated for a sinusoidal imposed heat flux, and several examples of its utility were provided.

3.2 Triangular-pulse solution

In the previous section, the step-change approximation was used to provide the surface temperature. While the step response is conceptually intuitive, it has accuracy limitations. The primary accuracy concern originates from the step itself; it will always be lagging one step back. The step-change solution output depends only on the previous input heat flux. However, with the triangular-pulse method discussed below the solution output can depend on the previous *and* the current input.

An improved analytical solution to the transient heat conduction problem of thermal barrier coatings in reciprocating internal combustion engines is presented in this section. The current technique provides a solution to the problem of both domain-end boundary conditions being functions of time, and approximates the applied boundary conditions as a series of triangular pulses that combine to give a piece-wise linear approximation. Transfer functions are derived for any interface location, not just the surface, and rely only on the material architecture, *i.e.* material thermal properties and thickness. The analytical approach is developed first, then it is demonstrated for a simplified scenario, this is followed by an evaluation of all interface temperature histories for a full drive cycle with an emphasis on assessing the computational efficiency. Finally, surface responses are explored in the frequency domain to provide a comprehensive understanding of the coating performance.

3.2.1 Unit Triangular Pulse

In engine heat transfer analysis, the boundary conditions are not known as a continuous function. Rather, temperature or heat flux data are provided only in a discrete fashion from a numerical solution. The boundary conditions can be approximated as sequential step changes, as in Section 3.1, or straight-line interpolation. It has been shown that linear interpolation is equivalent to the sum of triangular pulses and offers higher accuracy than the step-change method [111, 112, 113].

Heat flux and temperature signals contain a large number of frequency components. Figure 3.14 shows how an ideal continuous function is approximated as discrete via the step-change and linear interpolation approximation methods. It is clear that the step function approximation method would require smaller time steps than the linear interpolation method to give the same accuracy. In the linear interpolation approximation method, two adjacent triangular time-based pulses (shown with red dashed lines) are overlapped and their sum forms a trapezoidal pulse (straight red line) of width Δ.

A triangular pulse is built from three time-interval ramp functions, as shown in Fig. 3.15,

$$\begin{aligned} p(\theta_n) &= 0, && \text{for} \quad \theta_n \leq 0 \\ &= y_1 = \frac{\theta_n}{\Delta}, && \text{for } 0 < \theta_n \leq \Delta \\ &= y_1 + y_2 = 2 - \frac{\theta_n}{\Delta}, && \text{for } \Delta < \theta_n \leq 2\Delta \\ &= y_1 + y_2 + y_3 = 0, && \text{for} \quad \theta_n > 2\Delta \end{aligned} \tag{3.45}$$

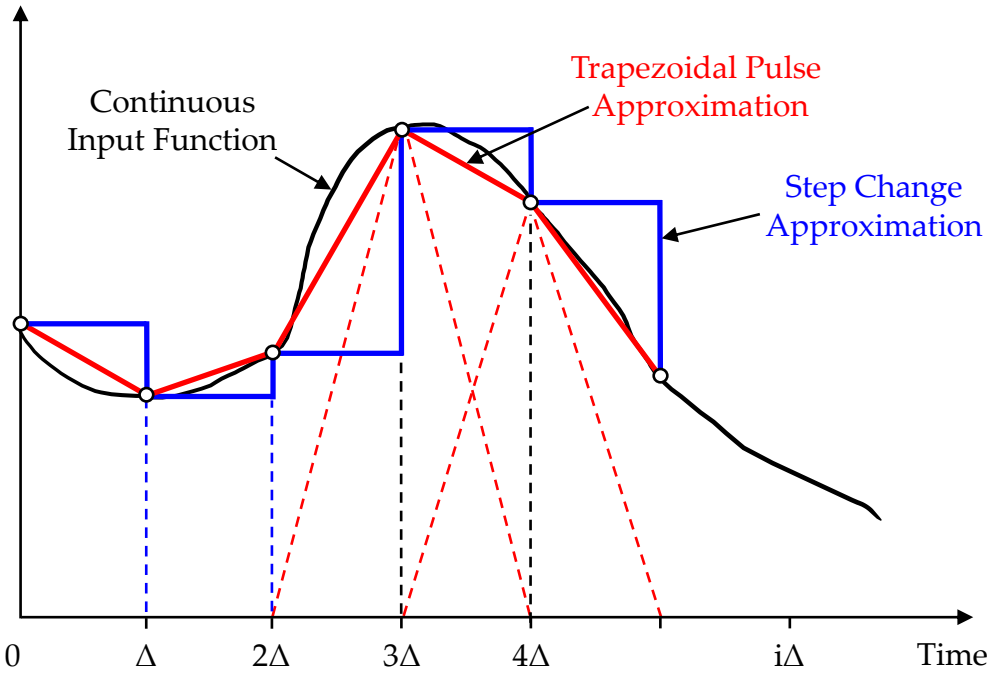

Figure 3.14: Representation of a continuous (black) boundary condition input as successive step changes (blue) and the sum (solid red) of two trapezoidal pulses (dashed red), shown on a time step Δ basis.

The Laplace transform of $p(\theta_n)$ is given by

$$
\begin{aligned}
y_1 &= \frac{1}{\Delta}\theta \overset{\mathcal{L}}{\longleftrightarrow} \hat{y}_1 = \frac{1}{\Delta s^2} \\
y_2 &= \frac{-2}{\Delta}(\theta - \Delta) \overset{\mathcal{L}}{\longleftrightarrow} \hat{y}_2 = \frac{-2}{\Delta s^2} e^{-s\Delta} \\
y_3 &= \frac{1}{\Delta}(\theta - 2\Delta) \overset{\mathcal{L}}{\longleftrightarrow} \hat{y}_3 = \frac{1}{\Delta s^2} e^{-2s\Delta}
\end{aligned} \tag{3.46}
$$

and by overlapping the ramp transform functions in the same manner as in time-

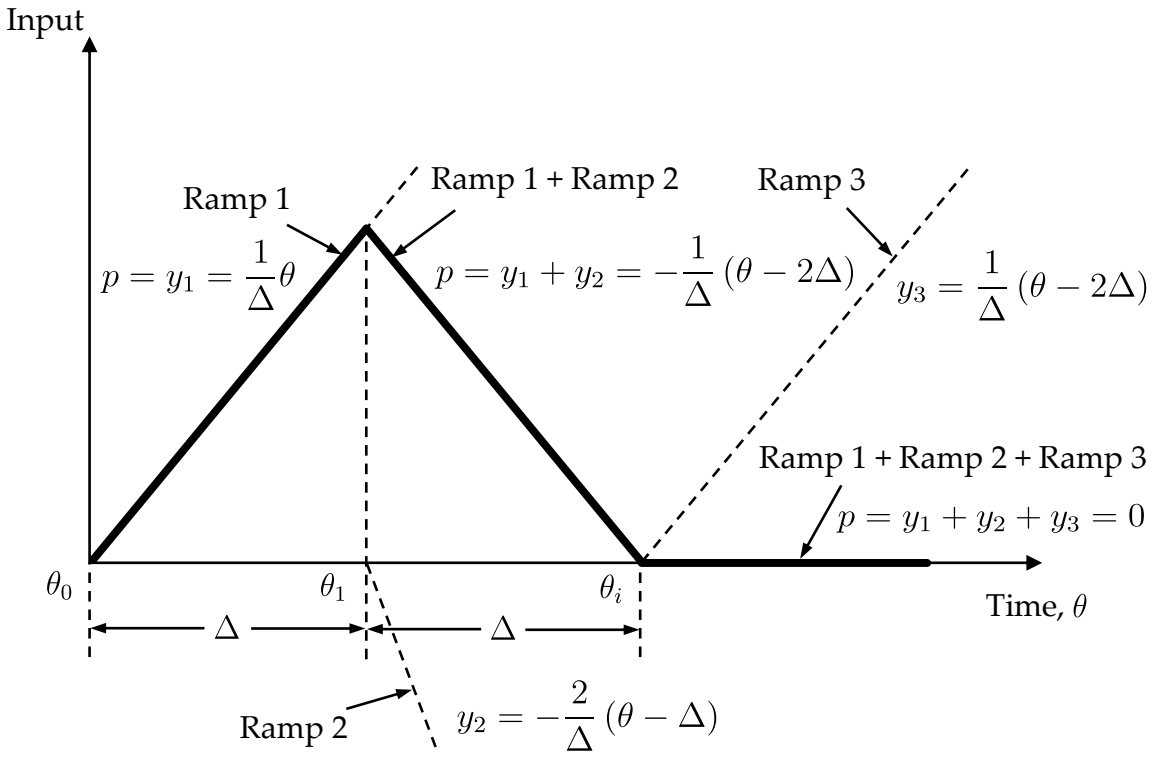

Figure 3.15: Unit triangular pulse composed of three time-based ramp functions [112].

domain, the resulting triangular transform function becomes

$$\begin{aligned} \hat{p}(s) &= \frac{1}{\Delta s^2}, && \text{for } 0 < \theta_n \leq \Delta \\ &= \frac{1}{\Delta s^2}\left(1 - 2e^{-s\Delta}\right), && \text{for } \Delta < \theta_n \leq 2\Delta \\ &= \frac{1}{\Delta s^2}\left(1 - e^{-s\Delta}\right)^2, && \text{for } \theta_n > 2\Delta \end{aligned} \tag{3.47}$$

where s is the Laplace transform variable.

3.2.2 Surface Temperature Subject to Unsteady Combustion Chamber Surface Heat Flux and Backside Surface Temperature

3.2.2.1 Residue-Calculus Laplace Transform Inversion

Using the notation $\hat{t}_o$ is the Laplace transform of the gas-side surface temperature, and likewise $\hat{q}_o$ is the Laplace transform of the combustion-chamber surface heat flux, one can write for an engine wall composed of any number of layers

$$\begin{bmatrix} \hat{t}_o \\ \hat{q}_o \end{bmatrix} = \begin{bmatrix} A & B \\ C & D \end{bmatrix} \begin{bmatrix} \hat{t}_N \\ \hat{q}_N \end{bmatrix} \tag{3.48}$$

where N is the number of layers and $\hat{t}_N$ and $\hat{q}_N$ are the transform of t and $\dot{q}''$ at the coolant/oil surface. The coefficients of the matrix in Eq. (3.48) define the *overall* transfer matrix that is comprised of the product of transfer matrices of each individual layer, see Eq. (3.16). The transfer matrix for each layer is defined earlier as Eq. (3.13).

The overall equation for the multilayer wall is given in Eq. (3.25). The combustion surface temperature transform, subject to transient combustion heat flux and coolant temperature, is

$$\hat{t}_o = \left(\frac{B}{D}\right)\hat{q}_o + \left(\frac{1}{D}\right)\hat{t}_N \tag{3.49}$$

and must be inverted from the frequency to time domain using the Laplace transform residue-calculus inversion technique. The difference from Section 3.1 is that $\hat{t}_N \neq 0$ as previously assumed.

The two terms in Eq. (3.49) share a common denominator, D; the numerator includes the triangular pulse $\hat{p}$, since $\hat{q}_o = \hat{p} \cdot q_o$ and $\hat{t}_N = \hat{p} \cdot t_N$, scaled by either B (heat flux) or unity (back-side temperature), and can be cast as

$$\Psi = \left(\frac{\hat{p}\psi}{D}\right) \tag{3.50}$$

Utilizing the general formula of the inverse Laplace transform, one gets

$$\mathcal{L}^{-1}\{\Psi\} = \frac{1}{2\pi j}\int_{\gamma-j\infty}^{\gamma+j\infty} \Psi \cdot e^{s\theta} ds \tag{3.51}$$

where $j = \sqrt{-1}$ and the constant γ is a large positive real number approaching infinity. Inverse transforms of this kind are neither listed in standard tables nor given by computer software packages (even for a relatively simple two-layer problem). The residue theorem provides a powerful tool to evaluate integrals such as Eq. (3.51) as the sum of the residues at the poles of Ψ. A complete derivation of an inversion for the step-change input solving only the transient combustion chamber heat flux can be found in Section 3.1 along with an analytical solution for the limit of negligible coating thermal inertia.

Following the same approach as Section 3.1.3.3,

$$\mathcal{L}^{-1}\{\Psi\} = \text{Res}(\Psi; 0) + \sum_{m=1}^{\infty} \text{Res}(\Psi; -\beta_m) \tag{3.52}$$

where the first term arises from singularities at $s = 0$, and the second term represents the residues at the poles $s = -\beta_m$.

There is a double pole at $s = 0$ when the triangular approximation is used. Using Eq. (3.47) the residue is given by

$$\begin{aligned} \text{Res}(\Psi; 0) &= \left[\frac{\psi}{D}\right]_{s=0} + \frac{1}{\Delta}\frac{d}{ds}\left[\frac{\psi}{D}\right]_{s=0}, \text{ for } 0 < \theta_n \leq \Delta \\ &= \quad\quad - \frac{1}{\Delta}\frac{d}{ds}\left[\frac{\psi}{D}\right]_{s=0}, \text{ for } \Delta < \theta_n \leq 2\Delta \\ &= 0, \quad\quad\quad\quad\quad\quad\quad\quad \text{for} \quad \theta_n > 2\Delta \end{aligned} \tag{3.53}$$

since

$$\frac{d}{ds}\left[\frac{\psi}{D}\right]_{s=0} = \left[\frac{\frac{d\psi}{ds}}{D} - \frac{\psi\frac{dD}{ds}}{D^2}\right]_{s=0} \tag{3.54}$$

The second term of the right-hand side of Eq. (3.52) represents the summation of all residues that lie on the negative real axis as described in Section 3.1. Finding the pole locations β_m requires numerical evaluation because $D(s) = 0$ becomes transcendental for walls with more than a single layer [114, 108]. The residues at $s = -\beta_m$ are

$$\begin{aligned}
\text{Res}\left(\Psi; -\beta_m\right) &= \Omega_m \cdot e^{-\beta_m \Delta}, && \text{for } 0 < \theta_n \leq \Delta_0 \\
&= \Omega_m \cdot \left(1 - 2e^{\beta_m \Delta}\right) \cdot e^{-2\beta_m \Delta}, && \text{for } \Delta < \theta_n \leq 2\Delta \\
&= \Omega_m \cdot \left(1 - e^{\beta_m \Delta}\right)^2 \cdot e^{-i\beta_m \Delta}, && \text{for } \quad \theta_n = n\Delta > 2\Delta
\end{aligned} \tag{3.55}$$

where

$$\Omega_m = \frac{\psi(s)\big|_{s=-\beta_m}}{\Delta\beta_m^2 \frac{dD}{ds}\Big|_{s=-\beta_m}} \tag{3.56}$$

The inverse functions $X(\theta) = \mathcal{L}^{-1}\{\Psi(\psi = B)\}$ and $Y(\theta) = \mathcal{L}^{-1}\{\Psi(\psi = 1)\}$ at discrete times $\theta_n = n\Delta$ $(n = 0, 1, 2...)$ for unit magnitude of p are found by

evaluating (3.52) with (3.53) and (3.55)

$$
\begin{aligned}
X_i(\theta_o) \text{ or } Y_i(\theta_o) &= \left[\frac{\psi}{D}\right]_{s=0} + \frac{1}{\Delta}\frac{d}{ds}\left[\frac{\psi}{D}\right]_{s=0} \\
&\quad + \sum_{m=1}^{\infty} \Omega_m \cdot e^{-\beta_m \Delta}, \text{ for } n = 0 \\
X_i(\theta_1) \text{ or } Y_i(\theta_1) &= -\frac{1}{\Delta}\frac{d}{ds}\left[\frac{\psi}{D}\right]_{s=0} \\
&\quad + \sum_{m=1}^{\infty} \Omega_m \cdot \left(1 - 2e^{\beta_m \Delta}\right) \cdot e^{-2\beta_m \Delta}, \text{ for } n = 1 \\
X_i(\theta_n) \text{ or } Y_i(\theta_n) &= \sum_{m=1}^{\infty} \Omega_m \cdot \left(1 - e^{\beta_m \Delta}\right)^2 \cdot e^{-(n+1)\beta_m \Delta}, \text{ for } n = 2, 3, \ldots
\end{aligned}
\tag{3.57}
$$

where the subscript $i = 0$, refers to the combustion chamber surface. The full solution for t_o using the time-dependent X_o and Y_o responses will be discussed below.

The values of B, D, $\frac{dB}{ds}$ and $\frac{dD}{ds}$ need to be known at $s = 0$ and $s = -\beta_m$ ($m = 1, 2\ldots$) where β_m are the roots of D, *i.e.*, $D(s = -\beta_m) = 0$, which lie on the negative real-axis as shown by Carlslaw and Jaeger [105]. The transfer matrix and its analytical derivative with respect to the frequency variable can be found in Section 3.2.5.

Multilayer walls result in transcendental characteristic equation $D(s) = 0$ that must be solved numerically. The root-finding algorithm involves scanning between the range $0 < \beta \leq \beta_{\max}$, where the value of cut-off frequency $\beta_{\max}$ can be estimated. The contribution of the $\beta_{\max}$ term to X or Y is at most $e^{-\beta_{\max}\Delta}$ where Δ is the time step. To ensure a precision of 5×10^{-5}, for example, one can safely neglect the contribution from those roots for which $e^{-\beta_{\max}\Delta} < 5 \times 10^{-5}$ or $\beta_{\max}\Delta > 10$.

It is critical that all of the roots up to and including $\beta_{\max}$ are identified. If a root is missed, energy conservation cannot be satisfied. The steady state case limiting scenario, *i.e.*, $\dot{q}''_o$ and t_N are constants, requires the summation of X_o and Y_o to approach the total thermal resistance and unity, respectively. A useful check is to

ensure that

$$\sum_{j=0}^{n_x} X_{o,j} = R_{\text{total}} \tag{3.58}$$

and

$$\sum_{j=0}^{n_y} Y_{o,j} = 1 \tag{3.59}$$

where the subscript $0, j$ refers to the combustion chamber surface at timestep j, where $0 \leq j < n_x$ and $0 \leq j < n_y$ with n defined as the summation term of the response X and Y, respectively. The wall surface temperature solution for the time of interest θ_n can then be found as

$$t_o(\theta_n) = \sum_{j=0}^{n_x} X_{o,j} \cdot \dot{q}''_{o,\theta_n - j\Delta} + \sum_{j=0}^{n_y} Y_{o,j} \cdot t_{N,\theta_n - j\Delta} \tag{3.60}$$

where X_i and Y_i come from Eq. (3.57). The summation corresponds to the contribution of all previous pulses for both heat flux and backside temperature. Equation (3.60) can be seen as the convolution (denoted with $\circledast$) of the unsteady combustion surface heat flux $\dot{q}''_o$ with X_o and the convolution of the coolant surface temperature t_N with Y_o, as

$$t_o(\theta_n) = X_o \circledast \dot{q}''_o + Y_o \circledast t_N \tag{3.61}$$

The convolution can be found quickly using a Fast Fourier Transform (FFT, $\mathcal{F}$), *e.g.*, $X_o \circledast \dot{q}''_o = \mathcal{F}^{-1}\left\{\mathcal{F}\left\{X_o\right\} \cdot \mathcal{F}\left\{\dot{q}''_o\right\}\right\}$. A computational efficiency comparison to a standard finite difference scheme is given below.

Convergence is defined by both the number of summations terms included in the X and Y time-series and the number of roots in Eq. (3.57), which are functions of the wall properties. Convergence criteria can be established to estimate the practical number of roots and response function duration.

The poles of *single* layered engine walls have a pure analytic form

$$\beta_m = \frac{\pi^2 (2m+1)^2}{4RC} \tag{3.62}$$

A straightforward substitution of the roots shown above to the procedure developed earlier could reveal wall temperature for any *single* layered engine wall. For multi-layered walls, the roots are found numerically.

The root-finding algorithm evaluates $D(\beta)$ at each step. When the current value of $D(\beta)$ changes sign compared to the previous value, an iteration procedure initiates to identify the precise root location in that interval. During root searching, some pairs of roots may be very close to each other. If the interval is large enough, the root-finding algorithm will step over this pair without detecting any sign change of $D(\beta)$. Reducing the step size to become unreasonably small to capture this pair or roots might not be the optimal solution. The transfer matrix element C can be utilized in the root finding search. It has been shown that a root of $C(\beta)$ exists between each root of $D(\beta)$ [115]. Keeping track of the sign changes between the functions C and D, large steps could be taken without missing pairs of roots [115]. A uniform step of 0.5 Hz provided sufficient results for a wide variety of traditional and modern coatings on top of typical reciprocating engine walls of power cylinder components.

3.2.2.2 Initial Conditions

Engine walls with large thermal mass, *e.g.*, thick coatings on steel substrates, require a long time for the wall to heat up. Solving a cyclic heat conduction problem solely with the boundary conditions shown in Eq. (3.2)-(3.5) will require a large number of cycles to reach the periodic converged solution. Finite difference approaches have the same issue. An appropriate initial condition can mitigate this transient period by starting from an approximate steady state condition.

The general solution given in Eq. (3.61) can be expanded to include initial

conditions as

$$t_o(\theta_n) = \bar{q}''_o \left(R_{\text{total}} - \sum_{j=0}^{n_x} X_{o,j} \right) + X_o \circledast \dot{q}''_o + t_{\text{N,ini}} \left(1 - \sum_{j=0}^{n_y} Y_{o,j} \right) + Y_o \circledast t_N \tag{3.63}$$

where $\bar{q}''_o$ and $t_{\text{N,ini}}$ are the cycle-mean steady state heat flux and initial backside temperature, respectively.

Consider first the heat flux. The term $\bar{q}''_o R_{\text{total}}$ is the steady surface temperature due to a steady $\bar{q}''_o$, but its effect dissipates for $\theta > 0$ as it is replaced by $\dot{q}''_o$. The decay rate is given by X_o, and from Eq. (3.58) one sees that that the first term in Eq. (3.63) goes to zero over time. The effect is analogous for the backside temperature as $\left(1 - \sum Y_{o,j}\right)$ approaches zero at long times.

3.2.2.3 Initial Condition Due to Combustion Surface

The initial condition effect based on the combustion surface boundary condition is depicted in Fig. 3.16 using Eq. (3.63). The coolant surface temperature remained fixed at $\bar{t}_c$ = 420K. The heat flux profile is similar to Fig. 3.5, but the peak heat flux was set at 5 MW/m^2 at an equivalent of 1000 rpm engine speed. Temperature history of a typical uncoated piston is shown for two different cases. For the solid line, the steady state heat flux, $\bar{q}''$, was used as the initial condition, but for the dashed case $\bar{q}'' = 0$. The first case converges in a much shorter time.

The concept of the initial condition period starts at times $\theta < 0$, where a steady state heat flux $\bar{q}''$ is assumed into the wall from the combustion surface establishing a linear temperature distribution. At time $\theta = 0$, this steady state heat flux turns off and as time $\theta > 0$ progresses, its contribution decays over time. This contribution has to be subtracted from the wall (*i.e.* term $-\bar{q}'' \sum X_i$ in Eq. (3.63)), while the steady state temperature term (*i.e.* term $\bar{q}'' R_{\text{total}}$ in Eq. (3.63)) is added in the full solution to compensate for the previous loss. The net effect is equivalent to solving

the problem with an initial temperature distribution across the computational domain of a steady state case.

This initial condition concept applies to steady state engine conditions where convergence criteria have to be satisfied in a reasonable time manner. However, transient drive cycles normally initiate at ambient conditions and, therefore, the steady state heat flux term could be assumed zero, $\bar{q}'' = 0$. Similarly, Eq. (3.63) may also be used for the unusual cases where transient events are simulated using initial conditions for both surfaces. Maximum efficiency with this approach can be realized when $\bar{q}''$ is close to cycle mean heat flux. On the other hand, if such a value is unknown for the coated wall then either a crude approximation or the baseline uncoated wall will be sufficient.

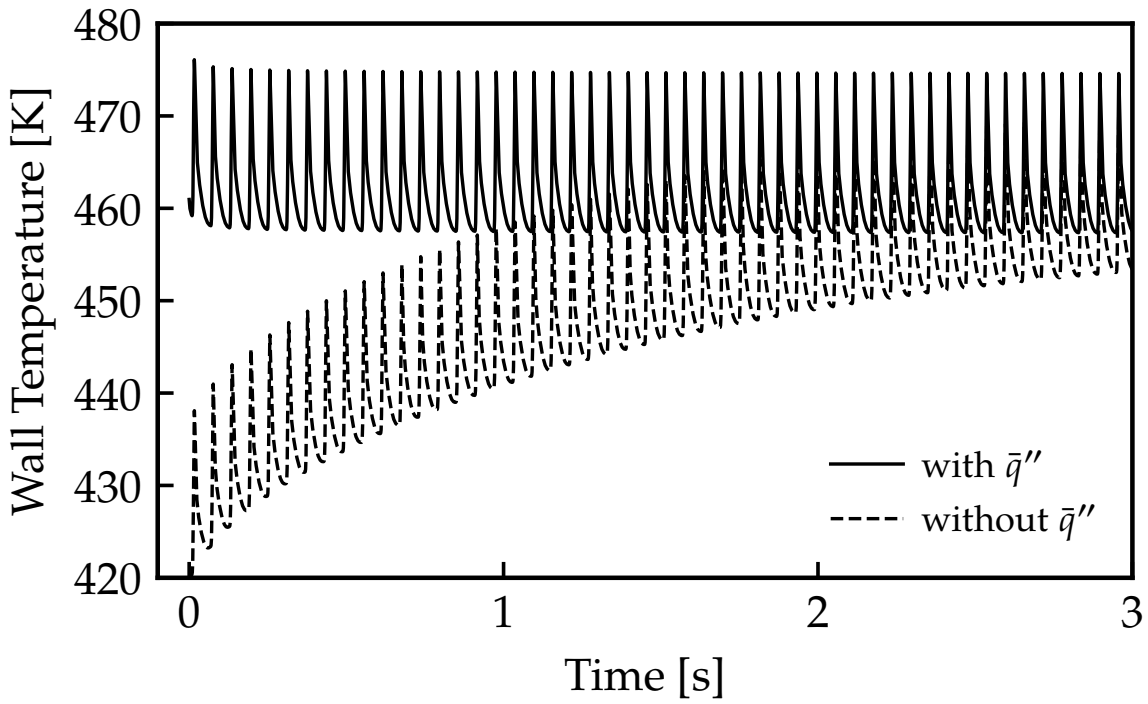

Figure 3.16: Uncoated piston surface temperature history as a function of time with (solid) and without (dashed) the initial condition steady state heat flux term $\bar{q}''$ in Eq. (3.63).

3.2.3 Interface Temperatures

The combustion chamber surface temperature may not be the only temperature of interest. The same approach can be used to find the temperature at any location inside the coated wall.

3.2.3.1 Interface Temperature Subject to Unsteady Combustion Chamber Heat Flux

Consider the case where an interfacial temperature of a multilayer wall is of interest, as seen in Fig. 3.17. Positive heat flow is considered in the direction from the combustion chamber, $x = 0$, to the wall back surface, $x = L$. The interface location of interest splits the problem into two spatial domains. The upstream part starts from the combustion surface and ends at the interface location; the downstream part starts from the interface and ends at the backside surface. Upstream and downstream transfer matrices are shown in Eq. (3.64) and Eq. (3.65), where $\hat{t}_i$ and $\hat{q}_i$ are the Laplace transforms of the interface temperature and heat flux.

$$\begin{bmatrix} \hat{t}_o \\ \hat{q}_o \end{bmatrix} = \begin{bmatrix} A_u & B_u \\ C_u & D_u \end{bmatrix} \begin{bmatrix} \hat{t}_i \\ \hat{q}_i \end{bmatrix} \tag{3.64}$$

$$\begin{bmatrix} \hat{t}_i \\ \hat{q}_i \end{bmatrix} = \begin{bmatrix} A_d & B_d \\ C_d & D_d \end{bmatrix} \begin{bmatrix} \hat{t}_N \\ \hat{q}_N \end{bmatrix} \tag{3.65}$$

The interface temperature solution can be found from the upstream section by inverting the matrix and using the fact that the determinant is unity for each individual layer and any combination of layers

$$\begin{bmatrix} \hat{t}_i \\ \hat{q}_i \end{bmatrix} = \begin{bmatrix} D_u & -B_u \\ -C_u & A_u \end{bmatrix} \begin{bmatrix} \hat{t}_o \\ \hat{q}_o \end{bmatrix} \tag{3.66}$$

which relates interface i information to the combustion surface. The interface

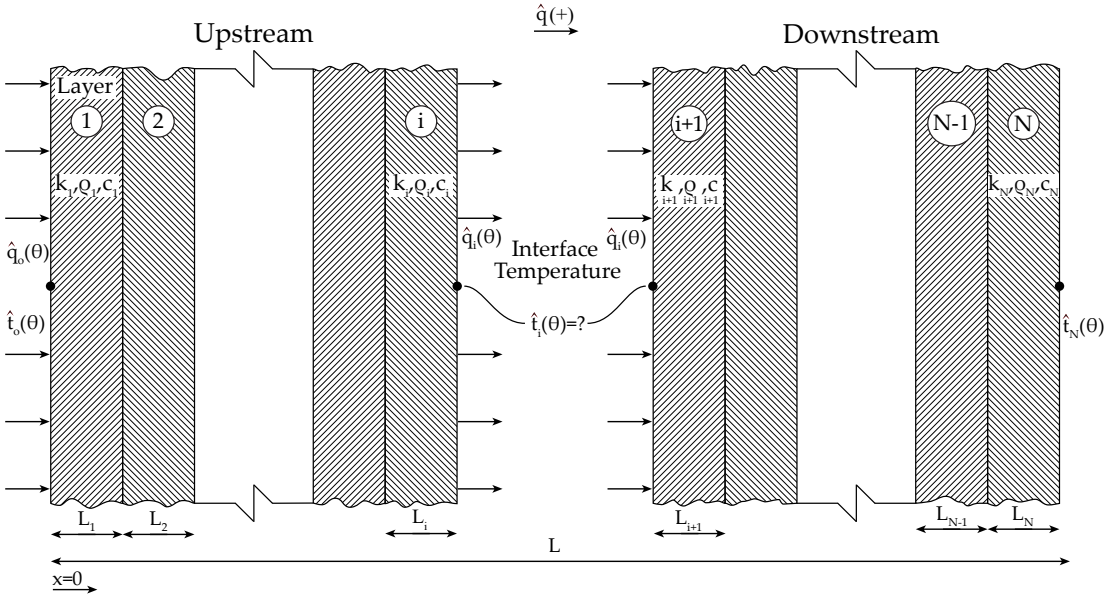

Figure 3.17: A multilayer reciprocating engine wall scheme, divided into the upsteam and downstream section, to derive any interface wall temperature subject to unsteady combustion chamber heat flux. Positive heat flow is considered the direction to the right; from the combustion gas to the wall.

temperature transform can then be writtern as

$$\hat{t}_i = D_u \hat{t}_o - B_u \hat{q}_o \tag{3.67}$$

Assuming $\hat{t}_N$ is zero, Eq. (3.49) can be used to replace $\hat{t}_o$ and get the interface temperature as exclusively a function of $\hat{q}_o$.

$$\hat{t}_i = \left(\frac{D_u B - D B_u}{D} \right) \hat{q}_o \tag{3.68}$$

By multiplying the upstream and downstream matrices one can find

$$\begin{bmatrix} A & B \\ C & D \end{bmatrix} = \begin{bmatrix} A_u & B_u \\ C_u & D_u \end{bmatrix} \cdot \begin{bmatrix} A_d & B_d \\ C_d & D_d \end{bmatrix} \tag{3.69}$$

which becomes

$$B_d = D_u B - D B_u \tag{3.70}$$

This allows the interface temperature transform $\hat{t}_i$ to be found as

$$\hat{t}_i = \left(\frac{B_d}{D} \right) \cdot \hat{q}_o \tag{3.71}$$

where B_d and D are the downstream and overall transfer matrix coefficients, respectively. The inversion of Eq. (3.71) to find interface temperature t_i, therefore, follows the same procedure as shown in Eq. (3.57) with $\psi = B_d$ and does not require the effort of finding any other poles.

The interface temperature t_i can be seen as the convolution of surface unsteady combustion surface heat flux $\dot{q}_o''$ with the interface response function X_i as

$$t_i(\theta_n) = X_i \circledast \dot{q}_o'' \tag{3.72}$$

3.2.3.2 Interface Temperature Subject to Unsteady Backside Temperature

The interface temperature subject to unsteady backside temperature changes can be solved separately. The problem is formulated as linear, thus, superposition with the previous sub-problem comprises the general solution.

Consider negative heat flow entering the wall from the coolant or oil surface. The "Upsteam" and "Downstream" terms were attributed to the positive heat flow direction and that same nomenclature is maintained. The interface temperature can be expressed from Eq. (3.65)

$$\hat{t}_i = A_d \hat{t}_N + B_d \hat{q}_N \tag{3.73}$$

by assuming $\hat{q}_o = 0$, Eq. (3.25) gives $\hat{q}_N = \frac{-C}{D} \hat{t}_N$, which provides the interface

temperature exclusively as a function of $\hat{t}_N$.

$$\hat{t}_i = \frac{A_d D - B_d C}{D} \hat{t}_N \tag{3.74}$$

By multiplying the upstream and downstream matrices one finds

$$D_u = A_d D - B_d C \tag{3.75}$$

so the interface temperature $\hat{t}_i$ to be found to be

$$\hat{t}_i = \left(\frac{D_u}{D} \right) \cdot \hat{t}_N \tag{3.76}$$

where D_u and D are the upstream and overall transfer matrix coefficients, respectively. The inversion of Eq. (3.76) to find the interface temperature t_i which is the contribution associated with time-varying backside temperature, therefore, again does not require finding new poles and follows the same procedure as Eq. (3.57) with $\psi = D_u$ giving rise to the transfer function, Y_i. Eq. (3.76) can be treated in an analogous manner as Eq. (3.71). Finally, the total interface temperature solution can be found similarly to Eq. (3.72).

3.2.4 Alternative Non-linear Boundary Conditions

In-cylinder engine heat transfer may be investigated with non-linear boundary conditions. The proposed method can handle alternative boundary conditions types and examples are discussed below.

3.2.4.1 Convection and Radiation from Combustion Gas

The boundary condition on the combustion chamber surface may be considered as the sum of convective and radiative heat transfer

$$\dot{q}'' = \dot{q}''_{\text{conv}} + \dot{q}''_{\text{rad}} = h \left(t_g - t_{w,o} \right) + \sigma \epsilon \left(t_g^4 - t_w^4 \right) \tag{3.77}$$

where $\dot{q}''_{\text{conv}}$ represents the convective heat flux, h is the convective heat transfer coefficient and t_g is gas temperature. In addition, $\dot{q}''_{\text{rad}}$ represents the radiative heat flux, σ is the Stefan-Boltzmann constant and ϵ is the surface emissivity. By iterating Eqs. (3.63) and (3.77) the temperature and heat flux may be obtained.

For the case where radiation is neglected, the surface heat flux can be recovered directly without iteration. Consider the case where a multilayered coated engine is under steady state conditions. The oil temperature t_N is fixed. Recasting Eq. (3.77) with the surface temperature $t_o\left(\theta_n\right) = \sum_{i=0}^{n_x} X_{o,i} \cdot \dot{q}''_{o,\theta_n - i\Delta} + t_N$ from Eq. (3.60), the surface heat flux can be obtained for the time of interest θ_n as

$$\dot{q}''_{o,\theta_n} = \frac{t_g - \left(\sum_{i=1}^{n_x} X_{o,i} \cdot \dot{q}''_{o,\theta_n - i\Delta} + t_N\right)}{1 + hX_o} \tag{3.78}$$

3.2.4.2 Convection from Coolant/Oil Fluid

The backside medium of the combustion chamber may be air, coolant, water, oil or a combination of the above. In modern liquid-cooled engines, the coolant flow is controlled to maintain a constant coolant temperature. Thus, it would be more practical to use these temperatures in the proposed solution instead of the metal backside surface temperature. Further, the vast majority of modeling approaches takes the backside boundary condition as convective heat transfer.

The proposed solution can easily treat the backside as having an additional layer with negligidle heat capacity. An air layer with negligible heat capacity to model a convective boundary condition on the backside would lead to

$$\left[M_i\right]_{s=0} = \begin{bmatrix} 1 & 1/h \\ 0 & 1 \end{bmatrix} \tag{3.79}$$

where h is the convective heat transfer coefficient. All the elements of the transfer matrix derivative of this layer would be zero.

3.2.5 Evaluation of Transfer Matrix and its Derivative

The transfer matrix and its derivative with respect to the frequency variable are necessary to calculate the inverse Laplace transform exactly. The matrix describing layer i is

$$[M_i] = \begin{bmatrix} A_i(s) & B_i(s) \\ C_i(s) & D_i(s) \end{bmatrix} \tag{3.80}$$

and the overall matrix, consisting of N layers, is

$$[M] = \prod_{i=1}^{N} [M_i] \tag{3.81}$$

It is convenient to set $s = -\beta_m$ for root-calculating purposes so that β becomes a positive real number. Invoking the assumption that the poles lie on the negative real axis [105], M_i can be written as

$$[M_i] = \begin{bmatrix} A_i & B_i \\ C_i & D_i \end{bmatrix} = \begin{bmatrix} \cos\sqrt{\beta R_i C_i} & \frac{R_i}{\sqrt{\beta R_i C_i}} \sin\sqrt{\beta R_i C_i} \\ \frac{-\sqrt{\beta R_i C_i}}{R_i} \sin\sqrt{\beta R_i C_i} & \cos\sqrt{\beta R_i C_i} \end{bmatrix} \tag{3.82}$$

The derivative of M_i is simply

$$\frac{d}{ds}[M_i] = \begin{bmatrix} \frac{d}{ds}A_i & \frac{d}{ds}B_i \\ \frac{d}{ds}C_i & \frac{d}{ds}D_i \end{bmatrix} \tag{3.83}$$

and by setting $s = -\beta_m$, the matrix derivative becomes

$$\begin{aligned} \left[\frac{dM_i}{ds}\right] &= \frac{R_i C_i}{2} \times \\ &\times \begin{bmatrix} \frac{\sin\sqrt{\beta_m R_i C_i}}{\sqrt{\beta_m R_i C_i}} & \frac{1}{\beta_m C_i}\left\{\frac{\sin\sqrt{\beta_m R_i C_i}}{\sqrt{\beta_m R_i C_i}} - \cos\sqrt{\beta_m R_i C_i}\right\} \\ \frac{1}{R_i}\left\{\frac{\sin\sqrt{\beta_m R_i C_i}}{\sqrt{\beta_m R_i C_i}} + \cos\sqrt{\beta_m R_i C_i}\right\} & \frac{\sin\sqrt{\beta_m R_i C_i}}{\sqrt{\beta_m R_i C_i}} \end{bmatrix} \end{aligned} \tag{3.84}$$

For the pole at $s = 0$ one should use

$$[M_i]_{s=0} = \begin{bmatrix} 1 & R_i \\ 0 & 1 \end{bmatrix} \tag{3.85}$$

$$\left[\frac{dM_i}{ds}\right]_{s=0} = \frac{R_i C_i}{2} \begin{bmatrix} 1 & R_i/3 \\ 2/R_i & 1 \end{bmatrix} \tag{3.86}$$

which results from the limit $s \to 0$.

When more than one layer is considered, the overall matrix derivative should be calculated by applying the chain rule as follows:

$$\begin{aligned} \left[\frac{dM}{ds}\right] = \begin{bmatrix} \frac{dA}{ds} & \frac{dB}{ds} \\ \frac{dC}{ds} & \frac{dD}{ds} \end{bmatrix} = \begin{bmatrix} \frac{dA_1}{ds} & \frac{dB_1}{ds} \\ \frac{dC_1}{ds} & \frac{dD_1}{ds} \end{bmatrix} \cdot \begin{bmatrix} A_2 & B_2 \\ C_2 & D_2 \end{bmatrix} \cdots \begin{bmatrix} A_N & B_N \\ C_N & D_N \end{bmatrix} \\ + \begin{bmatrix} A_1 & B_1 \\ C_1 & D_1 \end{bmatrix} \cdot \begin{bmatrix} \frac{dA_2}{ds} & \frac{dB_2}{ds} \\ \frac{dC_2}{ds} & \frac{dD_2}{ds} \end{bmatrix} \cdots \begin{bmatrix} A_N & B_N \\ C_N & D_N \end{bmatrix} \\ + \quad \ldots \quad + \begin{bmatrix} A_1 & B_1 \\ C_1 & D_1 \end{bmatrix} \cdot \begin{bmatrix} A_2 & B_2 \\ C_2 & D_2 \end{bmatrix} \cdots \begin{bmatrix} \frac{dA_N}{ds} & \frac{dB_N}{ds} \\ \frac{dC_N}{ds} & \frac{dD_N}{ds} \end{bmatrix} \end{aligned} \tag{3.87}$$

or in a compact notation the overall matrix derivative can be described as

$$\left[\frac{dM}{ds}\right] = \sum_{i=0}^{N-1} \left\{ \left[\prod_{j=0}^{i-1} [M_j] \right] \cdot \left[\left[\frac{dM_i}{ds}\right] \right] \cdot \left[\prod_{j=i+1}^{N-1} [M_j] \right] \right\} \tag{3.88}$$

3.2.6 Demonstration of the Method

An example to illustrate the surface and interface responses X_i and Y_i in a multilayer coated wall is presented to demonstrate application of the method. The thermal properties for each layer can be found in Table 3.5. This coating architecture can be characterized as a traditional thermal barrier coating for diesel engines [49]. The bond coating increases adhesion to the metal piston and the gradient coating is added to reduce the thermal coeffient of expansion mismatch between coating and

substrate to improve durability. The backside of the wall experiences convection with a constant heat transfer coefficient h_{back}. A 120 μs time step was selected for a total simulation time of 0.6 s. By following the above description, 191 poles for a maximum cut-off frequency $\beta_{\max}$ of 134 kHz were used along the negative real-axis.

Figure 3.18 (a) shows the response functions X_i for all of the interfaces of this coating structure. The negative time on the plot abscissa emphasizes the fact that *past* heat flux pulses are contributing to the *current* wall temperature. The surface (solid) and interface (dashed) time-response functions X assume a heat flux change of unity at the combustion chamber surface while the coolant or oil surface temperature is fixed. The surface response starts at a high value because it is directly exposed to the applied heat flux, then attenuates rapidly. The interface response functions start at zero due to the finite time required for the thermal wave to reach the interior locations, then peak in sequence according to their depth.

Table 3.5: Thermo-mechanical properties of wall architectures investigated, with k: thermal conductivity; ρ: density; c: specific heat capacity; L: thickness; and h_{back} heat transfer coefficient on the backside surface

Material	k [W/m-K]	ρ [kg/m^3]	c [J/kg-K]	L [μm]	h_{back} [W/m^2-K]
YSZ	0.77	4713	387.5	210	–
Gradient	0.85	3886	385.1	70	–
Bond	4.07	6255	152.6	70	–
Aluminum Piston	123	2702	949	8250	–
Oil	–	–	–	–	1750

The X_i shown in Fig. 3.18 (a) can be used to generate temperature histories given the surface heat flux. For this demonstration, a step change in heat flux from 0 to 1 MW/m^2 was taken. The resulting surface and interface temperatures are shown in Fig. 3.18 (c). The oil temperature was maintained fixed at 430 K and initial condition was neglected, *i.e.* $\bar{q}'' = 0$ for $\theta < 0$. The higher surface temperature is mainly due to the low thermal conductivity of the top coat. It serves as thermal insulator for the rest of the multilayer engine wall.

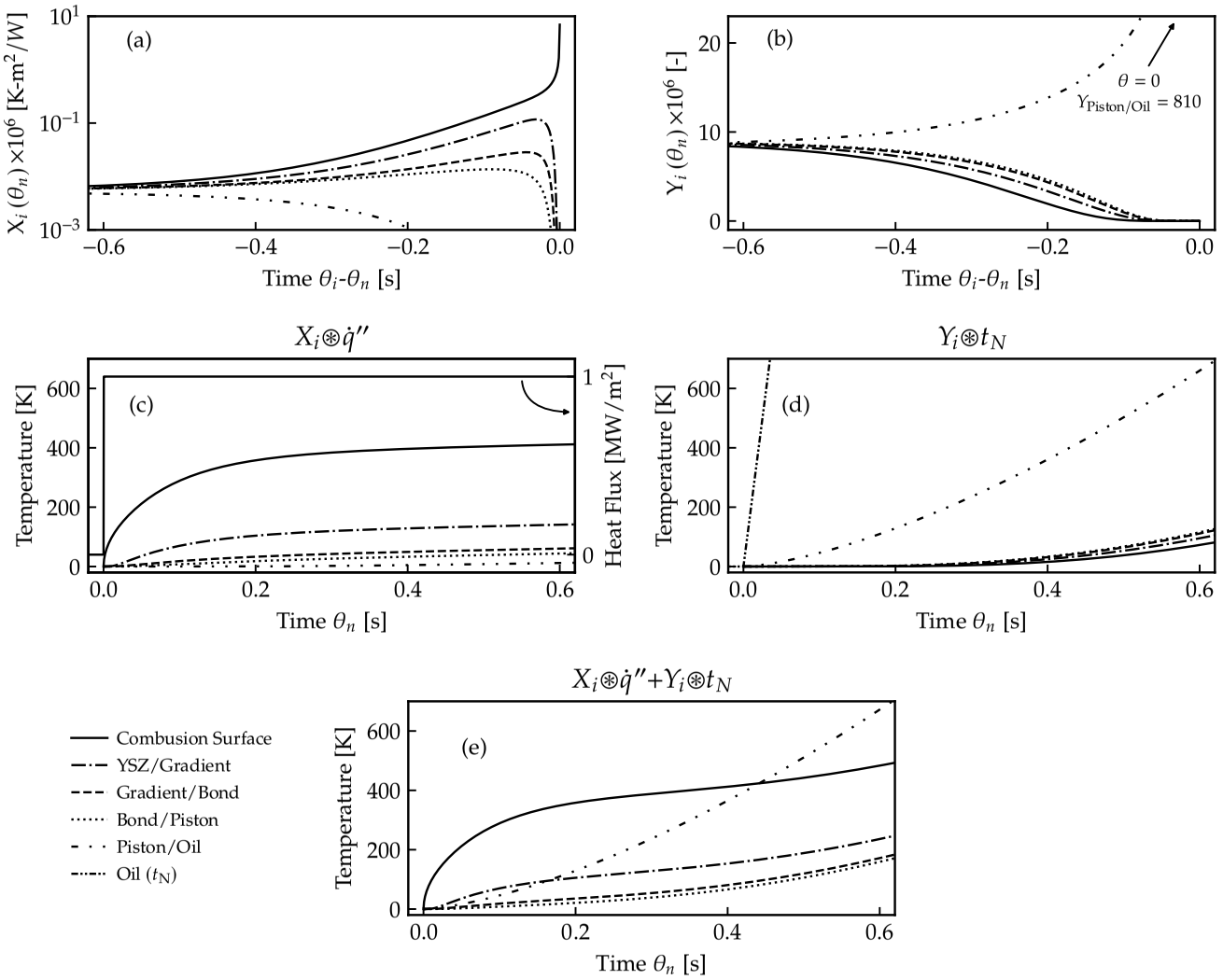

Figure 3.18: Surface and interface time response functions (a) X_i and (b) Y_i are shown for a multilayer thermal barrier coating on an engine piston. (c) The temperature at the interfaces due to time-varying heat flux at the combustion chamber surface, $\dot{q}''_o$, and (d) time-varying temperature at the backside surface, t_N. (e) The combined effect of both boundary conditions. See text for additional information about thermal properties and thicknesses.

The same multilayer architecture was used to illustrate the surface and interface response functions, Y_i, which are shown in Fig. 3.18 (b). These time-response Y functions were convolved with a linear temperature change at the backside surface, as shown in Fig. (3.18) (d), while the combustion surface heat flux was maintained at zero. The convection heat transfer resistance is high and accounts for the big difference between oil and backside wall temperature. Lastly, the combined effects of Figs. 3.18 (c) and (d) are depicted in Fig. 3.18 (e). The surface and interface temperatures illustrate the superposition of a heat flux change at the combustion surface and a temperature change at the backside surface.

3.2.7 Computational Speed and Accuracy Comparison

3.2.7.1 Comparison with Finite Difference Scheme

A surrogate of the in-cylinder heat flux profile was developed as the sum of a sinusoidal function with a period that corresponds to one engine cycle at 1300 rpm and a Gaussian pulse to represent the combustion event. The applied heat flux is shown in Fig. 3.19, as a function of crank angle. The Gaussian term had a peak heat flux of 3 MW/m^2 and a full-width at half-maximum value of 5.1 ms. The sinusoidal term, which had an amplitude of 0.25 MW/m^2, modeled the background heat flux due to the reciprocating piston motion.

A two-layer wall was considered with Layer 1 being a 100μm thermal insulation coating and Layer 2 an aluminum wall; the total domain length was 5 mm. The backside temperature was steady at 373 K. The cycle-averaged heat flux $\bar{q}''$ of the profile was used as the initial condition.

Figure 3.19 shows the surface temperature output for: a high resolution finite difference solution, the step-change method from Section 3.1, and the current triangular pulse method. The finite difference solution used a Crank-Nicolson scheme with 2^{20} nodes divided evenly between the coating and substrate. The simulation time step was 2^{19}, 2^{16} and 2^{16} for the finite difference and the step, and triangular solutions, respectively. The finite difference was considered as the reference or "exact" solution. The triangular pulse (solid) was resolved using Eq.

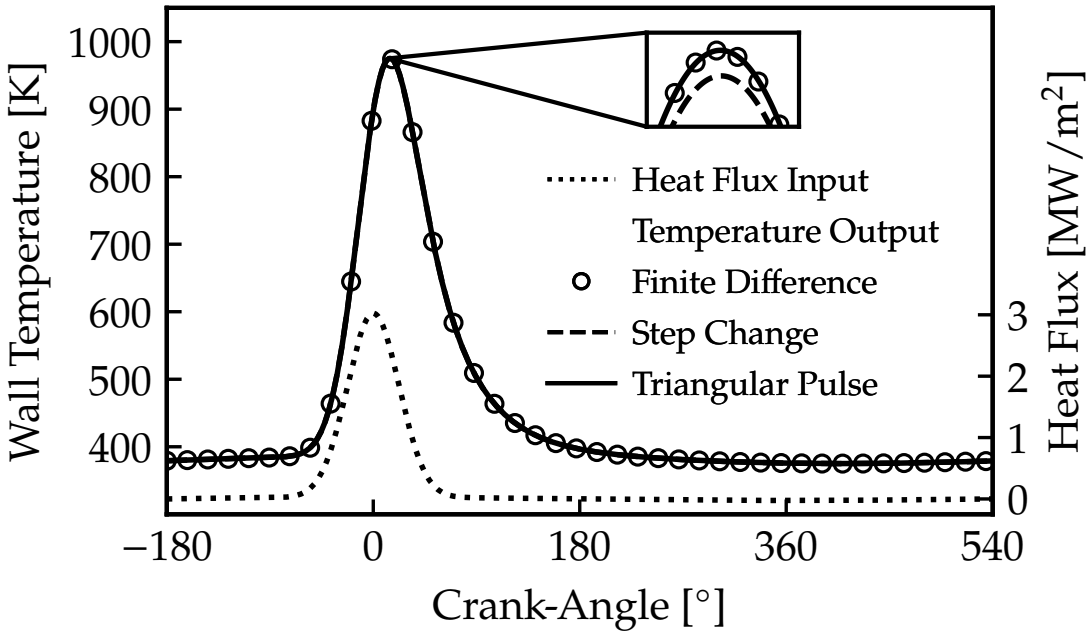

Figure 3.19: Crank-resolved surface temperature of a two-layer engine wall subject to the unsteady surface heat flux shown with dash-dot line and right axis. The finite difference (circles), step change (dashed), and proposed triangular pulse method (solid) surface temperatures provide excellent agreement. Material properties can be found in [114].

(3.63). The step and triangular pulse methods were compared at a fixed number (70) of roots.

All three techniques show excellent agreement, however, the step-change solution has a small error (0.02 K) in peak wall temperature as shown in the expanded view of Fig. 3.19.

Figure 3.21 (a) shows the computational time versus maximum error for each of the aforementioned methods. The maximum error was based on the "exact" finite difference scheme, discussed above. Only two cycles were simulated and the maximum error was calculated for just the second cycle to avoid initial transient errors. The CPU time shown was for both cycles. The three methods were evaluated for different numbers of time steps ranging from 2^5 to 2^{16}, in multiplicative steps

of two. The finite difference results are shown as a family of dashed curves; each individual curve represents a fixed number of spatial nodes calculated using the different time step sizes.

Consider the finite difference solution with 2^{11} nodes. The lower right-most point corresponds to 2^5 time steps, and the upper left-most point corresponds to 2^{16} time steps. As the number of time steps increases the error decreases and the computational time increases proportionally. Finally, a condition is reached where the errors of spatial discretization dominate, and the curve becomes vertical. This pattern is seen for all but 2^4 and 2^5 spatial nodes, which are solely vertical due to the low spatial resolution.

The step response and triangular pulse analytical techniques were evaluated using a common computational approach and thus took the same CPU time, but they vary substantially in accuracy. The convolution was calculated via Fast Fourier Transform (FFT), see Eq. (3.61), using the entire heat flux history, *i.e.*, in just one step. The FFT convolution offers substantial computational speed improvement relative to the direct form convolution approach in Eq. (3.60).

The analytical step-response method showed significant speed advantage relative to the finite difference cases, however, the accuracy was limited to ~0.1 K maximum error. The accuracy of this method would have been improved if the time step was reduced, but this is impractical. The limited accuracy stems from the poor representation of the step change to the continuous input function, as shown in Fig. 3.14.

The triangular pulse approximation, which fits the continuous input function better in Fig. 3.14, gives the best performance in Fig. 3.21 (a). The triangular pulse offers two to three orders of magnitude reduction in computational time compared with the finite difference approach at similar error levels. In addition, the error is much smaller relative to the step-change solution, which requires the same computational effort.

3.2.7.2 Engine Drive Cycle Demonstration

Computing component temperatures during long engine transients, *e.g.*, cold starts or drive cycles, is of interest. Thermodynamic and heat transfer analysis was performed on a production John Deere 4045 diesel engine using the commercial simulation code GT-Power augmented with the wall temperature solver using the triangular pulse method. Details of the implementation process and a discussion of the results can be found in Chapter 5. The purpose of this discussion is to demonstrate the computational efficiency of this method. The Non-Road Transient Cycle (NRTC) is an international transient certification cycle used to assess non-road engine vehicle performance, fuel consumption and emissions. The cycle lasts about 20 minutes; official certification involves running an NRTC from cold start, followed by a 20-minute soak period, and finally an NRTC from hot start. The hot NRTC is used to evaluate performance and fuel consumption.

The piston heat flux and backside temperature histories were exported from the model results and used as time-varying boundary conditions. The initial conditions were set at 0 MW/m^2 and 353 K (80°C) for the combustion chamber heat flux and oil temperature, respectively. The same multilayer coating discussed in Table 3.5 was utilized for this example. All temperature histories were computed using Eq. (3.63). The surface temperature required frequency response functions $\left(\frac{B}{D}\right)$ and $\left(\frac{1}{D}\right)$ at the combustion and backside surface, respectively. Each of the interface temperatures required frequency response functions $\left(\frac{B_d}{D}\right)$ and $\left(\frac{D_u}{D}\right)$ at the combustion and backside surface, respectively. The data produced by the simulation were 16,777,216 sequential data points with a time step of 75 μs.

Fig. 3.20 (a) shows the temperature histories at all interfaces in the coated piston during the full drive cycle. The surface wall temperature shows two differences relative to the other interfaces. First, it reaches significantly higher temperatures due to the low conductivity of the top coat. Second, the low-volumetric heat capacity of the top coat causes the surface temperature to respond quickly to the heat flux changes. The measured oil temperature history, used as boundary condition, is shown as a reference. Figure 3.20 (b) shows a magnified time. Shortly after

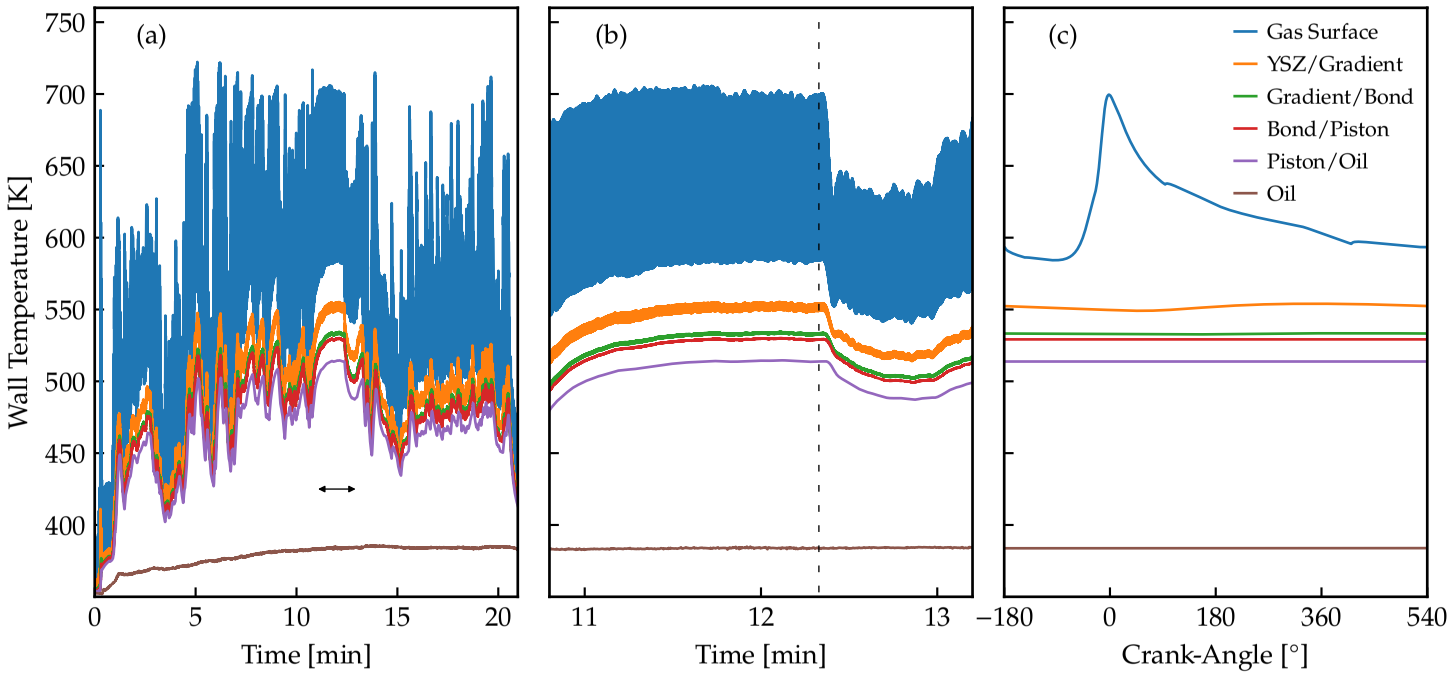

Figure 3.20: Temperature histories of a multilayer coated engine wall for: (a) full drive, (b) magnified 11^{th}-13^{th} minute window indicated by the horizontal arrow in (a), and (c) individual cycle indicated by the vertical dashed line of (b). Details about the boundary conditions can be found in [116].

the vertical dashed line location, the engine experiences a sudden load decrease, see Figure 5.12. This has an immediate effect on the engine heat transfer; all the temperatures decrease. In addition, the vertical dashed line also indicates the engine cycle shown in Fig. 3.20 (c). This cycle generated a relatively high instantaneous surface temperature. The intra-cycle interface temperature variations are minor progressing from top coat to the aluminum piston. The YSZ/Gradient interface has an intra-cycle temperature swing of only 5 K.

Figure 3.21 (b) shows a comparison between the CPU time and the cumulative simulated real time for three different computational approaches. A maximum error threshold of 0.1 K was selected for the finite difference case, and from Fig. 3.21 (a), this level of error can be achieved by using 2^7 and 2^6 nodes in the coating and substrate, respectively, for peak computational efficiency. The other two results are based on the triangular pulse analytical solution proposed in this work. The Single Block FFT computes the convolution using an FFT similar to the procedure followed in Fig. 3.21 (a). A constant ratio in computational time was realized; the Single Block FFT was more than $10^2\times$ faster than the finite difference case. On top of this benefit, additional computational performance can be achieved with an advanced convolution treatment. The Overlap-add FFT method is used to decompose long signals into smaller segments for easier digital signal processing [117]. In this Overlap-Add algorithm application, the heat flux $\dot{q}''$ is the very long signal and the response function X_o is the finite-impulse-response filter. The Overlap-add FFT approach provided more than a $10^4\times$ speed increase relative to the finite difference equivalent. In particular, the finite difference CPU time for the full drive cycle was $3,105$ sec. and that using the Overlap-FFT was 0.25 sec.

3.2.8 Frequency Response Characterization

The fact that the wall response function is convolved with the applied heat flux to find surface temperature suggests that the system can be modeled as a filter or transfer function. The function $X(\theta)$ is analogous to the finite impulse response. It is instructive to view the transfer function in the frequency domain, which can be

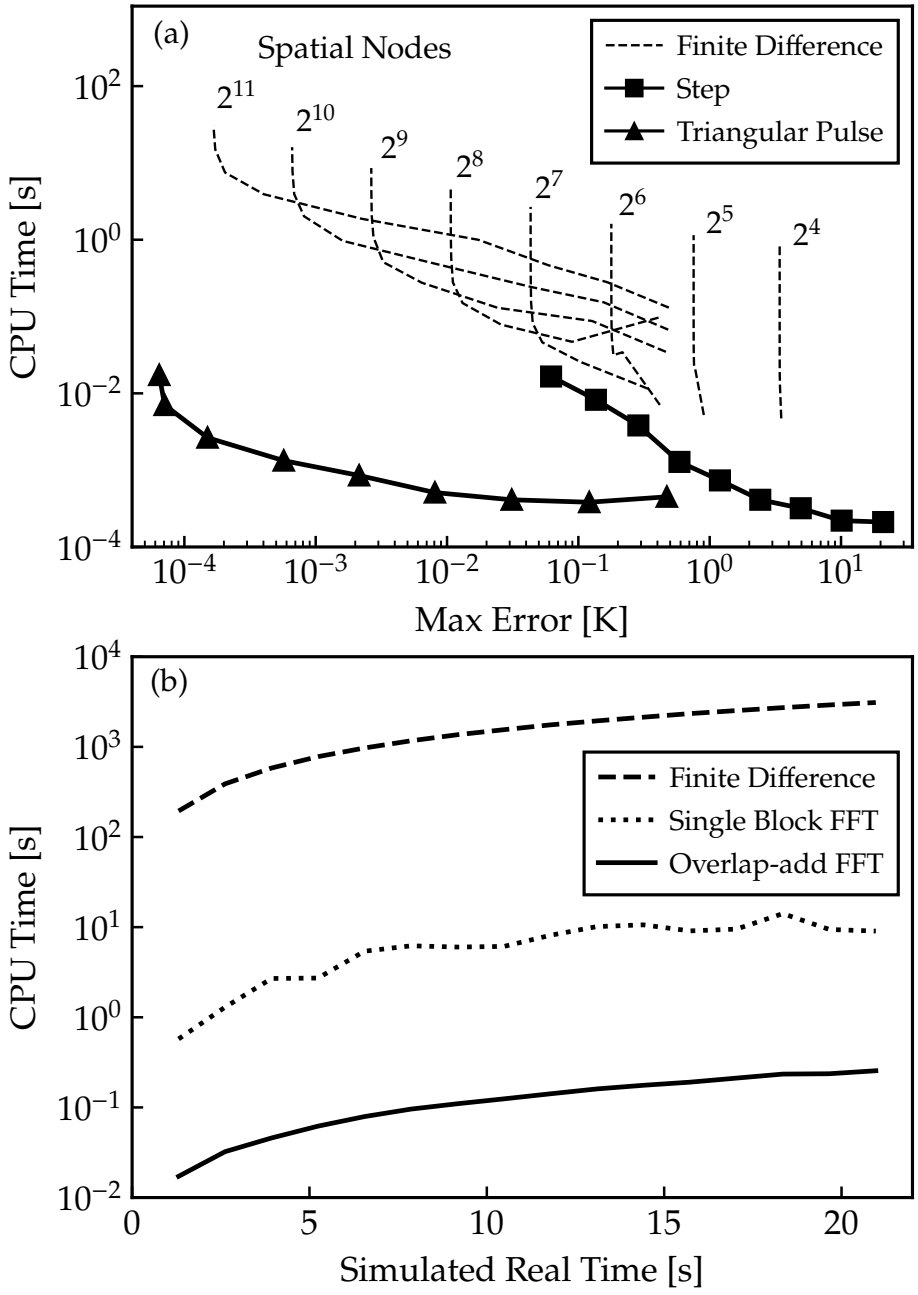

Figure 3.21: (a) Computational time and maximum surface temperature error for different solution methods. Finite Difference (dashed) curves refer to simulations with varying time step and the total number of grid points shown. The analytical techniques of step change (solid square) and triangular pulse (solid triangle) are solved using the FFT method for different time step sizes. For further details, see text. (b) Comparison between computational time and simulated real time for 2^8-node finite difference, single block FFT, and Overlap-add FFT solution methods.

found by taking the power spectral density of X.

The frequency response can also be directly evaluated using the analytical approach. Consider the case where the backside temperature is fixed, $\hat{t}_N = 0$, and the combustion surface heat flux is varying periodically, $\dot{q}''_o(\theta) = \sin(\omega\theta)$, where $\omega = 2\pi f$ is angular velocity and f is frequency. The system transfer function in the Laplace domain, *i.e.* the temperature response to a heat flux input, is given by $\hat{t}_o/\hat{q}_o$

$$\frac{\hat{t}_o}{\hat{q}_o} = \frac{B}{D} \tag{3.89}$$

One can convert from the Laplace to the Fourier frequency domain using $s = j\omega$. In the case of a single sinusoidal input at ω, the inversion to the time domain simply gives

$$|\hat{X}_o(j\omega)| = \left|\frac{B(j\omega)}{D(j\omega)}\right| \tag{3.90}$$

where $|\hat{X}_o(j\omega)|$ is the magnitude of the complex function $\frac{B}{D}$. The magnitude, which is of primary interest instead of the phase, determines the relative temperature response to an applied heat flux. The system response magnitude in Eq. (3.90) can be viewed in the frequency domain to distinguish the dynamics of different coating structures.

Consider the example of an uncoated and coated aluminum wall with thermal properties shown in Table 3.5, excluding the oil layer. Figure 3.22 (a) shows the surface response, X_o [K-m^2/W], in the time domain. Note, these results are nearly identical to Fig. 3.18 (a) except that the time axis is not reversed and a logarithmic abscissa is used. There is a significant difference between the uncoated and coated wall at short times, which is intuitive for a thermal-swing coating as was chosen for this example. At long times, however, the response of the different wall types is indistinguishable. In fact, the time constant for the YSZ coating, $\tau = RC$, is 0.1 s, which is shown with the vertical dashed line in Fig. 3.22 (a). This time scale is found to define the transition from coating-dominated performance well. For times longer than τ the layer with the longest time scale, usually the substrate, dominates.

Figure 3.22 (b) illustrates the coated and uncoated magnitude of surface re-

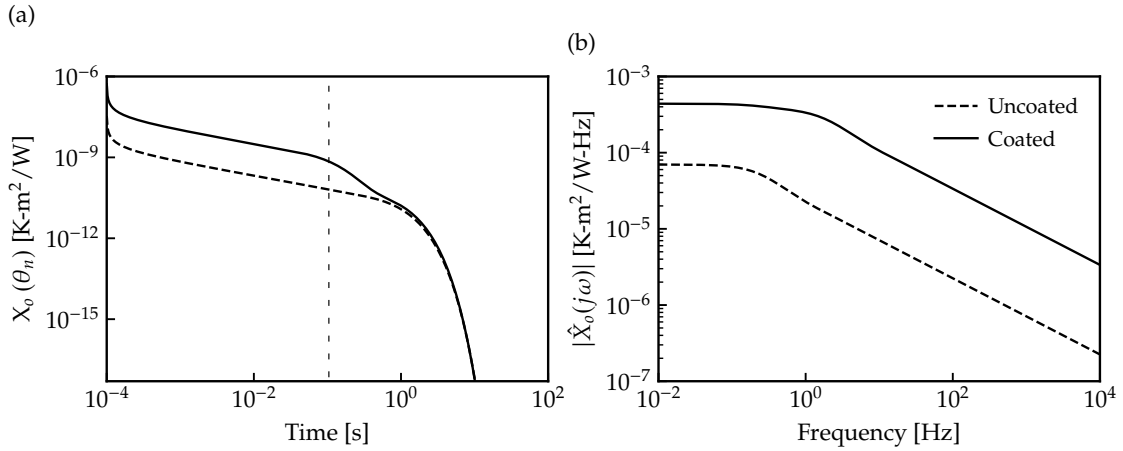

Figure 3.22: (a) Time- and (b) Frequency surface response X_o for an uncoated and coated engine wall.

sponse, $|\hat{X}_o(j\omega)|$ [K-m^2/W-Hz] in the frequency domain, which gives a complementary view to the time-domain response. The value of the magnitude at the lowest frequency is representative of the steady state resistance of the wall. This is made clear by the way that the temperature response at a given frequency is calculated

$$\hat{t}_o(j\omega) = \hat{X}_o(j\omega) \cdot \hat{q}_o(j\omega) \tag{3.91}$$

is simply the product of the "effective" resistance and the applied heat flux at that frequency. For all frequencies, the coated wall has a higher response than the uncoated wall. As expected, the response of the wall to an applied heat flux decreases as the frequency increases. At low frequencies, the coated wall has higher steady response, or thermal insulation ability, which was not apparent in the time domain plot. At high frequencies, the coated wall surface has increased ability to follow the gas temperature transients, a desirable attribute for a thermal-swing coating.

3.2.9 Summary and Conclusions

Unsteady heat conduction in multilayer walls was investigated analytically under the assumption of one-dimensional heat flow. Time-varying heat flux and temperature boundary conditions were applied to the domain. This approach can be applied to a number of applications, but the specific problem of interest was thermal barrier coatings applied to the surfaces of reciprocating internal combustion engines.

The matrix method coupled with complex analysis for Laplace transform inversion was used to analyze the problem. The boundary conditions were approximated as a unit-magnitude triangular pulse; the superposition of adjacent pulses in the time domain provides a piece-wise linear approximation of the applied heat flux or backside temperature profile. The temperature at any interface is found as the discrete-time convolution of the heat flux or backside temperature time history with a transfer function, X_i or Y_i, respectively, where the subscript i denotes the interface of interest. The transfer functions describe the exact heat transfer response and only depends on material properties and geometry, therefore, they can be computed *a priori*.

This method provides paramount computational efficiency while guaranteeing the accuracy of an analytical solution. At a fixed level of accuracy, it was at least two orders of magnitude faster than a finite difference scheme. The discrete triangular pulse approximated the continuous input boundary condition with substantially higher accuracy that the step-change method presented in Section 3.1; the computational time is the same, but accuracy is two to three orders of magnitude better. Applying this method to long drive cycles, and using the Overlap-add FFT, the computational times were up to four orders of magnitude shorter than a finite difference method at matched temperature accuracy.

Investigation of the wall response functions in the frequency domain reveal complementary information to that of the time domain. At low frequencies, the thermal insulation ability difference between an uncoated and coated wall was indistinguishable in the time domain, but shows a clear difference in the frequency

domain, consistent with coated cases having lower net heat transfer.

4 FRACTURE MECHANICS

This section develops a framework for predicting coating failure in reciprocating internal combustion engines that combines a rigorous analysis of thermal transients during an engine cycle with a thermomechanical analysis of coating stress and the driving forces for delamination. The highly transient nature of the heat flux in reciprocating engines requires many computations to be evaluated. High computational efficiency was achieved through an analytical treatment of the mechanics following Begley and Hutchinson [97]; energy release rates were computed assuming equi-biaxial stress followed by plane strain delamination. The results reveal unique insights into when in the cycle and where in the coating failure is expected for reciprocating engines.

4.1 Problem Description

The analysis was performed for the geometry shown in Fig. 4.1 relevant to steady-state edge delamination, for clarity only a single coating layer applied to a flat substrate having uniform thickness (the engine piston in this case) is shown. The combustion chamber lies above the coating which is thin compared to the substrate; the latter is cooled on its bottom surface. Distributions of the temperature, t, through the layered system are sketched in the figure (with the higher temperature to the right). At a time during the intake stroke the gas temperature is low (~350 K) and heat flows from the coating/substrate multilayer into the gas. At a time during the combustion event the gas temperature is high (~2500 K) and the heat flows from the gas into the multilayer. Depending on the coating properties, the temperature at the top surface ($y = 0$) can vary several hundred Kelvin during a cycle. A temperature distribution at an intermediate time during the expansion stroke is also illustrated. In an actual engine the coating temperature varies significantly both temporarily and spatially, *i.e.*, $t = t(\theta, x, y)$, while the substrate temperature has a relatively weak variation in time but varies spatially. In this work, the focus will be on the

temperature variations in the hottest regions experienced by the multilayer, and thus we idealize the problem by restricting consideration to temperature variations that are dependent only on time and the coordinate normal to the interfaces, $t = t(\theta, y)$.

As it will be seen in the results to follow, the coating stresses driving delamination failures of the intact coating are equibiaxial compression, *i.e.*, $\sigma_x = \sigma_z < 0$. Two types of delamination can occur under compression: edge delamination and buckling delamination. Both types require initial flaws in the coating or coating/-substrate interface to trigger delamination, but for thin systems the size of these flaws need only to be quite small, typically on the order of the coating thickness for edge delamination. For edge delamination, the flaw can be a small crack in the coating or on the interface at an actual edge. The flaw could also be located at a through-crack or gap in an interior region of the coating. For buckling delamination, a crack-like flaw parallel to the interface is required, either within the coating or on the interface, large enough to initiate local buckling of the portion of the coating above the flaw. Both types of delamination are driven by the elastic energy per area in the coating at the instant in question. For the simplest example in which the stress in the coating is uniform and delamination occurs at the interface, the elastic energy per area in the coating, U, is proportional to $\sigma_x^2 L/E$, where L is the coating thickness and E is its Young's modulus. The precise result for the energy release rate of a steady-state edge crack delaminating under plane strain conditions for the uniformly stressed coating is $G = \sigma_x^2 L/\left(2\bar{E}\right)$, independent of σ_z, where $\bar{E} = E/\left(1-\nu^2\right)$. The condition for growth of the delamination is $G = G_c$, where G_c is the toughness (measured in energy/area, Jm^{-2}) of the coating or interface depending on the location of the delamination crack. To attain steady-state the edge crack must have advanced on the order of several times L, depending on where it originates [97]. Once steady-state conditions are attained, G remains at the steady-state value. The special relevance of steady-state delamination is that, if the stress and crack length for this condition are attained or exceeded (*i.e.*, $G \geq G_c$), large patches of the coating will fail. With uniform compressive stress in the coating and separation at the interface, the energy release rate at each crack tip of a buckle delamination is $G = f\sigma_x^2 L/\left(2\bar{E}\right)$, where the factor f increases as the buckle spreads,

approaching unity, if it is straight-sided. Thus, a sufficiently large straight-sided buckle delamination has the same energy release rate as the edge crack. The factor f approaches a limit that is slightly different from unity, depending on Poisson ratio, ν, if the delamination is circular [97]. The edge crack has mode II conditions at the crack tip, while the buckling delamination tip is mixed mode but becomes increasingly mode II as it spreads.

To reveal the essence of conditions driving delamination of coatings on the piston surface of a compression ignition diesel engine, results are computed and presented results for the steady-state energy release rate of an edge crack as dependent on the coating properties and engine running conditions. The steady-state energy release rate combined with the criterion, $G < G_c$, ensures that large patches of delamination will not occur. Based on the above discussion, the steady-state edge crack results will pertain as well to the crack-driving force for buckle delamination, at least approximately. It is also evident from the above discussion that the toughness, G_c, controlling spread of the delamination should be the mode II toughness, at least approximately. It should be noted however that experience with many other thin film and coating systems has suggested that the condition, $G < G_c$, based on the steady-state energy release rate, G, is not overly conservative, most probably due to the fact that thin films and coatings cover vast area compared to their thickness providing ample opportunities for flaws [97].

4.2 Thermal Model

One-dimensional transient heat transfer is assumed through the coating and substrate. Conventional diesel combustion has considerable in-cylinder heat flux spatial variability [52], however, the focus of a heterogeneous surface temperature distribution was outside of the scope of this work. Such problem can be practically dealt with by adding an appropriate safety factor to the applied spatially averaged heat flux. An unsteady heat flux (described below) was used as the boundary condition on the combustion chamber surface side of the domain, and a steady temperature of 100°C was assumed at the piston underside. A Crank-Nicolson nu-

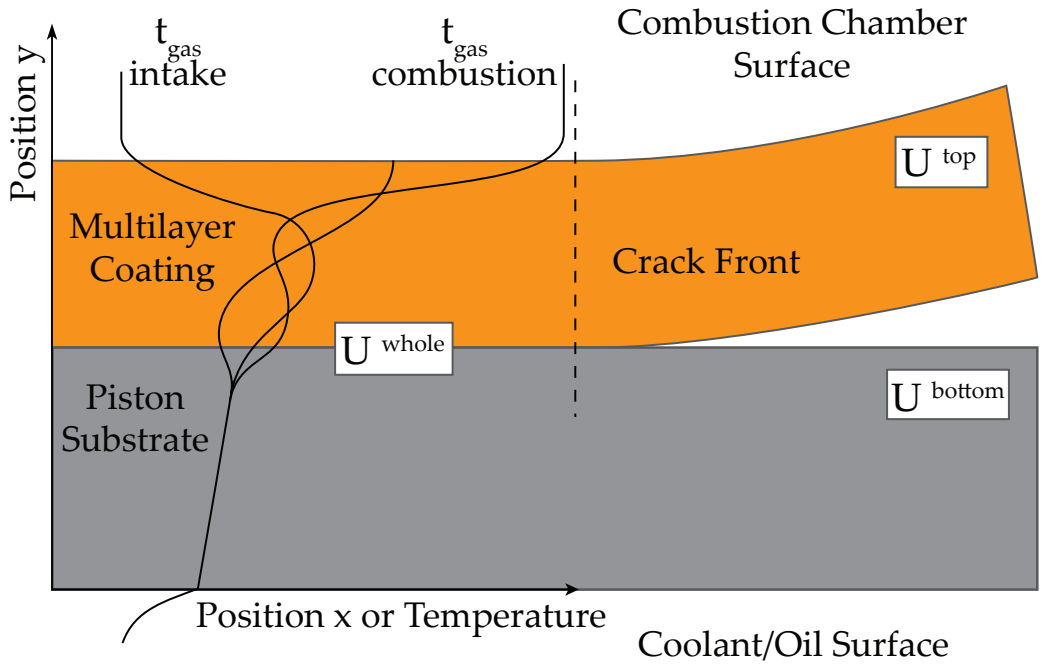

Figure 4.1: Schematic illustration of a thermal barrier coated piston exposed to combustion chamber gases (top) and coolant/oil (bottom). On the left side the intact (whole) wall temperature distribution is illustrated at three times during the cycle, *i.e.* intake, combustion, and mid-expansion. The right side depicts a delamination scenario where the energy release rate G overcomes the toughness and cracking occurs. The stored elastic strain energy of the intact structure and for the upper and lower parts behind the crack, indicated as U^{whole}, U^{top} and U^{bottom}, are used to calculate the energy release rate as given in Eq. (4.25).

merical scheme was used to integrate the unsteady, one-dimensional heat diffusion equation [114, 106]. The spatial domains, *i.e.* the piston substrate and the coating, were linearly discretized with 2^5 and 2^7 nodes, respectively. Further details about the finite difference convergence criteria can be found in Sections 3.1.3.4 and 3.1.4.

4.2.1 Experimental Setup

Experimental heat transfer data from an AVL 530 single-cylinder research engine at the U.S. Army Ground Vehicles Systems Center were utilized as the input for this work [3]. The engine was modified for high-power output diesel operation and is rated for 107 kW at 2750 rpm. Detailed engine geometric specifications can be found in Table 4.1. The engine peripherals, *i.e.*, intake, exhaust, coolant, oil and fuel subsystems, were instrumented and the exhaust composition was measured to allow *global* thermodynamic measurements to be performed and compared with the *local*, high-bandwidth in-cylinder heat flux measurements. The consistency between these two data sets provides confidence in the measured experimental heat flux [118, 3].

Table 4.1: Single-cylinder research engine geometric specifications.

Displacement [L]	1.49
Bore [mm]	122
Stroke [mm]	128
Connecting Rod Length [mm]	239
Number of Valves [−]	4
IVO [°aTDC]	-354
IVC [°aTDC]	-158
EVC [°aTDC]	346
Swirl Ratio [−]	1.3

A wireless piston telemetry system was used to acquire fast-response surface temperature data at fifteen radial locations; the microwave-based telemetry system has an advertised bandwidth of 10 kHz. The thermocouples were coaxial, J-type surface thermocouples with a mix of plated and sliver junctions depending on the piston curvature. The surface temperature data were ensemble averaged, then low-pass filtered at 2 kHz before the Fourier decomposition method was used to recover heat flux. Heat flux data were acquired using three injector clocking positions, and the results were interpolated to find the spatial heat flux distribution for a sector of the piston corresponding to one injector plume. The data were then integrated (spatially) to find a global heat transfer that represents the total

in-cylinder heat transfer, and finally normalized by the piston sector area to recover an area-weighted heat flux. The area-weighted data were utilized in this work. The reader is referred to [3, 118] for more detailed information about data processing, *i.e.* outlier elimination, filtering, and area-averaging.

4.2.2 Boundary Conditions

The heat flux data were measured on a standard, uncoated metal piston. Global heat transfer measurements with coated and uncoated pistons [3] did not indicate a significant change to heat transfer for any of the coated pistons. Therefore, utilizing the metal piston heat flux data as an estimate for the heat flux to a coated piston was considered reasonable for the purpose of developing the fracture mechanics model.

A wide range of operating conditions were explored by Gingrich *et al.* [118], including some very high output conditions. Three engine conditions were selected for study based on medium, high and very high power output. Details of the operating conditions are given in Table 4.2. The most advanced start of injection (SOI) for each condition, which is the most thermally severe [3], was selected to evaluate structural integrity.

Table 4.2: Single cylinder research engine operating conditions under investigation.

Condition	Speed [rpm]	IMEPg [bar]	AFR [–]	SOI [°aTDC]	Injection Duration [°]
50% Load	1700	12.3	29	-22	10.7
Rated Power	2500	20.3	26.8	-29	21.6
Combat Rated Power	2750	29.7	25.5	-9	40.5

IMEPg: Gross Indicated Mean Effective Pressure; AFR: Air-Fuel Ratio; SOI: Start of Injection

The area-weighted heat fluxes for these operating conditions are shown in Fig. 4.2 as a function of time. The heat flux data have different durations since they were acquired at different engine speeds. The 50% Load case has a peak heat flux of 5 MW/m^2, which is typical of a light-to-medium duty commercial vehicle. The nearly

12 MW/m^2 area-weighted peak heat flux of the Rated Power condition is quite high for medium- and heavy-duty engines. It is worth noting that the Combat Rated Power condition, which represents a condition of maximum power that can be achieved for short duration, has a peak heat flux almost 2.5× lower than the Rated Power condition. The cause for this behavior is the extended ignition duration and late combustion phasing to avoid mechanical failure [3], see Table 4.2.

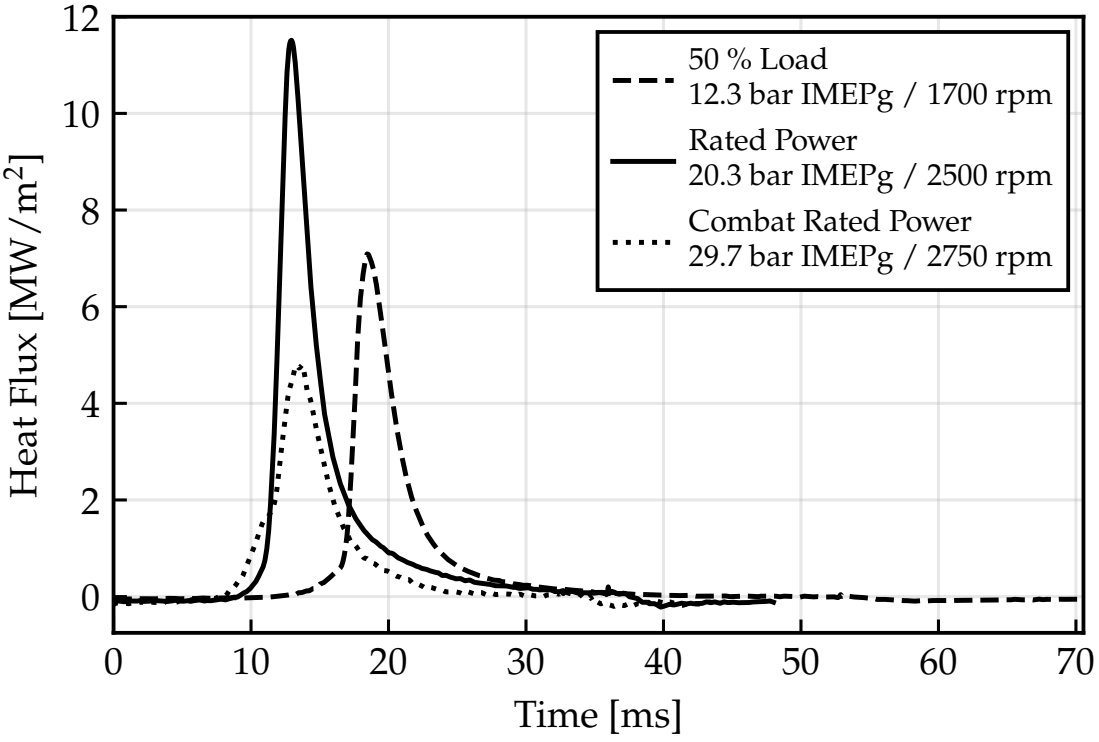

Figure 4.2: Experimental area-weighted heat fluxes obtained via telemetry measurements on an uncoated-piston. Details of the engine operating conditions can be found in Table 4.2.

4.3 Delamination Model

The impact of the thermal transients on coating mechanics is analyzed using well-established techniques [97]. The temperature profiles obtained in the previous section are used as inputs to compute the local thermal stresses and strain energy density in the multilayer at each point in time. The presented analysis ignores the fact that the delamination crack at the interface may impede the heat flow through the interface region in the manner considered and thereby change the temperature distribution near the crack tip and in the delaminated region. In turn, this change in the temperature distribution may alter the energy release rate. However, if the delamination crack advances rapidly, as would be expected if the energy release rate exceeds the toughness, there would not be time for thermal redistribution to take place, and the results derived would be valid. Both the coating and the substrate are assumed to be isotropic, elastic layers that experience stretching in the plane of the layers and bending about the in-plane axes. Durability is assessed in terms of the energy release rate for delamination cracks that run parallel to the coating; given the transient nature of the temperature distribution, the driving force for cracks at arbitrary depths relative to the surface and all times are considered.

For layers whose in-plane dimensions greatly exceed their thickness, the total strain in both layers can be approximated as $\epsilon(y) = \epsilon_o - \kappa \cdot y$, where y is the position measured from the bottom of the substrate. Here, ϵ_o denotes the stretch of the bottom axis of the layer, while κ denotes the curvature of the layer that induces bending strains. The stretch and curvature are evaluated from the resultant moment and force at each time, as will be evident below. As will be demonstrated, these bending strains are negligible for the present cases that involve relatively stiff, thick substrates. The above kinematics applies to both the substrate and the coating; however, bonded and debonded sections have different stretch and curvatures due to differences in in-plane stresses. To compute the strain energy in the system, one must compute the stretch and curvatures for each section, *i.e.* the intact region, and regions above and below the delamination plane, and the associated strain energies. In all regions of the bilayer, the stress normal to the interface, *i.e.* σ_y, and shear

stresses are assume to be negligible.

It is assumed that cracking relieves the in-plane stress in the layer above the delamination crack, but does not change of the out of plane deformation. This corresponds to the following relations for total strain components:

$$\begin{aligned} \text{Intact section: } \epsilon_x = \epsilon_z &= \epsilon_o^i - \kappa^i y && (4.1) \\ \text{Above the crack: } \epsilon_z &= \epsilon_o^i - \kappa^i \cdot y \\ \epsilon_x &= \epsilon_o^{\text{top}} - \kappa^{\text{top}} y && (4.2) \\ \text{Below the crack: } \epsilon_z &= \epsilon_o^i - \kappa^i \cdot y \\ \epsilon_x &= \epsilon_o^{\text{bot}} - \kappa^{\text{bot}} y && (4.3) \end{aligned}$$

where ϵ_o^i and κ^i are the stretch and curvature of the intact section of the bilayer respectively, and ϵ_o^{top} and κ^{top} are the stretch and curvature of the layer above the delamination respectively; ϵ^{bot} and κ^{bot} are the stretch and curvature of the layers below the delamination plane, respectively, which is a bilayer provided the crack location is not at the interface.

For each section, the unknown stretch and curvature can be computed from the resultant moment and force acting on the bilayer; in the present analysis, the reaction reaction forces/moments due to constraint of the substrate edges are assumed to be negligible, such that $M = \int_{\text{bot}}^{\text{top}} \sigma_x(y) y dy = 0$, and $N = \int_{\text{bot}}^{\text{top}} \sigma_x(y) dy = 0$. Using the above kinematics and the thermoelastic constitutive law $\epsilon_x = \sigma_x/E - v\sigma_z/E + \alpha\,[t(y) - t_{\text{ref}}]$ (and similarly for ϵ_z), where α is the coefficient of thermal expansion, one obtains two algebraic equations for the two unknowns, *i.e.* ϵ_o and κ. These integrals can be conveniently performed on a piece-wise basis using the numerical grid of the temperature analysis; the crack can be placed at any point on the grid, with the above kinematics applied in corresponding layers. Complete details of the stretch and curvature computation are provided in Section 4.3.1.

Literature information related to the stress-free temperature of coatings for reciprocating engines were not available. The reference temperature was taken as the mean surface temperature measured during the plasma spray deposition [119].

The effect of different residual stresses is discussed below. In this work, it was assumed that the coatings do not undergo creep relaxation during operation.

The strain energy released during delamination defines the energy release rate for a delamination crack; for a crack length that is much longer than layer thickness, the "steady-state" energy release rate is at its maximum and is independent of crack length. This steady-state energy release rate is given by:

$$G = U^i - \left(U^{\text{top}} + U^{\text{bottom}}\right) \tag{4.4}$$

where U^i is the strain energy per unit length in the intact section of the bilayer, while U^{top} and U^{bot} are the strain energies per unit length in the two sections formed by the delamination crack. In terms of stresses, the strain energy is given by [120, 97]:

$$U = \int_{y_{\min}}^{y_{\max}} \left[\frac{1+v}{2E} \left(\sigma_x^2 + \sigma_z^2\right) - \frac{v}{2E} \left(\sigma_x + \sigma_z\right)^2 \right] dy \tag{4.5}$$

where the integral of the strain energy density takes into account position-dependent stresses that arise from position-dependent properties, temperatures, per the thermal model, and different stretch and curvature values for each section. Delamination is expected when G exceeds the corresponding material toughness at the location of the crack, G_c. In the present study, the additional complication of a mode-dependent toughness is neglected; see [97] and [121] for a treatment of these effects.

The analytical relationship found in Section 4.3.1 offers significant computational advantages as compared to other numerical integration approaches [97]. It is worth noting a similar analytical form of elemental strain energy has been published by Jackson and Begley [121] assuming plane strain deformation ($\epsilon_z = 0$). Computational efficiency is particularly important for establishing energy release rate calculations in the unsteady environment of reciprocating engines. In practice, several hundred energy release rate evaluations are required per each engine cycle. For this study, the energy release rate was calculated every 1 crank angle, *i.e.* 720 evaluations for every thermodynamic cycle.

4.3.1 Outline of the Stress Analysis and Energy Release Rate Calculations

The proposed mechanics technique assumes that the time is takes a stress wave (traveling with the speed of sound) to propagate through the wall is considerably faster than for the temperature to change; *i.e.* dynamic stresses are neglected. As such, the conduction heat transfer problem is unsteady while the mechanical problem is quasi-steady.

The state of deformation is different prior to and during the delamination process. Equi-biaxial deformation is taken for the pre-delamination process, while plane strain is assumed for the delamination process. The corresponding controlling moduli and effective thermal strain coefficients of each stress/deformation state are given in Table 4.3.

Table 4.3: Effective moduli and misfit strain coefficients prior and during the delamination process

Mechanics Process	Pre-Delamination	Delamination
State of Deformation/Stress	Equi-biaxial	Plane Strain
Effective modulus, $\bar{E}$	$E/(1-\nu)$	$E/\left(1-\nu^2\right)$
ϑ coefficient, $\bar{c}$	1	$1+\nu$

By solving the constitutive law for two-dimensions, $\epsilon_x = \frac{1}{E}\left[\sigma_x - \nu\left(\sigma_y + \sigma_z\right)\right] + \vartheta$ and $\epsilon_z = \frac{1}{E}\left[\sigma_z - \nu\left(\sigma_x + \sigma_y\right)\right] + \vartheta$, the state of stress at any instant in an engine cycle, depth, and direction is given by

$$\sigma_x(y) = \frac{E}{1-\nu^2}\left[\epsilon_x + \nu\epsilon_z - (1-\nu)\,\vartheta\right] \tag{4.6}$$

$$\sigma_z(y) = \frac{E}{1-\nu^2}\left[\epsilon_z + \nu\epsilon_x - (1-\nu)\,\vartheta\right] \tag{4.7}$$

with total strains varying through the multilayer according to

$$\epsilon_x = \epsilon_{o,x} - \kappa_x y \tag{4.8}$$

and

$$\epsilon_z = \epsilon_{o,z} - \kappa_z \left(y + H_b\right) \tag{4.9}$$

where $\epsilon_{o,x}$, $\epsilon_{o,z}$ and κ_x, κ_z are the elongation and curvature of the x- and z-direction, respectively. The bottom sub-multilayer height is denoted as H_b. The thermal strain distribution ϑ is defined as

$$\vartheta\left(y\right) = \alpha\left(t\left(y\right) - t^{\text{ref}}\left(y\right)\right) \tag{4.10}$$

where α is the thermal expansion coefficient, $t\left(y\right)$ is the current temperature distribution, and $t^{\text{ref}}\left(y\right)$ is the reference temperature distribution.

The reference or stress-free temperature defines the state at which the multilayer is at a relaxed, stress-free condition. In practice, this is defined by the temperature at which the substrate is pre-heated prior to coating deposition. The effect of the residual stresses may be an important control parameter for combustion engine coating design.

The mechanical system response initially estimates the elongation and curvature of the system using the steps illustrated below. Let ϑ_t^i and ϑ_b^i be the thermal strain at the top and bottom node of element i, respectively. Assuming a piece-wise linear distribution through each element i, one gets

$$\vartheta^i\left(y\right) = \vartheta_b^i + \frac{y - y_b^i}{y_t^i - y_b^i}\left(\vartheta_t^i - \vartheta_b^i\right) \tag{4.11}$$

where y_t^i and y_b^i is the position of the top and bottom of element i, respectively.

Force and moment equilibria in the absence of external loads, for a N number of nodes system, require that

$$\sum_{i=1}^{N} \int_{y_b^i}^{y_t^i} \sigma_x\left(y, \vartheta_b^i, \vartheta_t^i\right) dy = 0 \tag{4.12}$$

and

$$\sum_{i=1}^{N} \int_{y_b^i}^{y_t^i} y \cdot \sigma_x \left(y, \vartheta_b^i, \vartheta_t^i \right) dy = 0 \tag{4.13}$$

which results in a set of two linear equations governing $\epsilon_{o,x}$ and κ_x

$$\begin{bmatrix} a_{11} & a_{12} \\ a_{21} & a_{22} \end{bmatrix} \begin{bmatrix} \epsilon_{o,x} \\ \kappa_x \end{bmatrix} = \begin{bmatrix} b_1 \\ b_2 \end{bmatrix} \tag{4.14}$$

where the a and b coefficients for solving (4.14) are given below

$$a_{11} = \sum_{i=1}^{N} \bar{E}_i \ell_i \tag{4.15}$$

$$a_{12} = a_{21} = -\sum_{i=1}^{N} \frac{\bar{E}_i \ell_i}{2} \left(y_t^i + y_b^i \right) \tag{4.16}$$

$$a_{22} = \sum_{i=1}^{N} \frac{\bar{E}_i \ell_i}{3} \left[\left(y_t^i \right)^2 + y_t^i y_b^i + \left(y_b^i \right)^2 \right] \tag{4.17}$$

$$\begin{aligned} b_1 = \sum_{i=1}^{N} \Bigg[& \frac{\bar{c}_i \bar{E}_i \ell_i}{2} \left(\vartheta_t^i + \vartheta_b^i \right) - \bar{E}_i \ell_i \nu_i \epsilon_{o,z} \\ & + \frac{\bar{E}_i \ell_i}{2} \left(y_t^i + y_b^i + 2H_b \right) \nu_i \kappa_z \Bigg] \end{aligned} \tag{4.18}$$

$$b_2 = -\sum_{i=1}^{N} \Bigg\{ + \frac{\bar{c}_i \bar{E}_i \ell_i}{6} \left[y_b^i \left(2\vartheta_b^i + \vartheta_t^i \right) + y_t^i \left(\vartheta_b^i + 2\vartheta_t^i \right) \right] + \frac{\nu_i \bar{E}_i \ell_i}{2} \left(y_t^i + y_b^i \right) \left(\epsilon_{o,z} - \kappa_z H_b \right) + \frac{\nu_i \bar{E}_i \ell_i}{3} \left[\left(y_t^i \right)^2 + y_t^i y_b^i + \left(y_b^i \right)^2 \right] \Bigg\} \tag{4.19}$$

where

$$\ell_i = y_t^i - y_b^i \tag{4.20}$$

such that

$$y_t^i = \sum_{p=1}^{i} \ell_p \qquad y_b^i = \sum_{p=1}^{i-1} \ell_p \qquad y_b^1 = 0 \tag{4.21}$$

Although similar a coefficients can be found in [97, 121], the b coefficients are unique to the problem of equi-biaxial stress prior to delamination followed by plane strain after delamination. The a coefficients depend on the element effective moduli $\bar{E}_i$ and position $y_{t/b}^i$, and the b coefficients additionally are functions of the thermal strain ϑ^i, its coefficient $\bar{c}_i$ and the z-direction elongation and curvature and the bottom sub-multilayer height H_b. The elongation $\epsilon_{o,x}$ and curvature κ_x are determined by solving the linear system in Eq. (4.14) together with Eqs. (4.11) and (4.15)-(4.21).

Crack growth is initiated when the energy release rate overcomes fracture toughness.

$$G \geq G_c \tag{4.22}$$

The change in strain energy is directly related to the energy release rate. The strain

energy, U_i, contained in element i is found from

$$U_i = \int_{y_b^i}^{y_t^i} \left[\frac{1+\nu}{2E} \left(\sigma_x^2 + \sigma_z^2 \right) - \frac{\nu}{2E} \left(\sigma_x + \sigma_z \right)^2 \right] dy \tag{4.23}$$

Combining the thermal strain distribution $\vartheta(y)$ from Eq. (4.11) and both stress components $\sigma_x(y)$ and $\sigma_z(y)$ as a function of position from Eq. (4.6) and (4.7) one gets

$$\begin{aligned}
U_i = & \frac{E_i \ell_i}{2\left(1-\nu^2\right)} \left[\epsilon_{o,x}^2 + \epsilon_{o,z}^2 + 2\nu \epsilon_{o,x} \epsilon_{o,z} \right. \\
& \qquad \left. - \left(2\nu \epsilon_{o,x} + 2\epsilon_{o,z} - \kappa_z H_b \right) \kappa_z H_b \right] \\
& - \frac{E_i \ell_i}{2\left(1-\nu^2\right)} \left(y_t^i + y_b^i \right) \left[\epsilon_{o,x} \left(\kappa_x + \nu \kappa_z \right) \right. \\
& \qquad \left. + \left(\epsilon_{o,z} - \kappa_z H_b \right) \left(\kappa_z + \nu \kappa_x \right) \right] \\
& + \frac{E_i \ell_i}{6\left(1-\nu^2\right)} \left[\left(y_t^i \right)^2 + y_t^i y_b^i + \left(y_b^i \right)^2 \right] \left(\kappa_x^2 + \kappa_z^2 + 2\nu \kappa_x \kappa_z \right) \\
& - \frac{E_i \ell_i}{2\left(1-\nu\right)} \left[\left(\vartheta_t^i + \vartheta_b^i \right) \left(\epsilon_{o,x} + \epsilon_{o,z} \right) - 2\vartheta_b \kappa_z H_b \right] \\
& + \frac{E_i \ell_i}{6\left(1-\nu\right)} \left\{ \left[y_b^i \left(2\vartheta_b^i + \vartheta_t^i \right) + y_t^i \left(\vartheta_b^i + 2\vartheta_t^i \right) \right] \left(\kappa_x + \kappa_z \right) \right. \\
& \qquad \left. + 3 \left(\vartheta_t^i - \vartheta_b^i \right) \kappa_z H_b \right\} \\
& + \frac{E_i \ell_i}{3\left(1-\nu\right)} \left[\left(\vartheta_b^i \right)^2 + \vartheta_b^i \vartheta_t^i + \left(\vartheta_t^i \right)^2 \right]
\end{aligned} \tag{4.24}$$

The energy release rate G at any interior location is determined by the difference between the strain energy of the intact (whole) multilayer ahead of the crack and the total strain energy contained in the two (top and bottom) layers formed by the crack interface, such as

$$G = U^{\text{whole}} - \left(U^{\text{top}} + U^{\text{bottom}} \right) \tag{4.25}$$

where U^{whole} and $\left(U^{\text{bottom}} + U^{\text{top}}\right)$ is the strain energy of the intact multilayer and the strain energy sum of the piston substrate, U^{bottom}, and coating, U^{top} (top), respectively.

4.4 Results and Discussion

Two thermal barrier coatings from the modern engine literature were selected for investigation. The first was yttria-stabilized zirconia, YSZ, a traditional engine coating [49] and the second was Cordierite-YSZ, a novel low thermal conductivity, low volumetric heat capacity coating [122]. Detailed coating property data can be found in Table 4.4. The thermal properties for these coatings are provided in the references; the mechanical properties of both coatings were provided by the Thermal Spray Lab of Stony Brook University [119]. The piston substrate was 4140 steel, which is often used in heavy-duty applications [123, 124]. The coating thickness was fixed (200 μm) except for in the section below where it was parametrically varied. The term *wall* is used to define the intact multilayer, *i.e.* bonded coating and substrate, unless otherwise specified.

Table 4.4: Thermo-mechanical properties of wall architectures investigated, with k: thermal conductivity; ρ: density; c: specific heat capacity; L: thickness; E: Young's modulus; α: coefficient of thermal expansion; and ν: Poisson ratio

Material	k [W/m-K]	ρ [kg/m^3]	c [J/kg-K]	L [μm]	E [GPa]	α [ppm K^{-1}]	ν [–]
YSZ [49, 119]	0.77	4713	388	200	41	12	0.2
Cordierite-YSZ [119, 122]	0.37	2855	347	200	18	6.8	0.25
Steel 4140 Piston [123, 124]	39	7850	520	4800	180	13.5	0.29

The surface temperature behavior as a function of piston position is illustrated for the 50% Load case in Fig. 4.3. The heat flux profile from Fig. 4.2 is superposed to illustrate the phasing difference between the heat flux and temperature profiles. The YSZ (blue) and Cordierite-YSZ (red) coatings provide a surface temperature swing of 290°C and 560°C, respectively. One may expect the Cordierite-YSZ coating to increase engine thermal efficiency due to the higher temperature swing,

which would give less heat transfer during the expansion stroke, but the higher surface temperature during the intake stroke may have a negative impact on engine breathing[116].

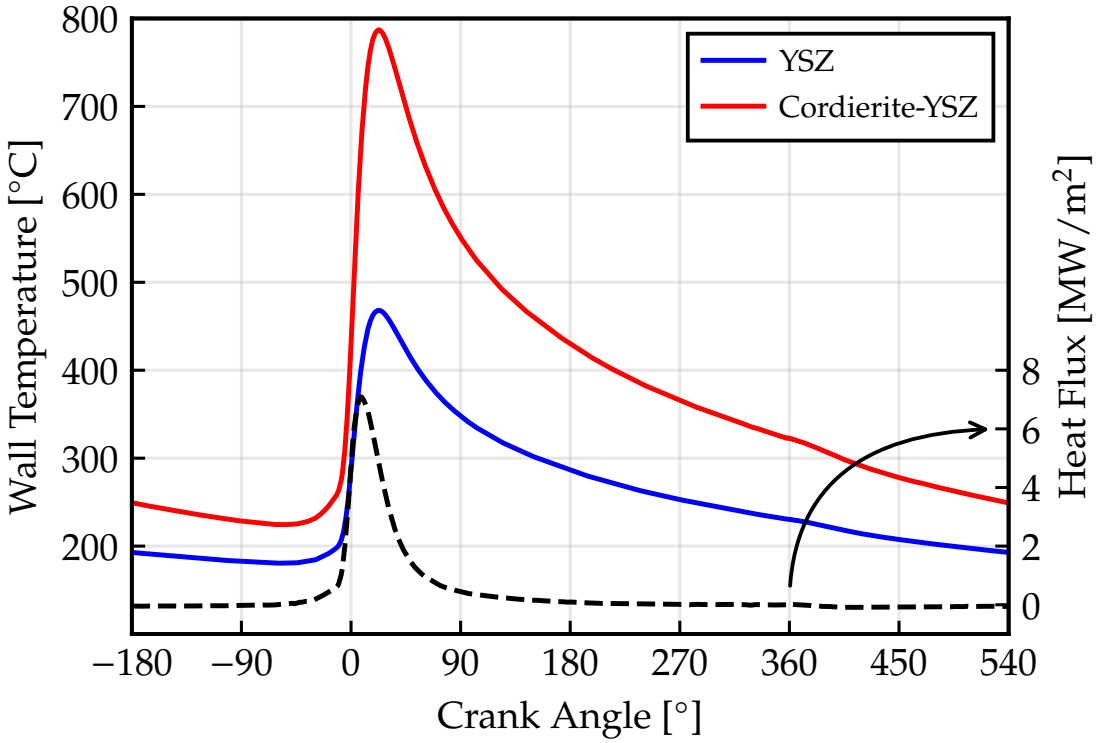

Figure 4.3: Surface temperature (solid lines, left axis) evolution as a function of crank angle for a YSZ (blue) and a Cordierite-YSZ (red) coating. Both coatings have 200 μm thickness. The applied heat flux is shown on the right axis. Note, the cycle shown corresponds to a total time of 48 ms.

4.4.1 Engine Cycle Histories

The coupled analysis is demonstrated for the Rated Power engine condition and the YSZ coating in Figures 4.4 and 4.5. The results shown in Figures 4.4 through 4.6 (discussed below) are typical of all the cases considered. Only the 360 crank angle degrees of the engine cycle during compression and combustion, where most of the

changes take place, are shown in Figure 4.5. This time period corresponds with the heat flux impulse shown in (a), for reference also see Figure 4.2. The temperature histories at four discrete locations are shown in Fig. 4.5 (b). The coating surface ($y = 0$) temperature follows the rapid increase of heat flux up to its peak value at 30°aTDC, but the temperature decays much slower than the heat flux. The amount of intra-cycle temperature change reduces progressing deeper into the wall; *e.g.* the coating-piston interface temperature varies by less than 4 K. The intra-cycle temperature variations in the piston substrate are negligible.

The temperature distribution is utilized as input to perform the deformation analysis. Figure 4.4 (a) shows the elongation and the curvature is shown in Fig. 4.4 (b) for a 200 μm YSZ coating on the piston substrate. Three curves are shown in each plot. Assigning a position $y = 0$ to the back side of the piston, per Fig. 4.1, the solid orange curve corresponds to a position y=4800 μm, *i.e.*, the bottom of the coating, while the other two curves, which are dashed and shown on the right axis, correspond to a position $y = 0$. The data shown in the legend as "Whole Material" ($\epsilon^w_{o,x}$ or κ^w_x) refers to the intact, combined structure. Equi-biaxial deformation is assumed for the pre-delamination process. The "Coating" and "Substrate" curves, $\left(\epsilon^t_{o,x}, \kappa^t_x\right)$ and $\left(\epsilon^b_{o,x}, \kappa^b_x\right)$, respectively where the t and b superscripts refer to top or bottom in Fig. 4.1, correspond to cases where the individual layer was subjected to the same time-varying temperature field as the intact structure without the constraint of the other material. Plane strain deformation is assumed for the delamination process.

Positive and negative elongation imply that the wall elongates and contracts, respectively. Negative and positive magnitudes of curvature denote that the wall curves downward and upward, respectively. Starting at the combustion event near 0°, the heat flux increases, as seen in Fig. 4.3. Localized surface heating, as it can be seen in Fig. 4.4 (a), causes the bottom of the coating to contract and the bottom of the substrate to elongate. During the latter part of the expansion stroke, from 60° to 180°aTDC, the heat flux has significantly diminished. The moment created by the localized surface heating and expansion has reduced and, in turn, the top coating experiences less elongation while the piston substrate undergoes less contraction

during the rest of the cycle. Meanwhile in Fig. 4.4 (b), the bottom of the coating begins to curve less downward up until the end of compression stroke.

The stress histories at the same through-thickness locations are shown in Fig. 4.5 (c). Negative and positive values indicate compressive and tensile stress, respectively. The vast majority of the thermal barrier coating is under compression; in this case, the reference temperature was set at 230°C [119]. As the surface temperature is increasing due to combustion, the compressive stresses in the coating increases. The maximum stress in the wall is observed to be exactly when and where the temperature distribution is maximized, *i.e.*, 30°aTDC at the surface.

The energy release rate, G, as a function of engine crank-angle (time) is shown in Fig. 4.5 (d). Immediately after the start of combustion, the energy release rate increases due to heating of the coating surface. The energy release rate histories show that the peak driving force for delamination occurs later in the cycle, around 60°aTDC, past the instant in time where the surface temperature and stress in the coating are at their maxima.

At a peak cylinder pressure of 25 MPa the compressive stress, *i.e.* σ_y, is about 10% of the maximum stress seen at the surface. However, the time at delamination (peak energy release rate time) in question occurs later in the cycle. There is a significant delay between the peak pressure (stress) and peak energy release rate – at least 30°. At the time of peak energy release rate in the expansion stroke (about 60°aTDC), the cylinder pressure is reduced to about 2 MPa, which is considered negligible compared to the compressive stresses generated due to thermal loading (about 250 MPa at 70°aTDC).

Figure 4.5 shows only four spatial locations for clarity. In reality, since the maximum energy release rate occurs at an unknown time and location, it needs to be computed at all times and locations. These data are shown in Figure 4.6, which provides a more comprehensive view of the temperature, stress and energy release rate distributions throughout the coating and engine cycle. The engine conditions are the same as Fig. 4.5. The horizontal and vertical axes represent crank-angle (time) and position through the wall, respectively. The latter has two different linear scales: 0-200 μm for the coating, and 200-5000 μm, for the substrate. The

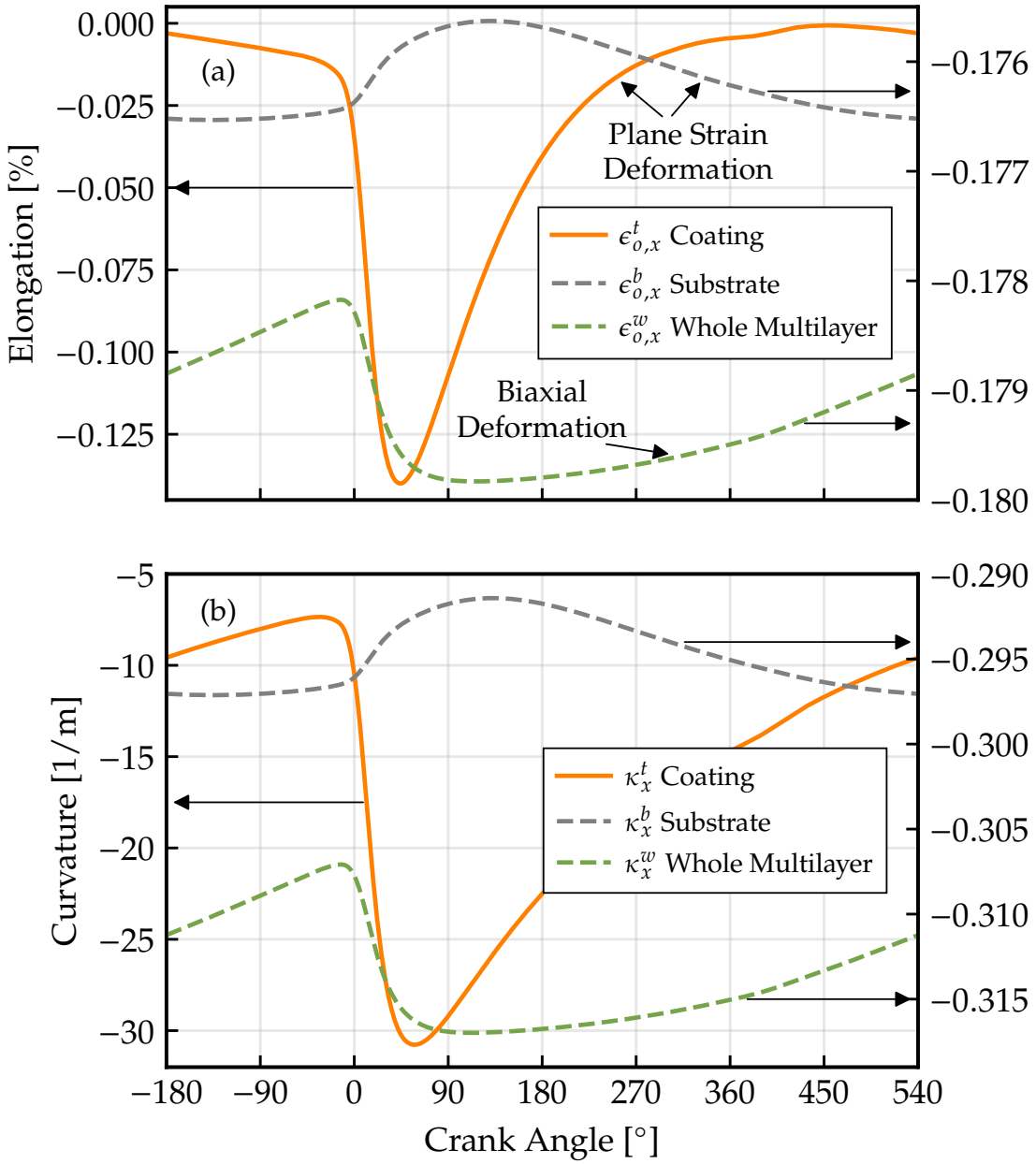

Figure 4.4: Elongation (a) and curvature (b) on the x-direction of the coating as top layer (orange solid line left axis), the piston wall as bottom layer (gray dashed line right axis), and the whole multi-layer (green dashed line right axis) as a function of crank angle. Equi-biaxial stressing is assumed for whole multi-layer during pre-delamination. Plane strain delamination is followed for the coating and substrate layers during delamination. The Rated Power engine condition specifications and the thermomechanical properties of YSZ/Steel can be found in Table 4.2 and 4.4, respectively.

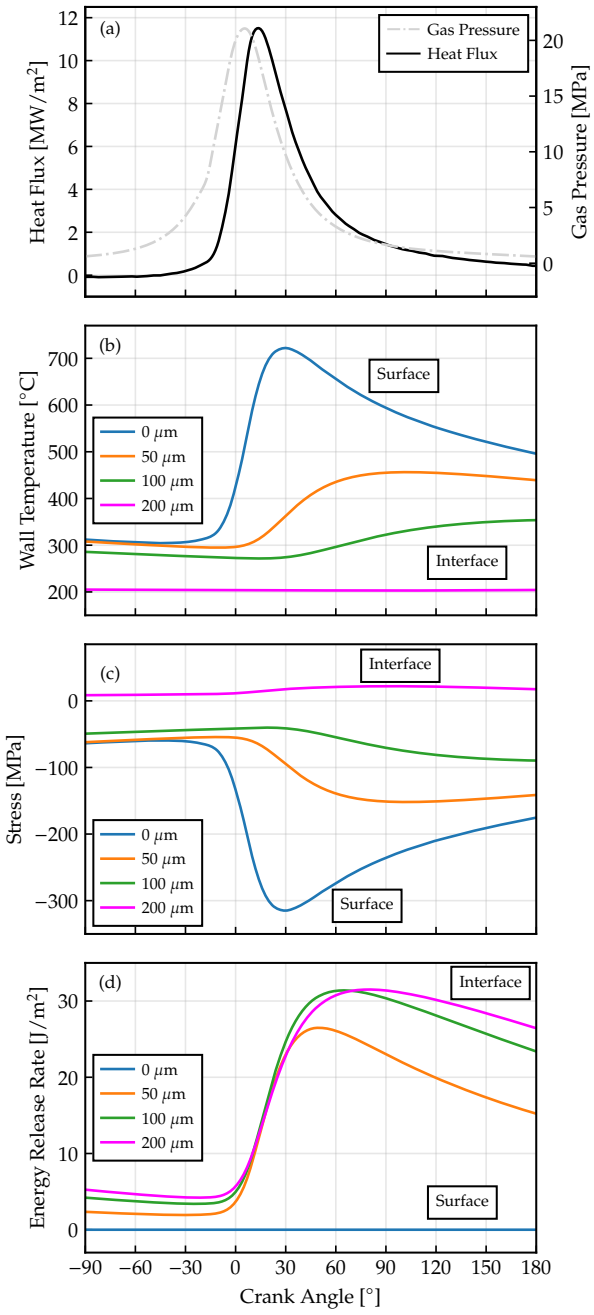

Figure 4.5: Crank resolved evolution combustion chamber cylinder pressure (grey) and heat flux (black) (a), wall temperature distribution (b), x-direction stress distribution (c) and elastic energy release rate distribution (d) are shown during an engine cycle for the Rated Power condition. The surface (blue), 50 μm (orange), 100 μm (green) and interface 200 μm (pink) is depicted on (b), (c) and (d). Stress-free temperature and coating thickness was held constant at 230°C and 200 μm, respectively. The Rated Power engine condition specifications and the thermomechanical properties of YSZ/Steel can be found in Table 4.2 and 4.4, respectively.

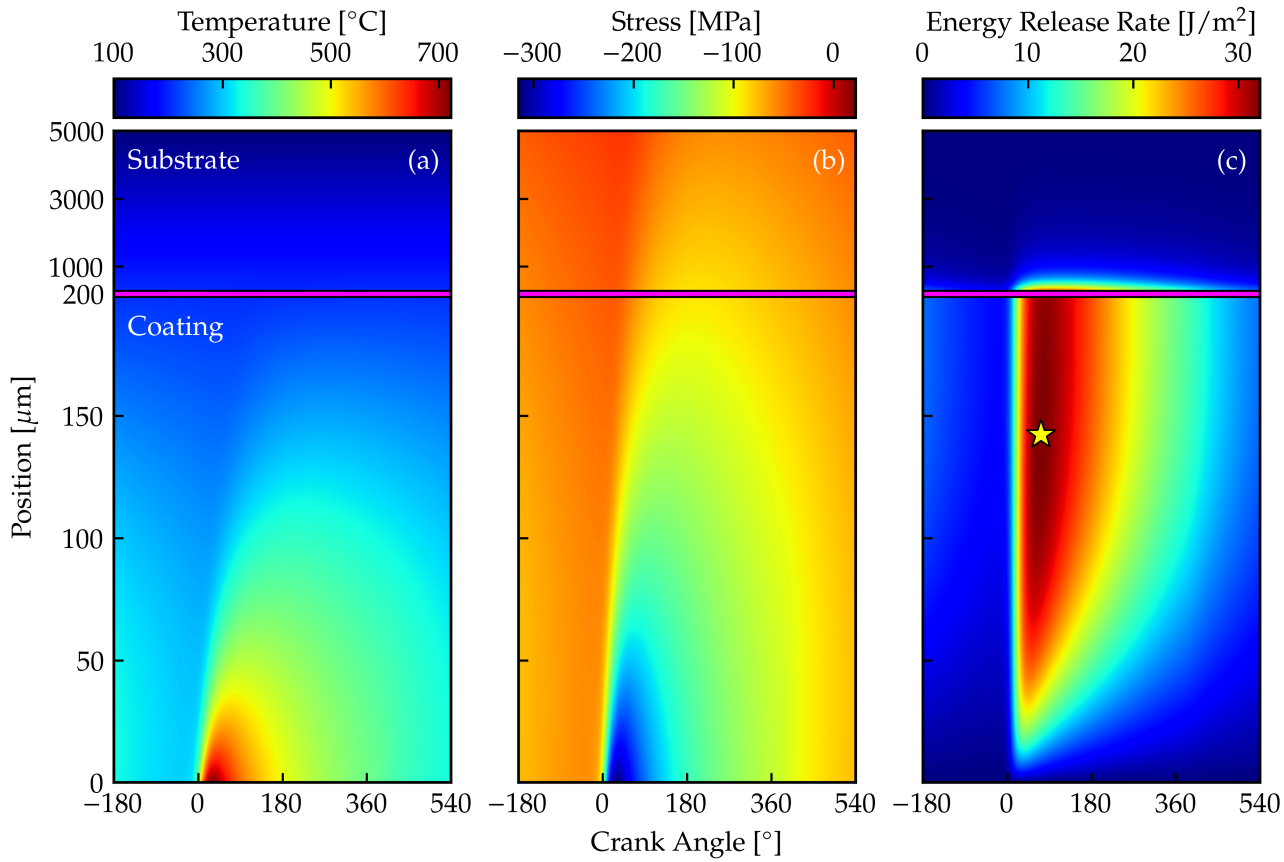

Figure 4.6: Spatial and temporal (in crank angle domain) evolution of temperature (a), stress (b) and energy release rate (c) using a YSZ thermal barrier coating on top of a piston substrate of an internal combustion engine cycle for the Rated Power condition. Combustion chamber surface and oil surface is at $y = 0$ and $y = 5000$, respectively. Coating-piston interface is indicated with the horizontal pink at 200 μm. The stress-free temperature was at 230°C. Wall architecture and operating condition was equivalent to Fig. 4.5.

coating-substrate interface lies on the horizontal pink line, at 200 μm. The contour maps in Fig. 4.6 are broadly representative of all cases considered in this work. Figure 4.6 makes it easy to see the penetration of the thermal (and corresponding quasi-steady stress) profile into the coating, and the resulting evolution of the energy release rate distribution.

The maximum energy release rate, highlighted with the yellow star, occurs during the expansion stroke, at 72°aTDC at a depth of 142 μm. At this time of the cycle, the surface of the coating is cooling but the interior region is still heating. It is interesting to note that the position of the maximum energy release rate is near the mid-coating region. This behavior suggests that, for cases where energy release rate exceeds the toughness, the coating would have higher likelihood to crack at the mid-coating area than at the coating-substrate interface. This is a unique feature brought on by the cyclic thermal loading of the engine, and is discussed more below.

4.4.2 Effect of Coating Material

A comparison of the spatial distribution (normal to the wall) of the energy release rate for the two different coating materials at the Rate Power condition is shown in Figure 4.7. The full domain is shown at the left, and a magnified view of the coating is shown at the right. The shaded region ranging from 0 to 200 μm corresponds to the coating material, with the combustion chamber gas (heat flux input) to the left. Results are shown for three distinct times in the cycle, denoted by line style, and both coatings, denoted by color. Both coatings had a fixed stress-free temperature of 230°C. The two coatings follow a very similar pattern, but the energy release rate for the YSZ coating is higher in magnitude at all times. The Cordierite-YSZ coating has lower thermal conductivity and volumetric heat capacity, and therefore experiences a higher temperature swing and higher peak temperature in the cycle than the YSZ, which would suggest higher energy release rates. However, the higher coefficient of thermal expansion and Young's modulus of the YSZ outweigh the more severe thermal environment for Cordierite-YSZ, resulting in the observed trend.

In Figure 4.6 it was shown that the maximum energy release rate was found within the coating, not at the interface. This effect is seen to occur for both coating materials in Figure 4.8, which depicts the data on a temporal basis. The maximum energy release rate, shown on the right axis, is seen to peak at the same crank angle for both coatings. The ratio of the maximum energy release rate at a given time to the corresponding value at the coating-substrate interface is shown on the left axis of Figure 4.8. The times of most interest are those with high energy release rate, *i.e.* after top dead center. It can be seen that during this period the maximum value exceeds the interface value by up to 8%, and is about half of that magnitude at the time of peak energy release rate. The data in Fig. 4.7 confirm that the maximum value lies within the coating. Qualitatively, this result agrees with the findings of Thibblin and Olofsson [67] shown in Fig. 2.6 of the Introduction.

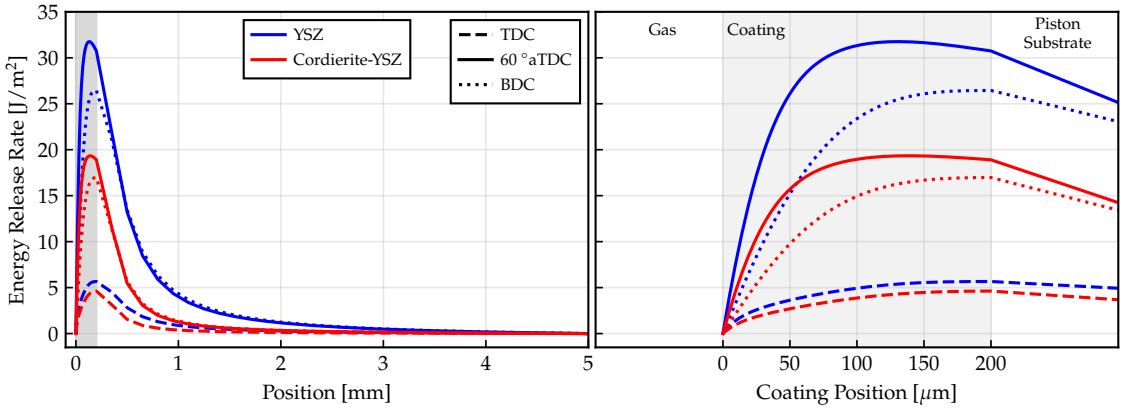

Figure 4.7: (a) Energy release rate spatial distribution is shown for the entire engine wall, *i.e.* coating and substrate. Two different coatings and three distinct crank angle locations are illustrated. The shaded area highlights the coating YSZ (blue) and Cordierite-YSZ (red) coating. The results shown are at TDC (dashed), 60°aTDC (solid) and BDC (dotted). The same engine condition as Fig. 4.5 and 4.6 were used. The stress-free temperature was 230°C. Thermomechanical properties can be found in Table 4.4. (b) Expanded version of the energy release rate spatial distribution in the coating.

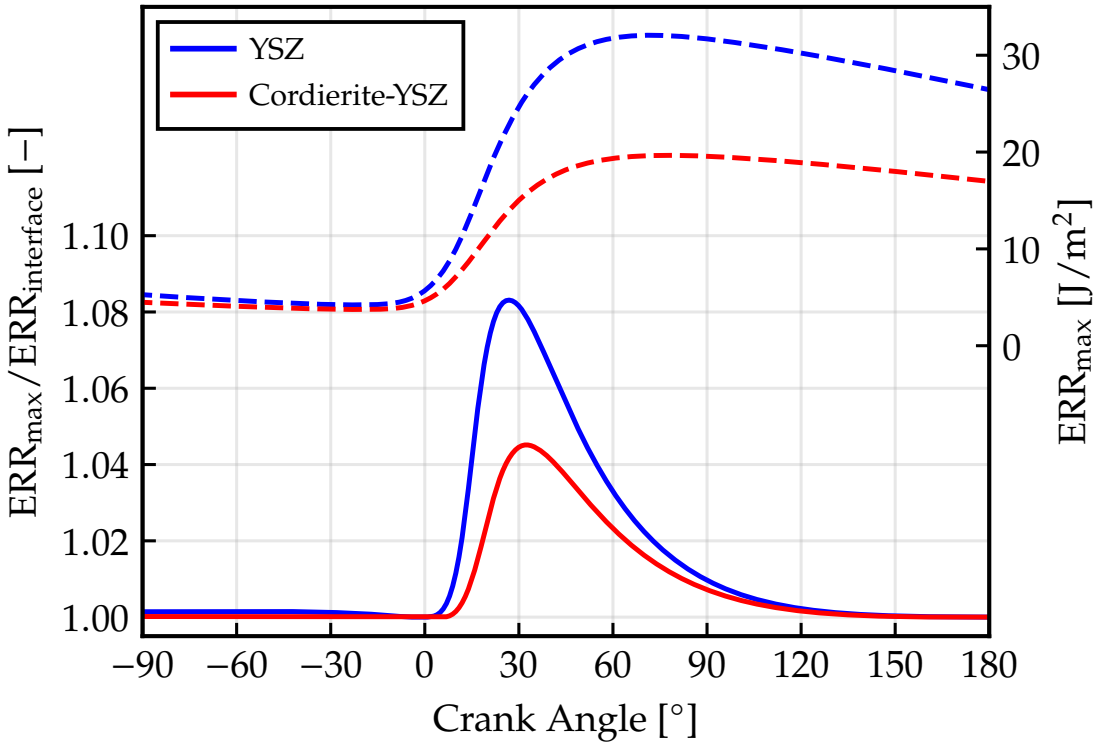

Figure 4.8: Ratio between maximum and interface energy release rate (left axis) and maximum energy release rate (right axis) during the compression and expansion stroke for the YSZ and Cordierite-YSZ coatings.

4.4.3 Effect of Coating Thickness

The thickness is a critical parameter that controls coating performance. A thicker thermal barrier coating reduces heat transfer, but may have negative effects on overall engine performance and coating durability. The energy release rate of a gas-turbine coating, assuming a heating or cooling scenario, scales linearly with thickness [97, 101]. There are a few fundamental differences between a coated piston and a coated gas turbine blade. The first is the time scale of the transient processes. Second, the backside temperature for the piston is considered constant during an engine cycle, but for the turbine blade it may change substantially during a take-off or landing thermal transient.

Figure 4.9 (a) shows the effect of the coating thickness, ranging from 50 μm to 300 μm, on the maximum energy release rate during a cycle for all three engine operating conditions, denoted by line style, and both coatings, denoted by color. The peak energy release rate is seen to increase with coating thickness, as expected, but in a nonlinear manner. The nonlinear dependence is driven by the transient heat flux conditions. The highest peak energy release rates were observed for the Rated Power condition, which has the highest heat flux, see Fig. 4.2. The other two engine conditions, had comparable peak heat flux and behaved similarly to each other.

The magnitude of the maximum energy release rate, however, does not encapsulate all of the coating thickness effects. Figure 4.9 (b) shows the ratio of the depth of the maximum energy release rate to the coating thickness as a function of the coating thickness; a value of unity indicates that the maximum energy release rate is at the piston-coating interface. For the Cordierite-YSZ coating, the maximum energy release rate was at the interface for both the 50% Load and Combat Rated Power conditions, while for YSZ the maximum value was found within the coating for all three cases. For cases where the ratio was less than unity, *i.e.,* the maximum occurs in the coating, the location is dependent on the coating thickness. As the coating thickness increases up to around 200 μm, the location of the maximum energy release rate moves further into the coating. This suggests that thicker coatings may be prone to ablate as compared to peel. For thickness greater than 200 μm, the location of the maximum energy release rate moves towards the interface.

The maximum energy release rate is also found at different times during the engine cycle as coating thickness changes. Figure 4.10 shows the relationship between the crank angle location of the maximum surface temperature to the corresponding value of maximum energy release rate. The coating thickness is represented by the size of the marker and corresponds to the range of values used in Fig. 4.9. The time of maximum energy release rate is seen to always lag the time of peak surface temperature or stress maximum, *i.e.*, lie below the 1:1 line. The maximum energy release rate may occur anywhere between 5 to almost 60°aTDC later in the expansion stroke than the maximum temperature.

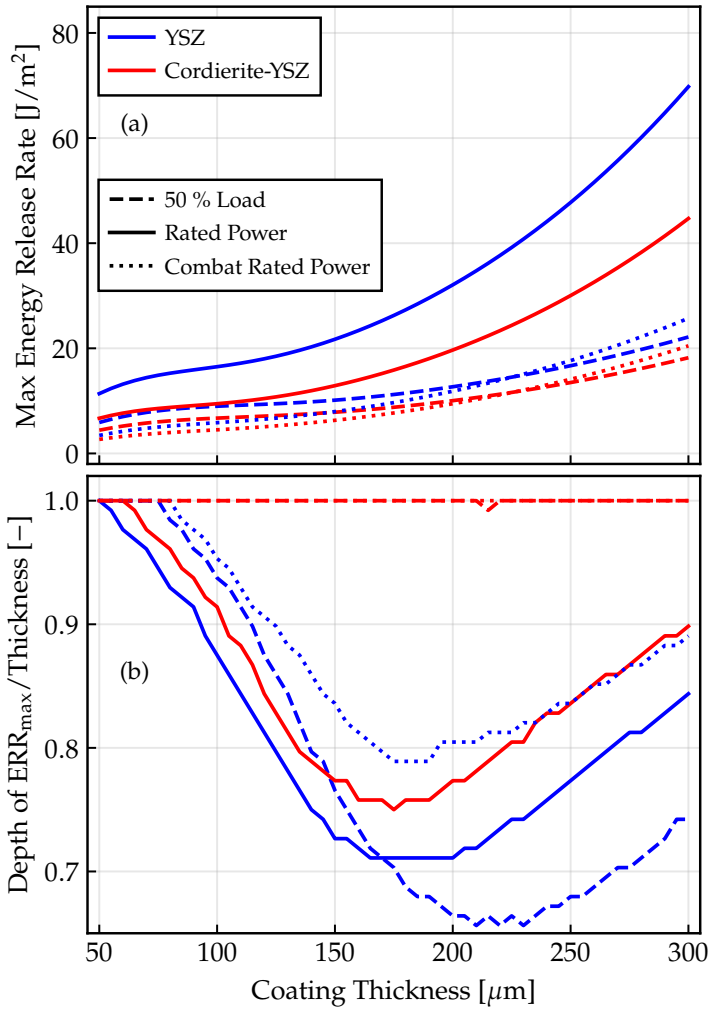

Figure 4.9: Effect of increasing coating thickness on (a) the maximum energy release rate, and (b) the ratio between the depth of maximum energy release rate and coating thickness. Engine conditions details for the 50 % Load (dashed), Rated Power (solid) and Combat Rated Power (dotted) can be found in Table 4.2. Thermomechanical properties of the YSZ (blue) and the Cordierite-YSZ (red) coating can be found in Table 4.4. The stress-free temperature was 230°C.

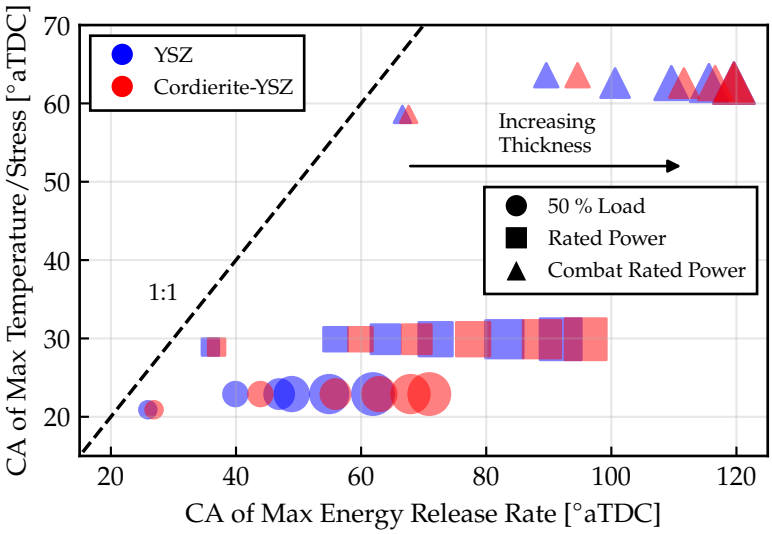

Figure 4.10: Comparison of crank angle location of maximum surface temperature or stress to the crank angle location of maximum energy release rate observed in a cycle. Every point lies below the 1:1 line, indicating that the energy release rate maximum occurs later in the cycle than the maximum of temperature or stress. The marker size indicates increasing coating thickness from 50 μm to 300 μm.

4.4.4 Effect of Deposition (Residual) Stresses

The majority of aircraft engine coating studies[97] assume that the stress-free temperature is the highest steady-state temperature that the coating experiences when exposed to combustion gases, *i.e.* $t_{\text{wall}} \geq 1300°\text{C}$ at the surface. The rationale is that at such high temperatures the coatings will relax and creep. This is not valid for reciprocating engine operation, however. Even under the most extreme conditions (analogous to the current Rated Power case), the maximum temperature of the coating is held for only a couple of milliseconds, and the peak temperature is localized at the surface. The inner part of the wall/coating experiences lower temperatures. Therefore, the stress-free temperature is not dominated by the combustion gas temperature. It is more likely that the stress-free state is defined by the temperature that the substrate was preheated to prior to and during coating deposition. This process-related temperature may be an important design parameter for thermal

barrier coatings in reciprocating engines.

Fig. 4.11 shows the effect of the reference temperature on the maximum energy release rate during a cycle for all three engine conditions and both coatings. The reference temperature range, from 100 to 350°C, was chosen to be representative of plasma spray deposition techniques. The coating thickness was held fixed at 200 μm. For increasing reference temperature the maximum energy release rate in the cycle is increased. Generally, higher reference temperature results in higher compressive stress, and thus strain energy at room temperature. For engine operation, the reference temperature adds an extra compressive stress component to the total compressive stress, as can be observed from Eqs. (4.6) and (4.10). As a practical example, for the Cordierite-YSZ coating the results suggest that the maximum energy release rate can be reduced 3× simply by decreasing the reference temperature from 350°C to 100°C.

Recall, this stress-free temperature does not alter the heat transfer physics of the problem, and it can be modified by the manufacturing process.

4.5 Summary and Conclusions

Failure analysis of thin thermal barrier coatings for reciprocating engines was performed using a coupled thermomechanical approach. An analytical method to evaluate transient energy release rate assuming equi-biaxial stress followed by plane strain after delamination was utilized. The highly unsteady nature of the applied heat flux and resulting thermal wave in the solid require evaluation at all times in the engine cycle to determine when and where the peak energy release rate is likely to occur. A transient finite difference solution of the 1-D heat diffusion equation was used to determine the temperature distribution. The method was demonstrated for two thermal barrier coatings and three high output diesel engine operating conditions.

The proposed approach to analyze durability of reciprocating engine coatings was fracture-based as compared to other stress-based approaches. The key results from this analysis are:

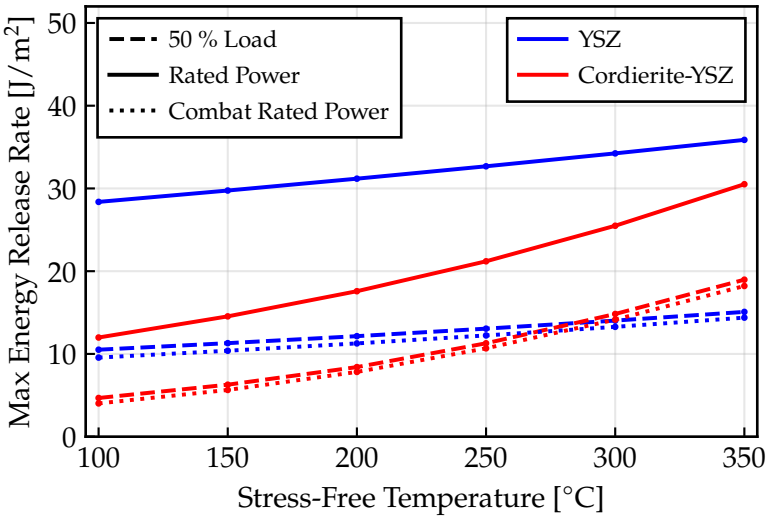

Figure 4.11: Effect of stress-free/reference temperature (ranging from 100 to 350°C) on maximum energy release rate observed in a cycle for different engine conditions and coating architectures. The coating thickness remained fixed at 200μm. Engine conditions details for the 50 % Load (dashed), Rated Power (solid) and Combat Rated Power (dotted) can be found in Table 4.2. Thermomechanical properties of the YSZ (blue) and the Cordierite-YSZ (red) coating can be found in Table 4.4.

i) The peak energy release rate was found to occur at a time in the expansion stroke significantly later than the time that the peak surface temperature and stress were observed. At this time the surface is cooling, but a significant fraction of the coating is still undergoing heating.

ii) The peak energy release rate did not always coincide with the coating-substrate interface. Under the most severe thermal conditions (highest peak heat flux) the location was found to lie within the coating. This suggests that the coating may begin to fail via spalling rather than pealing off the substrate.

iii) The peak energy release rate was found to scale directly with coating thickness, but in a nonlinear manner. This was a result of the unsteady nature of the applied heat flux.

iv) The location of peak energy release rate within the coating was found to

vary with coating thickness in a non-monotonic fashion. The time in the cycle of peak energy release rate was found monotonically increase with coating thickness, which is consistent with the longer time for thermal wave penetration.

v) The magnitude of the peak energy release rate was found to vary directly with the stress-free temperature, which is a manufacturing process variable; for engine applications there is not a significant amount of time spent at high temperatures, unlike in gas turbine applications where creep dominates and the reference temperature is governed by operating temperatures.

5 ENGINE PERFORMANCE

This chapter presents a coupling between the heat conduction solution developed in Chapter 3 with engine analysis. Section 3.1 uses the step-response solution, shown in Eq. (3.31), for a traditional and contemporary coating on a single-cylinder engine model using steady state and short transient event operation. Section 3.2 fully demonstrates the triangular-pulse response solution, shown in Eq. (3.63), embedded in a commercial system simulation software package. The software package was used to simulate the effects of various coating architectures applied to a multi-cylinder engine over a full drive cycle.

5.1 Initial Demonstration of Surface Temperature Prediction

5.1.1 Demonstration

A simple model was constructed to demonstrate the coated wall temperature solution methodology based on the step-response discussed in Section 3.1.5. The engine model is crude, but suffices for the demonstration of the wall temperature calculation. A closed-cycle (from IVC to EVO) single-zone model was created with the chemical kinetics solver Cantera in Python [125]. The cylinder contents are uniform throughout the combustion chamber. Fuel was added to the system at a mass flow rate that was prescribed by a Wiebe function with the parameters tuned to match data provided by John Deere. Ignition and combustion were calculated directly using a 45 species / 155 reaction kinetic mechanism [126]. The model fuel was *n*-heptane. Convective heat transfer to the wall is given as

$$\dot{q}'' = h\left(t_g - t_w\right) \tag{5.1}$$

where h is the heat transfer coefficient, t_g is the bulk gas temperature from the gas-phase kinetics solver and t_w is the coated wall temperature. According to literature cited in the Introduction, the heat transfer coefficient can be altered in a coated engine. In this work, the effect of the coating on the heat transfer coefficient was not included. The heat transfer coefficient was calculated according to the Annand correlation [127]

$$h = C\frac{k}{B}Re^{0.7} \tag{5.2}$$

where C is a constant coefficient taken as 0.5, k is the gas conductivity, B is the cylinder bore and Re is the Reynolds number

$$Re = \frac{\rho \bar{S}_p B}{\mu} \tag{5.3}$$

where ρ and μ are the air density and dynamic viscosity, respectively, $\bar{S}_p$ is the mean piston speed, and B as the cylinder bore.

The open portion of the cycle was modeled in three parts. First, the gas temperature was linearly interpolated between EVO and BDC from the EVO temperature to the temperature arising from an isentropic expansion from the EVO state to the exhaust pressure. Second, during the exhaust stroke until gas-exchange TDC, the gas temperature remained constant. Finally, from TDC until 30° aTDC, during the filling process, the gas temperature dropped linearly to the IVC temperature where it remained constant until IVC. The heat transfer coefficient remained constant at 400 W/m^2-K during the open part of the cycle.

5.1.1.1 Engine Model Comparison

Data from two engine conditions were provided by John Deere for the 4045 engine geometry, see Table 5.1. The first case, referred to hereafter as the low load case, was 7.2 bar IMEPg at 1300 rpm. The second case, referred to hereafter as the high load case, was 17.2 IMEPg bar at 1300 rpm.

The closed-cycle cylinder pressure was approximated with the Cantera code. A comparison of the model pressure to the data provided by John Deere is shown

Table 5.1: John Deere 4045 single-cylinder engine geometry

Number of cylinders	1 [–]
Displacement volume / cylinder	1.125 L
Stroke	127 mm
Bore	106.5 mm
Connecting Rod	203 mm
Compression Ratio	17.0:1
Intake Valve Close	-154° aTDC
Exhaust Valve Open	126° aTDC
Coolant temperature	373 K

in Figure 5.1 (top). Overall, it can be seen that there is good agreement for the closed-cycle period using the relatively simple model. The bulk gas temperature, see Fig. 5.1 (bottom), also matches the John Deere data quite well during the closed portion of the cycle. The approximations of the open portion of the cycle are also, for the present purposes, seen to be sufficient.

5.1.1.2 Quasi-steady Simulation

The low load scenario was chosen to illustrate the quasi-steady solution. The following cases are compared: (1) a one-layer aluminum wall of 5 mm thickness, (2) a two-layer, TS-coated aluminum wall, and (3) a four-layer, YSZ coated aluminum wall. The coating material thermal properties and layer thicknesses are described above in Table 3.2. The response factors for the test cases were calculated using 100 roots. A temperature difference was calculated between the current and previous cycle's value, and when an absolute convergence criteria of wall temperature difference of 0.05 K (maximum over a cycle) was reached, the simulation ended.

As expected, the wall temperature solutions required few cycles to converge, mostly due to the contribution of the initial step $-\bar{q}''$ decay and the volumetric heat capacity of the multi-layer structure.

In Fig. 5.2, the one-layer aluminum wall (black) results in an almost negligible temperature swing [128], and took five (5) cycles to fully converge. The four-layer YSZ (blue) case required required four (4) cycles to converge. The combination of

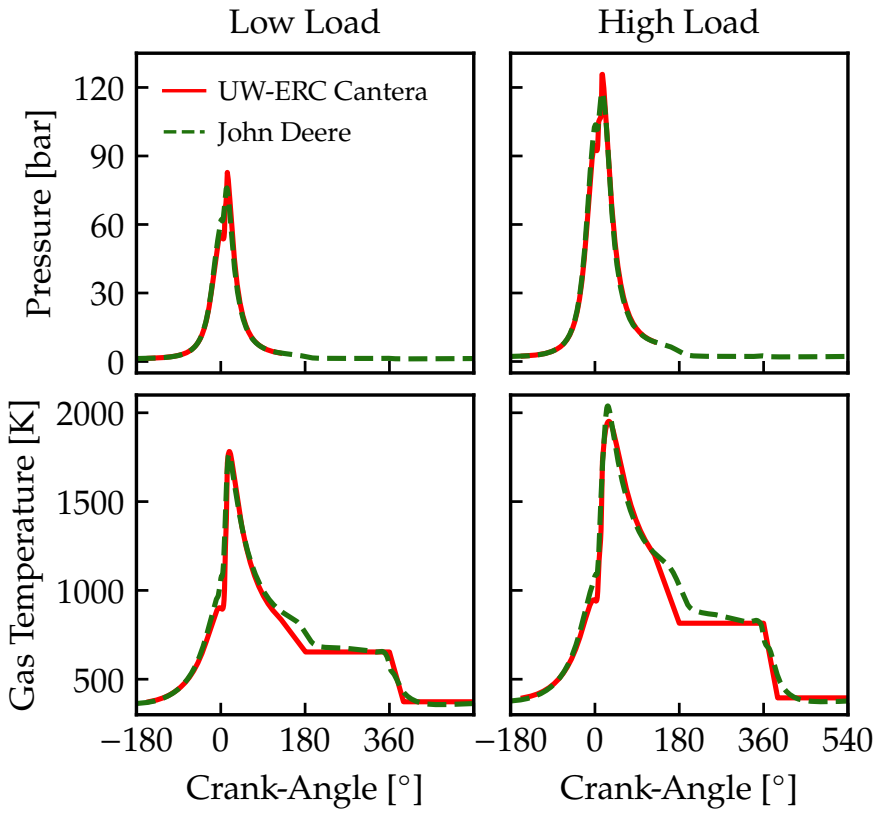

Figure 5.1: Pressure (top) and gas temperatures (bottom) traces as a function of crank-angle. Matching conditions between UW-ERC Cantera and John Deere models at low and high load test cases.

low thermal conductivity and high volumetric heat capacity of the structure led to a significantly elevated cycle-average wall temperature, which may be detrimental for engine applications. Finally, the two-layer TS case (red) needed only two (2) cycles for complete convergence. The low thermal conductivity and low volumetric heat capacity of the coating makes the results promising because the wall temperature follows the gas temperature much closer.

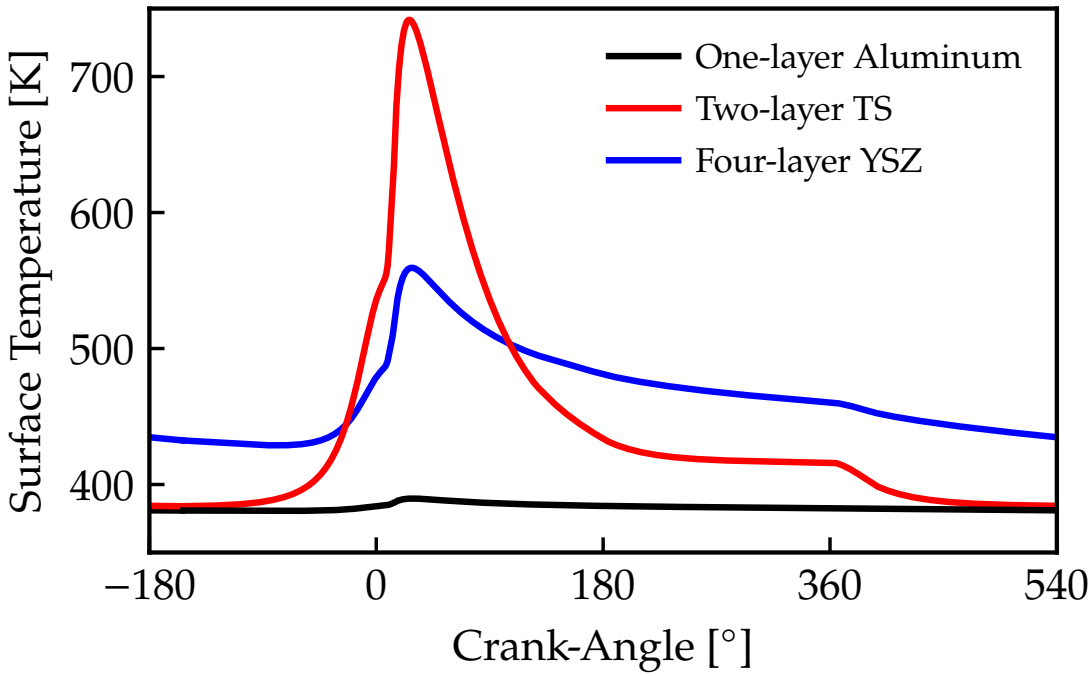

Figure 5.2: Coated surface wall temperature for the low load scenario of the converged cycle for an one-layer aluminum wall (black), a two-layer TS coating (red) and a four-layer YSZ coating (blue).

5.1.1.3 Transient Simulation

As discussed above, the high accuracy and low computational cost associated with this method make it well suited for transient analysis. A transient simulation scenario of a step load change is illustrated below. The simulation was for a load step change at a constant speed of 1300 rpm using the John Deere 4045 engine. The first 10 cycles were at the low load condition, and the 11^{th} and all subsequent cycles were at the high load condition, refer to Fig. 5.1 for operating details. Both the TS and YSZ coating structures described above were simulated.

Results of the simulation are shown in Fig. 5.3. Only three cycles of the simulation are shown for the TS coating: cycle 10 - the last low-load cycle (dashed), cycle 11 - the first high-load cycle (open circles), and cycle 100 - the final cycle (solid).

Due to its low-volumetric heat capacity, the TS coating (red) required very little time to respond fully to the sudden load step change. This can be seen by how closely cycle 11 matches the final cycle of the simulation, which is essentially the fully converged solution for operation at the high load condition. It is also interesting to note that the wall temperature during the intake stroke is, at the scale of Fig. 5.3, independent of engine load. This is the manifestation of the very rapid decrease in X_{step} with time for the TS coating that is seen in Fig. 3.8, *i.e.*, there is very little memory of the past heat flux events.

The YSZ coating (blue) shows a very different response to the step change in load. Inspection of cycle 11 shows that initially (and not surprisingly) the wall temperature follows the history of the previous low-load cycle. At the combustion event, the higher heat flux pushes the wall temperature to a value that is close to that of cycle 100 (the nearly converged high-load condition). But, significant differences exist between cycles 11 and 100. These differences are the result of the longer 'memory' of the YSZ-coated wall seen in Fig. 3.8. The larger total resistance of the YSZ-coated wall results in a higher average temperature for the high load condition in comparison to the low-load conidition.

Figure 5.4 shows results for the entire transient simulation. The temperature at the start of the compression stroke (BDC) is shown for all 100 cycles. The TS coating (red) responds in almost two cycles while the YSZ (blue) requires nearly five cycles to respond. The resulting steady state temperature difference at BDC between the low- and high-load conditions are 6 and 38 K for the TS and the YSZ, respectively.

5.2 Engine System-Level Performance over a Full Drive Cycle

This section presents a coupling between the analytical methodology for multilayer coated wall surface temperature prediction and a commercial system-level simulation software package (GT-Power). The wall surface temperature at each time

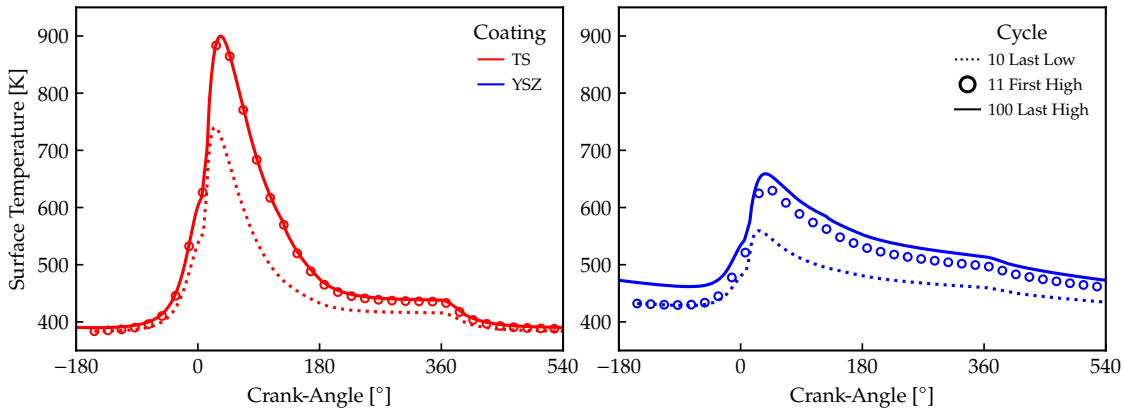

Figure 5.3: Transient simulation results of the coated wall surface temperature for 100 cycles. Cycle 10 (dashed) is the last low load cycle, cycle 11 is the first high load (circle) cycle, cycle 100 is the last high load (solid) cycle. The two-layer TS coating (red) results are shown at left and the four-layer YSZ coating (blue) results are at right.

step was calculated efficiently by convolving either X or Y with the time-varying surface boundary condition, *i.e.*, in-cylinder heat flux and coolant temperature. The implementation allows the wall to be treated as independent head/piston/liner components.

5.2.1 Wall Architectures

Five wall coating architectures, specifically designed for reciprocating internal combustion engine applications, with various thermal properties and thickness were collected from the modern thermal barrier coating literature and will be investigated, see Table 5.2. All of these coatings have been validated experimentally and showed favorable results. Coating #1: A plasma-sprayed gadolinium zirconate (GdZr) deposited on a piston surface extended the low-load (or misfire) operating envelope of a gasoline homogeneous charge compression ignition (HCCI) engine [29]. The combustion efficiency was increased by 1.5% and, the indicated thermal efficiency by 5%, relative to an uncoated baseline. Lower unburned hydrocarbons (uHC) and carbon monoxide (CO) emissions suggested faster near-wall chemical

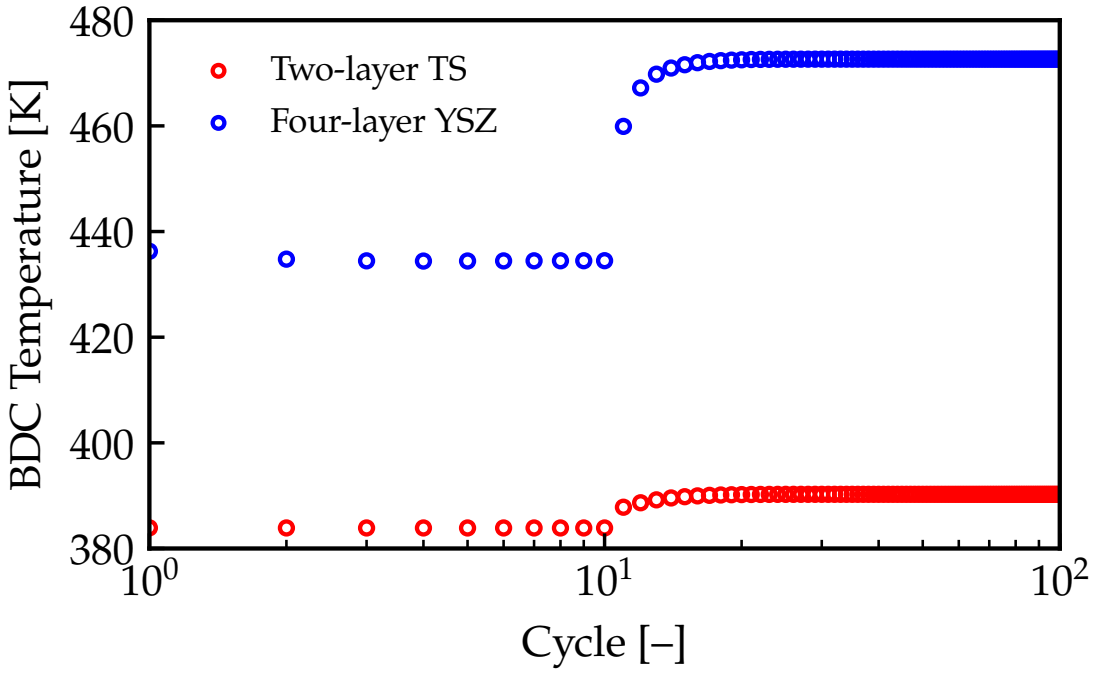

Figure 5.4: Coated wall temperature at BDC for the 100 cycle transient simulation, for the two-layer TS coating (red) and the four-layer YSZ coating (blue)

kinetics. Coating #2: A traditional atmospheric plasma-sprayed yttria-stabilized zirconia (YSZ) coating with gradient and bond coats [49] was tested over a range of high-output diesel operating conditions. Various roughness and thickness were applied to the piston surface. Most of the rough (as-coated) pistons showed an increase in fuel consumption, but a smooth version showed an increase of gross indicated thermal efficiency up to 3.5% (relative to the uncoated case). Coating # 3: Reliable operation in a spark-ignited engine environment was demonstrated using a high volume low pressure (HVLP) coating method [36]. These coatings include aluminosilicate particles dispersed in an organic polysilazane or metal phosphate binder [129]. Coating #4: A production silica reinforced porous anodized aluminum (SiRPA) coating developed by Toyota [32] that showed lower fuel consumption and higher cold-start efficiency in diesel engine experiments

[33, 34]. An energy balance revealed a reduction in cooling requirements and, thus, an increase in brake power and exhaust loss. Coating #5: Several coating structures were developed under the European project EAGLE [130]. The coatings were designed to operate in a light duty, lean-burn spark ignited gasoline engine environment. The coating surface temperature swing was measured via laser-induced phosphorescence in an optical engine setup. The most promising coating (case #E, which was selected in this study for evaluation) reached a temperature swing of 100°C. A metal engine with identical geometry was used to measure performance and emissions. The same coating showed negligible indicated thermal efficiency change, however less cooling losses, better combustion efficiency and higher heat release rates were reported [85]. Even though this is a multi-layer coating, only effective properties of a single layer were provided [131]. The material properties of each coating can be found in Table 5.2.

5.2.2 Engine Model Specifications

The coated wall temperature methodology was implemented in GT-Power [91]. The production John Deere 4045 engine, see Table 5.3, was modeled. All major subsystems in this model use bench data or have been suitably calibrated, including the head flow, EGR valve, exhaust throttle, turbocharger, wastegate, fuel rate of injection profiles, and combustion parameters. Input settings were extracted from the production ECU calibration, and include fuel injection scheduling, rail pressure, air system actuator positions, and other boundary conditions applicable to the 4045 engine. While maintaining accuracy to the production engine, this model is not over-calibrated; it is capable of making valid predictions for steady-state and transient operating conditions.

The convective in-cylinder heat flux to the wall is given as

$$\dot{q}'' = h\left(t_{\mathrm{g}} - t_{\mathrm{w}}\right) \tag{5.4}$$

where h is the heat transfer coefficient by the classical Woschni correlation with swirl term [4] (center swirl is about 1.4), t_{g} is the bulk gas temperature from the

Table 5.2: Thermal properties of wall architectures investigated for the drive-cycle scenario.

Wall structure	Layer	k [W/m-K]	$\rho c \times 10^{-6}$ [J/m^3-K]	L [μm]
Baseline	global wall	85	3.8	9000
	head	26	4.5	10000
	piston	123	2.6	8600
	liner	45	3.9	6800
#1, ref. [29]	top	0.65	1.3	180
	bond	4.2	3.1	70
	global wall	85	3.8	8750
#2, ref. [49]	top	0.77	1.8	210
	gradient	0.85	1.5	70
	bond	4.07	0.9	70
	global wall	85	3.8	8650
#3, ref. [36]	top	0.35	0.4	100
	global wall	85	3.8	8900
#4, ref. [34]	top	0.67	1.3	65
	global wall	85	3.8	8935
#5, ref. [131]	top	0.85	2.3	180
	global wall	85	3.8	8820

Table 5.3: John Deere 4045HFC04 engine geometry

Number of cylinders	4 [–]
Displacement volume	4.5 L
Stroke	127 mm
Bore	106.5 mm
Connecting Rod	203 mm
Compression Ratio	17.0:1 [–]
Firing order	1-3-4-2

gas-phase thermodynamics solver, and t_w is the coated wall temperature [132]. It is possible that the heat transfer coefficient could be altered by the coated wall, but this effect was not included.

5.2.3 Wall Treatment Scenarios

In the following sections, two different heat flux treatments are examined. First, all combustion chamber surfaces are assumed to have the same wall architecture, referred to hereafter as the global heat flux method. Second, the heat flux is split into individual heat fluxes to the head (including intake/exhaust valves), piston and liner and, thus, each surface can become a unique multi-layer wall with different material characteristics.

5.2.3.1 Global Heat Flux

The version of GT-Power used (v2020 b2) [91] can only provide the total in-cylinder heat transfer rate $\dot{q}_{\text{global}}$ for each cylinder. The instantaneous heat flux $\dot{q}''_{\text{global}}$ is found as

$$\dot{q}''_{\text{global}} = \frac{\dot{q}_{\text{global}}}{A_{\text{total}}} \tag{5.5}$$

where A_{total} is the instantaneous in-cylinder surface area exposed to combustion gases. The resulting global heat flux is used, $\dot{q}''_{o,n}$, and convolved with the response function, X_o, as previously shown in Eq. 3.63 to find the correct t_w for the next time step. For the *steady state* scenarios presented in this section, the coolant temperature was considered constant. For the *drive cycle* the measured coolant temperature history was convolved with the response function Y to provide the contribution of the back-side wall to the full solution in Eq. (3.63).

5.2.3.2 Split Heat Flux Wall

The global heat flux wall treatment assumed that the combustion chamber consisted of a single multi-layer wall architecture. In this section, a methodology to allow splitting the global heat flux into individual heat fluxes to the head, piston and

liner is developed. With the split heat flux methodology, one can use different wall thermal properties (and coatings) for each component.

In the current GT-Power version the individual-component heat fluxes can not be directly exported. The global heat transfer rate is the sum of the head, piston and liner heat transfer rates, such that

$$\dot{q}_{\text{global}} = \dot{q}''_{\text{head}} A_{\text{head}} + \dot{q}''_{\text{piston}} A_{\text{piston}} + \dot{q}''_{\text{liner}} A_{\text{liner}} \tag{5.6}$$

where $\dot{q}_{\text{global}}$ is the in-cylinder total heat transfer rate of each cylinder, which is provided by GT-Power for every time step and cylinder. The terms $\dot{q}''_{\text{head}}$, $\dot{q}''_{\text{piston}}$ and $\dot{q}''_{\text{liner}}$ are the head, piston and liner heat fluxes, respectively, and the terms A_{head}, A_{piston} and A_{liner} are the corresponding surface areas. The liner area varies with crank angle while the others are constant. Convective heat transfer is assumed for each of the surfaces, such that

$$\dot{q}''_{\text{head}} = \hat{h}(t_g - t_{\text{w,head}}) \tag{5.7}$$

$$\dot{q}''_{\text{piston}} = \hat{h}(t_g - t_{\text{w,piston}}) \tag{5.8}$$

$$\dot{q}''_{\text{liner}} = \hat{h}(t_g - t_{\text{w,liner}}) \tag{5.9}$$

where $\hat{h}$ is a modified heat transfer coefficient to match total in-cylinder heat loss. By solving for $\hat{h}$

$$\hat{h} = \frac{\dot{q}_{\text{global}}}{t_{\text{gas}} A_{\text{total}} - \left(t_{\text{w,head}} A_{\text{head}} + t_{\text{w,piston}} A_{\text{piston}} + t_{\text{w,liner}} A_{\text{liner}}\right)} \tag{5.10}$$

one can use Eq. (5.7), (5.8) and (5.9) to get the individual head, piston and liner heat fluxes. Attention should be given to the denominator of Eq. (5.10) to avoid singularities. The back-side boundary condition is treated similarly as described earlier, with the only difference being that the head/liner and piston are exposed to coolant and oil, respectively.

The default GT-Power explicit time step was used for the flow calculations (pipe flows and in-cylinder combustion flows). A Python user-defined function was

called every time step, *i.e.* 100μs, to compute the coated wall surface temperature. The X and Y response functions are fully calculated only once at time equal zero, since they depend only on material properties and thickness of each layer. Each power cylinder component had its own responses. While the response can be calculated for infinite time, a finite length was chosen based on machine accuracy and tolerance criteria for computational efficiency purposes. An absolute tolerance of 10^{-12} [m^2-K/W] was set for the head, piston, and liner structure. If the scenario was a transient event, the contribution of the backside to the wall surface temperature could have been calculated *a priori* because it was dependent on the pre-recorded thermocouple data. The instantaneous surface area is computed with respect to the piston position, which is followed by the heat flux calculation as shown in Eq. (5.5) or Eqs. (5.7) to (5.9) for each time step and cylinder. Each wall temperature output is used as input to the cylinder objects that in turn calculate the heat fluxes of the next time step.

5.2.4 Steady State Analysis

Coating performance was evaluated for two conditions of the John Deere 4045 speed-load map. The first was a low-speed/medium-load case that had a 10.9 bar IMEPg at 800 rpm. The second was a high-speed/low-load case that had a 2.7 bar IMEPg at 2400 rpm.

All of the simulations were performed for a constant value of *brake torque*. This control was achieved by adjusting the mass of fuel injected. Therefore, one must be careful when comparing the normalized results that are presented because the normalization has been calculated using the case-specific mass of fuel.

The steady-state coated wall surface temperatures for the low-speed/medium-load case are shown as a function of crank-angle, in Fig. 5.5, for each of the six unique engine wall architectures using the global wall treatment described above. Numerical values of wall surface temperature swing and the gas-exchange (EVO-IVC) cycle-mean temperature are given in Table 5.4.

The stock power cylinder wall consists of three parts (head/piston/liner) with

Table 5.4: Wall surface temperature swing, integrated wall temperature mean during gas-exchange (EVO-IVC), peak heat flux and integrated heat transfer are reported for all wall architectures using the global wall heat flux treatment for the low-speed/medium-load engine operating condition.

Wall	Temperature Swing [K]	Average Wall Temperature during gas-exchange (EVO-IVC) [K]	Peak Heat Flux [MW/m^2]	Integrated Heat Transfer [kJ]
Baseline	12.5	387	3.6	21.93
1	220	422	3.19	19.53
2	171	442	3.26	19.77
3	426	395	2.76	18.19
4	203	389	3.21	20.35
5	149	415	3.33	20.31

different material properties and thicknesses. An area-average technique based on the individual area and thickness of each component was used to estimate the stock "global wall" properties shown in Table 5.2 as *Baseline*.

In Fig. 5.5, the baseline (blue) stock engine wall has almost negligible surface temperature variation during the cycle (≈10 K) while the five coated cases wall surface temperatures swing substantially throughout the cycle. Most of the coated wall structures have a surface temperature swing in the 150 to 220 K range. Coating #1 has higher a temperature swing than coating #2, but the latter tends to retain heat throughout the cycle leading to higher wall temperatures during the exhaust, intake and compression strokes.

Coating #3 provided the highest temperature swing (≈ 430 K) among all the coatings selected from the modern literature. This coating also releases most of its thermal energy during the power stroke. During the exhaust stroke coating #3 tends to have the second to lowest temperature, with coating #4 being lowest. It important to note that there is a period where the trend reverses; during the first third of the intake stroke until the second third of the compression stroke coating #4 has the lowest wall temperature. This is a clear indication that less heat flows *from* the engine wall *to* the inducted air charge during the intake valve open period,

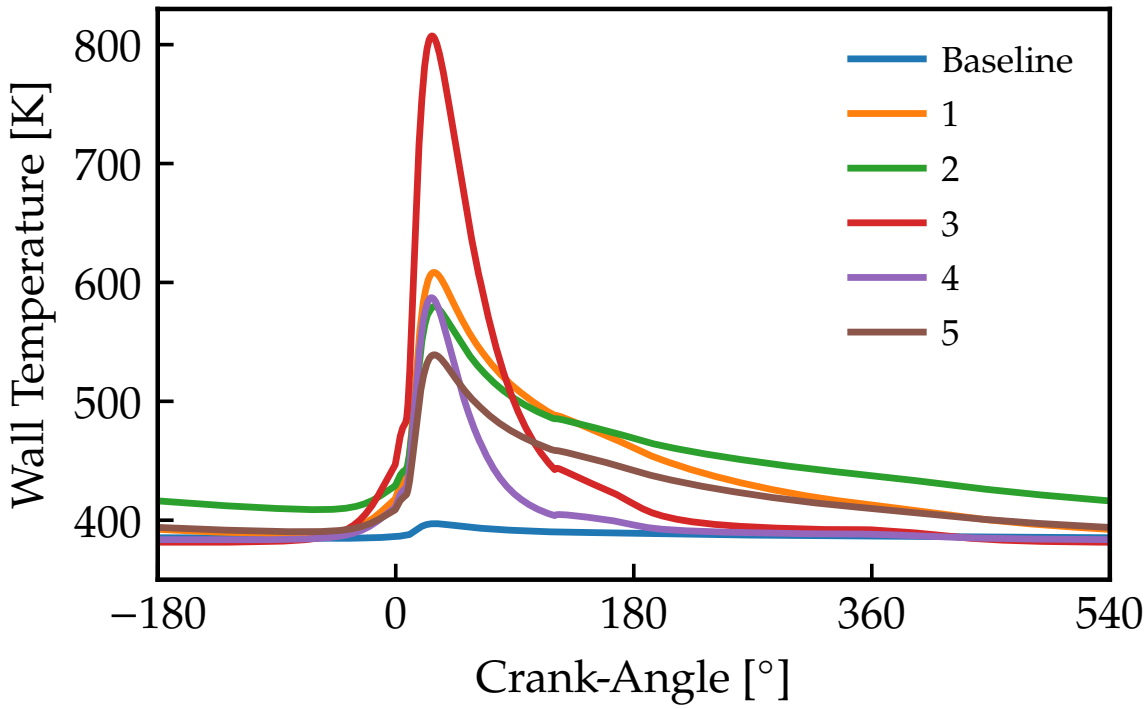

Figure 5.5: Steady state coated wall surface temperature as a function of crank-angle for the low-speed/medium-load engine condition for the baseline stock wall and various other coating architectures using the global wall heat flux treatment. The material properties of each architecture can be found in Table 5.2.

improving volumetric efficiency.

The Toyota SiRPA, coating #4, has almost the same temperature swing as coating #2, but its thermal properties led to much lower cycle-mean temperature during gas exchange. In addition, the SiRPA coating releases heat very quickly mostly due to the fact that it is the thinnest of all structures examined. Coating #5 showed the lowest temperature swing, but from the middle of the exhaust stroke to the end of compression stroke it closely matched coating #1.

The resulting surface heat flux for each coating architecture is shown in Fig. 5.6. The highest peak flux is observed from the baseline case and the lowest from coating #3. It is worth noting that coatings #1 and #4 have notably different wall temperature histories throughout the cycle in Fig. 5.5, yet their heat flux traces

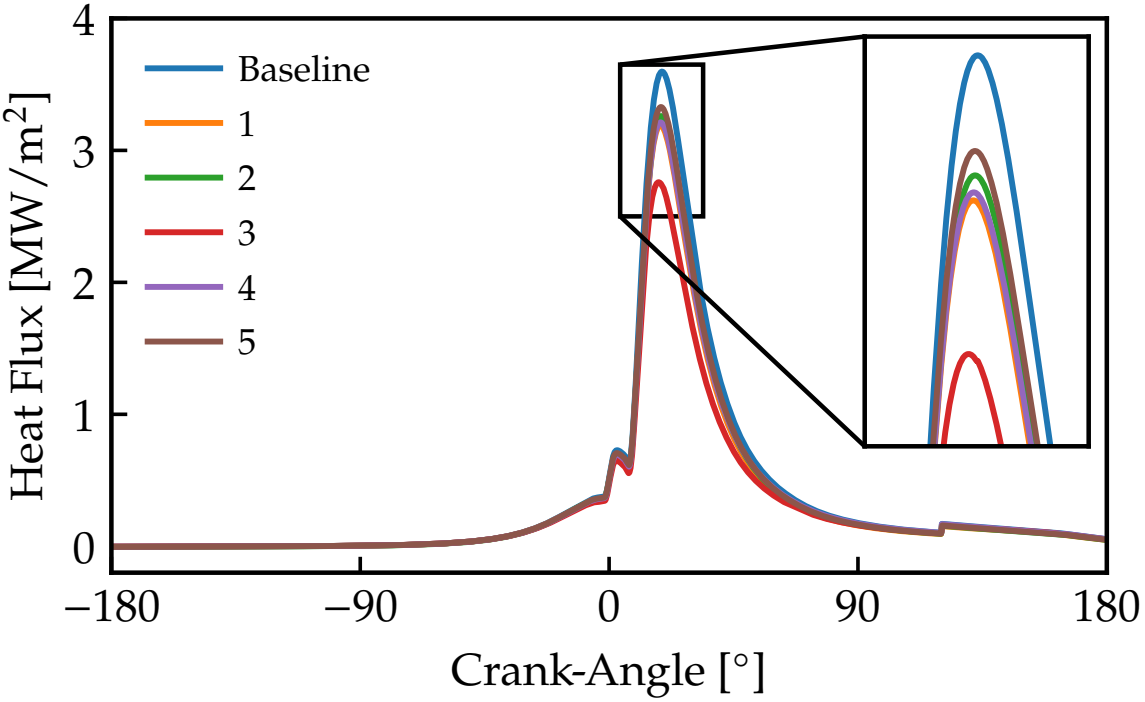

Figure 5.6: Steady state surface heat flux as a function of crank-angle for the low-speed/medium-load engine condition for the baseline stock wall and various other coating architectures using the global wall heat flux treatment. The material properties of each architecture can be found in Table 5.2.

in Fig. 5.6 match closely for this low-speed/medium-load condition. Numerical values of peak surface heat flux and integrated heat transfer are given in Table 5.4.

The wall temperature swing is a strong function of engine condition. A simple example is shown in Fig. 5.7 for coating #3. The low-speed/medium-load and high-speed/low-load wall temperatures are compared for all four cylinders for the duration of one 800 rpm cycle. The high-speed/low-load case has a much smaller temperature swing than the low-speed/medium-load condition mostly due to the reduced time for heat transfer and lower fuel energy provided.

The split heat flux methodology was also investigated using the steady-state approach. An example of the individual combustion chamber surface temperatures for cylinder 1 is shown in Fig. 5.8. Instead of using a single set of material properties

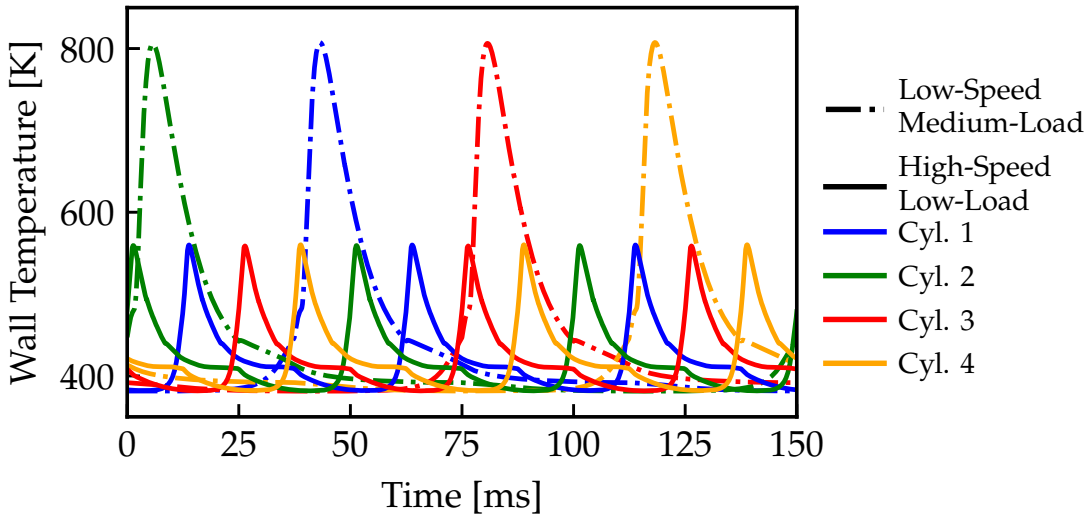

Figure 5.7: Steady state coated wall surface temperature using coating #3 as a function of time for the low-speed cycle duration. The low-speed/medium-load and high-speed/low-load cases are compared for all four engine cylinders using the global wall heat flux treatment.

(as was previously done for the global wall), the split heat flux methodology allows each surface to have its own properties. The stock power cylinder material properties can be found in Table 5.2. Only the piston was coated with coating #1, see Table 5.2. Compression ratio remained fixed in this analysis by removing the total coating's thickness from that of the stock piston.

The head, piston, and liner surface temperatures are shown in Fig. 5.8 as a function of crank angle. As expected there is a mean temperature difference between the three different surfaces, with the coated piston showing the most intra-cycle variation. The head and liner have very small temperature variation throughout the cycle (≈20 K). The coated piston temperature swing (≈220 K) is similar to that observed for the global case in Fig. 5.5.

To get a crude evaluation of coating performance under steady state operation, a system-level analysis was performed for the low-speed/medium-load and high-speed/low-load engine conditions. The former is a relatively high efficiency point,

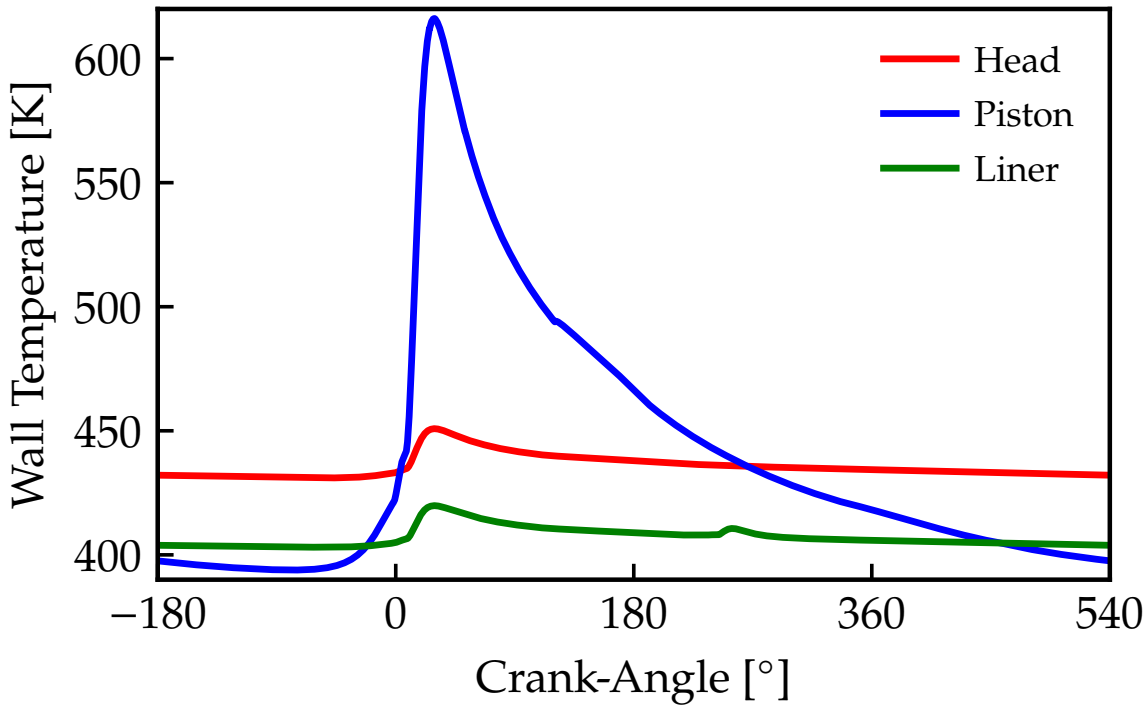

Figure 5.8: Steady state coated wall surface temperature of stock head, coated piston and stock liner for cylinder 1 at the low-speed/medium-load engine condition of coating #1. Material properties can be found in Table 5.2.

while the latter is a poor efficiency point since the engine makes almost no brake torque (≈10 Nm). The fuel mass per cycle, in-cylinder heat transfer and exhaust loss are compared using the global wall heat flux method, and the split heat flux method where only the piston was coated. The baseline condition performance metrics for the global and split heat flux wall treatments can be found in Table 5.6, and the coated results measured relative to these baseline values are shown in Fig. 5.9 with their numerical values given in Table 5.5. The changes relative to the baselines (global or split wall heat flux treatment) in Table 5.5 were calculated for every performance metric as:

$$\% \text{ change} = 100 \times \frac{\text{Coated} - \text{Uncoated}}{\text{Uncoated}} \tag{5.11}$$

Table 5.5: Engine performance metrics change in [%] basis relative to the baseline for all coatings using the global and split heat flux wall treatment for the low-speed/medium-load and high-speed/low-load steady state condition.

	Low-Speed/Medium-Load									
	Fully coated					Piston coated				
Coating	#1	#2	#3	#4	#5	#1	#2	#3	#4	#5
Fuel mass	-2.17	-1.42	-4.36	-1.90	-1.34	-1.04	-0.80	-1.20	-0.01	0.22
In-Cylinder Heat	-10.94	-9.82	-17.03	-7.19	-7.38	-6.24	-5.79	-8.79	-4.28	-3.96
Exhaust Loss	2.47	3.50	1.11	0.31	1.96	0.56	0.81	1.17	1.00	1.40
	High-Speed/Low-Load									
	Fully coated					Piston coated				
Coating	#1	#2	#3	#4	#5	#1	#2	#3	#4	#5
Fuel mass	-1.34	-0.80	-2.27	-1.48	-1.03	-0.66	-0.67	-1.32	-0.60	-0.45
In-Cylinder Heat	-12.04	-13.58	-14.40	-6.13	-8.84	-4.43	-5.15	-6.47	-2.75	-3.15
Exhaust Loss	4.64	6.24	3.82	0.97	3.41	1.05	1.41	0.86	0.29	0.78

Table 5.6: Uncoated baseline data for the global and split heat flux wall treatment

	Low-Speed Medium-Load		High-Speed Low-Load	
	Global	Split	Global	Split
BSFC [g/kW-hr]	219.8	220.1	2098	2045
Fuel mass [mg/cyc]	273.94	274.00	73.25	71.33
Heat Transfer [kW]	21.93	21.93	18.06	16.72
Fuel Power [kW]	77.79	77.81	62.44	60.80
Brake Power [kW]	29.89	29.89	2.51	2.51
Exhaust Loss [kW]	17.69	17.92	25.32	25.61
Other [kW]	30.48	30.26	34.82	32.89

In-cylinder heat transfer was reduced for all of the coatings studied, as shown in Fig. 5.9. The largest in-cylinder heat transfer reduction (17%) was seen using coating #3 with the full chamber coated at the low-speed/medium load condition. This coating generates the largest temperature swing and minimum peak heat flux, as shown earlier in Fig. 5.5 and 5.6 or Table 5.4. For this condition, the heat transfer benefit reduces by half when only the piston is coated, see Fig. 5.9.

The fuel mass per cycle data show that a savings is predicted for all the global wall calculations. Coating #3 provides the highest fuel savings (4.5%) for the low-

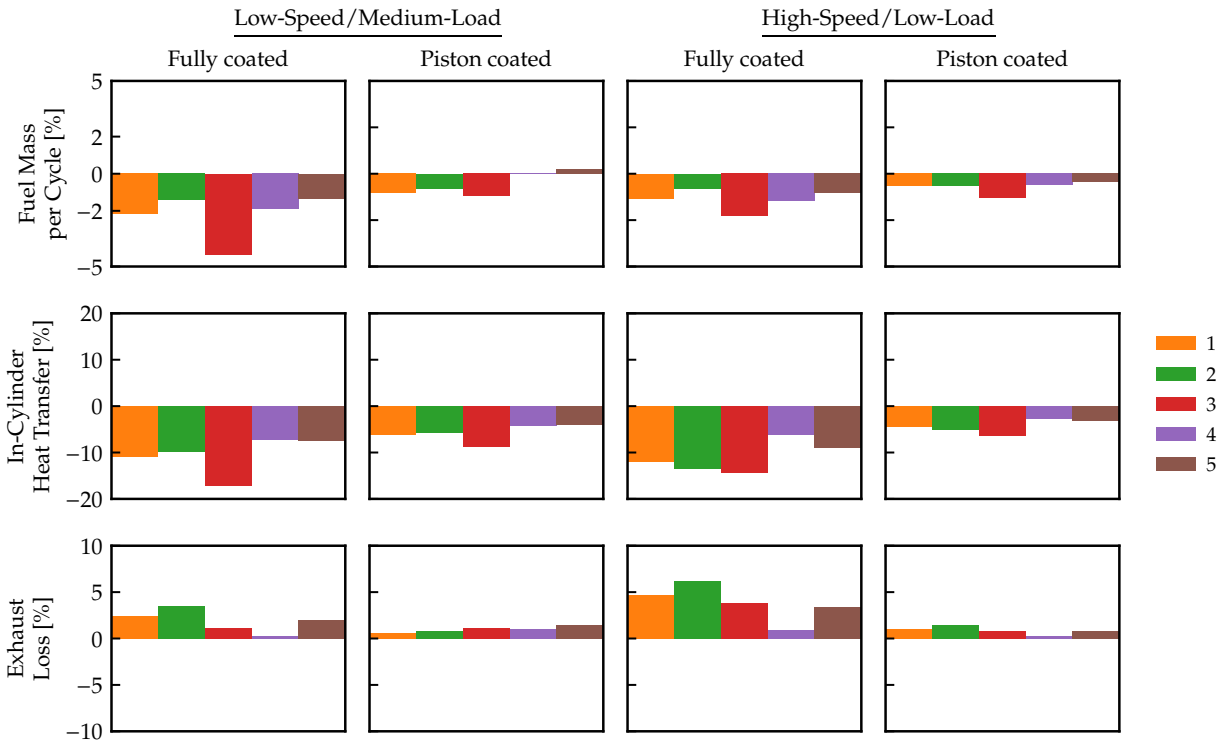

Figure 5.9: Fuel mass, in-cylinder heat transfer, and exhaust loss changes relative to the uncoated baseline results given in Table 5.6. The coating architectures are given in Table 5.2.

speed/medium-load case. Reducing the coated area to just the piston, the effect is reduced four-fold to 1.2%. However, the results for just coating the piston indicate cases where there is no effect (coating #4) or a slight increase in fuel consumption (coating #5).

The exhaust loss, *i.e.* exhaust sensible enthalpy, was found to increase for all of the coatings. This is noteworthy because, as mentioned above, the normalization was performed using the baseline data. Thus, using the global wall treatment for coating #3 as an example, there is an increase of exhaust enthalpy in spite of nearly 5% less fuel going into the engine. The global wall treatment, as expected, shows a larger effect than just the coated pistons. A maximum exhaust loss increase of about 6% is achieved in the high-speed/low-load case from coating #2, but the

effect reduces by 4× when only the piston surface is coated. Coating #2 releases the heat slowly, and thus has increased wall surface temperature as can be seen in Fig. 5.5 or by comparing the cycle-mean wall temperatures during gas-exchange (EVO-IVC) in Table 5.4.

The steady-state results provide a mixed picture of the coatings' performance. The fuel mass per cycle *savings* for the split case (only piston coated) wall treatment is in the best case one half the global prediction and in one case there is actually a reversal of sign, *i.e.*, the piston-coated case used more fuel. Additionally, for the two operating conditions explored, the predicted fuel consumption benefit can vary by a factor of two. All of these results are explained by the complicated nonlinear coupling between the multiple effects at play. Therefore, in order to provide a comprehensive comparison between an uncoated and a coated engine the full drive cycle needs to be considered.

5.2.5 Drive Cycle Analysis

A brief review of the NRTC drive cycle is given first, followed by the implementation of experimental boundary conditions. A total of six (five coated and one uncoated baseline) drive cycle simulations were performed. Results are presented for stock baseline and two different coated wall architectures (coating #2 and #3) for a fully coated (global heat flux scenario) and piston-coated (split heat flux scenario) setup, integrated over the full drive cycle.

5.2.5.1 Drive Cycle Boundary Condition Specifications

The Non-Road Transient Cycle (NRTC) is an international transient certification cycle used to assess non-road engine vehicle performance, fuel consumption and emissions. The dynamometer transient driving schedule lasts ≈20 minutes with normalized (by rated values) speed and brake torque set points, with an average speed of 68% and average load of 39% (of rated), as shown in Fig. 5.10. Official certification involves running an NRTC from cold start, followed by a 20-minute soak period, and finally an NRTC from hot start. The hot NRTC is considered

here to evaluate performance and fuel consumption. Pollutant emissions were not considered.

The drive cycle was run experimentally and the data were recorded to be used as boundary conditions in GT-Power. The engine speed, brake torque, common rail pressure, exhaust throttle and EGR valve angles, and fluid temperatures (coolant, oil, intercooler and ambient), are shown in Fig. 5.10, and were imposed for all the transient cases. The coolant and oil temperature histories were particularly useful for the heat conduction analysis, as they are was used to set the backside time-varying temperature.

The drive cycle simulations were performed using a torque controller so that the brake power was constant for all simulations regardless of coating architecture but the mass of fuel varied. The same treatment was performed for the steady state results. The comparison of global quantities based on normalized results, which used the baseline conditions as the reference, need to consider the reduction of fuel mass as appropriate.

5.2.5.2 Global Heat Flux Results

The wall surface temperature (top) and heat flux (bottom) are shown for three wall architectures (baseline, coating #2 and coating #3) and all four engine cylinders, in Fig. 5.11, over the full drive cycle using the global heat flux wall treatment. During the first 5 minutes of the baseline case (top left), the cycle-mean wall temperature increases due to both the coolant temperature increase, see Fig. 5.10, and the thermal energy that is absorbed. The surface temperature behavior differs significantly for the two coated cases. Coating #2 gives roughly half of the temperature swing achieved by coating #3, and the low-temperature envelope for coating #2 is higher than for coating #3 suggesting a lower volumetric efficiency.

The coatings' thermal performance, via the heat flux, is also shown in Fig. 5.11. The highest heat flux is observed for the baseline case. Coating #2 shows a reduced peak heat flux, and an even larger reduction is achieved with coating #3.

The time window from 11-13 minute is interesting. During this time, as seen

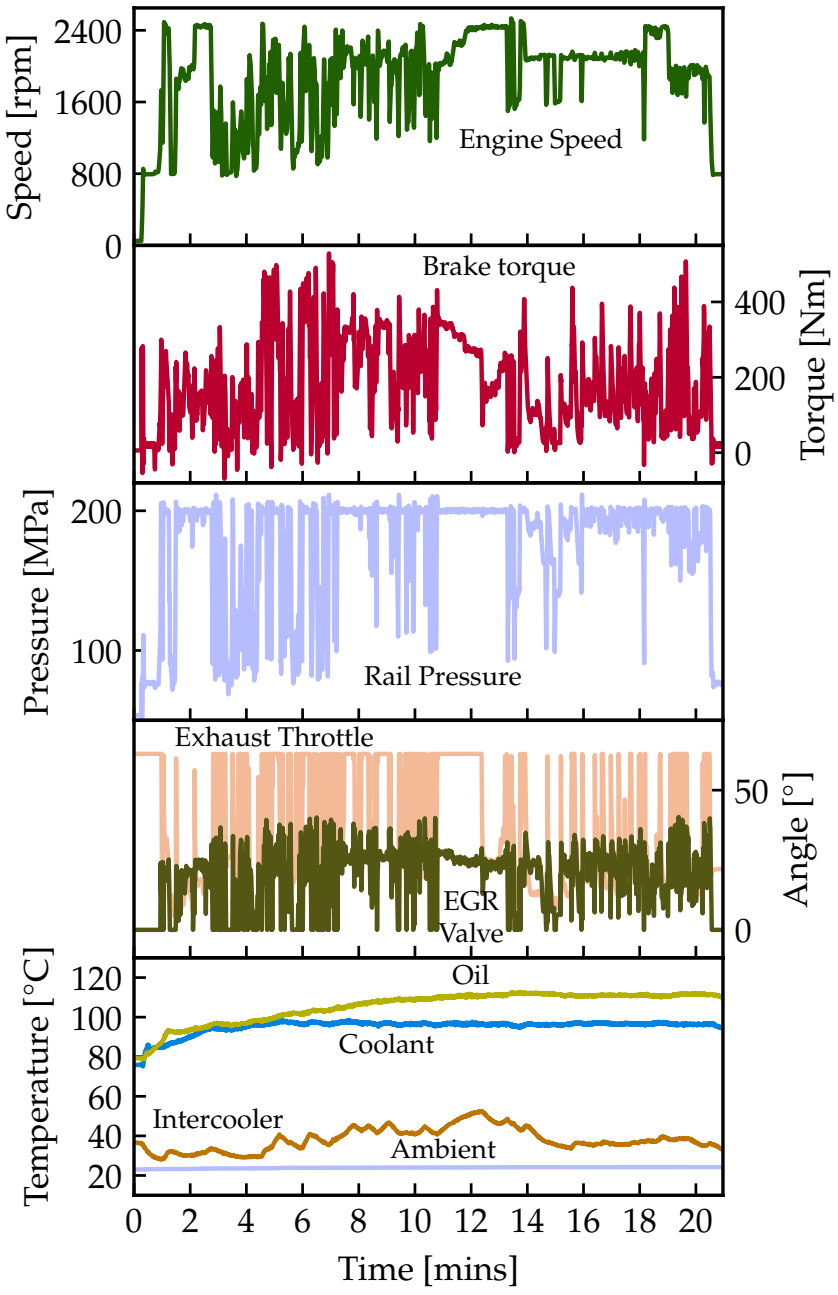

Figure 5.10: Engine dynamometer transient driving schedule (engine speed and brake torque) and recorded experimental data (rail pressure, exhaust throttle and EGR valve angle, and oil, coolant, intercooler and ambient temperature) of a Non-Road Transient Cycle (NRTC). The experimental data were used as boundary conditions to a fully calibrated system-level simulation, and were provided by Deere & Co.

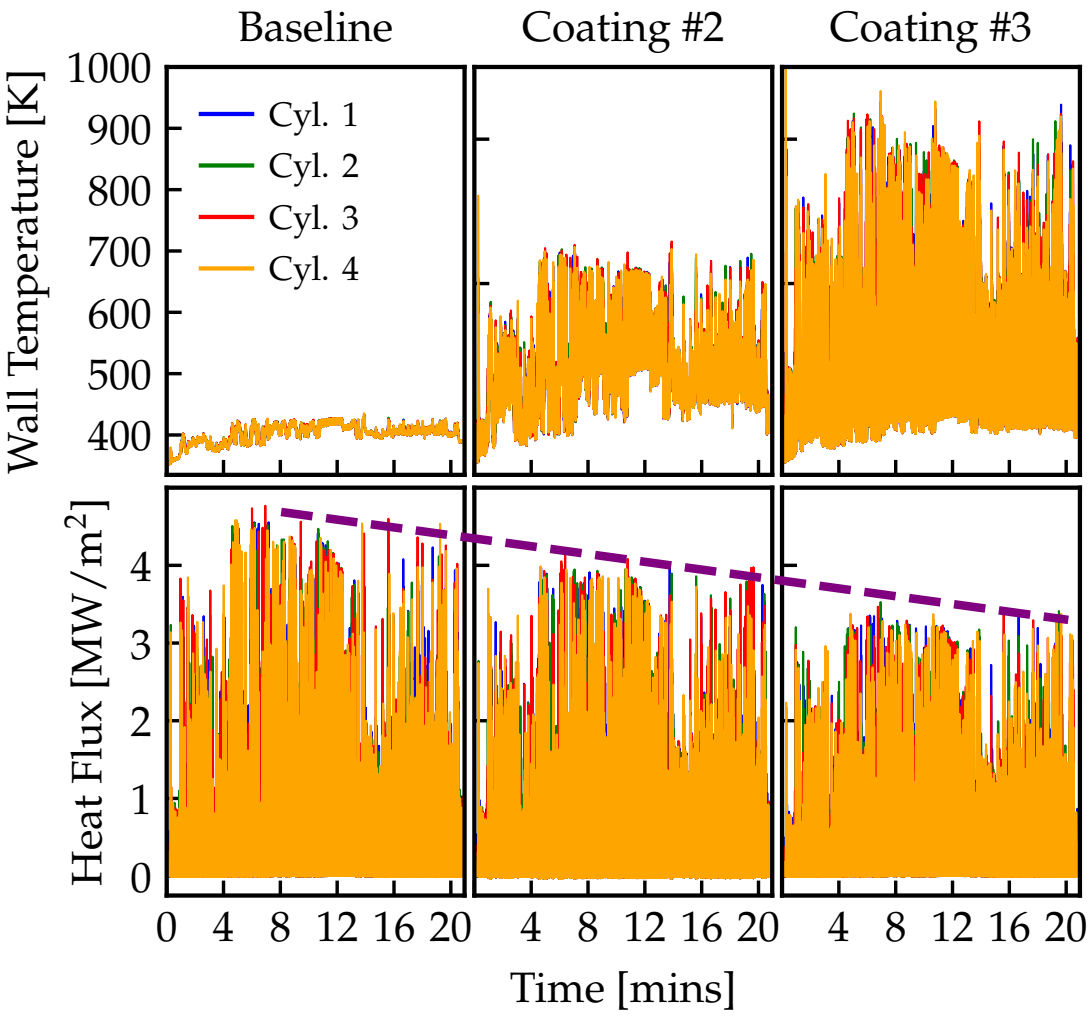

Figure 5.11: Wall temperature (top) and heat flux (bottom) temporal evolution during a NRTC drive cycle using the global wall heat flux treatment for all four cylinders and combustion chamber wall architectures starting from left: baseline, coating #2 and coating #3.

from the expanded view in Fig. 5.12, the engine speed first ramps up from 2000 rpm to 2400 rpm and is held there. During the speed ramp the load is decreased at a slower rate from 340 N-m to 280 N-m, then starting from the 12th minute load suddenly drops to 60 N-m and then ramps back up to 220 N-m at steady speed. During the speed ramp both coatings show a small decrease in the surface temperature swing (part of which is attributed to the slightly decreased load), and the minimum surface temperature during gas exchange is slightly increased. This speed change is relatively small, but the observed effect of engine speed on coating performance is consistent with literature [114]. At higher speeds, there is less time available to absorb thermal energy in the coating and then release it back to the gas. An inherent difference is seen between the two coatings during the step load change and ramp in the latter part of the time window of Fig. 5.12. For coating #2 the minimum surface temperature shows a significant reduction (note the relevant reference to measure against is the intake air temperature) when the load decreases. In contrast, for coating #3 the minimum (gas exchange) surface temperature is relatively unaffected because of the low thermal inertia of the coating.

5.2.5.3 Split Heat Flux Results

The temporal evolution of the stock head, coated piston (coating #3), and stock liner wall surface temperature over the full drive cycle are presented in Fig. 5.13. The coated piston has the highest temperature and temperature swing among the components. The stock head and liner may have similar thermal properties, see Table 5.2, but their large temperature difference is attributed to the difference in thickness; the head is thicker hence has more thermal resistance. Additionally, the liner is coolest because of its variable surface area exposure; when the heat flux is maximum during combustion the liner surface area is near its minimum value.

The integrated transient energy balance is shown in Fig. 5.14 for the baseline global heat flux case. The final integrated results of the baseline for both global and split heat flux wall treatment, are given in Table 5.7. The sum of all terms in Table 5.7 is the instantaneous fuel energy consumed over the drive cycle. *Brake*

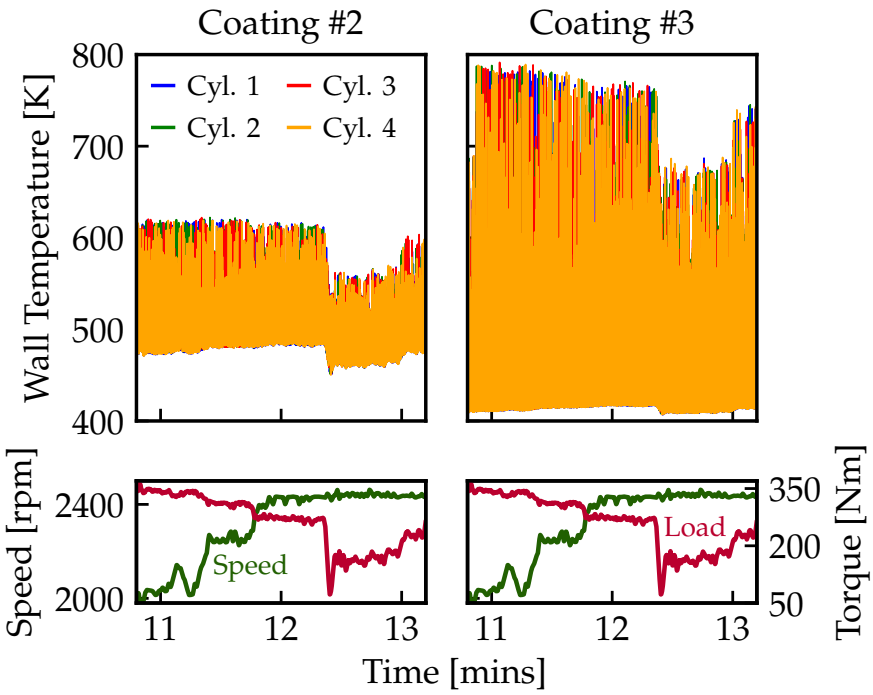

Figure 5.12: Expanded view of coating #2 and coating #3 wall surface temperature (top) and speed/load curve (bottom) temporal evolution during the 11^{th} and 13^{th} minute of the NRTC drive cycle for all engine cylinders.

work is the integral of the average engine crankshaft brake power. *In-Cylinder Heat* energy is the integrated in-cylinder heat transfer for all four cylinders. *Exhaust* energy refers to the integrated exhaust sensible enthalpy. Finally, the term *Other* is attributed to any other energy pathway *e.g.*, heat transfer to EGR cooler, charge air cooler, heat rejection to coolant/oil in the cylinder head, and heat transfer to surroundings from the block/manifolds/turbine/pipes. It is interesting to note that the baseline total fuel mass is nearly identical for the global and split treatments.

In Fig. 5.15, the relative changes in integrated fuel mass and in-cylinder heat transfer, exhaust loss and other losses are presented for the global and split wall heat flux treatment for coatings #2 and #3. The tabulated data are given in Table 5.8. Note that the integrated brake work remained fixed for all the cases tested.

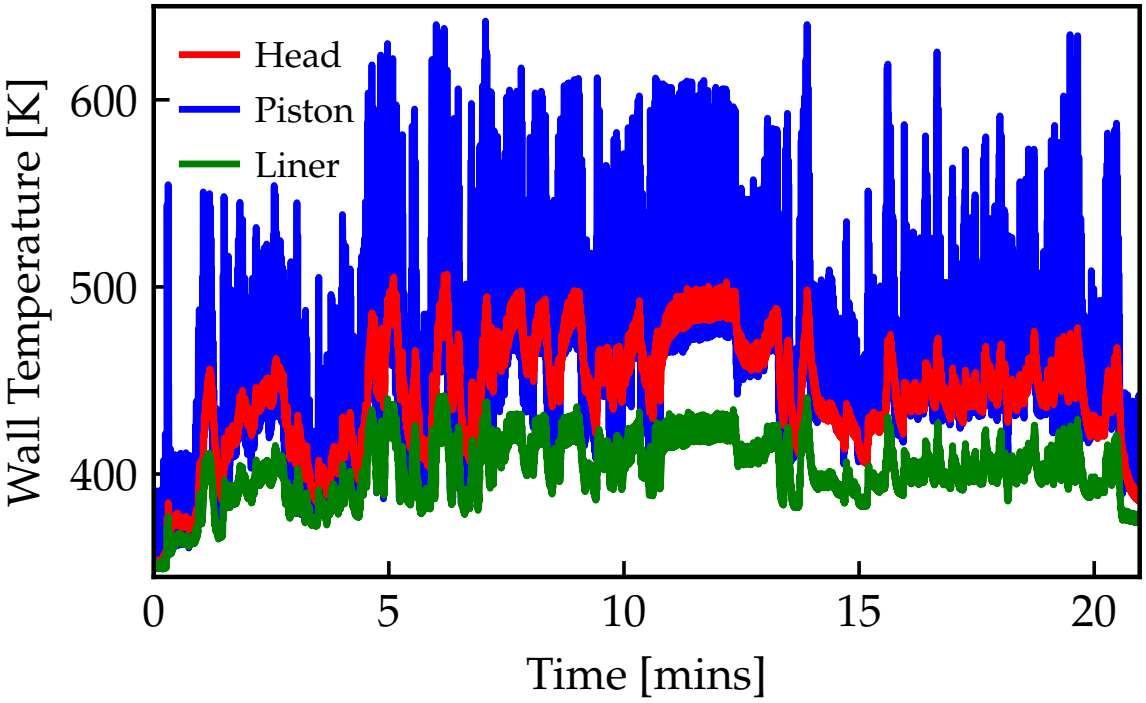

Figure 5.13: Stock head, coated piston and stock liner wall temperature temporal evolution over NRTC drive cycle using the split heat flux wall treatment. Material properties of coating #3 used on top of the stock piston wall can be found in Table 5.2.

Table 5.7: Uncoated baseline energy balance breakdown and total fuel mass shown for the global and split heat flux wall treatment over the full NRTC drive cycle.

	NRTC Drive Cycle	
	Global	Split
Brake Work [MJ]	47.67	47.67
In-Cylinder Heat Transfer [MJ]	31.06	30.35
Exhaust Loss [MJ]	38.59	39.17
Other [MJ]	24.39	23.96
Total Fuel mass [kg]	3.325	3.311

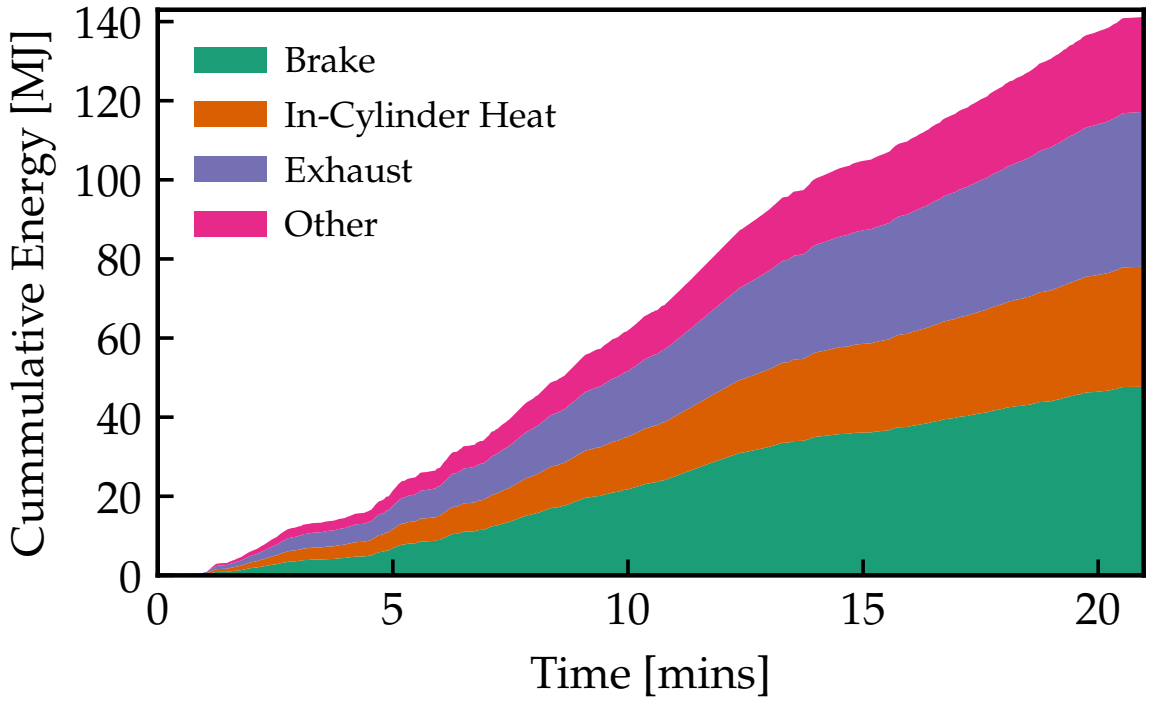

Figure 5.14: Temporal evolution of the integrated energy over the NRTC drive cycle for the baseline John Deere 4045 engine using the global heat flux wall treatment.

Table 5.8: Engine performance metrics change in [%] basis relative to the baseline for coating #2 and #3 using the global and split heat flux wall treatment over a full NRTC drive cycle.

	Drive Cycle			
	Fully coated		Piston coated	
Coating	#2	#3	#2	#3
Fuel mass [%]	-1.27	-2.99	-0.77	-1.49
In-Cylinder Heat [%]	-16.14	-18.45	-6.12	-7.97
Exhaust Loss [%]	5.56	2.54	1.31	0.52
Other [%]	4.38	2.09	1.08	0.48

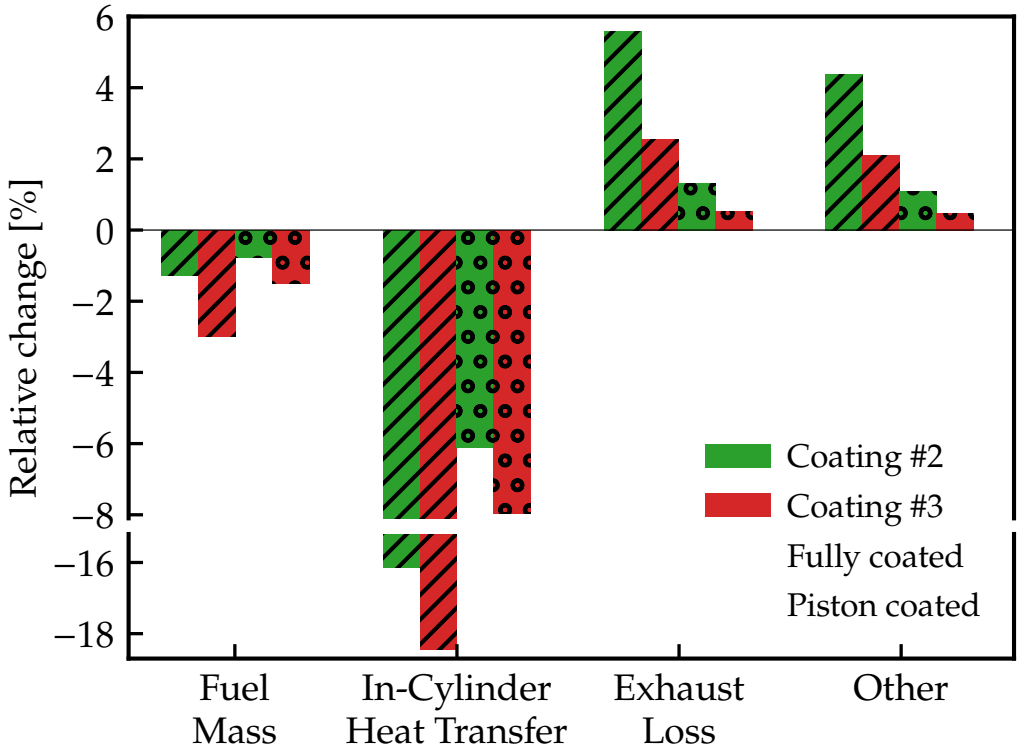

Figure 5.15: Relative changes (relative to baseline in Table 5.7) of fuel mass and integrated powers for coatings #2 and #3 using the global and split wall heat flux treatment over the duration of a full NRTC drive cycle. For numerical values see Table 5.8.

A maximum in-cylinder heat transfer reduction of 18.5% is recorded for coating #3 with a fully coated chamber. Limiting the coating to just the piston surface reduces the heat transfer benefit nearly 40%. The low-volumetric heat capacity and thickness of coating #3 absorbs heat quickly during the power stroke and releases it during the expansion and gas-exchange times.

A total fuel mass savings of 3% (≈100 gr) was predicted from coating #3 with the global wall treatment, but the effect drops to 1.5% when only the piston is coated. Coating #3 is predicted to reduce fuel mass more than coating #2. This trend is consistent with the steady state results given above.

The exhaust loss was predicted to be highest for coating #2 with the fully coated chamber. This 6% increase in exhaust heat loss corresponds to about a 10 K increase in drive-cycle-mean turbine outlet temperature. It is important to note that this temperature increase might seem small, but there 1.27% *less* fuel energy put into the engine during the drive cycle time. If that energy would have been provided, the exhaust enthalpy would have been even higher. The other losses scale directly with exhaust loss, as one would expect.

The piston-coated scenario is the most likely for practical application, and will be the basis for this brief summary of the coatings' effects during a complete drive cycle evaluation. Both coatings were effective at reducing in-cylinder heat transfer, with a substantial reduction predicted (6 or 8% depending on the coating). This effect should be considered an upper limit as there is some evidence that the surface roughness of the coating may adversely affect the local conditions [46, 44, 49]. The reduction in heat loss to the combustion chamber surface did not result in a commensurate reduction in fuel consumed. There was a predicted reduction in fuel consumption of 0.78% or 1.49% depending on coating, but there was also an increase in the exhaust enthalpy and other losses, *i.e.*, the energy not lost to the combustion chamber surfaces is redistributed in many ways. The normalization scheme employed underestimates these effects; the increase in exhaust enthalpy, for example, would be larger when calculated with a fuel energy normalization scheme. The overall effect of a thermal barrier coating, however, is that there is predicted to be a reduction of fuel consumed and an increase in exhaust gas temperature, which may be useful for exhaust aftertreatment considerations.

5.2.6 Summary and Conclusions

The analytical method to predict surface wall temperature of multilayer thermal barrier coated walls was implemented in a commercial system-level simulation software package. The wall temperature at each time step was calculated by convolving the engine wall response function with the time-varying surface boundary condition, *i.e.*, in-cylinder heat flux and coolant temperature. The wall response

function depends only on material properties and thickness of each layer and therefore can be computed once *a priori*. The convolution process is computationally efficient.

Two different wall heat flux treatment scenarios were investigated. The global heat flux scenario assumed that the combustion chamber had uniform wall properties while the split heat flux scenario allowed the head/piston/liner to have unique thermal characteristics and, therefore, unique temperatures.

A fully calibrated production engine model was coupled with this tool to evaluate the performance of five modern, engine-specific coatings selected from the literature.

The steady-state results revealed an engine-condition dependence and provided a mixed picture of the coatings' performance. A fully coated chamber, as expected, showed more promising results than reducing the coated area to just the piston. Under fixed brake torque conditions, all coatings (global or piston-coated) reduced in-cylinder heat transfer, but that did not guarantee a reduction in fuel consumption. Furthermore, all coatings resulted in higher exhaust enthalpy even though less fuel was injected. The predicted exhaust losses were higher by two-to-four times for the fully coated chamber scenario than for the piston-only coating scenario. The fuel savings were found to vary by a factor of two, depending on operating condition.

Experimental drive cycle data along with ECU data were used as boundary conditions in the model to simulate the full NRTC drive cycle. Two coating structures were chosen for analysis. Both coatings were predicted to provide a significant reduction of in-cylinder heat transfer, which led to a reduction in fuel consumption. The reduction in fuel consumption only accounted for a fraction of the reduced energy loss due to heat transfer. The exhaust enthalpy was found to increase by 0.5%, even though less fuel mass was consumed when coatings were present. For the likely scenario of a coated piston, one may expect to see up to a 1.5% reduction in fuel consumption and and a corresponding brake specific CO_2 reduction over the drive cycle, depending on the coating architecture. The coated-wall thermal insulating properties provided higher wall surface temperature and thus lower heat transfer energy across the drive cycle, altering the engine performance. Lower

heat transfer led to increased gas temperature and thus increased cylinder pressure during the expansion stroke. Right before the beginning of the intake stroke, the wall had already released heat efficiently and the surface temperature was close to the inducted air, minimizing the negative heat transfer which in turn led to higher volumetric efficiency than coating #2. The same amount of work was achieved with less injected fuel. The drive cycle showed 5-15% (relative) additional fuel savings and a 10% (relative) larger in-cylinder heat transfer reduction when compared to the steady state conditions examined.

6 DELAMINATION FAILURE EXPERIMENTS

This Chapter presents a coupling between the mechanics model developed in Chapter 4 with *a posteriori* observations of a collaborative project between the U.S. Army Ground Vehicles Systems Center (GVSC) and the Center for Thermal Spray Research (CTSR) of Stony Brook University.

The ability of the analytical mechanics model to predict the delamination was tested against qualitative results of several thermal-barrier-coated pistons that were tested by the U.S. Army GVSC laboratory in a high-output, single-cylinder diesel engine. Some of the coatings delaminated during engine operation. The analysis presented in Chapter 4 was applied, and results are presented for two thicknesses of the same coating material, and for two similar coatings with different levels of stiffness. All the coating thermomechanical properties such as thermal conductivity, density, volumetric heat capacity, thickness, elastic modulus, coefficient of thermal expansion, Poisson ratio and toughness, were measured at CTSR prior to engine testing at GVSC. Previous measurements of the piston transient heat flux, based on fast-response surface temperature data, in the same engine were used as an input to calculate the multilayer wall temperature distribution. Some of the coatings chosen for study were durable, and others failed, which provides a good test for the model.

6.1 Experimental setup

6.1.1 Single-cylinder Research Engine

Engine experiments were conducted at GVSC on a single-cylinder research engine designed for high-output diesel operation. Full details of the engine laboratory can be found in Gingrich *et al.* [118]. A brief summary of the engine is provided here with engine specifications given in Table 6.1. Air was provided by an external compressed air system that dries the air to a dew point less than -40°C. The intake air was temperature- and flow-controlled to simulate a turbocharger for steady-state measurement points. Exhaust back pressure was controlled via ball valves in the

exhaust system. Air was delivered using a control valve, with feedback from a Coriolis flow meter plumbed in series. A high-pressure common rail fuel system was used to deliver fuel to the combustion chamber at pressures up to 2000 bar. A Bosch CRIN3 injector with an 8×167 μm hydro-ground nozzle (147° included angle) was used. All experiments were run with an AC dynamometer absorbing load and maintaining speed control of the engine.

Table 6.1: Single-cylinder research engine specifications

Displacement volume	1.49 L
Stroke	128 mm
Bore	122 mm
Connecting Rod	239 mm
Compression Ratio	14.0:1 [–]
Number of valves	4 [–]
Swirl ratio	1.3 [–]
Peak firing pressure	250 bar

Experiments were performed at the five different operating conditions shown in Table 6.2. For each operating condition a start of injection (SOI) sweep was conducted. The injection duration was held constant, which meant load varied slightly with changes to SOI. In most cases, the earliest injection timing was limited by excessive peak in-cylinder pressure, and the latest injection timing was limited by either excessive exhaust temperature or exhaust smoke.

Table 6.2: Summary of engine operating conditions

Condition	Speed [rpm]	IMEPg [bar]	AFR [–]	Fuel Pressure [bar]	Duration [°]
1	1700	12.3	29	1200	10.7
2	1500	23.8	24.5	1700	18.6
3	2500	20.3	26.8	2000	21.6
4	1700	30.3	24.5	2000	25.0
5	2750	29.7	25.5	2000	40.5

The conditions were primarily selected to explore the performance and heat rejection benefits of thermal barrier coatings at high-load engine operation. Addi-

tional details of each operating condition can be found in Gingrich *et al.* [49]. This work will not discuss engine performance; it utilizes the cumulative engine run time and thermal loading to explore coating durability. Additionally, the piston heat flux has been extensively measured for these conditions, discussed in the following section, and these measurements served as an input to the analytical thermo-mechanics model to predict coating delamination.

6.1.2 Piston Heat Flux

Piston heat flux data, summarized here, were acquired at GVSC in a previous study [118] on an uncoated steel piston for engine operating conditions 1-5. A thermocouple-instrumented piston with a wireless telemetry system was used to record the high-speed piston surface temperature. Figure 6.1 shows the position of 15 fast-response thermocouples flush-mounted in the piston crown. The thermocouples were installed in a plane perpendicular to the piston wrist pin with roughly equal spacing along the piston diameter.

The time-resolved temperature data at each location were used to calculate heat flux to the metal wall. Assuming a semi-infinite wall with periodic boundary conditions, the solution is in the form of a Fourier series, and therefore a fast Fourier transform (FFT) can be used to decompose the surface temperature data and reconstruct the heat flux. That is not the case for multilayer engine walls. The FFT method, as it is commonly known, has been widely used to calculate surface heat flux in internal combustion engines [109, 133].

The FFT solution is a two-part solution with a steady state and transient portion. The transient portion of the solution only requires the instantaneous surface temperature, whereas the steady-state term requires a second, steady-state temperature, at a known distance below the first. The thermocouples used to calculate heat flux did not include a backside temperature measurement, so only the transient solution could be calculated. An *ad hoc* method was used to recover the steady-state portion of area-averaged heat flux based on the mean piston surface temperature and instantaneous gas temperature crossover point during the cycle. The resulting

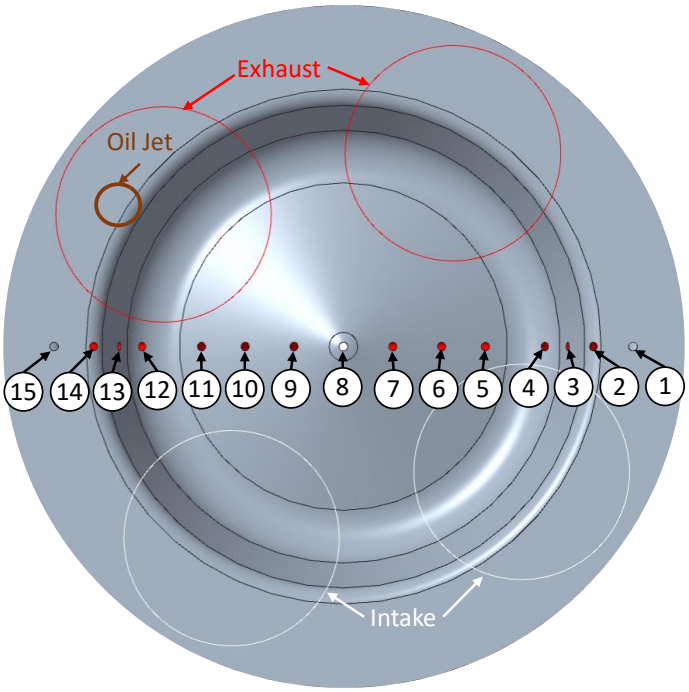

Figure 6.1: Location of 15 fast-response thermocouples on the metal piston in reference to other engine features. Taken from [3].

area average heat transfer was then compared to other independent measurements of engine heat transfer and showed good agreement across all operating conditions. For details on heat flux calculation and validation see Gingrich *et al* [118].

Figure 6.2 (a) shows the average and local heat flux data grouped by piston location for operating condition 3 (2500 rpm, 20.3 bar gross Indicated Mean Effective Pressure (IMEPg)), injection timing of -29° after Top Dead Center (aTDC). The highest heat flux was observed in the piston bowl area. Lower heat flux was observed toward the center of the piston and in the squish region (outer diameter). The area-average heat flux shown in Fig. 6.2 (a) only includes the transient solution. The larger variation of heat flux in the squish is believed to be related to spray plume variation which is expected to be larger in the squish. Regions of hot gas (on-plume) are likely more separated by cooler gas as the sprays travel radially outward. The "Squish" region nomenclature includes piston bowl lip thermocouples, which is a

transition region for spray plumes as they move radially outward and would likely be more sensitive to small variations in spray targeting. Figure 6.2 (b) shows the spatial distribution of heat fluxes integrated with respect to time (energy flux) from -20 to 100°aTDC. The analytical mechanics method to predict coating delamination presented in this paper utilized the average heat flux, including the steady-state solution, scaled by a factor of 1.5, as shown in Fig. 6.3. The scaled heat flux corresponds to the maximum expected heat flux in the piston bowl region and is considered a better representation than selecting a single location's value from Fig. 6.2 (a). The scale factor of 1.5 is derived from the approximate ratio of peak local heat flux to peak average heat flux in Fig. 6.2 (a).

Operating condition 3 at an injection timing of -29°aTDC was found to have the highest heat flux among all the conditions investigated in the uncoated metal piston testing [3], which is why it was selected and utilized in this paper as the worst case scenario to analyze for a possible coating delamination failure. Global heat transfer estimations based on measurements of fluid enthalpy and work did not indicate a significant change to heat transfer for any of the coated pistons, and therefore utilizing the metal piston heat flux as an estimate for the heat flux on a coated piston is reasonable. Overall, utilizing the highest heat flux operating condition from the uncoated telemetry experiments, scaled based on spatial gradients, should be representative of the maximum heat flux experienced on the piston during all testing.

6.2 Thermal Barrier Coatings

The collaboration between the CTSR and the GVSC resulted in a unique opportunity to explore the factors governing coating delamination in diesel engines. More than 20 coated pistons were produced, extensively characterized, and tested in a single-cylinder research engine. Of these, three coating scenarios are explored here. The first is a traditional YSZ-based thermal barrier coating system of two thicknesses, the second a novel low-thermal conductivity and low-volumetric heat capacity coating with two variations in compliance, and the third is a functionally graded coating

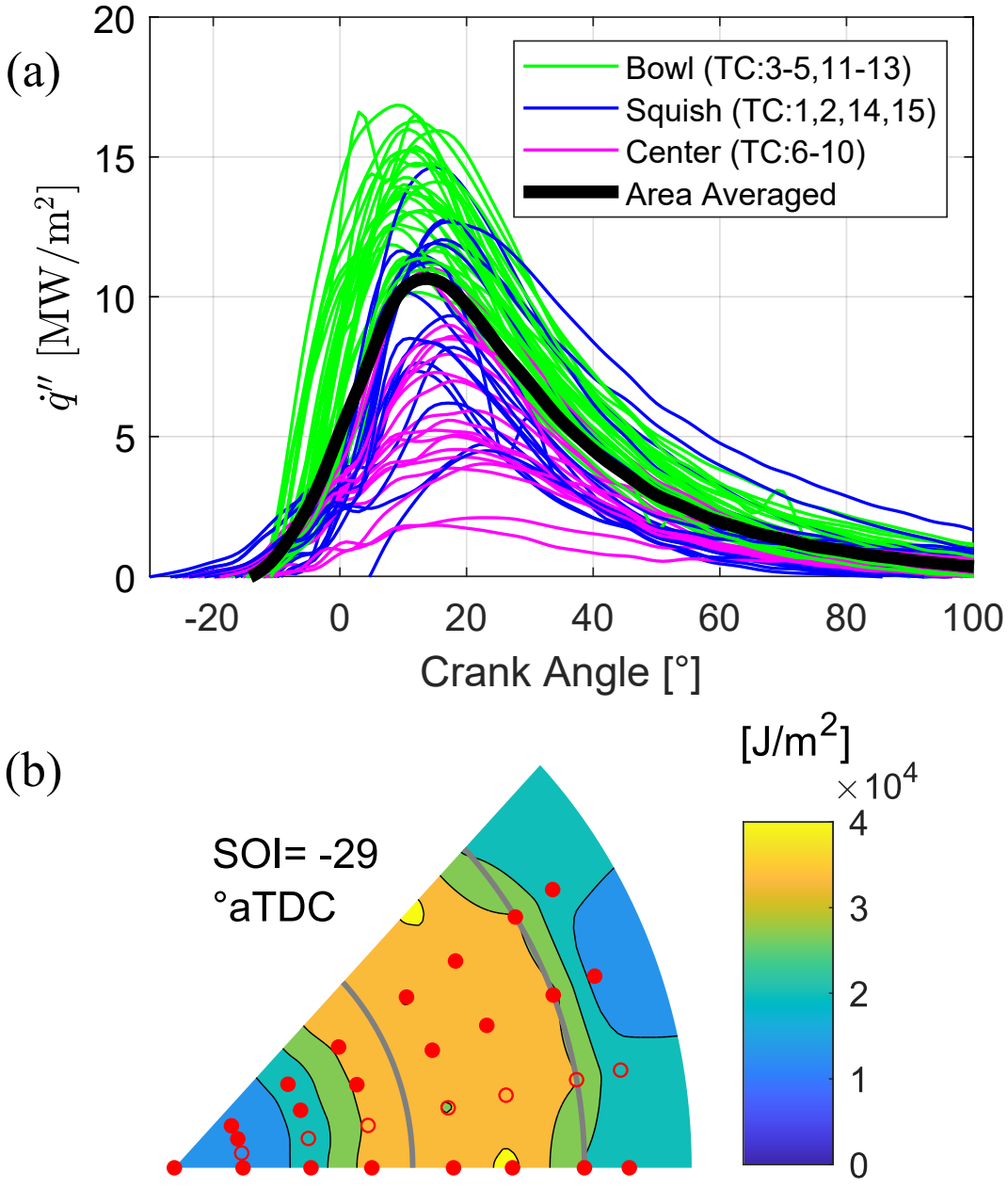

Figure 6.2: Operating condition 3 (2500 rpm, 20.3 bar IMEPg) SOI timing of -29°aTDC (a) area-averaged and individual heat flux with line color indicating piston location and (b) contour of heat flux integrated with time (energy flux) from -20 to 100°aTDC, adapted from Gingrich [3].

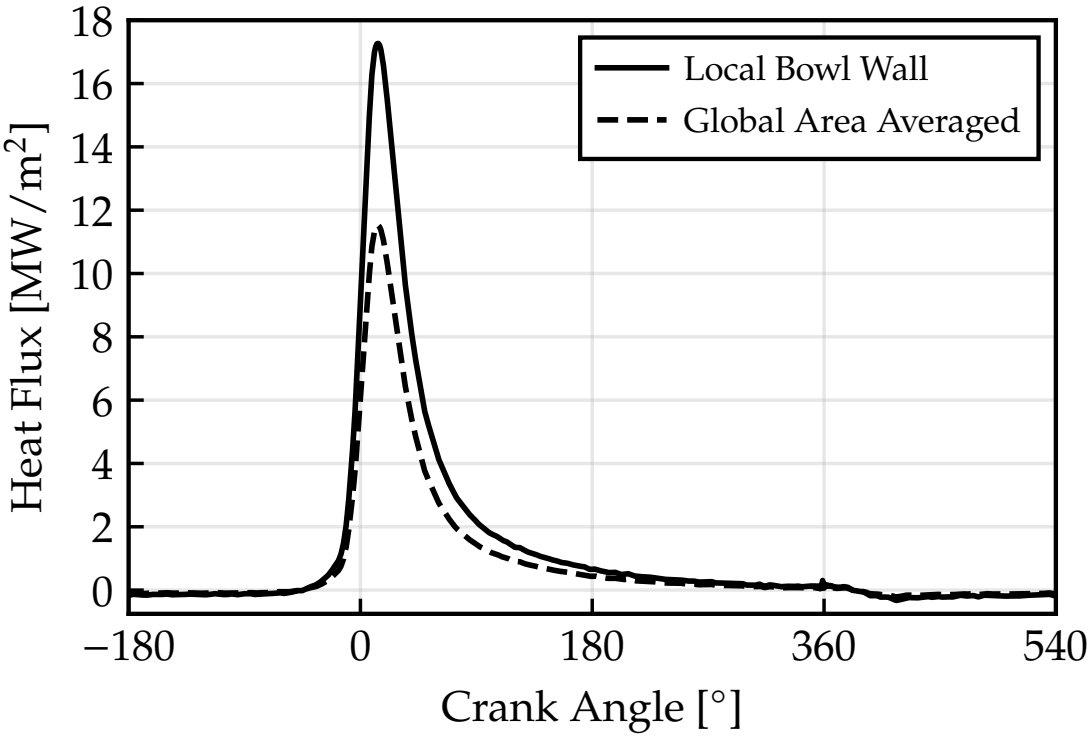

Figure 6.3: Estimated local bowl-wall and global area-weighted heat fluxes obtained via telemetry measurements on an uncoated piston, including the steady-state solution.

with performance benefits previously detailed [49]. These cases were selected as being representative of both traditional and contemporary coating designs.

Table 6.3 gives the details of each of the coatings and defines the nomenclature. All of the coatings except "YSZ Thick", were run for varying times at engine operating conditions 1-5. For "YSZ Thick", delamination was observed upon completion of a 4 hour break-in schedule, which consisted of progressively increasing load/speed and culminating in the two high load points (conditions 3 and 5). The total testing time for the other cases ranged from 26-75 hours and was primarily focused on performance testing. The "Cordierite-YSZ Stiff" coating also experienced a delamination that was not observed until after testing was complete, so the exact

time delamination occurred is unknown. Both coating delaminations occurred in the piston bowl area. Images of the "YSZ Thick" and "Cordierite-YSZ Stiff" can be found in Fig. 6.7 and 6.10, respectively.

Table 6.3: Summary of engine operating conditions

Wall Structure	TBC Material	Total TBC thickness [μm]	Functionally Graded	Conditions Run	Hours Run	Delamination
Four-layer YSZ [49]	YSZ	325	Yes	1-5	75	No
Thin	YSZ	325	No	1-5	26	No
Thick	YSZ	474	No	3, 5	4	Yes, at bowl wall
Compliant	Cordierite-YSZ	350	Yes	1-5	40	No
Stiff	Cordierite-YSZ	351	Yes	1-5	40	Yes, at bowl wall

6.2.1 Materials Fabrication and Property Measurement

Four material variations were produced: a composite NiCr-Al bond coat (443NS, Oerlikon-Metco, Westbury, NY, USA), an 8 wt% Yttria-Stabilized Zirconia TBC (SG204, St. Gobain Coating), and two variations of a Cordierite-YSZ glass-ceramic composite based on previous work [122]. The first cordierite-YSZ composite (Cordierite-YSZ Compliant) was produced from a coarse spray-dried cordierite feedstock (Superior Technical Ceramics, St. Albans, VT, USA) blended with YSZ feedstock fifty percent by volume before spraying. The latter (Cordierite-YSZ Stiff) was produced with a fine fused powder (Oerlikon-Metco, Westbury, NY, USA) similarly blended before spraying.

Thermal and mechanical properties of all coatings were measured at CTSR prior to engine testing. Thermal properties included diffusivity, specific heat capacity, expansion coefficient, density, and thickness. Generally, the coatings are assumed to be isotropic and linear-elastic for the mechanical properties measurements. Those properties included elastic modulus, Poisson ratio, and toughness. The reader is encouraged to see sections "Materials Fabrication", "Thermal Property Measurements", and "Mechanical Property Measurements" of Koutsakis *et al.* [134] for further details on the fabrication characteristics, property measuring instruments and standards followed.

Table 6.4: Thermo-mechanical properties of wall architectures investigated, with k: thermal conductivity, ρ: density, c: specific heat capacity, L: thickness, E: Young's modulus α: coefficient of thermal expansion, ν: Poisson ratio, t_{ref}: stress-free temperature and G_c: toughness

Wall Structure	Layer	Material	k [W/m-K]	ρ [kg/m^3]	c [J/kg-K]	L [μm]	E [GPa]	α [ppm K^{-1}]	ν [–]	t_{ref} [°C]	G_c [J/m^2]
Four-layer YSZ[49]	Top	8YSZ	0.77	4713	387	195	41	11.7	0.17	220	95±22
	Gradient	mix	0.85	3886	385	65	50	14.5	0.17	220	150
	Bond	443NS	4.07	6255	152	65	55	16.4	0.2	220	436
	Piston	4140	39	7850	520	4675	180	13.5	0.29	—	—
Thin	Top	8YSZ	0.89	5586	387	275	30	11.5	0.17	220	113±20
	Bond	443NS	4.85	7120	395.2	50	55	16.4	0.2	220	436
	Piston	4140 Steel	39	7850	520	4675	180	13.5	0.29	—	—
Thick	Top	8YSZ	0.89	5586	387	470	30	11.5	0.17	220	113 ±20
	Bond	443NS	4.85	7120	395.2	50	55	16.4	0.2	220	436
	Piston	4140 Steel	39	7850	520	4480	180	13.5	0.29	30	—
Compliant	Top	Cordierite	0.39	2894	347.4	275	15	7	0.17	240	53±11
	Bond	443NS	4.85	7120	395.2	50	55	16.4	0.2	240	436
	Piston	4140 Steel	39	7850	520	4675	180	13.5	0.29	—	—
Stiff	Top	Cordierite	0.89	3619	579	275	46.9	7.5	0.17	240	28±6
	Bond	443NS	4.85	7120	395.2	50	55	16.4	0.2	240	436
	Piston	4140 Steel	39	7850	520	4675	180	13.5	0.29	—	—

6.3 Durability Mechanics Approach

6.3.1 Four-layer YSZ Wall Architecture

In this section, the engine performance and mechanics characteristics are demonstrated for the four-layer YSZ [49] coating deposited on the steel piston substrate, see Table 6.4. Figures 6.4 (a) and (b) show the gas cylinder pressure, gas cylinder temperature, apparent chemical heat release rate (AHRR), and the estimated local bowl-wall heat flux as a function of crank angle from engine experiments at operating condition 3. The rated power condition gives peak pressure and temperature higher than 200 bar and 2000°C, respectively. A Crank-Nicolson finite difference scheme [114, 95] was employed to solve the 1-D heat conduction equation and generate the wall temperature distribution. The oil temperature on the backside remained fix at 100°C. The wall temperature histories of six discrete y-locations in the wall, where 0 is the combustion surface, are shown in Fig. 6.4 (c).

The x-direction stress histories, in the plane parallel to the piston surface, at the same y-positions are shown in Fig. 6.4 (d). Negative and positive values indicate compressive and tensile stress, respectively. It is worth noting that the vast majority of such coatings are under compression even at ambient temperature. This is due to the initial cool-down of the plasma-spray deposition process. The ceramic molten particles cause the surface to be in tension and, by reaction, the multilayer wall compresses. As heat flux and surface temperature increase due to combustion, the compressive stresses in the coating increase. The stress change at the interface is attributed more to static deformation owing to changes in the coefficients of thermal expansion between materials than temperature changes.

Energy release rate histories for the same y-positions are illustrated in Fig. 6.4 (e). The energy release rate is zero at the surface by definition. Figure 6.5, however, provides a more comprehensive view of the energy release rate distribution through the coated engine wall. The temporal and spatial evolution of the temperature (a), x-direction stress (b), and energy release rate (c) are shown for the same engine condition as Fig. 6.4. The horizontal and vertical axes represent crank-angle (or

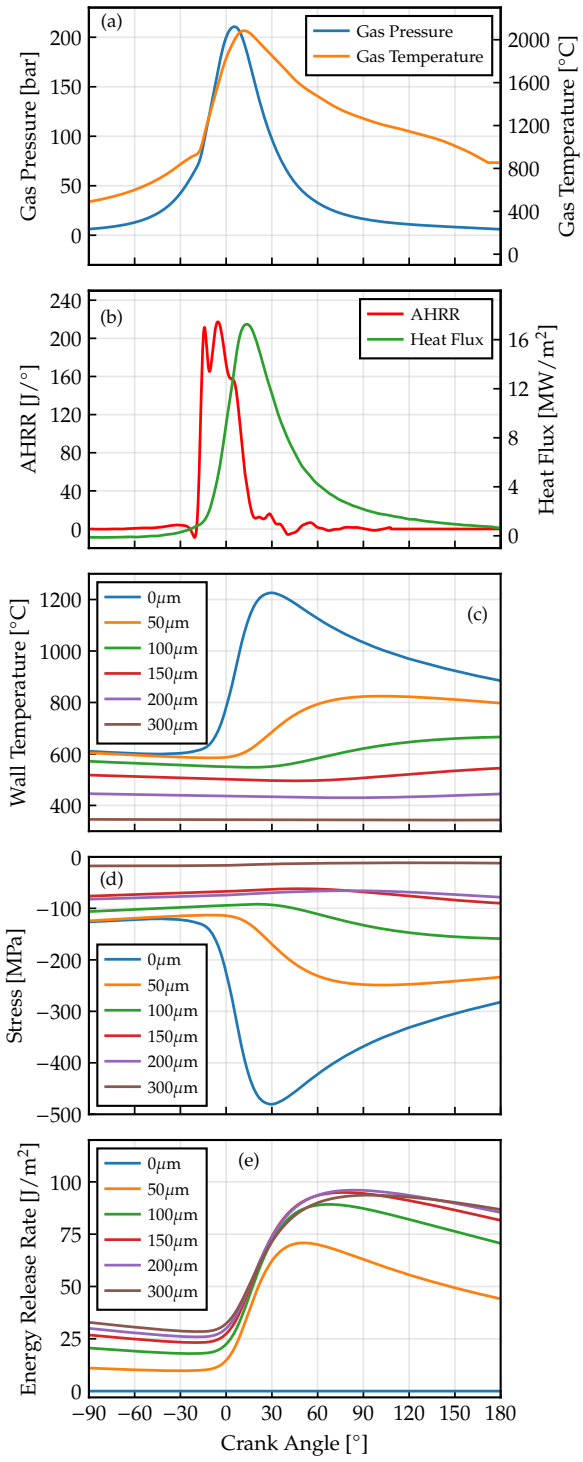

Figure 6.4: Temporal evolution, for the Four-layer YSZ wall architecture, (a) of gas pressure and gas temperature, (b) apparent chemical heat release rate and combustion chamber heat flux, (c) wall temperature distribution, (d) x-direction stress distribution, and (e) elastic energy release rate distribution. Stress-free temperature was held constant at 220°C.

time) and position in the wall, respectively. The latter has four different linear scales, which correspond to the thicknesses of the various layers of the multilayer coating: 0-195 μm, which is the top layer, 195-260 μm which is the gradient layer, 260-325 μm which is the bond layer and 325-5000 μm which is the piston substrate. The top-gradient, gradient-bond and bond-substrate interfaces are shown with horizontal pink lines. Further details on the behavior of the temperature, stress and energy release rate can be found in Fig. 4.6 for a two-layer structure.

A typical coated engine wall temperature distribution is shown in Fig. 6.5 (a). The YSZ coating reaches a maximum temperature on the surface at 30°aTDC, slightly delayed relative to the maximum cylinder gas pressure and gas temperature, which occur at 5.5°aTDC and 12°aTDC, respectively, as shown in Fig. 6.4 (a). The temperature swing rapidly diminishes while the thermal wave progresses deeper into the wall; the interfaces (pink) have temperature swings (starting from the combustion surface) of about 36, 7 and 4°C, respectively. The intra-cycle wall temperature variations in the piston substrate are negligible.

The thermal shock at the combustion chamber surface, starting from TDC, contracts the bottom of the substrate further as localized heating in the coating causes the top surface to elongate, inducing downward curvature [135]. Additionally, the stress-free temperature, fixed at 220°C, is responsible for compressive stresses in the coating seen in Fig. 6.5 (b). The maximum stress in the wall is observed to be exactly when and where the temperature is maximized at the surface, *i.e.*, 30°aTDC.

The energy release rate is seen in Fig. 6.5 (c). By definition the energy release rate at the edges (combustion chamber and coolant surface) are zero since there is no strain released there. Immediately after the start of combustion the energy release rate increases rapidly throughout the coating multilayer, even extending into the piston substrate. The maximum energy release rate is observed during the expansion stroke, at 82°aTDC at 192 μm (near the top-gradient interface) as highlighted with the yellow star. At this time of the cycle the coating surface is cooling while the interior of the coating is still heating. It is interesting to note that the position of the maximum energy release rate is near the mid-point of the top coat and the energy release rate is nearly constant through the gradient and bond coat.

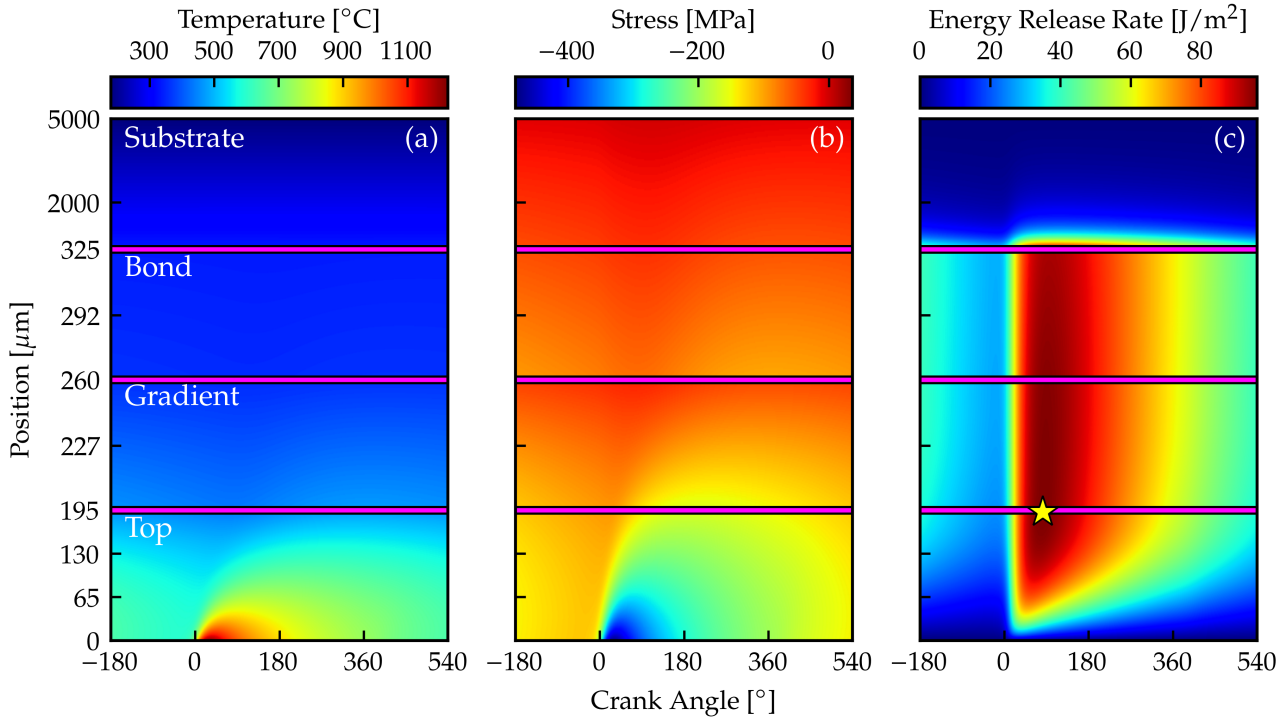

Figure 6.5: Spatial and temporal (in crank angle domain) evolution of (a) temperature, (b) stress and (c) energy release rate using the wall architecture "Four-layer YSZ". Combustion chamber surface and oil surface are at $y = 0$ and $y = 5000$ μm, respectively. The interfaces are indicated with the horizontal pink lines at 195, 260 and 325 μm. The stress-free temperature was 220°C. The yellow star highlights the location of the maximum energy release rate.

The surface layer has the lowest toughness and therefore controls the mechanics of this problem. This behavior suggests that, for cases where energy release rate exceeds the fracture toughness, the coating would have higher likelihood to crack at the top-gradient layer interface.

Figure 6.6 shows the spatial distribution of the energy release rate through the coating section (shaded area ranging from 0 to 325 μm). The combustion chamber gas and the piston substrate are to the left and right hand side of the shaded area, respectively. Energy release rate results are depicted for the crank angle times of TDC, 60°aTDC and BDC. It is evident that energy release rate is maximized near the mid-point of the top coat.

At TDC, the wall has only absorbed a small fraction of the total thermal energy and the temperature has not increased substantially. During the expansion stroke (60°aTDC), the energy release rate maximizes because the thermal wave has propagated through the coating and the surface temperature is decreasing from expansion cooling, as illustrated in Fig. 6.5 (a). At BDC, the thermal energy has penetrated most of the way through the coating.

The toughness of the top, gradient and bond layers are depicted in Fig. 6.6 with the horizontal orange, purple and green lines, respectively. The uncertainty given to the toughness measurements is provided with a 95% confidence interval, unless otherwise stated. The maximum energy release rate reaches almost the average top layer toughness, making it difficult to predict whether this structure would survive or fail. It is worth noting that the prediction is within the thermomechanical property uncertainties, indicated with the vertical orange error bar. Recall that in the lab experiments discussed above, the four-layer YSZ structure survived the testing schedule.

6.3.2 The Role of Coating Thickness

The role of coating thickness on the maximum energy release rate (in a cycle) was parametrically investigated in Chapter 4. The coatings studied showed a non-linear increase of the maximum energy release rate with thickness, and a similar trend is

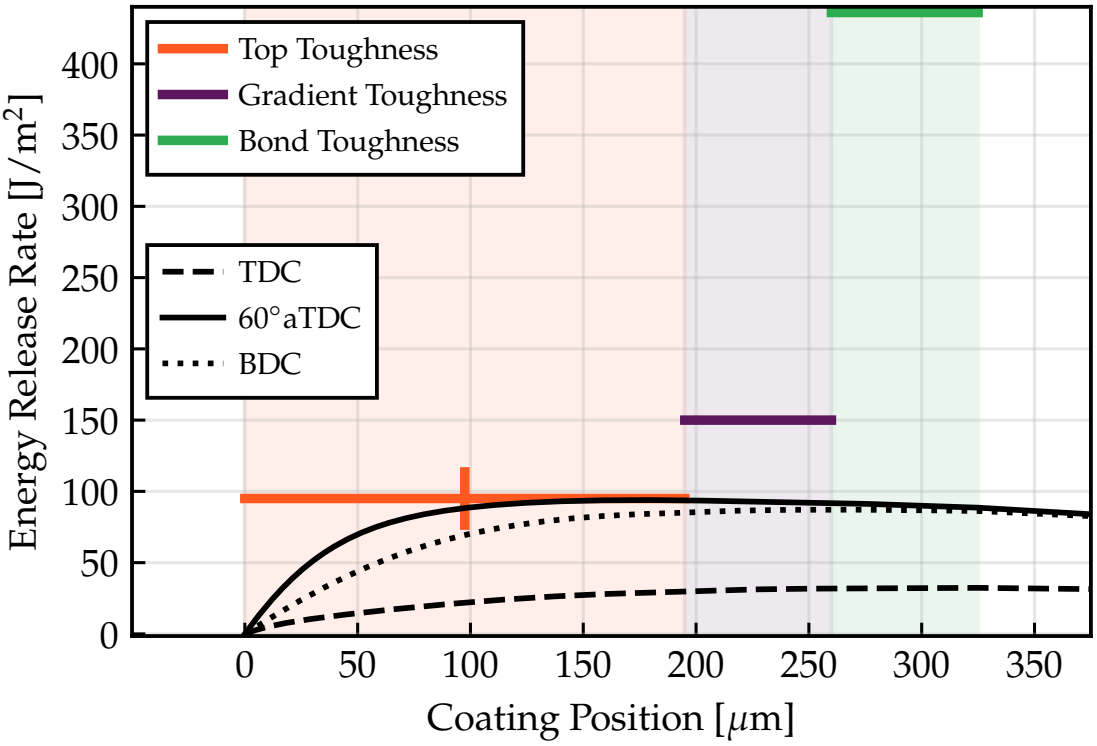

Figure 6.6: Energy release rate spatial distribution for coated region at three distinct crank angle locations is shown for the Four-layer YSZ architecture. The results shown are at TDC, 60°aTDC and BDC. The shaded areas highlight the top (orange), gradient (purple) and bond (green) coat thicknesses. The same engine condition as Fig. 6.4 and 6.5 was used.

observed for the YSZ thickness comparison described next. In the current work, the YSZ Thin (325 μm) and a YSZ Thick (520 μm) coating structure allowed the effect of thickness on the energy release rate to be tested. The key distinction between the four-layer YSZ and the "Thin" and "Thick" YSZ coatings is the absence of the gradient layer between the top and bond coat. The two cases matched all thermomechanical properties, but the (top layer) thickness differed by 2×, as shown in Table 6.4. The Thin version was operated across all engine conditions for a total of 26 hours and survived. However, the YSZ Thick version was observed to delaminate after the completion of an engine break-in test schedule, for which

the last two test points were single SOIs at conditions 3 and 5. Post-run inspection showed that the coating was delaminated in the bowl wall area, as shown in Fig. 6.7. Looking at the top view of Fig. 6.7, one can observe the coating spalled at multiple locations. There are missing chips at every spray impingement location (near the central area of the soot witness mark), plus at some inter-plume locations. The coating first delaminates and then the delaminated region spalls off. As a side note, this observation further supports the argument that the highest piston heat fluxes are located *on* the spray axis, as shown in Fig. 6.2 [2, 3]. The durability analysis was employed to assess whether the analytical mechanics model could predict the observed coating failure.

Figure 6.8 shows the energy release rate distribution as a function of the wall position through depth of the wall. The only crank-angle shown corresponds to the maximum energy release rate timing for each coating; the YSZ Thin and the YSZ Thick energy release rate distributions are shown at 87°aTDC and 106°aTDC, respectively. The vertical dashed blue and red lines indicate the coating-piston interface. Average toughness values are shown for the top and bond coating, respectively. The uncertainty from the average top layer toughness is depicted with the semi-transparent green rectangle, derived from 30 measurements on equivalent coupons.

The maximum energy release rate of YSZ Thin is *lower* than the toughness value, which is consistent with the engine testing where this coating survived. The maximum energy release rate for the YSZ Thick coating was *higher* than the toughness, indicating that such scenario could lead to coating failure, and this coating did fail in lab testing. The modeling results seem to capture the effect of thickness on the delamination crack-driving force and trendwise predict the coatings' mechanical performance.

6.3.3 The Role of Coating Stiffness

The dependence of energy release rate on the coating modulus is strictly linear in the steady state isothermal cooling scenario of coated gas turbine blades [104].

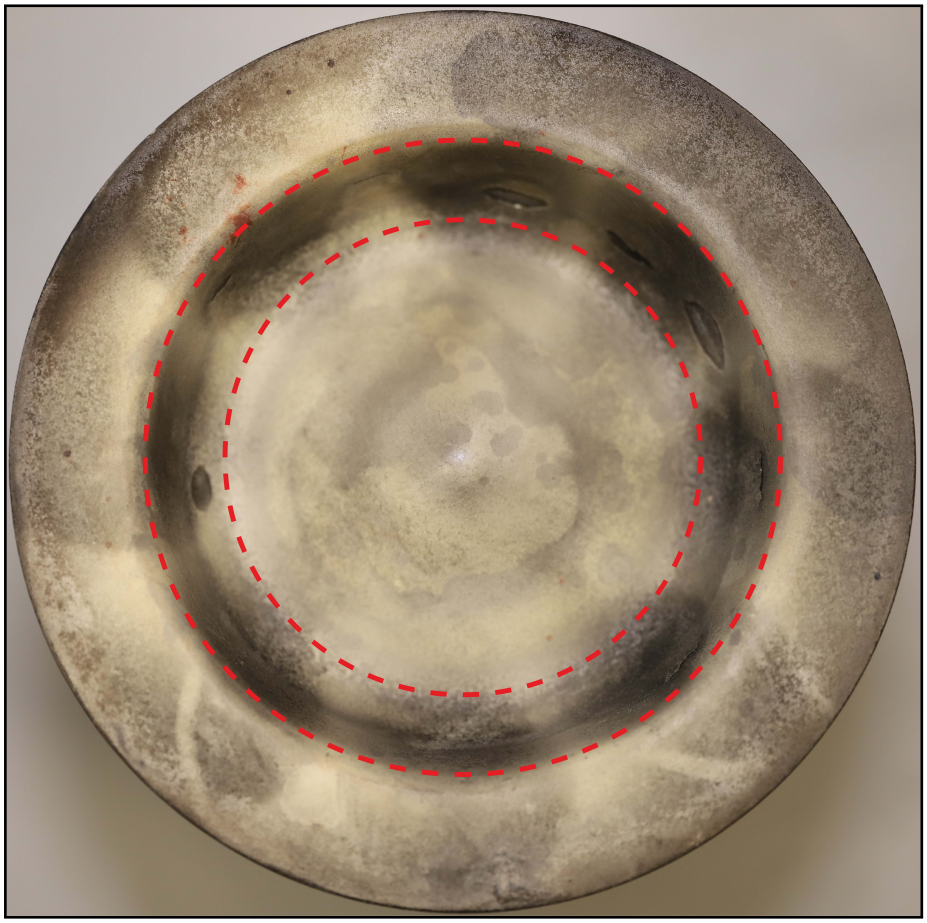

(a) Piston Top view

(b) View close to a delamination spot

Figure 6.7: Post-test images from GSVC of the YSZ Thick piston [134].

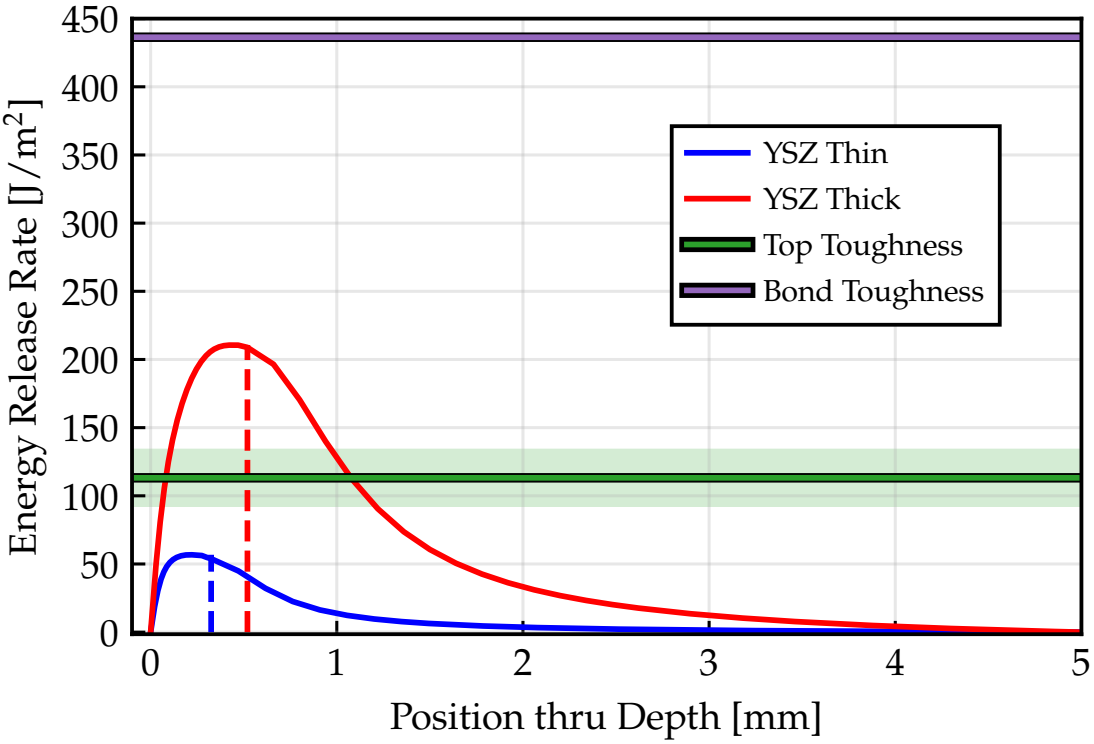

Figure 6.8: Energy release rate spatial distribution is shown for the full wall depth. The distributions are shown for the maximum energy release rate crank-angle location of each case. The same YSZ coating is compared for two different thicknesses. The shaded area highlights the top layer toughness uncertainty.

Internal combustion engines undergo rapid transient thermal cycling, therefore the energy release rate could have a different dependence on the coating modulus.

A Compliant (15 GPa) and a Stiff (47 GPa) Cordierite-YSZ structure were fabricated to assess the effect of modulus on the energy release rate. The two versions reasonably matched all thermomechanical properties, but the Young's modulus of the Stiff coating was more than 3× the Compliant coating, as shown in Table 6.4. The thermal property matching, however, was not perfect. The stiffer version was achieved by depositing finer powder onto the piston substrate, which increased the density and thermal conductivity. Each version was tested across all engine conditions for total of 40 hours and inspected post-test. The Compliant coating

survived the engine testing. The Stiff coating delaminated during testing.

Figure 6.9 shows the energy release rate distribution as a function of (a) total wall and (b) coating position. The dark grey and light grey shaded areas highlight the top and bond coat thickness, respectively. The only crank-angle shown corresponds to the time of maximum energy release rate. The Compliant and the Stiff energy release rate distributions are shown at 85°aTDC and 76°aTDC, respectively. Each coating structure has its own toughness, unlike the thickness comparison scenario above. Horizontal lines depict the average top layer toughness for the Compliant (blue outlined with black) and the Stiff (red outlined with black) coatings. The uncertainty from the average top layer toughness of each material is shown with the transparent rectangles, derived from 30 measurements on equivalent coupons.

The maximum energy release rate of the Compliant is *lower* than the average toughness, therefore the captures model correctly that this coating survives during engine testing. On the other hand, the maximum energy release rate of the Stiff is *nearly equal* to the average toughness making the prediction of whether this coating would delaminate difficult. Recall the Stiff coating failed during testing. By taking a closer look at the top view of the Stiff Cordierite-YSZ piston, see Fig. 6.10, one can clearly see that there are only a few delamination spots. In contrast, the YSZ Thick case showed signs of coating failure (coating and/or spalling) at every plume impingement location. The margin that the maximum energy release rate exceeded the toughness for the YSZ Thick case was substantial, see Fig. 6.8. The Stiff coating operated significantly closer to its mechanical limits, but it did not overcome them to the same level as the YSZ Thick. Trendwise, therefore, the model is performing well.

6.4 Summary and Conclusions

The structural integrity of five thermal barrier coated pistons, having different coating properties, was modeled and compared to test results from a high-output, single-cylinder diesel engine of GSVC. Two coating architectures delaminated

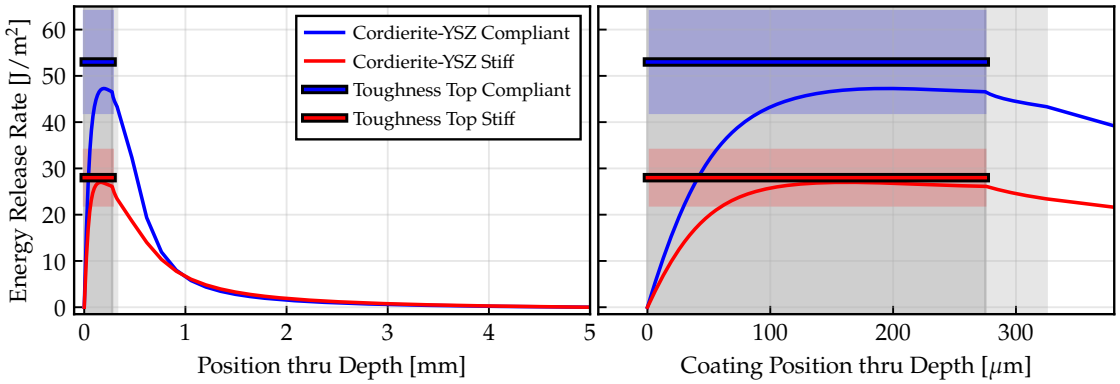

Figure 6.9: Energy release rate spatial distribution is shown for (a) the entire engine wall and (b) the coating region. The distributions are shown for the maximum energy release rate crank-angle timing of each case. The dark and light grey shaded area highlights top and bond coat thickness, respectively.

during engine operation. The analytical mechanics model was employed to predict the coating delamination.

Piston heat flux measurements from an earlier study on the same engine were used to estimate the highest heat flux observed in the bowl-wall region. The local bowl-wall heat flux data served as an input to a thermal model. The temperature distribution was predicted using a one dimensional finite difference method with boundary the time-varying heat flux and a fixed oil temperature applied to the combustion chamber surface and backside oil surface, respectively. The temporal and spatial temperature field were subsequently used in the mechanics model.

All coating thermomechanical properties were measured prior to engine testing by CTSR. The mechanics model predicted a maximum energy release rate at locations near the center of the multilayer coating, not at the piston-coating interface. However, the spatial gradient was modest through the gradient and the bond coat layers. The maximum energy release rates occurred about midway down the expansion stroke when the combustion surface was cooling while the interior wall was still undergoing heating.

The on-engine coating durability observations and model results were consistent, within the uncertainty limits, for all five thermal barrier coatings. Coatings with

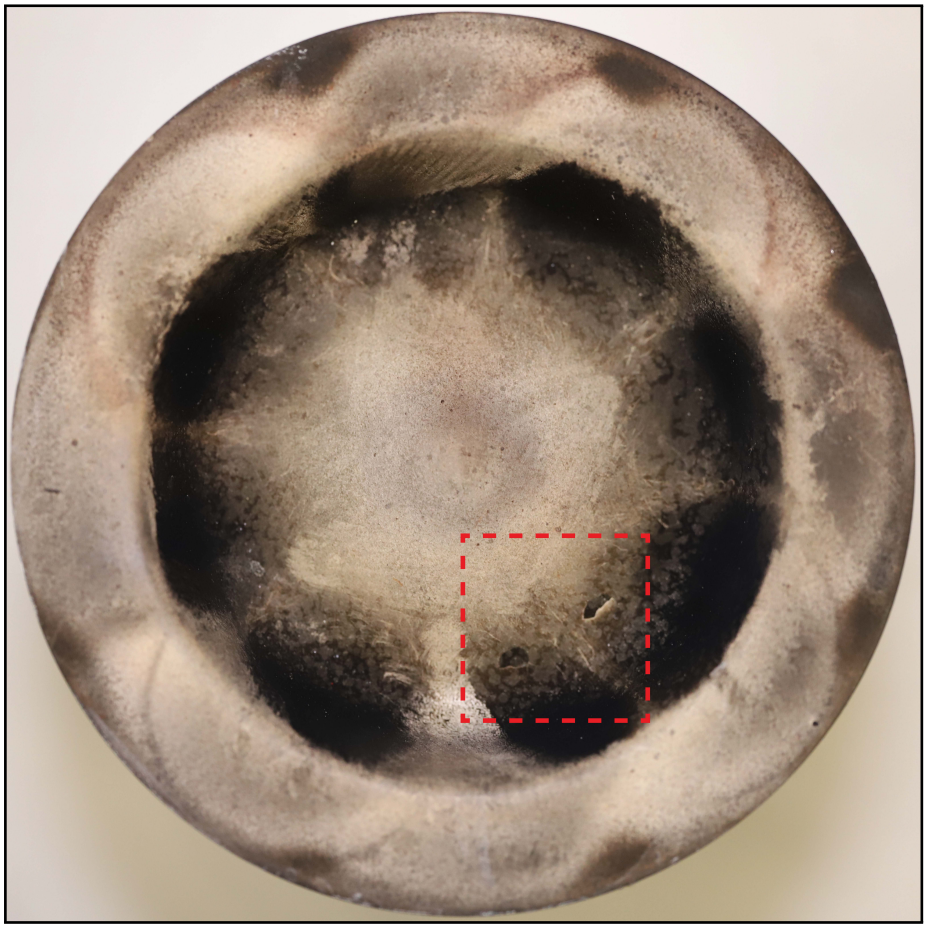

(a) Piston Top view

(b) View close to a delamination spot

Figure 6.10: Post-test images from GSVC of the Cordierite-YSZ Stiff piston [134].

maximum energy release rate that significantly exceeded the toughness failed; those with maximum energy release rate significantly below the material toughness survived. The Thick YSZ case, which had significantly higher maximum energy release than its toughness, spalled at multiple locations along the bowl wall area plus some inter-plume regions. The Stiff Cordierite-YSZ case, which had maximum energy release rate close to its toughness, spalled only on a couple locations along two of the spray plume axes, radially inward from the deepest part of the bowl. Clear evidence of delamination was seen for both failed cases. The four-layer YSZ case, however, which had maximum energy release rate nearly equal to the toughness and within its uncertainty showed no indication of durability issues. Therefore, the model shows good trendwise predictive capability but caution should be used when assessing borderline cases.

7 OPTIMIZATION OF THERMAL BARRIER COATING PERFORMANCE AND DURABILITY OVER A DRIVE CYCLE

The basis to independently analyze the heat conduction and fracture mechanics of multilayer engine coatings was established in chapters 3 and 4, and their analytical techniques were demonstrated for engine applications in chapters 5 and 6. In this chapter, the analyses are integrated into a single framework to demonstrate an optimization procedure for selecting coatings that includes both thermal and durability performance considerations over a full drive cycle. The optimization objective was to minimize the heat transfer to the engine wall while maintaining structural integrity of the coating. Over eight hundred candidate materials were investigated and the optimization required more than one million non-road transient drive cycle calculations; real materials were investigated to ensure a realizable result and the existence of thermal and mechanical properties. An uncoupled approach was utilized for the optimization, wherein the gas temperature and heat transfer coefficient profiles from a fully coupled and calibrated baseline model over the twenty-minute drive cycle were employed.

7.1 System-level Model Setup

A production system-level simulation powertrain model (GT-Power) from John Deere for the 4045 engine was provided, see Table 5.3 for engine specifications. The model is calibrated to predict steady-state or transient cycles. The transient cycle exercised was the NRTC [116, 136]. Further details about the production system-level engine model are provided in Chapter 5.

The conduction heat transfer was evaluated using the analytical relations developed and implemented into the commercial software package in Chapter 3 and 5, respectively. The time-responses of the candidate wall architecture X_o and Y_o were calculated before the simulation started. The X_o response referred to the surface temperature rise due to an input heat flux $\dot{q}''$ at the combustion surface

while the Y_o response referred to the surface temperature rise due to a temperature change of the back-side coolant/oil surface, t_N. For this work, the temperature histories of "Oil" and "Coolant" of Fig. 5.10 were used for the liner and head, and piston, respectively. The surface temperature was shown to be the convolution of the previous heat flux or coolant/oil temperature with the respective response function. The superposition of the two subproblems provides the instantaneous wall surface temperature $t_{\mathrm{o,wall}}$ for a multilayer as shown in Eq. (3.61). Both *coupled* and *uncoupled* approaches were utilized in this Chapter. Additional details about the conduction heat transfer methodology can be found in Koutsakis *et al.* [116, 137] and in Section 3.2.

7.2 Uncoupled Thermo-mechanical Analysis

Decoupling the heat transfer calculation from the full powertrain model, *i.e.,* using the uncoated piston heat flux from the full model for coated piston heat transfer simulation, can significantly reduce the computational effort for optimizing a piston thermal barrier coating. However, this requires assumptions about gas temperature and engine breathing. The validity of these assumptions is discussed below.

7.2.1 Baseline Gas Temperature Assumption

If one assumes that the combustion gas temperature and the heat transfer coefficient are minimally affected by the presence of the coating, one can take h and t_{gas} from the fully coupled baseline solution and independently compute $t_{o,\mathrm{wall}}$, from which an updated wall heat flux can be determined. After just a few iterations, in practice, a converged wall temperature solution can be achieved. The wall temperature drives the mechanical response without any feedback so the mechanical response can be solved after thermal convergence. This, however, requires that the gas temperature is not significantly affected by the change in heat loss due to the coating; the constant h assumption arises from an incomplete understanding of coating roughness effects [49, 41, 42, 43, 44, 46, 8].

Figure 7.1 shows a comparison of the fully coupled baseline (uncoated) case to the fully coupled coated case, and the uncoupled coated results. The data are for a steady-state cycle of the production John Deere 4045 engine. The load was held fixed at 10.9 bar IMEPg by adjusting the fuel mass injected and engine speed was 800 rpm. The stock piston material was used for the baseline uncoated case; a modern, low-volumetric-heat-capacity coating was used on top of the aluminum wall for the coupled and uncoupled coated cases. Material thermal properties of the engine wall architecture can be found in Table 7.1. The baseline wall thickness was 8.6 mm.

Table 7.1: Thermo-mechanical properties of wall architectures investigated, with k: thermal conductivity, ρ: density, c: specific heat capacity, L: thickness, E: Young's modulus α: coefficient of thermal expansion, ν: Poisson ratio, t_{ref}: stress-free temperature and G_c: toughness

Material	k [W/m-K]	ρ [kg/m^3]	c [J/kg-K]	L [μm]	E [GPa]	α [ppm K^{-1}]	ν [-]	t_{ref} [K]	G_c [J/m^2]
8YSZ+Polyester [122]	0.42	4473	358	300	20	11.5	0.33	473	40
Stock Al Piston	123	2702	949	8300	75	21	0.33	473	-

The gas and piston temperature are shown in Fig. 7.1(a) as a function of crank-angle. The coupled gas temperature solutions for the baseline and coated case are seen to match very well, which is a necessary but not sufficient condition because ultimately it is the heat transfer estimation that matters. The baseline uncoated wall surface temperature showed negligible temperature swing, as expected. The coupled coated case, which uses the simultaneously solved gas temperature, shows a significant temperature swing. The uncoupled coated piston temperature, which uses h and t_{gas} from the baseline calculation, also shows a significant swing, and the cycle-mean magnitude of the swing is seen to be almost 2.5 % higher than for the coupled case.

The piston heat flux is shown in Fig. 7.1(b) for the two coated cases. Recall, the uncoupled case uses the baseline uncoated gas temperature and heat transfer coefficient. It can be seen that there is quite good agreement between coupled and

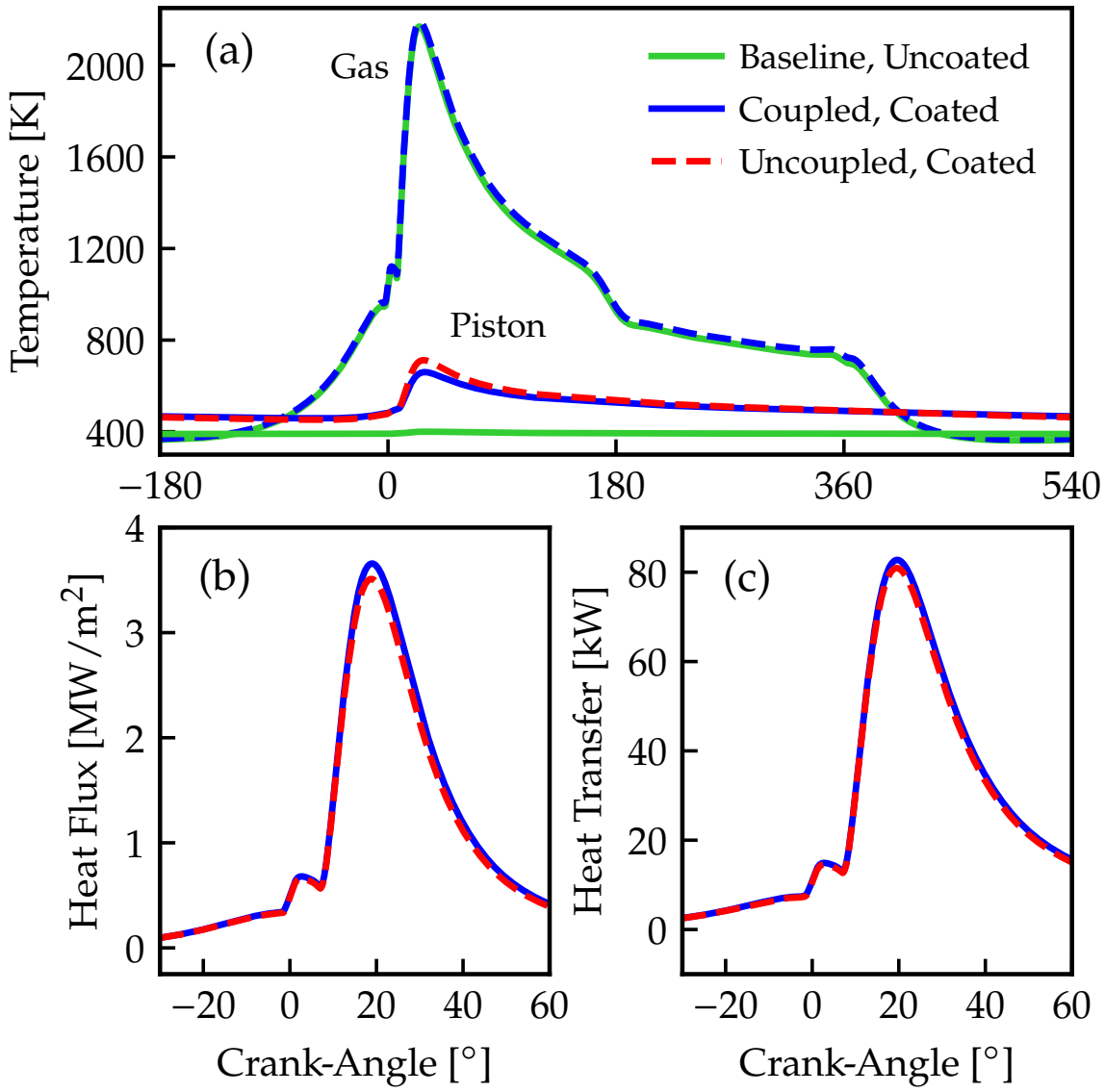

Figure 7.1: (a) Gas/wall temperatures and (b) instantaneous *piston* heat flux and (c) *total* heat transfer rates for a baseline aluminum and coupled/uncoupled case of a thermal swing coating. The total heat transfer percentage error between the coupled and uncoupled coated approach is 0.27 %.

uncoupled piston heat flux, *i.e.*, the slightly higher uncoupled gas temperature partially compensates for the slightly higher piston temperature.

The ultimate comparison, however, is to assess the uncoupled gas temperature assumption on the *total* heat transfer rate. The total heat transfer difference is suppressed because the cylinder head and liner heat transfer rates, which are minimally affected, are included in the calculation. The total heat transfer rate, $\dot{q}_{\text{total}}$, shown in Fig. 7.1(c), is given by

$$\begin{aligned}\dot{q}_{\text{total}}(\theta) = {} & \dot{q}''_{\text{head}}(\theta) A_{\text{head}} \\ & + \dot{q}''_{\text{piston}}(\theta) A_{\text{piston}} \\ & + \dot{q}''_{\text{liner}}(\theta) A_{\text{liner}}(\theta)\end{aligned} \tag{7.1}$$

where $\dot{q}''_{\text{head}}$, $\dot{q}''_{\text{piston}}$ and $\dot{q}''_{\text{liner}}$ are the head, piston and liner heat flux, respectively, and the terms A_{head}, A_{piston} and A_{liner} are the corresponding surface areas; the liner area varies with crank angle. For this operating condition, the percentage error between the uncoupled and coupled *total* heat transfer rate was 0.27 %.

The *coupled* solution requires evaluation of a direct form convolution *at each time step*, see Eq. (3.63); the current wall temperature is calculated based on the convolution of previous and current heat flux and backside temperature arrays and the wall responses.

The *uncoupled* solution, however, can be solved with a *single* convolution, which can be sped up significantly using the Fourier-domain properties of the convolution.

$$t_o = X_o \circledast q'' = \mathcal{F}^{-1}\left\{\mathcal{F}\left\{X_o\right\} \cdot \mathcal{F}\left\{\dot{q}''\right\}\right\} \tag{7.2}$$

where $\dot{q}''$ is the full heat flux history, which is known since t_g, t_o, and h are known for the full duration of interest. The symbols $\mathcal{F}$ and $\mathcal{F}^{-1}$ denote Fourier transform to the frequency and time domain, respectively. As discussed above, an iterative solution, where t_o is updated for each iteration, is required. Convergence was achieved in only a few iterations.

The *uncoupled* problem could also be resolved with a finite difference approach,

but that would incur significant computational cost. Each spatial node of the computation domain would have to be calculated (and iterated) for all the ~2^{24} time steps of the transient drive cycle. On the contrary, large heat flux histories can very efficiently be handled in the frequency domain [132] with the current analytical conduction technique. To maximize computational efficiency, convolution techniques such as the Overlap-Add can be employed, using the very long signal as the heat flux $\dot{q}''$ and the finite-impulse-response filter as the response function X_o [117].

According to all the above, the use of baseline gas temperature and heat transfer coefficient data and an uncoupled approach to investigate coating performance appears to be a reasonable assumption for this piston coating optimization study. This assumption will be revisited later.

7.2.2 Baseline Engine Breathing Assumption

One limitation of thermally insulated engines has historically been the reduction of volumetric efficiency due to the flow of heat from the wall to the gas during the intake stroke. A significant amount of heat transfer during the intake stroke could limit the applicability of an uncoupled approach. Morel *et al.* [10] defined the term "pumped heat" per unit area as

$$q''_{\text{pumped}} = \frac{1}{2}\left[\oint |\dot{q}''| \, \mathrm{d}\theta - \oint \dot{q}'' \, \mathrm{d}\theta\right] \tag{7.3}$$

which represents the amount of heat flux from the wall to the gas as illustrated in Fig. 2.8; the wall temperature is practically only higher than the gas temperature during the intake stroke. The integration is performed over a full engine cycle, hence the $\oint$. Thus, the pumped heat provides a useful metric to assess the breathing performance of the engine when it is computationally expensive to calculate the gas flow, and it can be utilized as a surrogate for the volumetric efficiency, *i.e.* a pumped heat increase results in a decrease of volumetric efficiency.

The pumped heat ratio of a piston-coated engine relative to a baseline engine is

defined as

$$\Gamma_{\text{pumped}} = 100\times\frac{\left[q''_{\text{pumped,piston,coated}} - q''_{\text{pumped,piston,uncoated}}\right] A_{\text{piston}}}{Q''_{\text{pumped,uncoated}}} \tag{7.4}$$

where the pumped heat of the baseline engine, $Q''_{\text{pumped,uncoated}}$, is defined as

$$Q''_{\text{pumped,uncoated}} = q''_{\text{pumped,head}}A_{\text{head}}+q''_{\text{pumped,piston}}A_{\text{piston}}+\oint \left(|\dot{q}''_{\text{liner}}| - \dot{q}''_{\text{liner}}\right) A_{\text{liner}}\,\mathrm{d}\theta \tag{7.5}$$

In order to assess whether the presence of the coating would affect engine breathing to an extent that an uncoupled solution would be insufficient, fully coupled simulations for the coating given in Table 7.1 and an expected optimal coating – Silica Aerogel – were performed. Figure 7.2(a) shows the volumetric efficiency, calculated for each cycle at IVC, as a function of drive cycle time for both coatings compared to the baseline. There was an average reduction of less than 0.5 % and 2 %, respectively, for the two coatings simulated.

Figure 7.2(b) correlates the pumped heat ratio, defined in Eq. (7.4), with the relative volumetric efficiency change for the two coatings. Each point represents a different cycle. It can be clearly seen that the pumped heat transfer is increasing – more heat is transferred from the wall to the inducted air – when there is a lower volumetric efficiency, but the relationship is not 1:1.

Figure 7.2(c) shows the mean value of Γ_{pumped} over the full drive cycle compared to the total change of volumetric efficiency for the drive cycle. Additional coatings for which fully coupled simulations were performed are also included. It can be seen that in spite of the modest level of cycle-by-cycle correlation, over the full drive cycle Γ_{pumped} is a good indicator of breathing penalty.

The engine breathing changes shown above are relatively small, and can be safely neglected when coating performance is estimated using an uncoupled approach.

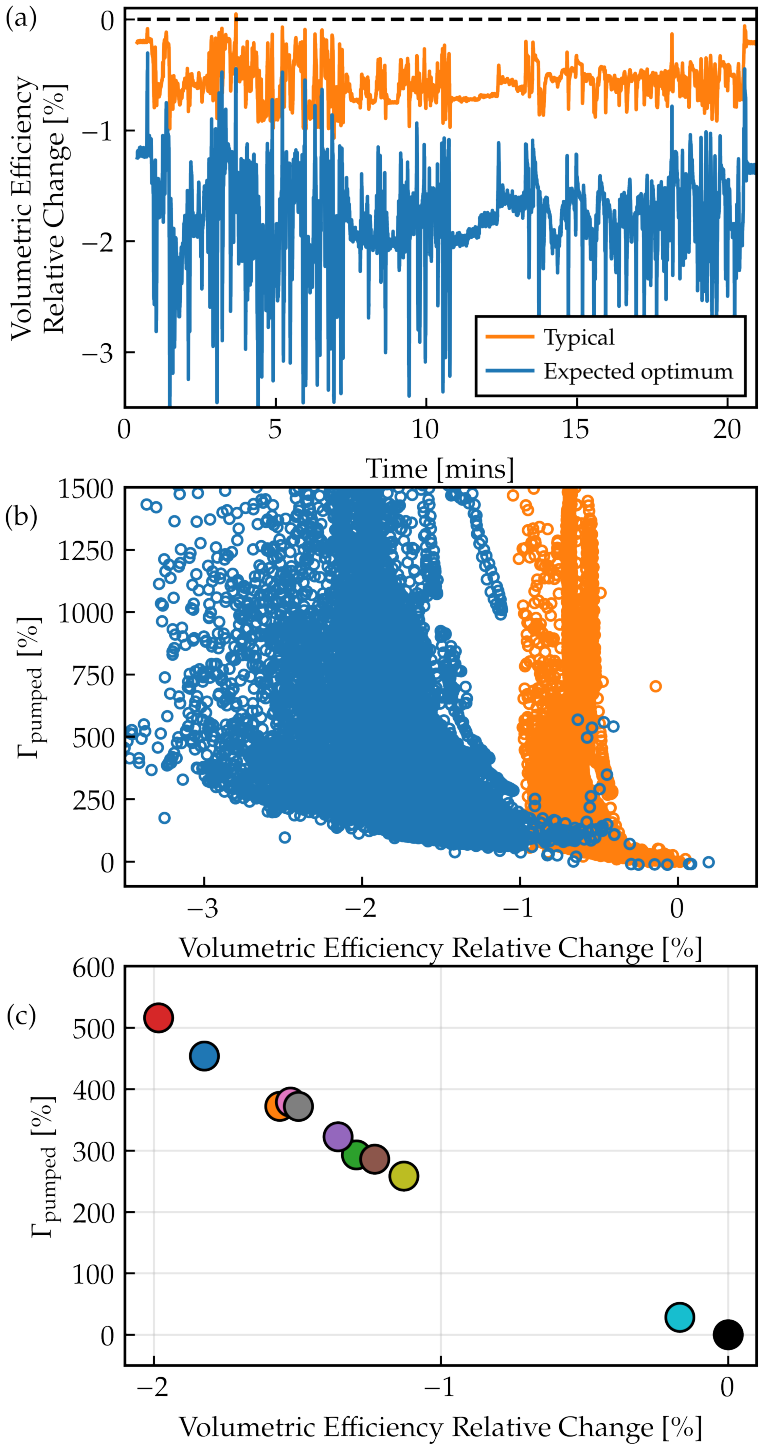

Figure 7.2: (a) Volumetric efficiency change relative to uncoated baseline as a function of drive cycle time. (b) Pumped heat transfer correlated with the volumetric efficiency on a cycle-by-cycle basis. (c) Drive-cycle-averaged comparison of Γ_{pumped} and volumetric efficiency change for multiple coatings.

7.2.3 Computational Time Comparison

The uncoupled approach was followed for conducting the optimization due to its substantial computational time advantage and its more-than-sufficient accuracy. An example of the elapsed times of each approach is provided for reference. A fully coupled simulation of the engine with the coating given in Table 7.1 over the NRTC drive cycle time (having a real time of 1258 sec. and requiring a total of 2^{24} time steps) on a modest workstation (Intel-i5 3GHz, 32GB RAM) took 108,188 sec. or 86× real time. It is to be noted that the primary source of slowdown relative to the uncoated case, *i.e.* 50× real time, was due to communication between the user-defined function and the main commercial code [91, 116]. On the other hand, the uncoupled simulation required only 7.5 sec. or 0.006× real time. Moreover, the uncoupled method was developed in Python, an open-source language, rather than the coupled simulation which relies on a commercial code. Thus, the uncoupled method could be freely parallelized.

7.2.4 Multilayer Mechanics Analysis

The release of elastic strain energy stored in the coating, which builds up due to thermal stresses, supplies the main driving force for delamination in thermal barrier coating systems. An analytical mechanics methodology was developed to predict coating delamination and was validated for reciprocating engines in Chapters 4 and 6, respectively. The method requires the full multilayer wall temperature distribution during an engine cycle for calculation, and depends on mechanical properties such as elastic modulus, coefficient of thermal expansion, and Poisson ratio. Figure 7.3 shows a thin thermal barrier coating bonded to an aluminum piston substrate. The left surface is exposed to the combustion gases while the right is oil-cooled. The combustion chamber surface temperature may vary anywhere between the intake stroke and combustion extremes, resulting in a wide temperature distribution envelope throughout the engine cycle.

The general methodology to calculate the energy release rate and the equations that estimate each strain energy, are given in Koutsakis *et al.* [135] and Chapter 4.

Earlier discussion, see text of Fig. 4.6, suggested that maximum energy release rates occur at locations within the coating layer; not at the coating-substrate interface. Thus, for this optimization work the energy release rate considered was only that at the mid-coating thickness, identified as the "Crack" in Fig. 7.3.

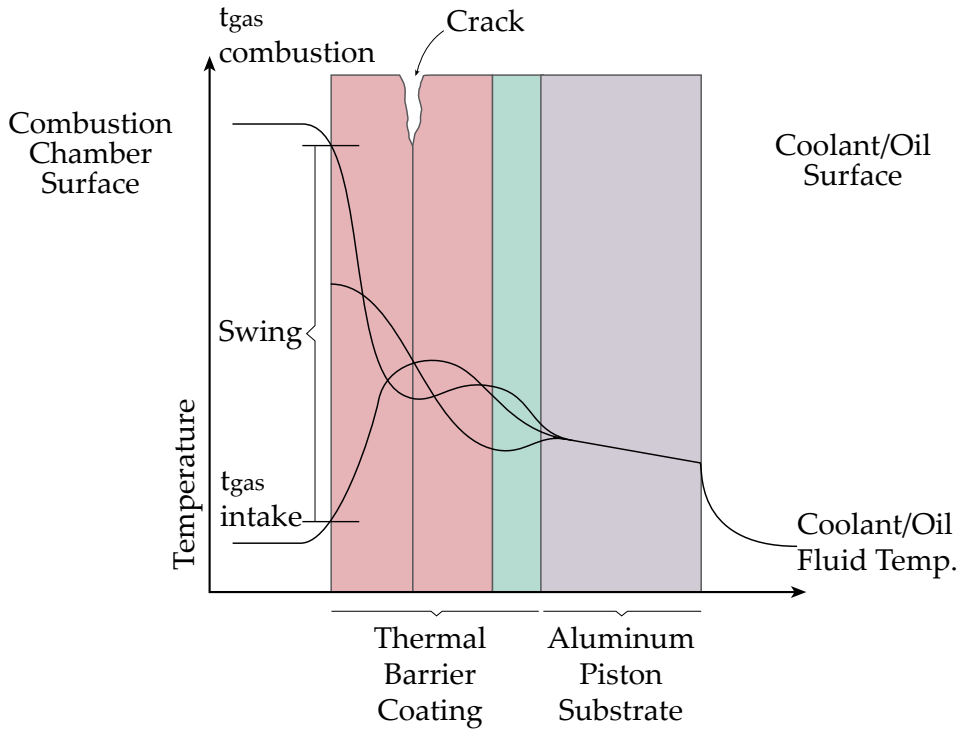

Figure 7.3: Schematic illustration of a thermal barrier coated aluminum piston wall exposed to combustion chamber gases (left) and coolant/oil (right). The wall temperature distribution is illustrated at various different times during the engine cycle, *i.e.* intake, combustion, mid-expansion. A delamination due to crack propagation is illustrated at the mid-coating region.

7.3 Optimization Setup

7.3.1 Mathematical Formulation

Thermal insulation can be exploited for various reasons: to increase engine efficiency and power output by decreasing heat rejection and cooling requirements; to provide thermal protection to the underlying power-cylinder components; or to increase exhaust enthalpy for enhancing conversion efficiency of emission after-treatment components.

This work focuses solely on providing in-cylinder heat insulation to maximizing engine efficiency over a large number of material candidates. The objective is met by minimizing the net in-cylinder heat transfer to the piston while ensuring *i*) the compression ratio remains fixed, *ii*) the coating/piston interface temperature is below the maximum service temperature of the metal, and *iii*) the coating has sufficient structural integrity. The above is achieved by optimizing the thickness of each individual material type.

The mathematical formulation of the proposed optimization problem is described as

$$\underset{\text{MatID,L}}{\text{minimize}} \quad \mathrm{w}_{\text{net}}\Gamma_{\text{net}}+\mathrm{w}_{\text{pumped}}\Gamma_{\text{pumped}} \tag{7.6a}$$

$$\text{subject to} \quad \mathrm{w}_{\text{net}} = 1 - \mathrm{w}_{\text{pumped}}, \tag{7.6b}$$

$$L_{\text{ini}} = \sum L_i, \tag{7.6c}$$

$$t_{\text{sub-int}} \leq t_{\text{max,service}}, \tag{7.6d}$$

$$G \leq G_{\text{max,service}} \tag{7.6e}$$

where the relative net and pumped heat transfer changes, Γ_{net} (defined fully below) and Γ_{pumped}, respectively, are treated as a single objective with corresponding weighting factors w_{net} and $\mathrm{w}_{\text{pumped}}$. The design variables are the material type and thickness, termed matID and L, respectively.

It was shown earlier that the volumetric efficiency penalty when optimizing a piston coating for the given drive cycle was quite small. But, in other instances, *e.g.* insulating the full combustion chamber, using other combustion strategies, or optimizing at specific engine conditions, volumetric efficiency losses may be important to consider. Thus, Γ_{pumped} is included in Eq. (7.6) although in this work w_{pumped} was taken as zero, which results in simply minimizing Γ_{net}. The full expression for the relative reduction in heat loss, Γ_{net}, is

$$\Gamma_{\text{net}} = 100 \times \frac{\left[\int_{\text{Coated}} \dot{q}''_{\text{o,piston}} \, \mathrm{d}\theta - \int_{\text{Uncoated}} \dot{q}''_{\text{o,piston}} \, \mathrm{d}\theta \right] A_{\text{piston}}}{Q_{\text{o,Uncoated}}} \tag{7.7}$$

where the numerator is the difference between the energy lost to the piston between coated and uncoated conditions, and the denominator is, with reference to Eq. (7.1)

$$Q_{\text{o,Uncoated}} = \int_{\text{Uncoated}} \dot{q}_{\text{total}}(\theta) \, \mathrm{d}\theta \tag{7.8}$$

7.4 Computational Approach

The optimization routine was written in Python using the `scipy.optimize.minimize` function from the SciPy[138] library. The selected minimization algorithm utilized a constrained trust-region method. Termination tolerances were set for the norm of the Lagrangian gradient, the change of independent variable and threshold on the barrier parameters were set as 10^{-10}, 10^{-10} and 10^{-4}, respectively. A computational node in a cluster would be given the material ID and would optimize coating thickness based on the given constraints. A demonstration of the full computational process will be given using the wall architecture from Table 7.1 for a 300 μm thickness. First, the heat transfer solution will be discussed followed by the mechanics analysis.

Boundary conditions of the baseline uncoated engine during the full drive cycle are imported, *i.e.* time, heat transfer coefficient, gas temperature, uncoated heat

flux (so that it only is calculated once) and the piston under-side temperature, which was computed using a detailed analysis in GT-Power, see Chapter 5 for the system-level model description. The coating thickness, set by the optimizer, is used to calculate the piston thickness based on the equality constraint (7.6c). The thermal properties, such as thermal conductivity k, specific heat capacity c and density ρ, of the coating material are imported from the materials library and the thermal resistance $R = L/k$ per unit area and capacitance per unit area $C = \rho c L$ are calculated for each layer; these parameters are required for the evaluation of X_o and Y_o. Once the wall functions X_o and Y_o are found from Eq. (3.57), the wall surface temperature is determined using Eq. (3.63), and the process is iterated until a convergence criterion of 0.1% RMS error of peak surface heat flux was met. The metal/coating interface temperature history was calculated in a similar manner, but with slightly different wall functions, X_i and Y_i, see Eq. (3.57) for details. It is worth noting that the wall surface and interface temperatures are evaluated with a single convolution. The maximum interface temperature over the drive cycle was found, and compared against the maximum service temperature of the aluminum substrate, 643 K (370°C), per constraint (7.6d).

Figure 7.4 shows the wall surface temperature (top) and heat flux (bottom) for the baseline and sample coated case over the drive cycle time. The interface temperature of the coated case, shown with red, satisfies the inequality constraint (7.6d). During the early part of the drive cycle the surface temperatures are increasing due to wall heating. The surface temperature for the coated case is significantly higher than for the baseline, which in turn gives significantly lower heat flux.

The coated piston heat flux allows one to evaluate the integrated net and pumped heat transfer rates over the drive cycle. The total (all four pistons) surface area was $A_{\text{piston}} = 0.011937$ m^2, giving the integrals of uncoated and coated piston net heat transfer of $\int_{\text{Uncoated}} \dot{q}''_{\text{o,piston}} A_{\text{piston}} \, \mathrm{d}\theta = 11.8$ MJ and $\int_{\text{Coated}} \dot{q}''_{\text{o,piston}} A_{\text{piston}} \, \mathrm{d}\theta = 8.8$ MJ. The total (head+piston+liner) net heat transfer of the baseline coupled case was imported from GT-Power, $Q_{\text{o,Uncoated}} = 30.35$ MJ. These values give $\Gamma_{\text{net}} = -9.7$ %, *i.e.*, nearly a 10% reduction in cylinder wall heat transfer. Following a similar procedure, one finds the relative pumped heat transfer change as $\Gamma_{\text{pumped}} = 320$ %.

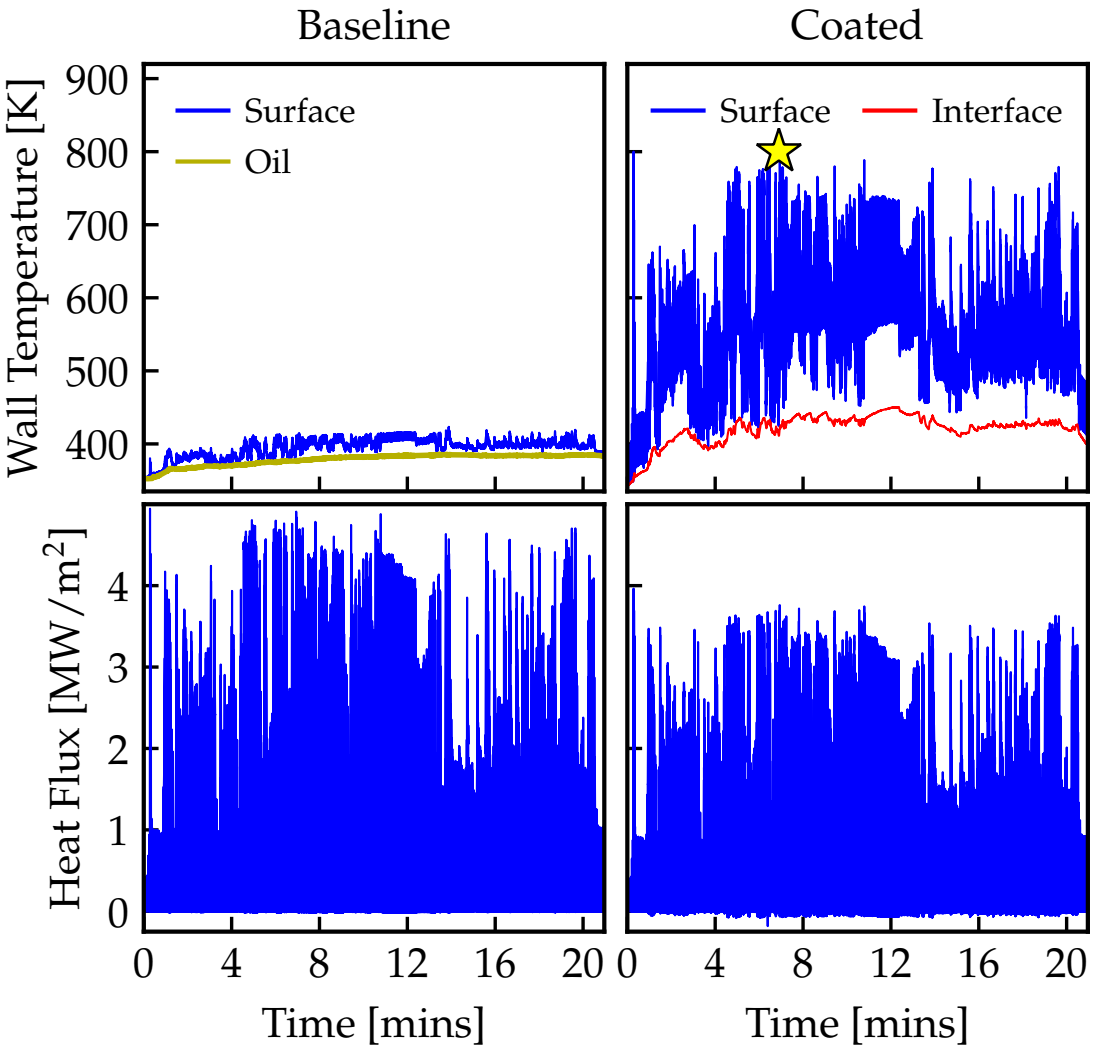

Figure 7.4: Wall temperature (top) and heat flux (bottom) temporal evolution of the baseline and a coated case during the drive cycle. The yellow star highlights the time of maximum surface temperature in the drive cycle.

The durability analysis is the last step before the optimizer decides whether or not this solution is feasible. The mechanics model described earlier in Chapter 4 is called separately because it is too computationally expensive to run at every time step. For all of the scenarios tested, the maximum energy release rate was found to occur on the cycle that had the highest surface temperature (other criteria tested included cycles with the highest heat flux, highest temperature difference between combustion and oil surface, and highest interface temperature). Additionally, previous results indicated that the peak energy release rate was found to occur later in the cycle than the peak surface temperature. Delamination was often located within the coating as compared to at the coating-substrate interface where there was a mismatch in coefficient of thermal expansion, or at the coating surface where the stress was maximum. Such a failure mechanism has been experimentally demonstrated in the modern reciprocating coating literature [67]. Based on results presented in Fig. 4.6, the mechanics analysis was only performed for the central location of the coating during the expansion stroke for the highest piston surface temperature cycle.

The mechanics model discretizes the wall into a finite number of individual layers. Thus, the temperature distribution within the wall is necessary. The analytical method could be used to solve for the entire wall distribution, but that would not be efficient; the main computational advantage is that it only solves at specific locations, *e.g.* the combustion chamber surface.

Figure 7.5 illustrates the procedure to estimate the highest energy release rate in the drive cycle, as described above. The time of the maximum wall surface temperature was found. For this example, this occurs shortly after the 416th second, as shown in Fig. 7.5 (a). A Crank-Nicolson finite difference heat transfer model was used to find the wall temperature distribution. In order to correctly match the initial conditions on the cycle of interest, the finite difference code was started 30 cycles prior to the hottest expansion stroke. An initial condition – based on the analytically derived surface heat flux up to that point of time – was provided to the numerical model. The two methods converge after a few cycles, as can be seen from the absolute difference curve in Fig. 7.5(a) (dotted black). The spatial domain,

comprised of the coating and the piston substrate wall, was linearly discretized with 2^6 and 2^4 nodes, respectively.

The wall temperature distribution was imported together with all the thermo-mechanical properties into the mechanics model to calculate the energy release rate at the mid-coating (green) and coating/piston interface (magenta) locations, see Fig. 7.5 (b). The mechanics model used the same grid spacing as the finite difference heat transfer model. The energy release rate (both at the center and the interface) increases for increasing surface temperature. Figure 7.5 (b) is shown for demonstration purposes only. The actual time period that the mechanics model was enabled during the optimization was from the crank-angle location of the maximum wall surface temperature until the BDC of that cycle. Results for this time period are shown in Fig. 7.5 (c). As the surface temperature decreases, starting from its maximum at about 30°aTDC, the energy release rate at the mid-coating location increases rapidly until reaching a peak at about 80°aTDC.

The maximum energy release rate is stored and used in the inequality constraint (7.6e). If the constraint is violated, the solution becomes non-feasible and the optimization solver attempts to reduce coating thickness until the constraint is satisfied.

Figure 7.6 depicts the trade-off between in-cylinder heat transfer, Γ_{net}, and crack driving force $G_{\max}/G_c$. The former is heat transfer reduction, per Eq. (7.7), while the latter is the ratio of maximum energy release rate and the material toughness. The results shown are derived based on the full drive cycle. As the coating thickness increases the heat transfer decreases but $G_{\max}/G_c$ increases rapidly, indicating the likelihood of a coating failure. The optimizer is minimizing the heat transfer according to the path defined by the dashed lines depicted in Fig. 7.6; it increases the thickness to get the "Best Performance" until reaching $G_{\max}/G_c = 1$, which is defined as "Crack Limit".

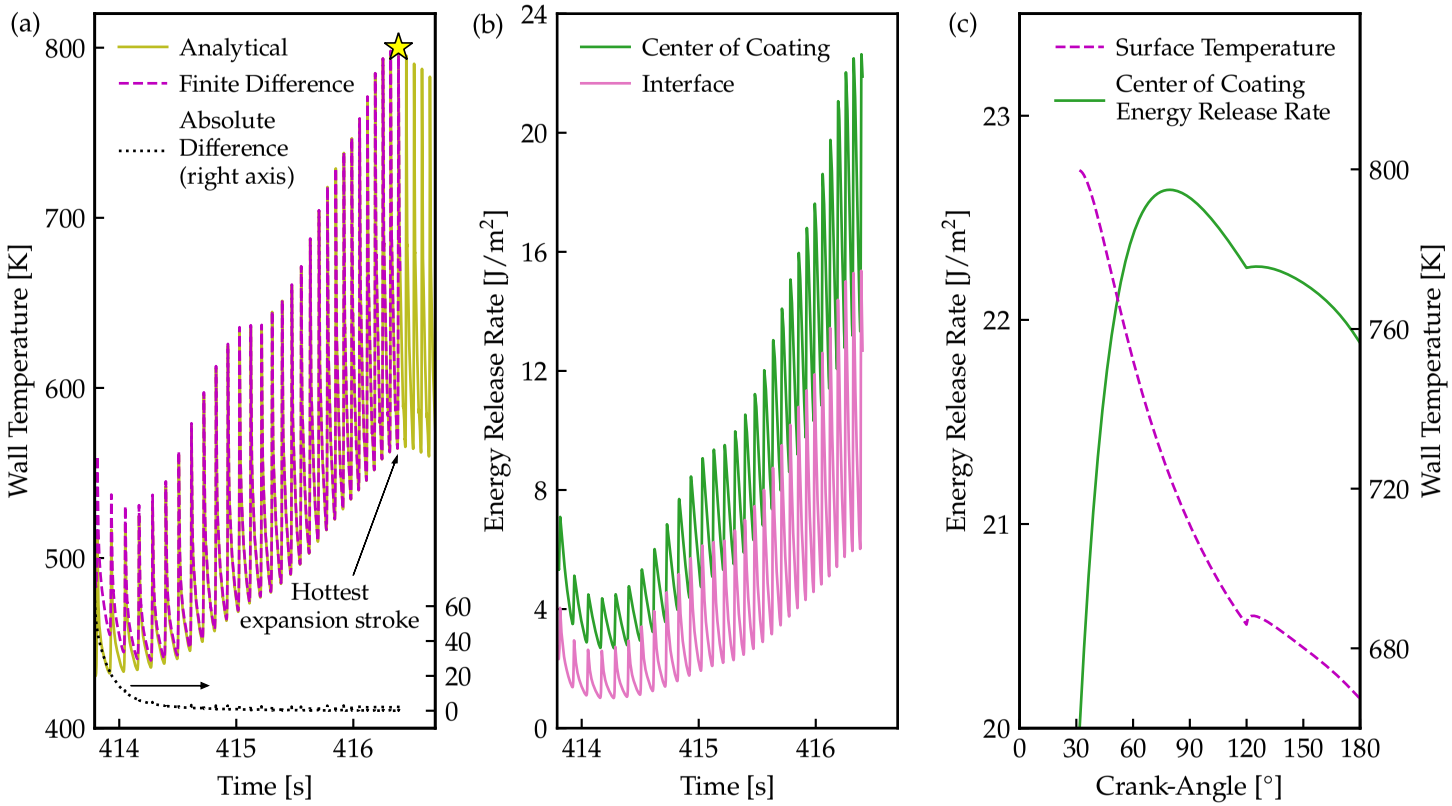

Figure 7.5: (a) Wall surface temperature comparison between the analytical and finite difference method as a function of time prior to the hottest expansion stroke. The yellow star highlights the time of maximum surface temperature in the drive cycle. (b) Mid-coating and interface energy release rate temporal evolution. (c) Surface temperature and mid-coating energy release rate.

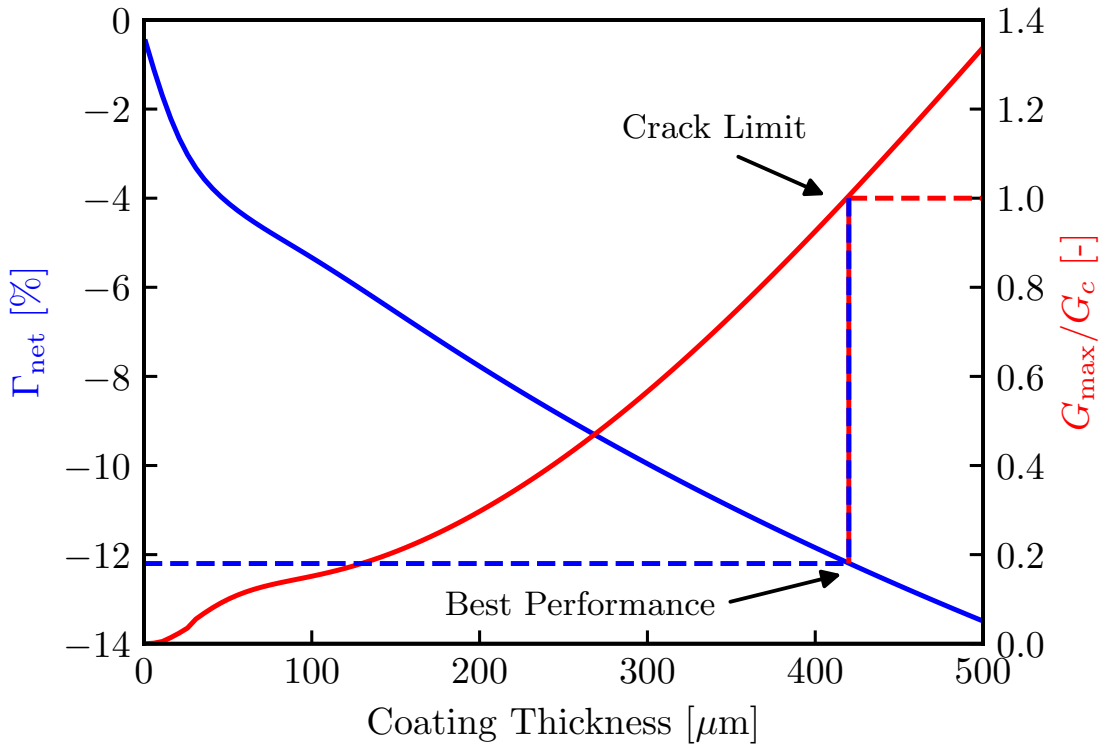

Figure 7.6: Trade-off between in-cylinder heat transfer reduction and maximum energy release rate for various coating thicknesses. Wall architecture thermomechanical properties can be found in Table 7.1.

7.4.1 Distributed Parallelization via High-Throughput Computing

The procedure described above was conducted to optimize the thickness of a single material. Both the material type and thickness were used as design variables in the optimization problem. This hierarchical-type optimization was performed in parallel. The parallel mode was run using the HTCondor scheduling software[139], which offered access to a pool of 2,000-6,000 execution nodes concurrently. A job was created for each material type and the jobs were distributed to all the "workers" around the pool. Each worker optimized the thickness of the given material. A large set of data were provided back to the master computer containing function

outputs of every evaluation including the optimum. A comprehensive list of the main optimization characteristics is provided in Table 7.2.

Table 7.2: Optimization specifications

Number of cycles	20,000
Number of materials	800
Stress-free temperature	473 K (200°C)
Maximum substrate temperature	643 K (370°C)
Lower/upper coating thickness bound	0/500 μm
Maximum mid-coating energy release rate	Parameterized*

* Five optimization scenarios were conducted: unconstrained, 10, 50, 100 J/m^2 and individual material's toughness.

The hierarchical optimization – with material type and thickness as design variables – was performed for five scenarios in total to demonstrate how the coating's structural integrity affects engine heat transfer performance. The scenarios were: mechanically unconstrained, mechanically constrained by energy release rate (three levels of constraint: 10, 50 and 100 J/m^2), and mechanically constrained by the toughness of each individual material.

7.4.2 Materials Library

An in-house materials property library was developed from thermomechanical properties found in the literature. The majority of the properties were collected from ANSYS Granta Selector[124], a commercially available database. All material families were included as long as they satisfied an initial-stage filtering. The data were filtered such that they had a thermal conductivity and maximum service temperature less than 30 W/m-K and greater than 500 K, respectively. This filtering process resulted in 781 potential materials. Another 15 thermal protection system (TPS) materials were also included from the TPSX library [140]. Unfortunately, the modern engine literature has limited thermomechanical property data. Nonetheless, a few extra materials were included based on experimentally measured data[29, 49, 122] via private communication with the authors.

The in-house library contained a total of 800 materials. The data included the matID, material name, material family (ceramic, glass, metal and polymer) thermal conductivity, density, specific heat capacity, Young's elastic modulus, Poisson ratio and toughness.

Figure 7.7, depicts the thermomechanical properties used in this optimization study. Figure 7.7 (a) shows the thermal conductivity versus volumetric heat capacity. Coatings with low thermal conductivity and low volumetric heat capacity have garnered recent interest. Several of the ceramic and glass materials satisfy these criteria, which is primarily achieved with high levels of porosity, *e.g.* aerogels and foams. The metals have the highest conductance and volumetric heat capacities. Polymers tend to have lower thermal conductivity, by at least one order of magnitude, but comparable volumetric heat capacity to that of metals.

Figure 7.7 (b) shows the coefficient of thermal expansion (CTE) against thermal conductivity. Polymers tend to have the highest CTE. Figure 7.7 (c) shows that the Young's modulus is a strong function of density. Figure 7.7 (d) shows toughness (or fracture energy) as a function of material density. Toughness is the ability of a material to absorb energy without fracturing with units of energy per unit area. Metals and polymers have the highest toughness, whereas ceramics and glasses are brittle materials and prone to failure. However, recall that the relevant issue is the energy release rate relative to toughness, not the toughness alone.

The material families that show attractive thermal properties, per Fig. 7.7 (a), are the ones that tend to have undesirable mechanical properties, per Fig. 7.7 (d). This trade-off is the reason why real materials were chosen for this study. An optimization based on just thermal properties can result in an unobtainable solution.

7.5 Optimization Results

Multiple optimization scenarios were performed, see Table 7.2. The rationale was based on the fact that the actual material properties of the *as-sprayed* coatings are

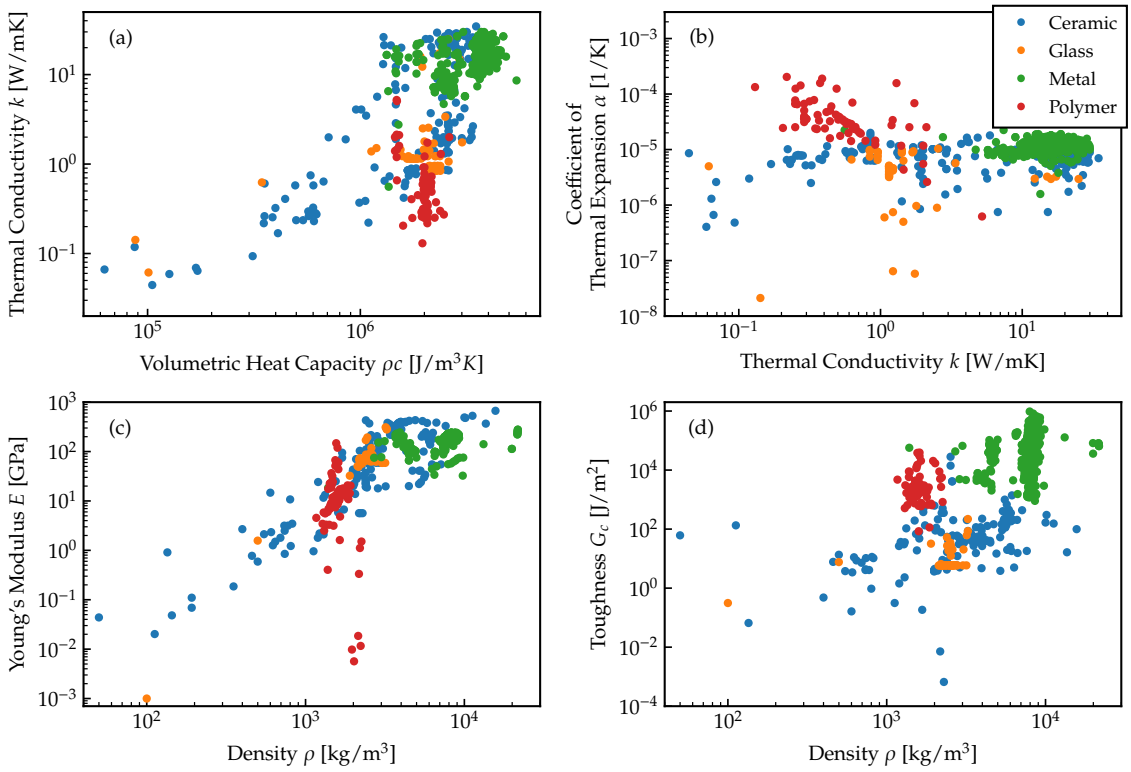

Figure 7.7: In-house thermomechanical property library of material candidates (ceramics, glasses, metals and polymers) used in the optimization study. Various properties are compared including (a) thermal conductivity k and volumetric heat capacity ρc, (b) coefficient of thermal expansion α and thermal conductivity k, (c) Young's modulus E and density ρ, and (d) toughness G_c and density ρ.

manufacturing-process-dependent, and the vast majority of the in-house material property library, discussed above, contained properties of bulk materials.

7.5.1 Engine Heat Transfer Performance

Figures 7.8 thru 7.13, discussed together below, represent the optimization results. Figures 7.8 and 7.10 show optimal heat transfer reduction relative to the baseline for each matID categorized by the material family: ceramics, glasses, metals and polymers. Figures 7.9 and 7.11 show the mechanically constrained results at three

levels of constraint: 10, 50 and 100 J/m^2, and the optimal results constrained by the individual material's toughness, respectively. All the above figures include the unconstrained optimization as reference since it is the best thermal insulation achieved, *i.e.* the thickest possible coating. Each data point represents the optimum for a given matID and toughness constraint. Figure 7.12 directly compares Γ_{net} between the unconstrained and constrained cases.

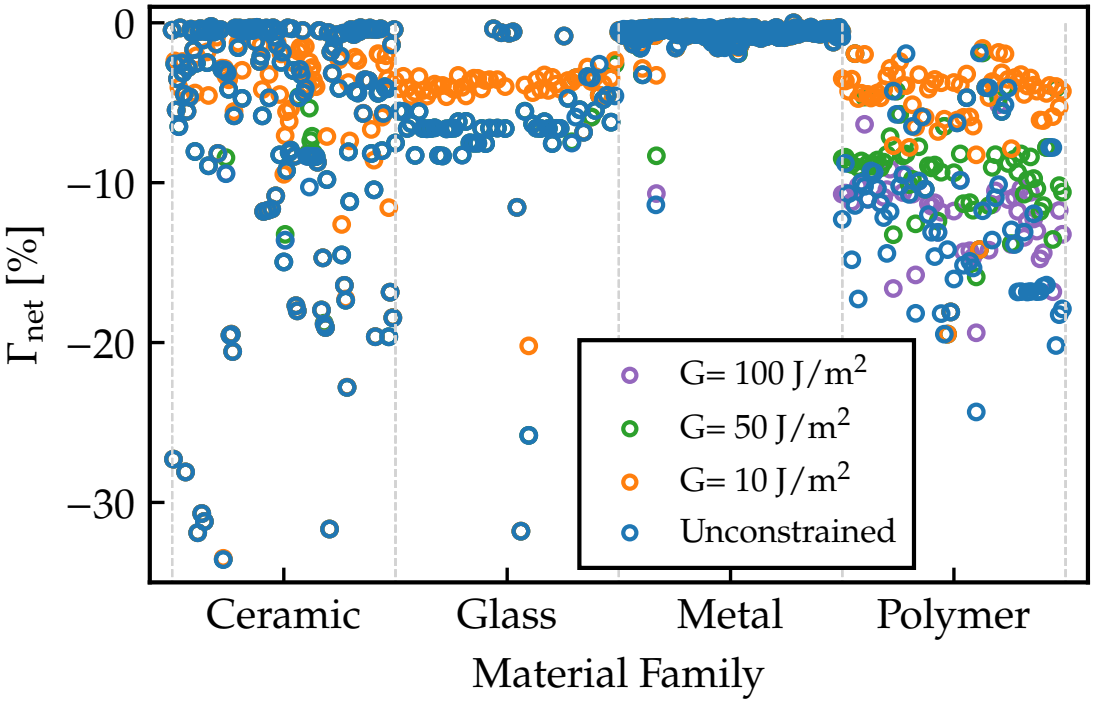

Figure 7.8: In-cylinder heat transfer reduction relative to the baseline, Γ_{net}, classified by material family (ceramics, glasses, metals and polymers) for the mechanical constraints at 10, 50 and 100 J/m^2, and the unconstrained case.

As expected, a number of the ceramics and glasses provide high heat transfer reduction, see Fig. 7.8 and 7.10. Almost all the ceramics with Γ_{net} lower than -10% were not penalized from the energy release rate constraints, see Fig. 7.8 and Fig. 7.12. Surprisingly, some of the materials did get penalized for the toughness-constrained case, as shown in Fig. 7.10. Polymers seem to perform quite well; however the

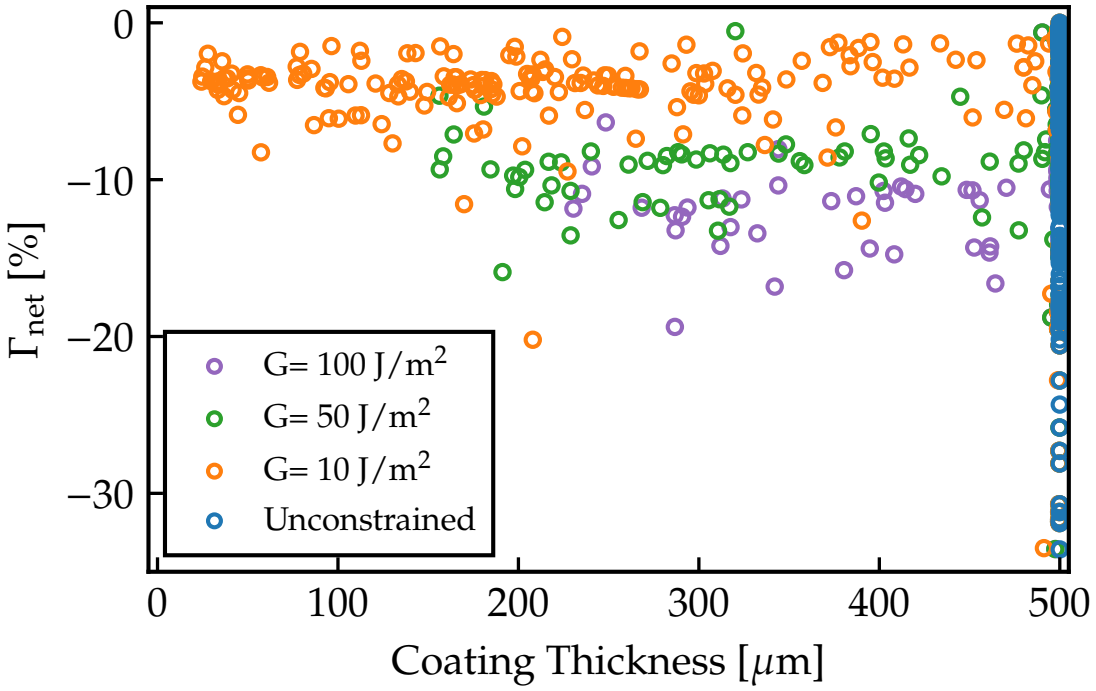

Figure 7.9: In-cylinder heat transfer reduction relative to the baseline, Γ_{net}, as a function of the optimum coating thickness for mechanically constrained cases.

dependence of heat transfer reduction on the mechanical constraint is much more apparent, *i.e.* the polymer optimal points are reasonably more distributed than the other material families in Fig. 7.8.

The optimal thickness of the unconstrained optimization is 500 μm, see Fig. 7.9 and 7.11. Many optimal thickness values are below the upper bound in Fig 7.9 and 7.11. In Fig. 7.9 as the maximum energy release rate limit is reduced the number of cases constrained grows. In addition, the optimal thicknesses of the toughness-constrained case is more distributed along the thickness range, see Fig. 7.11. The distribution of thickness optima is discussed below.

The effect of the energy release rate constraint on the optima can be more clearly illustrated in Fig. 7.12. The constrained versus the unconstrained Γ_{net} are compared for all the optimization scenarios described above. The vast majority of the solutions

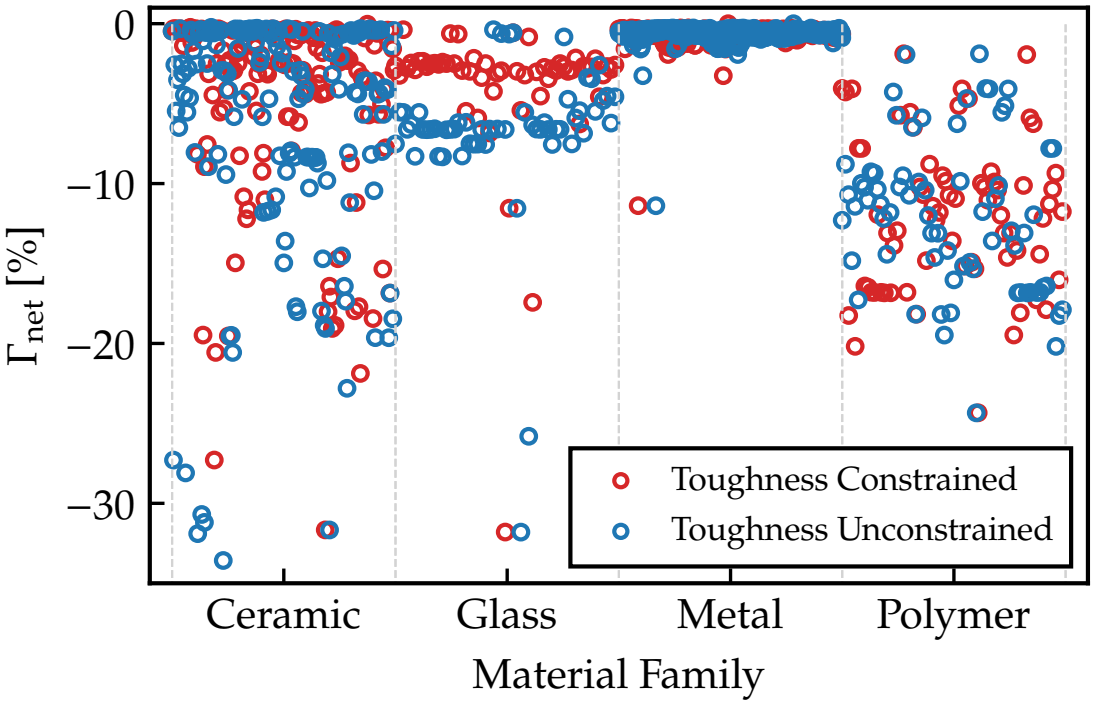

Figure 7.10: In-cylinder heat transfer reduction relative to the baseline, Γ_{net}, classified by material family (ceramics, glasses, metals and polymers) for the mechanically constrained by individual's material toughness case.

lie on the 1:1 line, indicating that these materials were not constrained mechanically or via the interface temperature limit. However, every point that lies above the 1:1 line has been forced to reduce its coating thickness, therefore the heat transfer reduction was lower.

The optimal thickness is illustrated using histograms in Fig. 7.13. The vertical axes of all figures represent the number of counts in a bin that spans thickness; 30 bins were used. The unconstrained case has been removed. In Fig. 7.13, it can be seen that the lowest constraint level case ($10\,J/m^2$) provides the most distributed optimal thickness distribution relative to the other constraints (50 and $100\,J/m^2$). The toughness-constrained optimization also shows high non-uniformity. While the majority of the cases are unaffected, a substantial number of solutions fall

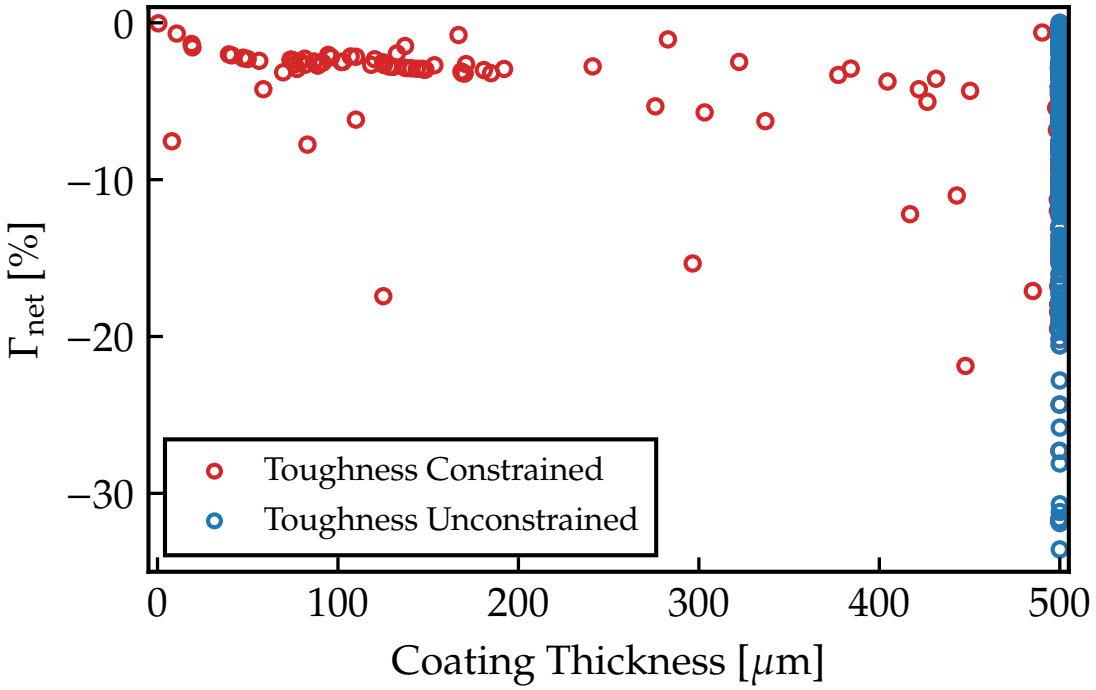

Figure 7.11: In-cylinder heat transfer reduction relative to the baseline, Γ_{net}, as a function of the optimum coating thickness for the toughness-constrained cases.

in the 0-200 μm range. It is worth highlighting that this optimization scenario results in some coatings with almost zero thickness, *i.e.*, they could not handle the thermomechanical loading.

Figure 7.14 shows Γ_{net} with respect to the maximum interface temperature during the drive cycle. It should be noted that the range of maximum interface temperature observed for all candidate materials and optimization scenarios was far below the 643 K (370°C) limit defined in Table 7.2. The maximum interface temperature seen was about 473 K (200°C), indicating that optimal solutions were not penalized from this constraint. The one-to-one relation between the interface temperature and Γ_{net} is easily explained using the heat transfer resistance analogy; the metal piston is effectively at steady state, and the back-side temperature was specified. Including a convective boundary condition could affect the results in Fig.

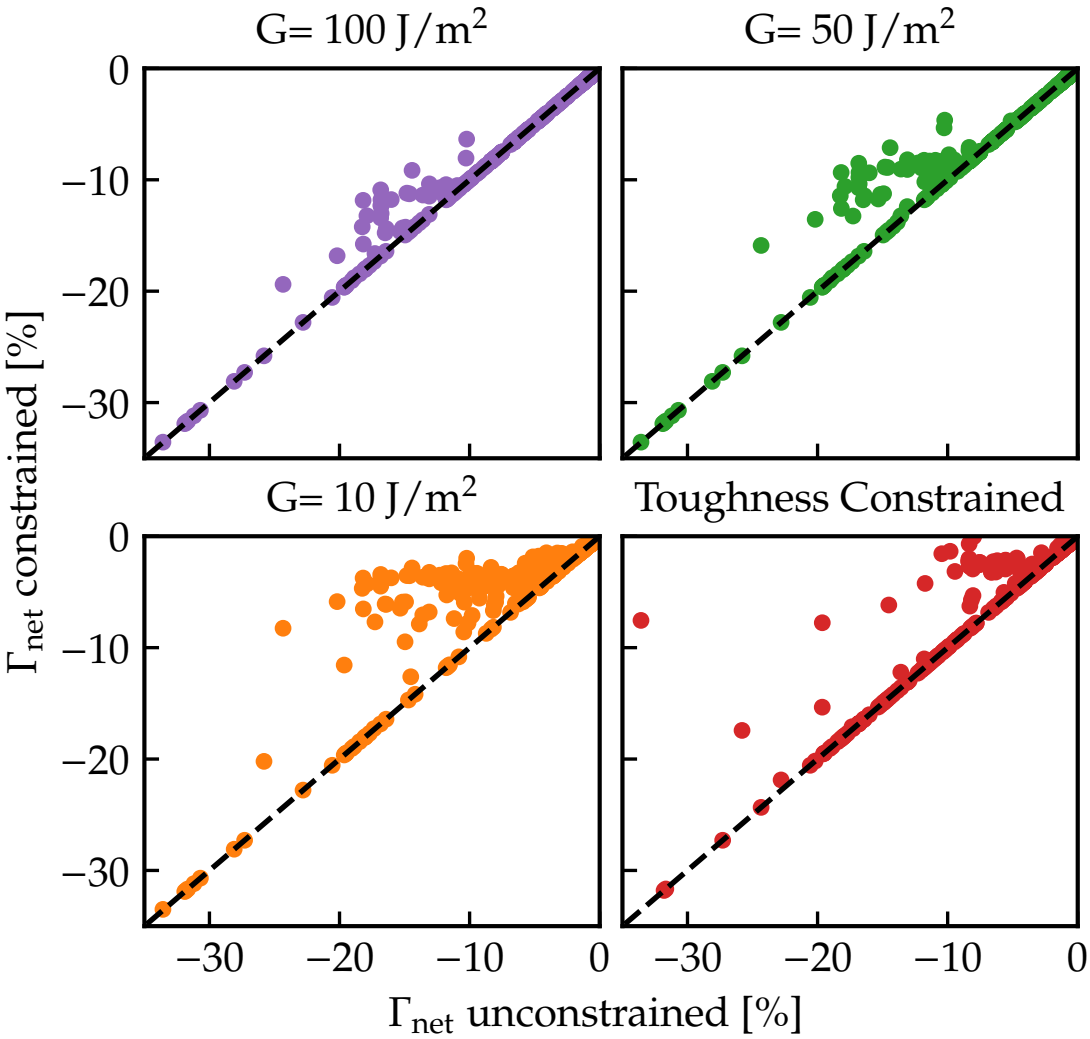

Figure 7.12: Comparison of the constrained versus the unconstrained in-cylinder heat transfer reduction for both mechanically constraints optimization scenarios.

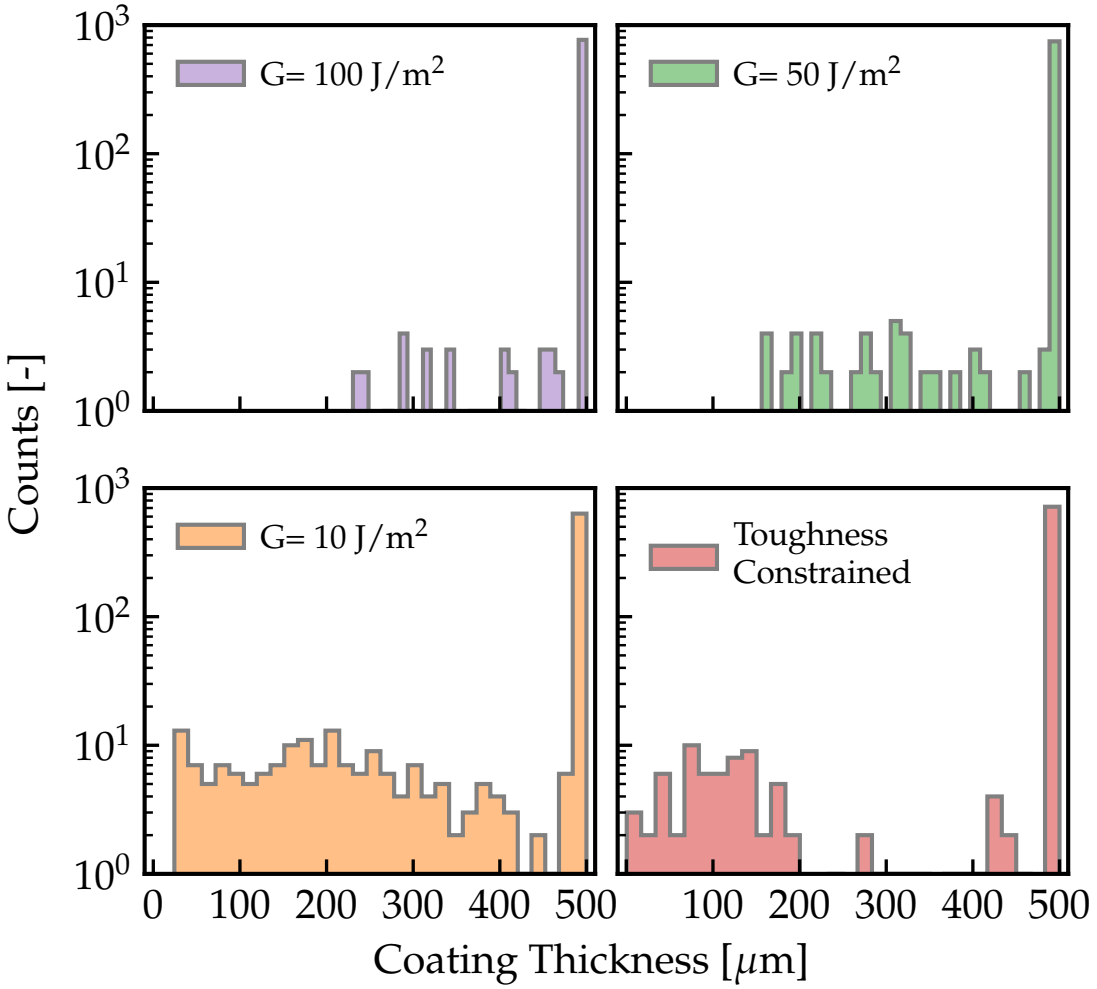

Figure 7.13: Histograms of optimal coating thickness for mechanically constrainted optimization scenarios.

7.14, but it is not expected to affect the ranking of coating materials.

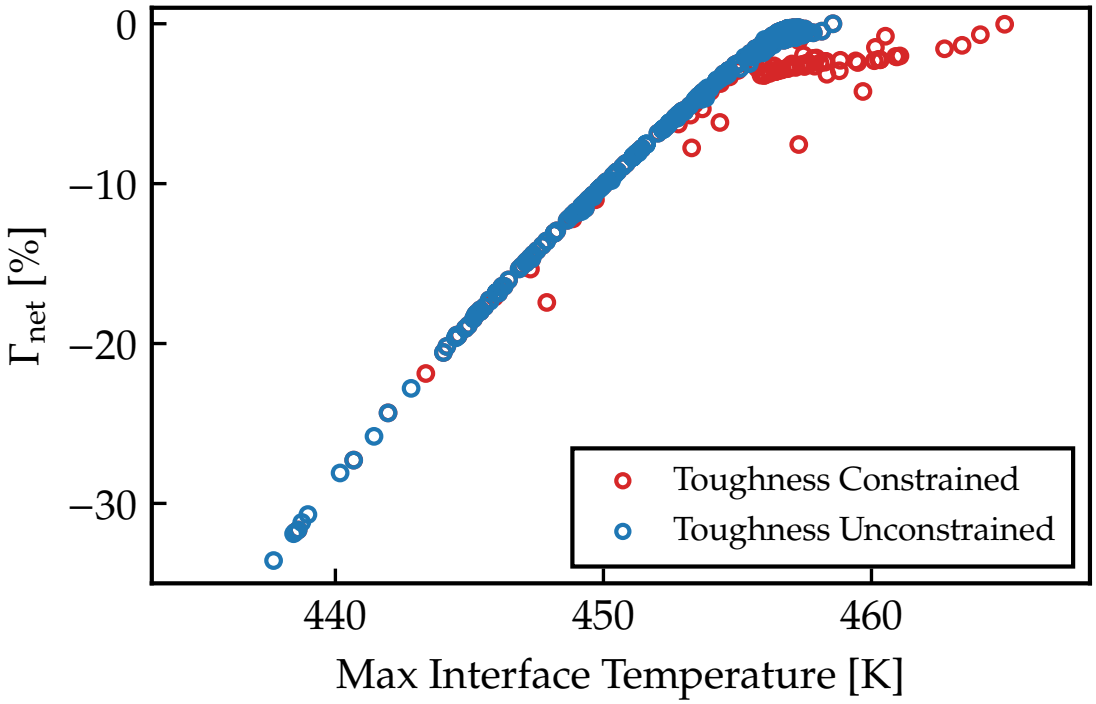

Figure 7.14: Comparison of Γ_{net} with the maximum drive cycle interface temperature for the mechanically constrained by individual's material toughness case (red) and the unconstrained (blue) case.

Figure 7.15 illustrates the trade-off between the engine thermal performance benefit, Γ_{net}, and the engine breathing losses, Γ_{pumped}, when a thermal barrier coating is deposited on the piston surface, see Fig. 7.2. Figure 7.15 shows that Γ_{net} decreases as Γ_{pumped} increases, as expected. Higher in-cylinder heat transfer reduction is accompanied with decreased volumetric efficiency. The differences between the different optimization scenarios are negligible. It is worth noting that in this study the Γ_{pumped} values were simply recorded when the optimum thickness and Γ_{net} were found. In situations where breathing losses are significant, Γ_{pumped} may be included in a single objective function as in Eq. (7.6a) or as a bi-objective optimization.

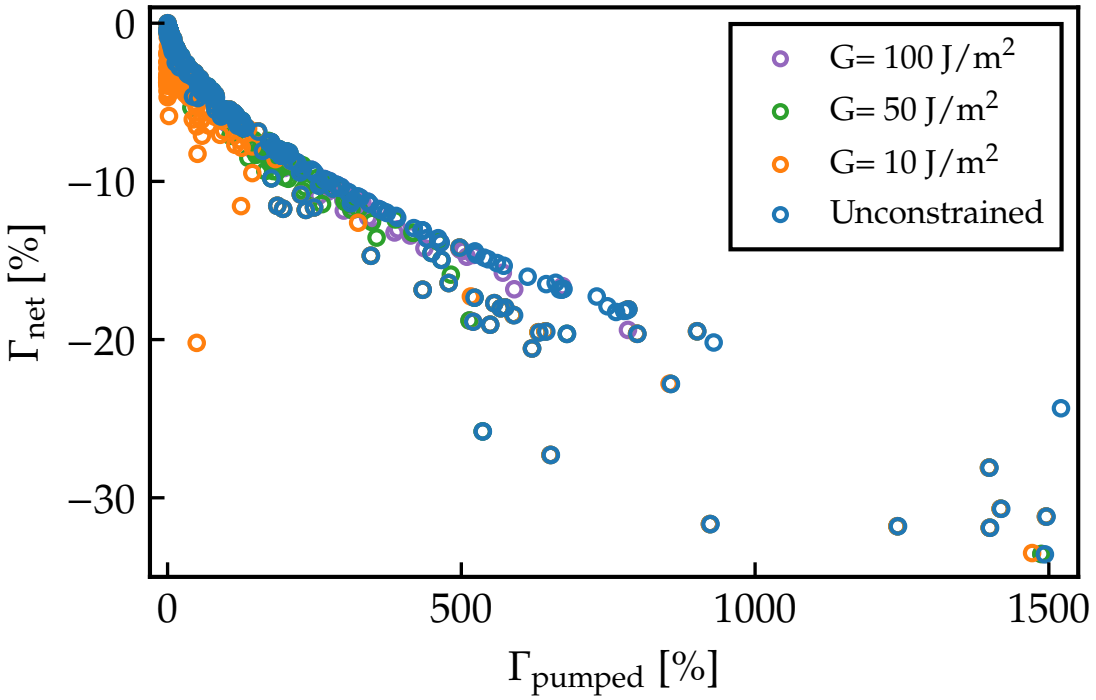

Figure 7.15: Trade-off between net and pumped in-cylinder heat transfer reduction relative to the baseline.

7.5.2 Mechanical Performance

Figures 7.16 and 7.17 show optimal results of the heat transfer reduction as a function of the maximum energy release rate. In Fig. 7.16, the maximum energy release rate is limited by the corresponding level of constraint (10, 50 and 100 J/m^2), while in Fig. 7.17, the maximum energy release rate is limited by the toughness of each individual material candidate. The toughness constraint not only allowed the maximum energy release rates to increase substantially (up to 400 J/m^2), but penalized cases that would have provided exceptional thermal performance but lacked structural integrity.

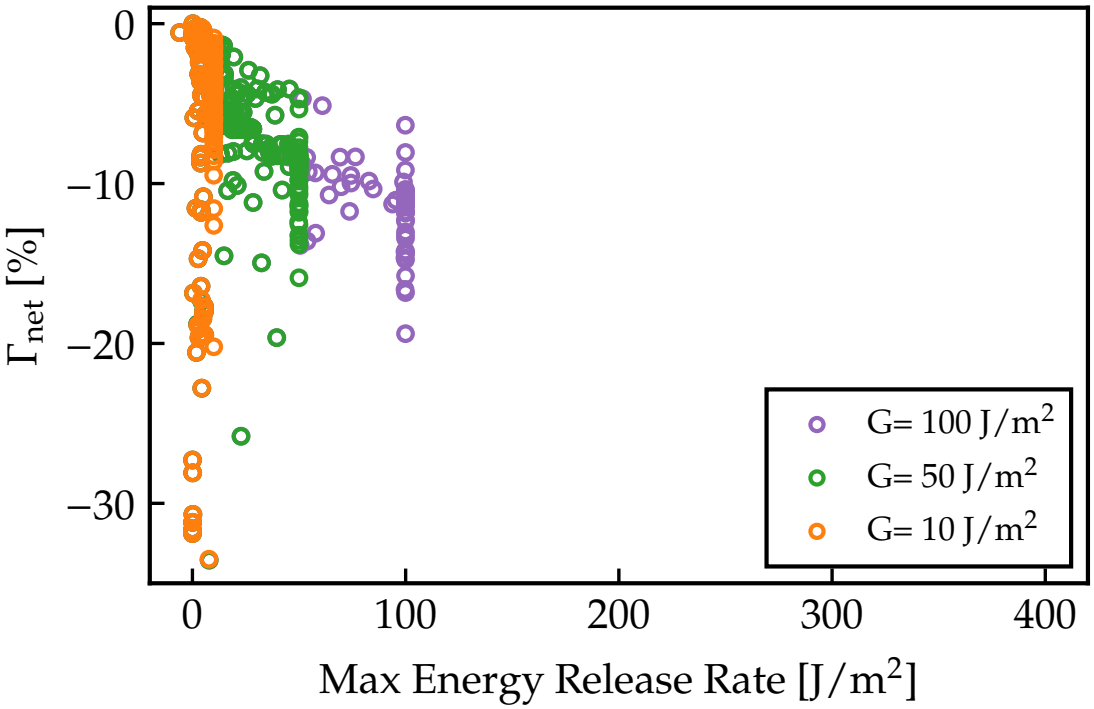

Figure 7.16: Comparison of Γ_{net} with the maximum energy release rate at the mid-coating location for the mechanically constrained by the three energy release rate levels.

7.6 Coupled Engine Simulations Using Best-performing Coatings

The performance of the best coatings identified in the optimization was verified by running the coatings in the fully coupled model. This also allows an *a posteriori* assessment of the uncoupled approach.

Table 7.3 shows the top 10 materials of the uncoupled toughness-constrained optimization ordered by Γ_{net}. Each row represents a material, and the columns contain performance data. As expected, the metals do not appear in this list due to their high density and conductivity, even though they have the highest toughness, see Fig. 7.7 (a) and (d). While it was expected that the majority of the best-

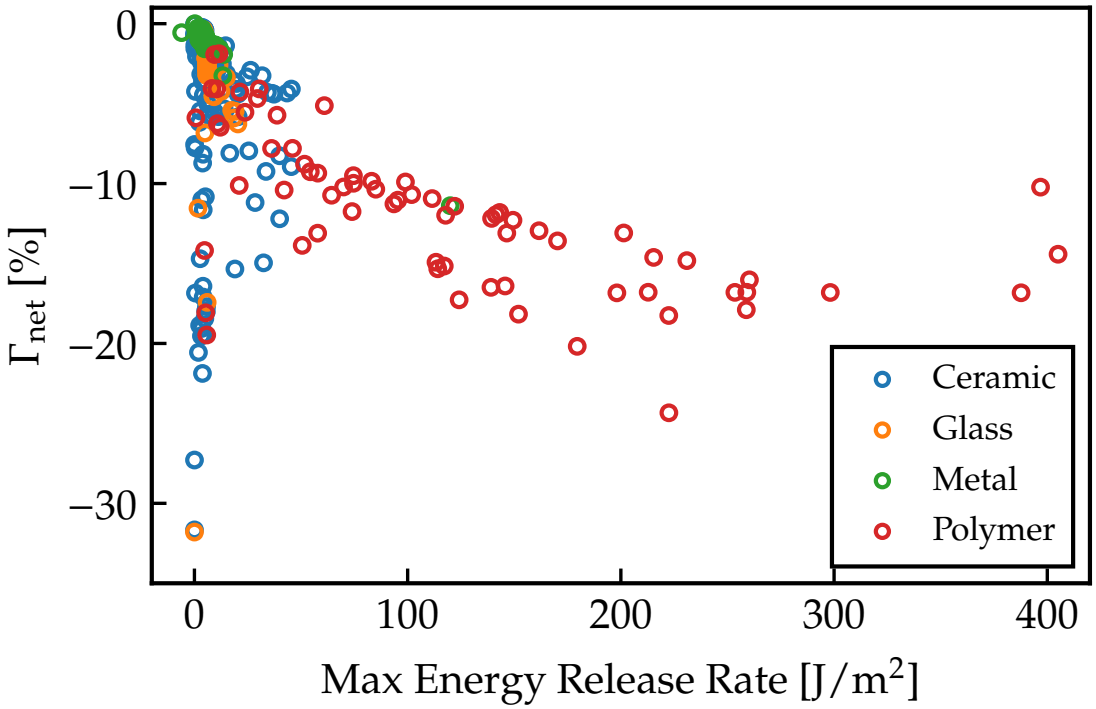

Figure 7.17: Comparison of Γ_{net} with the maximum energy release rate at the mid-coating location for the mechanically constrained by the toughness of each material candidate grouped by material family.

performing materials would be ceramics, three polymers feature in the list, with PI Kapton not only performing well mechanically, but also having good thermal performance. In general, the problem with polymeric materials is their ability to withstand high temperature. It is to be noted that one glass, Silica Aerogel, which was imported to the in-house library from TPSX[140], appears in Table 7.3. The maximum energy release rate for all of these materials, except for brick, was significantly below the toughness constraint.

The material ranking for the other mechanical constraints was different. For example, Glass Foam (0.13) [124] provided the best thermal performance with a Γ_{net} of almost 33.5%, see Fig. 7.8. However, its very low toughness limited the toughness-constrained Γ_{net} to 7.5% and a thickness of just 8 μm.

Table 7.3: Top 10 materials with the corresponding outputs are shown for the mechanically constrained by toughness optimization.

Material	Γ_{net} [%]	Thickness [μm]	Max ERR [J/m^2]	Toughness [J/m^2]	Material Family [–]
Silica Aerogel	-31.8	500	0.0033	0.313	Glass
Carbon foam	-31.7	500	0.03	61.5	Ceramic
Graphite foam	-27.3	500	0.03	134	Ceramic
PI Kapton	-24.3	500	222	5790	Polymer
Brick	-21.9	448	3.767	3.77	Ceramic
Mullite foam	-20.6	500	1.88	7.75	Ceramic
PEEK (30% Glass fiber)	-20.2	500	179	4340	Polymer
Perfluoro elastomer (FFKM)	-19.5	500	5.7	17000	Polymer
Zirconia magnesia foam	-19.1	500	3.5	11.4	Ceramic
Zirconia calcia foam	-18.9	500	2.4	15.5	Ceramic

Figure 7.18 shows the relative changes in integrated fuel mass, in-cylinder heat transfer, exhaust loss, and other losses obtained from the fully coupled simulation for the top five materials. The term "Other" is attributed to any other energy pathway *e.g.*, heat transfer to EGR cooler, charge air cooler, heat rejection to coolant/oil in the cylinder head, and heat transfer to surroundings from the block/manifolds/-turbine/pipes. For further details on how the cumulative energies are defined, see Chapter 5.

Note that the brake power remained fixed for all the cases modeled. First, it is important to highlight that the heat transfer results of the uncoupled and the coupled simulations, the latter shown as yellow triangles, are internally consistent with the materials rankings. This provides *a posteriori* validation that the uncoupled approach was valid for optimization.

The Silica Aerogel provided the maximum heat transfer reduction, almost 34.3 %, but the Carbon Foam provided a slightly larger fuel mass savings, almost 4.6 %, which is approximately 150 gr over the drive cycle. The fuel consumption benefit is accompanied by an increase in exhaust losses. It is worth noting that PI Kapton resulted in slightly higher exhaust loss than the Silica Aerogel, even though their thermomechanical properties and thermodynamic engine performance were

significantly different. The increase of exhaust losses may be advantageous for after-treatment strategies.

The PI Kapton and Brick gave equal fuel savings, however, PI Kapton performs better in terms of heat transfer reduction and exhaust losses. The exhaust losses and Other losses strongly correlate.

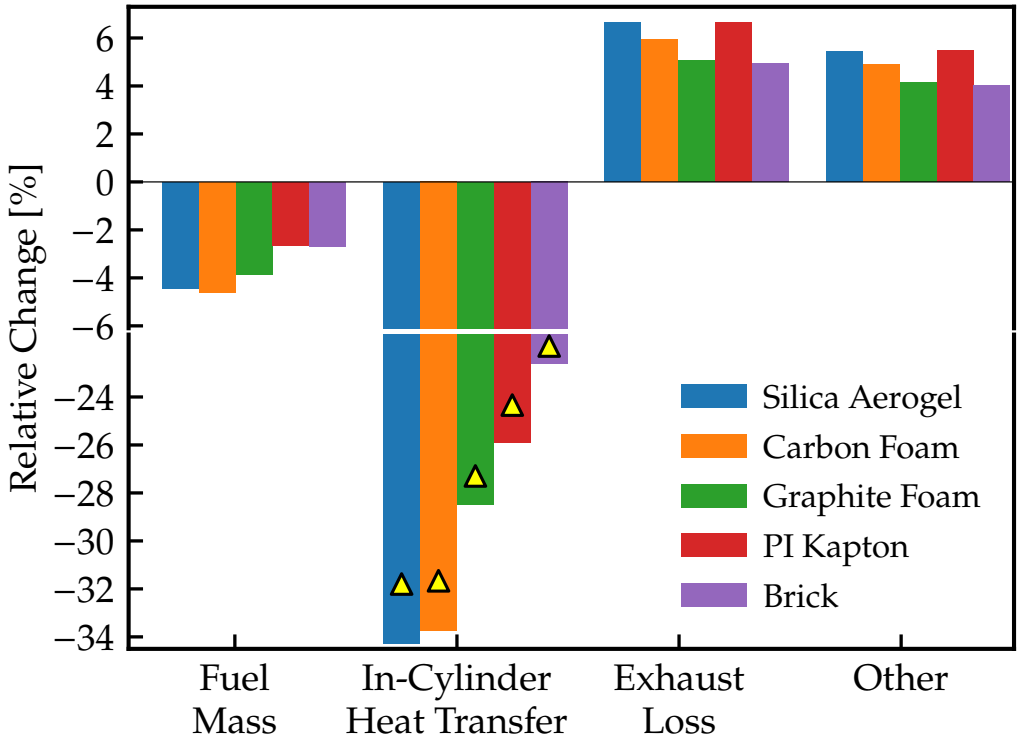

Figure 7.18: Relative changes of fuel mass and cumulative drive cycle energies for the top 5 piston coatings. The yellow triangles indicate the uncoupled toughness-constrained Γ_{net}.

Figure 7.19 compares some thermodynamic parameters with the Brake Specific Fuel Consumption (BSFC) for the top ten coatings. The data are represented as changes relative to the baseline, shown as the black dot. Figure 7.19 (a) shows that Γ_{net} correlates directly with BSFC. Figure 7.19 (b) shows that the drive-cycle-

mean turbine outlet temperature, $t_{\text{turb,out}} - t_{\text{turb,out,base}}$, is increased for decreasing BSFC. The thermal energy saved cannot be fully converted into brake work; a significant portion ends up as exhaust enthalpy. This temperature difference is directly proportional to the exhaust enthalpy relative losses shown earlier in Fig. 7.18. Using Silica Aerogel coating, the turbine outlet temperature can be increased, by almost 20 K over the drive cycle, which is significant considering that it occurs simultaneously with an almost 4.5% fuel mass saving. Finally, Fig. 7.19 (c) shows the volumetric efficiency penalties. In general, the correlation of the volumetric efficiency with the BSFC is not as linear as the previous metrics. Surprisingly, the PI Kapton, which has modest heat transfer benefits among the top-ten coatings, had the highest volumetric efficiency reduction reaching almost a 2% relative difference. The absolute magnitude of volumetric efficiency penalty is low.

Diesel fuel may be trapped in and gas may permeate into a porous coating, resulting in deterioration of engine performance and emissions. A potential solution is to seal the combustion surface by encapsulating the porous thermal barrier coating. An extra 5 μm layer of Silica (96%)[124] was added on top of the best coating of each material family shown in Table 7.3. The objective of this investigation was to evaluate the system-level engine thermodynamic effect of a thermal barrier coating system that includes a sealing layer. Figure 7.20 shows a comparison of the drive-cycle-mean turbine outlet temperature and the BSFC reduction for cases with (squares) and without (circles) the sealing layer. The cases with the sealing layer showed slightly increased exhaust temperatures and a penalty in fuel savings as compared to the cases without the sealing layer.

7.7 Frequency Response Characterization of Various Architectures

The following discussion is a derivative of Section 3.2.8 which investigated the surface response X_o in the frequency domain and revealed complementary information about coating performance.

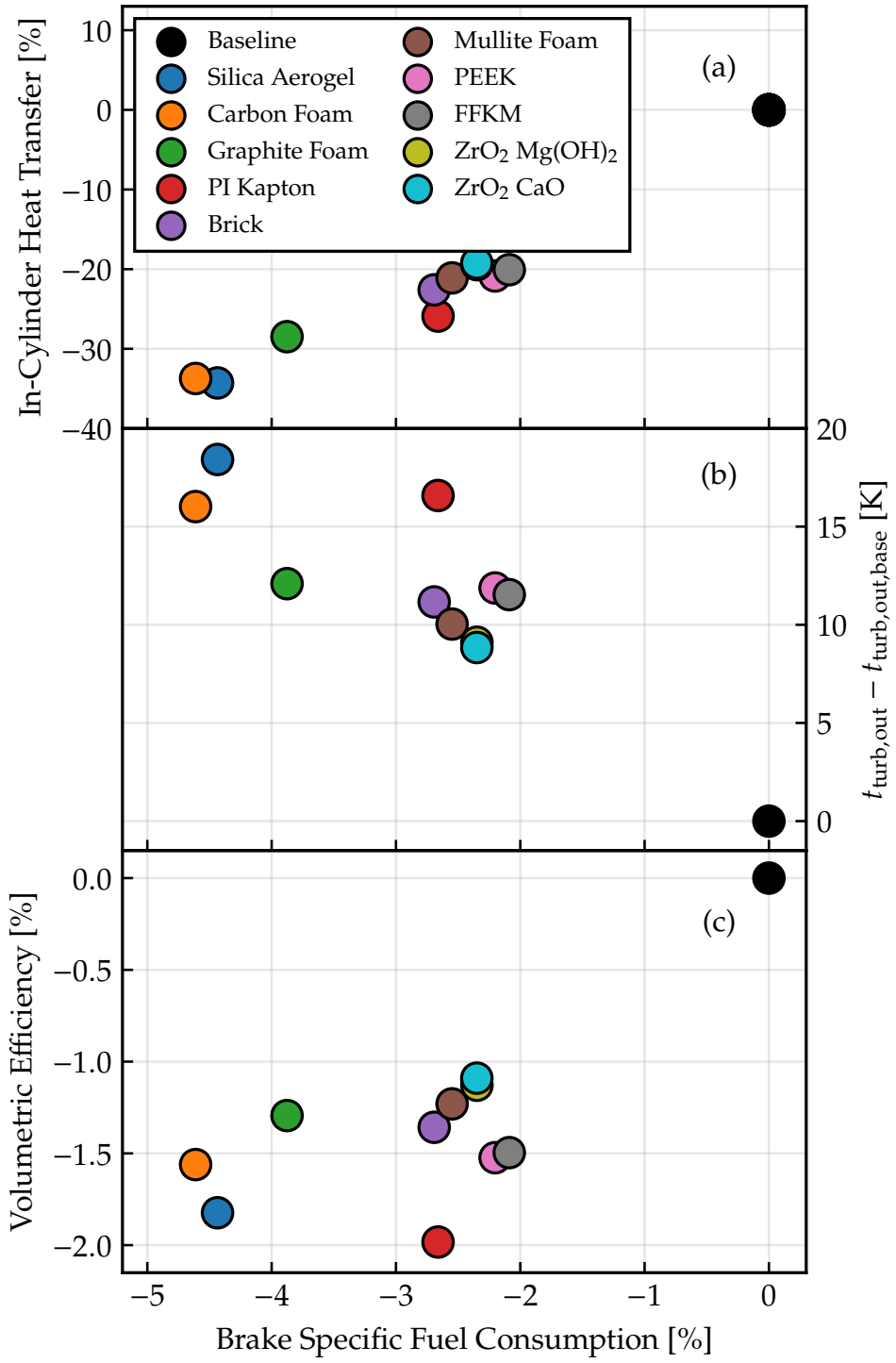

Figure 7.19: Comparison of (a) in-cylinder heat transfer, (b) drive-cycle-mean turbine outlet temperature, and (c) drive-cycle-mean volumetric efficiency with brake specific fuel consumption. All data are relative to the baseline.

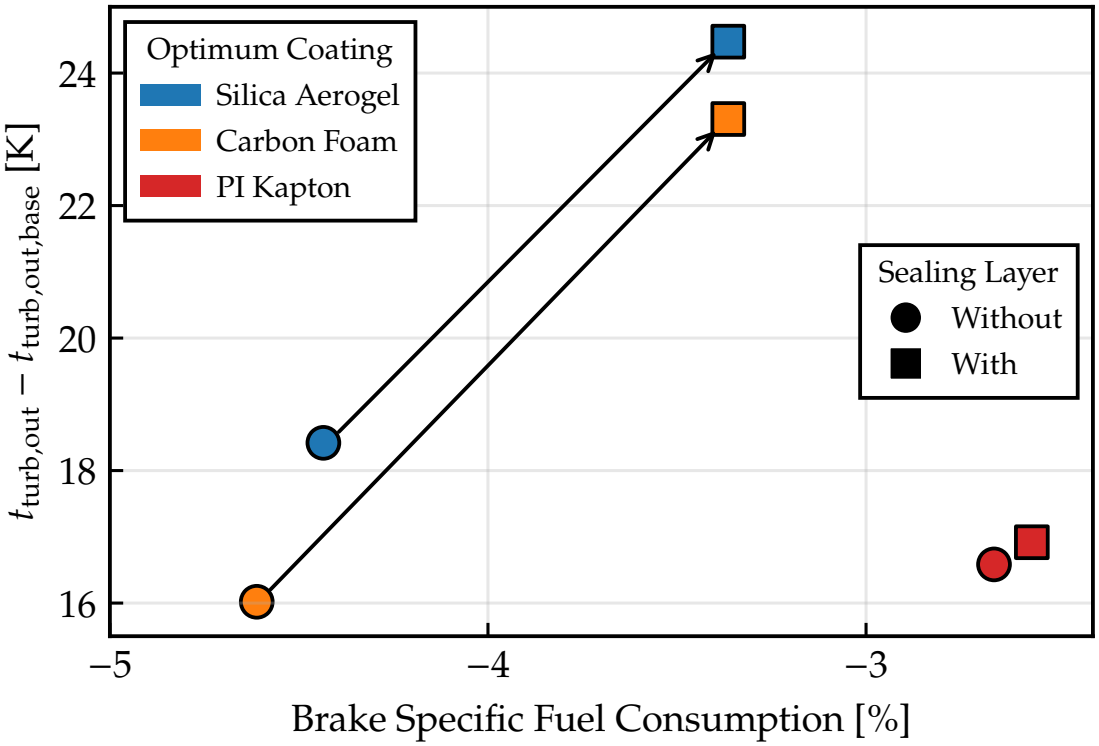

Figure 7.20: Comparison of the drive-cycle-mean turbine outlet temperature difference with the relative BSFC between coated and baseline. The coated cases were evaluated without (circles) and with (squares) a sealing layer.

Figure 7.21 compares a number of coatings in the frequency domain. The different colors represent coating architecture, and correspond roughly to periods of reciprocating engine coatings research. Engine performance is improved by coatings capable of delivering *i*) higher insulation ability at steady response, and *ii*) increased surface temperature swings at high frequencies. Thus, curves in the upper righthand corner represent the best performance.

Thermal properties for all the coatings in Fig. 7.21 are given in Table 7.4. The blue curve represents an aluminum baseline, which was used as the substrate for all the cases except #1 and #2. The orange family of curves (#1-4) represent single- and multi-layer monolithic ceramic engine walls (#1 and #2), air-gapped pistons

(#3), and thick thermal barrier coatings adapted from the gas-turbine industry (#4), which were investigated during the 1980s and 1990s. The green family of curves (#5-8) represent modern coatings, demonstrated during the 2010s, using alternative materials with lower volumetric heat capacity. The red curves (#9-10) represent two potential coating materials (silica aerogel and carbon foam) that emerged from a large-scale thermo-mechanical optimization. It is worth emphasizing that there is more than an order of magnitude opportunity for improvement, both in the low- and high-frequency regions, possible based on the optimization results. These materials have yet to be applied in a real-world application, and may not ultimately succeed in the engine environment, but this study outlines the potential that exists for improvement under the constraint of using real materials.

7.8 Conclusions

A constrained hierarchical optimization was performed to mininize heat transfer of a medium-duty diesel engine using multilayer-coated pistons subject to a structural integrity constraint. The output revealed the optimal materials and their corresponding thickness for a real-world drive cycle. Over eight hundred materials were investigated, and the optimization required more than one million evaluations of the non-road transient drive cycle. Only real materials were tested to ensure a realizable result and the existence of the thermal and mechanical properties. The material properties were acquired either from the literature or from commercial software packages. This study elucidates the importance of including mechanical considerations in the design of thermal barrier coatings.

A calibrated system-level model was used to provide boundary conditions to the uncoupled optimization. The uncoupled in-cylinder heat transfer reduction, Γ_{net}, closely followed the coupled value in an *a posteriori* comparison. The analytical solution methodology substantially increased the computational efficiency, allowing a wide array of materials to be tested over a full drive cycle calculation. Durability considerations were found to be important for coating design. The highest energy release rates were found in the mid-coating area during the cycle with

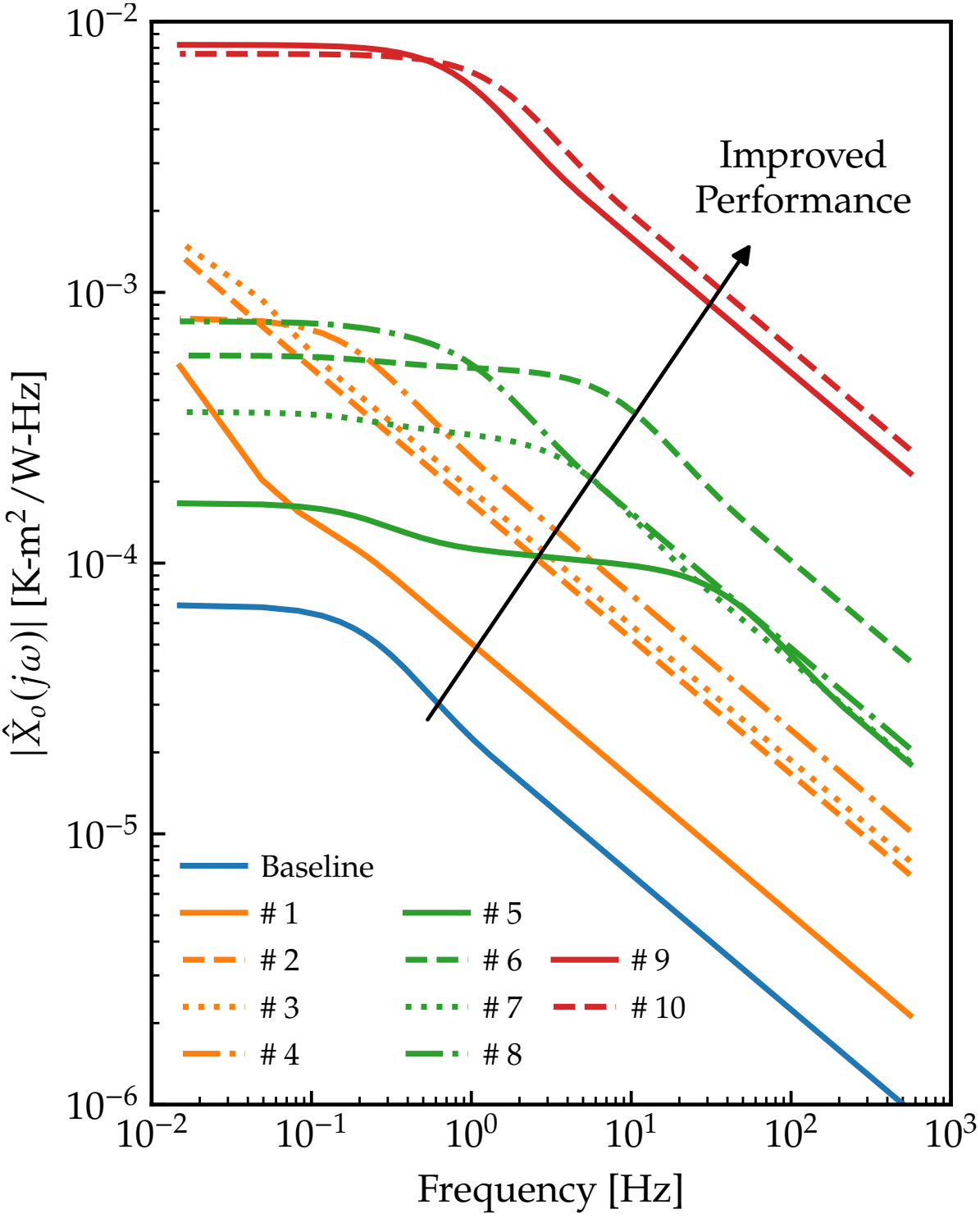

Figure 7.21: Surface response, X_o, for various coatings from the reciprocating engine literature. Table 7.4 gives properties of each coating and their original references. The arrow indicates the direction of the improved performance. The baseline, historic, modern and advanced walls are shown in blue, orange, green, and red, respectively.

Table 7.4: Thermal properties of wall architectures investigated, with k: thermal conductivity, ρ: density, c: specific heat capacity, and L: thickness

Wall	Layer	k [W/m-K]	$\rho c \times 10^{-6}$ [J/m^3-K]	L [μm]
Baseline	Aluminum	123	2.56	8600
#1, ref. [141]	PSZ	2.5	2.3	10000
#2, ref. [142]	PSZ	0.97	2.81	650
	MCrAlY	2.1	4.93	50
	Ti	13.5	2.6	250
	Braze	24.5	5.22	50
	Si3N4	22.5	2.22	2000
#3, ref. [8]	Nimonic 80A	15.25	4.11	5000
	Air-gap	0.044	0	2000
	Aluminum	123	2.56	5000
#4, ref. [143]	PSZ	0.67	1.3	65
	Aluminum	123	2.56	6600
#5, ref. [122]	Sample E	0.42	1.6	300
	Aluminum	123	2.56	8300
#6, ref. [144]	SPC	0.31	0.49	160
	Aluminum	123	2.56	8440
#7, ref. [29]	GdZr-SP	0.65	1.3	180
	NiCoCrAlY	4.2	3.08	70
	Aluminum	123	2.56	8350
#8, ref. [31, 32, 34]	SiRPA	0.67	1.3	65
	Aluminum	123	2.56	8535
#9, ref. [145]	Silica Aerogel	0.061	0.1	500
	Aluminum	123	2.56	8100
#10, ref. [145]	Carbon Foam	0.066	0.063	5000
	Aluminum	123	2.56	8100

the highest instantaneous surface temperature of the transient drive cycle. At this time, the surface was cooling while the rest of the interior wall was still undergoing heating. A trade-off between the in-cylinder heat transfer reduction and the coating structural integrity was quantified.

In this study, the maximum piston-coating interface temperature was significantly below the service limit and did not penalize the optimal coating thickness. The mechanically unconstrained scenario gave rise to the trivial solution, *i.e.*, the best thermal insulation was achieved with the thickest possible coating. However, the mechanical toughness constraint impacted a significant number of material candidates. Ceramics and glasses with outstanding thermal properties were penalized for having maximum energy release rate higher than their limit. The polymers had intermediate engine thermal insulation performance with small penalties due to the mechanical constraint. The metals had the poorest thermal insulation properties with the best mechanical properties. A trade-off between the net and pumped heat transfer was realized from the optimization results. Reduced levels of net heat transfer were accompanied by higher pumped heat transfer. The volumetric efficiency penalty was only up to 2 % over the drive cycle.

The ten highest-performing coating materials identified via uncoupled optimization were tested using a fully coupled system-level simulation. The uncoupled and coupled net heat transfer reduction showed good agreement. The optimal coatings gave significant heat transfer reduction, which led to fuel savings. The exhaust enthalpy, for the example of the Carbon Foam, was found to increase by almost 6 % in spite of 4 % less fuel being used during the drive cycle. These coatings provided a range of relative fuel savings benefit from 2 % to 5 %.

The thermal penalty of an extra sealing layer to prevent air/fuel migration in a porous coating was investigated. A sealing layer on a thermal barrier coating system may penalize the fuel consumption gains and increase exhaust temperature.

Finally, a comparison between various coating architectures from the reciprocating engine literature showed the improvement in thermal performance of coatings with development time, and highlighted the potential for future improvements.

8 SUMMARY AND RECOMMENDATIONS

8.1 Summary

An analytical unsteady heat conduction solution for multilayer walls was developed under the assumption of one-dimensional heat flow and constant thermal properties. Time-varying heat flux and temperature boundary conditions were applied to the domain. This framework outperforms significantly prior state of the art, both in terms of computational efficiency and accuracy. It can substantially accelerate the engine heat insulation design phase. This method only computes the output of interest, the surface temperature, but can easily be adapted to find the temperature at other locations, too. The mathematical formulation utilized matrix algebra as well as calculation of inverse Laplace transforms with the residue theorem from complex analysis. The resulting transfer functions describe the exact heat transfer response and only depend on material properties and geometry, therefore, they can be computed *a priori*. The surface temperature at a given time is found by convolving the heat flux or temperature histories with the appropriate response functions. As compared to finite-difference schemes, the analytical nature of the solution requires no spatial discretization and the accuracy is guaranteed. Applying this method to long time-records, *i.e.* full drive cycles, the computational times were up to four orders of magnitude shorter than its finite difference counterpart. The full analytical solution of a two-layer wall, *i.e.* coating and substrate, where $(k\rho c)_{\text{coating}} \ll (k\rho c)_{\text{substrate}}$, provided the impetus for defining a set of non-dimensional parameters that characterize uniquely the surface temperature swing for arbitrary periodic heat flux. The non-dimensional parameters encompass the controlling physics and can be used to find thermodynamically equivalent materials suitable for conjugate heat transfer engine thermal performance simulations. A coupling between the method to predict surface wall temperature of multilayer engine walls and a commercial, system-level simulation software package was demonstrated. Experimental boundary conditions along with calibration data from a production multi-cylinder diesel engine were provided and used to simulate

engine performance with coated components. Compared to an uncoated baseline, the in-cylinder heat transfer and fuel consumption were reduced, which provided a corresponding reduction in brake specific CO_2. Specific conclusions pertaining the heat conduction method and the system-level performance work can be found in Chapters 3 and 5, respectively.

A coating delamination framework was developed for multilayer reciprocating combustion engine coatings. The fracture theory was adopted from well-established techniques. The method evaluated transient energy release rates assuming equi-biaxial stress followed by plane strain after delamination. The peak energy release rate did not always coincide with the coating-substrate interface. Under the most severe thermal conditions the location was found to lie within the coating, suggesting that the coating may begin to fail via spalling rather than pealing off the substrate. The peak energy release rate was found to occur at a time in the expansion stroke significantly later than the time the peak surface temperature and stress were observed. At this time the surface cools down, but a significant fraction of the coating is still undergoing heating. The mechanics durability model was applied to investigate several thermal-barrier-coated pistons that had been tested in a high-output, single-cylinder diesel engine. The model was found to provide good trendwise comparison with the post-run coating integrity observations. Coatings with maximum energy release rate that exceeded the toughness significantly failed; those with maximum energy release rate significantly below the material toughness survived. Specific conclusions pertaining the fracture mechanics technique and the engine delamination failure experimental work can be found in Chapters 4 and 6, respectively.

An optimization was performed to mininize heat transfer of a medium-duty diesel engine using two-layer coated pistons subject to a structural integrity constraint. The output uncovered the optimum coating materials and their thickness for a real-world driving scenario. Over eight hundred real materials were investigated, and the optimization required more than one million evaluations of the non-road transient drive cycle. Only real materials were tested to ensure a realizable result and the existence of the thermal and mechanical properties. The material properties

were acquired either from the literature or from commercial software packages. This study elucidates the importance of including mechanical considerations in the design of thermal barrier coatings. The mechanically unconstrained scenario gave rise to the trivial solution, *i.e.*, the best thermal insulation was achieved with the thickest possible coating. However, the mechanical toughness constraint impacted a significant number of material candidates. The ten highest-performing coating materials identified via the uncoupled optimization were tested using the fully coupled system-level simulation. The optimal coatings gave significant heat transfer reduction, which led to fuel savings. A comparison of the frequency response of various coating architectures from the reciprocating engine literature showed the improvement in thermal performance of coatings with development time, and the materials identified by the optimization highlighted the potential for future improvements. Specific conclusions pertaining the optimization can be found in Chapter 7.

Finally, the major contributions of this work, are:

i) Developed and validated an analytical unsteady heat conduction solution for multilayer engine walls. This method can be utilized in a decoupled fashion, where it provides paramount computational efficiencies, or, integrated with engine combustion solvers for conjugate heat transfer simulations.

ii) Developed and validated an analytical fracture-based delamination framework for predicting coating failure. This technique can be utilized to design coating architectures which enchance durability based on mechanical properties.

iii) Established an optimization methodology for selecting coatings which considers the engine performance and coating durability trade-off. The output uncovered the optimum coating material and their thickness for a real-world driving scenario. This elucidated the importance of including mechanical considerations in the design of thermal barrier coatings for improved engine performance, resolving an open problem that has persisted for nearly five decades.

8.2 Recommendations

Recommendations for each section of this work are provided next.

8.2.1 Recommendations on Direct Heat Conduction

The current form of the coupled surface temperature output, see Eq. (3.60), depends only on the past and current inputs, *i.e.*, combustion chamber heat flux and backside coolant/oil temperature. While this approach provides significant computational efficiency as compared to previous state of the art solutions, even higher efficiency can be achieved. An alternative formulation of this solution may depend on the previous and current inputs *and* the previous outputs. Such formulation will require a significantly smaller response function, or number of coefficients. A potential method to achieve a causal system including feedback is via the z-transform method [111].

Unpublished work by the author attempted to choose an input function that has a known Laplace transform and z-transform using a ramp function. The Laplace transform of the output was the Laplace transform of the input multiplied by the Laplace transfer function. This output was converted into the z-domain and divided by the z-transform input. The quotient was the z-transform of the Laplace equivalent.

The formulation was successfully derived, however, the software implementation was sensitive to the floating-point arithmetics. In turn, that resulted to investigating Python libraries with floating-point arithmetics with arbitrary precision. For engine-like coating and metal properties, the coefficients required more than a hundred digits after the decimal. In a 64-bit setup, the z-transform convolution using arbitrary precision provided similar computational time relative to a two orders of magnitude larger size Laplace convolution using `float64`. A more complete study with different scenarios should be performed to investigate the merits of this approach.

8.2.2 Recommendations on Fracture Mechanics

The driving forces for delamination in layered structures can be normal stress, shear stress or a combination of the above [146]. The mode mix will be important once there is experimentally measured interface toughness of the reciprocating engine coatings. It is anticipated that if reciprocating engine coatings delaminate during operation, the interface toughness [147] may need to be considered or calibrate the coating designs as shown through the body of this work.

In this work, analytical mechanics was utilized and validated over real coating structures with measured properties. As a follow-up, a parametric analysis could also be performed to investigate the effect of the thermo-mechanical properties of the coating, *e.g.* coating and substrate coefficient of thermal expansion, on the energy release rate [104].

8.2.3 Recommendations on Engine Performance

The primary interest of this study was to investigate the system-level engine performance using thermal barrier coatings. Thus, the heat conduction method for multi-layer walls was implemented into a commercial system-level simulation software package. However, the identical approach could be utilized for 3-D computational fluid dynamics solvers to provide further insights about the in-cylinder heat flux and surface temperature spatial distribution of coated walls during an engine cycle.

There is significant evidence in the literature that shows higher exhaust enthaply using coatings. This effect could be used in favor of aftertreatment strategies during cold-start operation.

8.2.4 Recommendations on Delamination Failure Experiments

In this work, all thermo-mechanical properties, including residual stresses or reference temperature are measured before the coating engine testing. This immediately raises a question as to the extent in which the thermo-mechanical properties of the

coating vary during operation. It is suggested to investigate the complete set of thermo-mechanical coating properties before and after engine testing.

8.2.5 Recommendations on Optimization of Thermal Barrier Coating Performance and Durability over a Drive Cycle

The optimization procedure described above was formulated to optimize the thickness of a single coating material. Both the material type and thickness were used as design variables in a hierarchical-type optimization which was parallelized. However, the optimum wall architecture is likely to consist of multiple layers. Thus, another design variable could be added to the procedure; the number of layers. Such optimization problems require different handling and are suggested to be treated using categorical design variables [148].

The best performing coatings provide a guide towards what set of properties are optimal for reciprocating engines. Further experimental demonstrations on those structures are suggested to identify a feasible, from a manufacturing and cost perspective.

REFERENCES

[1] Myers, P S. 1989. Ceramics for transportation engines—siren or solution. *Applied Mechanics Reviews* 42.

[2] Hendricks, T L. 2011. Instantaneous heat flux measurements in internal combustion engines. Ph.D. thesis, University of Wisconsin-Madison.

[3] Gingrich, E. 2020. High-Output Diesel Engine Heat Transfer. Ph.D. thesis, University of Wisconsin-Madison.

[4] Heywood, J B. 1988. *Internal Combustion Engine Fundamentals*. McGraw-Hill.

[5] Kamo, R. 1978. Adiabatic turbocompound engine performance prediction. *SAE Technical Papers*.

[6] Bryzik, W, and R Kamo. 1983. TACOM/Cummins Adiabatic Engine Program. *SAE Transactions* 1063–1087.

[7] Kamo, R., and W. Bryzik. 1984. Cummins/TACOM Advanced Adiabatic Engine. *SAE Transactions* 93:236–249.

[8] Woschni, G, W Spindler, and K Kolesa. 1987. Heat insulation of combustion chamber walls—a measure to decrease the fuel consumption of IC engines? *SAE transactions* 269–279.

[9] Cheng, W K, V W Wong, and F Gao. 1989. Heat Transfer Measurement Comparisons in Insulated and Non-Insulated Diesel Engines. *SAE Technical Paper*.

[10] Morel, T, R Keribar, and P N. Blumberg. 1985. Cyclical Thermal Phenomena in Engine Combustion Chamber Surfaces. *SAE Technical Paper Series*.

[11] Assanis, D N, and J B Heywood. 1986. Development and Use of a Computer Simulation of the Turbocompounded Diesel System for Engine Performance and Component Heat Transfer Studies. *SAE transactions* 451–476.

[12] Kamo, R, D N Assanis, and W Bryzik. 1989. Thin thermal barrier coatings for engines. *SAE Transactions* 131–136.

[13] Uchida, Noboru. 2020. A review of thermal barrier coatings for improvement in thermal efficiency of both gasoline and diesel reciprocating engines. *International Journal of Engine Research*.

[14] Assanis, D N., K Wiese, E Schwarz, and W Bryzik. 1991. The Effects of Ceramic Coatings on Diesel Engine Performance and Exhaust Emissions. *SAE Technical Paper Series*.

[15] Osawa, K, R Kamo, and E Valdmanis. 1991. Performance of thin thermal barrier coating on small aluminum block diesel engine. *SAE Technical Paper*.

[16] Chan, S.H., and K.A. Khor. 2000. The Effect of Thermal Barrier Coated Piston Crown on Engine Characteristics. *Journal of Materials Engineering and Performance* 9(1):103–109.

[17] Mendera, K Z. 2000. Effectiveness of plasma sprayed coatings for engine combustion chamber. *SAE transactions* 3112–3121.

[18] Schihl, P, E Schwarz, and W Bryzik. 2001. Performance characteristics of a low heat rejection direct-injection military diesel engine retrofitted with thermal barrier coated pistons. *J. Eng. Gas Turbines Power* 123(3):644–651.

[19] Kamo, R, N S Mavinahally, L Kamo, W Bryzik, and E E Schwartz. 1999. Injection Characteristics that Improve Performance of Ceramic Coated Diesel Engines. *SAE International*.

[20] Dickey, D. W. 1989. The Effect of Insulated Combustion Chamber Surfaces on Direct-Injected Diesel Engine Performance, Emissions and Combustion. *SAE Technical Paper Series*.

[21] Morel, T, E F Wahiduzzaman, Sand Fort, R Keribar, and P N Blumberg. 1988. Methods for heat transfer and temperature field analysis of the insulated diesel, phase 3. *NASA*.

[22] Alkidas, A C. 1989. Performance and Emissions Achievements with an Uncooled Heavy-Duty, Single-Cylinder Diesel Engine. *SAE International*.

[23] Alkidas, A C. 1987. Experiments with an uncooled single-cylinder open-chamber diesel. *SAE transactions* 280–290.

[24] Furuhama, S, and Y Enomoto. 1987. Heat Transfer into Ceramic Combustion Wall of Internal Combustion Engines.

[25] Assanis, D N. 1992. The effect of thin ceramic coatings on petrol engine performance and emissions. *International Journal of Vehicle Design* 13(4): 378–387.

[26] Gatowski, J A. 1990. Evaluation of a selectively-cooled single-cylinder 0.5-L diesel engine. *SAE transactions* 1580–1591.

[27] Caputo, S, F Millo, G Boccardo, A Piano, G Cifali, and C F Pesce. 2019. Numerical and experimental investigation of a piston thermal barrier coating for an automotive diesel engine application. *Applied Thermal Engineering*.

[28] Rakopoulos, C D, and E G Giakoumis. 2007. Study of the transient operation of low heat rejection turbocharged diesel engine including wall temperature oscillations. *SAE Technical Paper*.

[29] Filipi, Z, M Hoffman, R O'Donnell, T Powell, E Jordan, and R Kumar. 2020. Enhancing the efficiency benefit of thermal barrier coatings for homogeneous charge compression ignition engines through application of a low-k oxide. *International Journal of Engine Research*.

[30] Yan, Z. 2021. An Assessment of Thermal Barrier Coatings for The Low-Temperature Combustion Family: From HCCI To GCI. Ph.D. thesis, Clemson University.

[31] Kosaka, H, Y Wakisaka, Y Nomura, Y Hotta, M Koike, K Nakakita, and A Kawaguchi. 2013. Concept of "Temperature Swing Heat Insulation" in

Combustion Chamber Walls, and Appropriate Thermo-Physical Properties for Heat Insulation Coat. *SAE International Journal of Engines* 6(1):142–149.

[32] Wakisaka, Y, M Inayoshi, K Fukui, H Kosaka, Y Hotta, A Kawaguchi, and N Takada. 2016. Reduction of Heat Loss and Improvement of Thermal Efficiency by Application of "Temperature Swing" Insulation to Direct-Injection Diesel Engines. *SAE International Journal of Engines* 9(3):1449–1459.

[33] Kawaguchi, A, H Iguma, H Yamashita, N Takada, N Nishikawa, C Yamashita, Y Wakisaka, and K Fukui. 2016. Thermo-Swing Wall Insulation Technology; - A Novel Heat Loss Reduction Approach on Engine Combustion Chamber. *SAE Technical Paper Series*.

[34] Kawaguchi, A, Y Wakisaka, N Nishikawa, H Kosaka, H Yamashita, C Yamashita, H Iguma, K Fukui, N Takada, and T Tomoda. 2019. Thermo-swing insulation to reduce heat loss from the combustion chamber wall of a diesel engine. *International Journal of Engine Research*.

[35] Durrett, R P, Paul M Najt, P P Andruskiewicz IV, T A Schaedler, G P Hill, J H Martin, and C J Ro. 2019. Internal combustion engine and method for coating internal combustion engine components. US Patent 10,190,533.

[36] Andrie, M, S Kokjohn, S Paliwal, L S Kamo, A Kamo, and D Procknow. 2019. Low Heat Capacitance Thermal Barrier Coatings for Internal Combustion Engines. *SAE Technical Paper Series* 1:1–13.

[37] Serrano, J R, F J Arnau, J Martin, M Hernandez, and B Lombard. 2015. Analysis of engine walls thermal insulation: performance and emissions. *SAE*.

[38] Olmeda, P, J Martín, R Novella, and D Blanco-Cavero. 2020. Assessing the optimum combustion under constrained conditions. *International Journal of Engine Research* 21(5):811–823.

[39] Andruskiewicz, P, P Najt, R Durrett, S Biesboer, T Schaedler, and R Payri. 2017. Analysis of the effects of wall temperature swing on reciprocating internal combustion engine processes. *International Journal of Engine Research*.

[40] Hoffman, M A, B J Lawler, O A Güralp, P M Najt, and Z S Filipi. 2015. The impact of a magnesium zirconate thermal barrier coating on homogeneous charge compression ignition operational variability and the formation of combustion chamber deposits. *International Journal of Engine Research* 16(8): 968–981.

[41] Tsutsumi, Y, K Nomura, and N Nakamura. 1990. Effect of mirror-finished combustion chamber on heat loss. *SAE Technical Paper*.

[42] Powell, T. 2018. Impacts of thermal barrier coating morphology and catalytic properties on low temperature combustion engine in-cylinder processes. Ph.D. thesis, Clemson University.

[43] Powell, T, R O'Donnell, M Hoffman, Z Filipi, E H Jordan, R Kumar, and N J Killingsworth. 2019. Experimental investigation of the relationship between thermal barrier coating structured porosity and homogeneous charge compression ignition engine combustion. *International Journal of Engine Research*.

[44] Somhorst, J, M Oevermann, M Bovo, and I Denbratt. 2019. Evaluation of thermal barrier coatings and surface roughness in a single-cylinder light-duty diesel engine. *International Journal of Engine Research*.

[45] Keskinen, K, W Vera-Tudela, M Wright, and K Boulouchos. 2020. Experimental investigation of wall heat transfer due to spray combustion in a high pressure/high temperature vessel. In *Thiesel*.

[46] Keskinen, K, W Vera-Tudela, Y M Wright, and K Boulouchos. 2021. Experimental investigation of wall heat transfer due to spray combustion in a high-pressure/high-temperature vessel. *International Journal of Engine Research*.

[47] Kogo, T, Y Hamamura, K Nakatani, T Toda, A Kawaguchi, and A Shoji. 2016. High Efficiency Diesel Engine with Low Heat Loss Combustion Concept-Toyota's Inline 4-Cylinder 2.8-Liter ESTEC 1GD-FTV Engine. *SAE Technical Paper*.

[48] Memme, S, and J S Wallace. 2012. The influence of thermal barrier coating surface roughness on spark-ignition engine performance and emissions. In *Internal combustion engine division fall technical conference*, 893–905. American Society of Mechanical Engineers.

[49] Gingrich, E, M Tess, V Korivi, P Schihl, J Saputo, G M Smith, S Sampath, and J Ghandhi. 2019. The impact of piston thermal barrier coating roughness on high-load diesel operation. *International Journal of Engine Research*.

[50] Huang, J C, and G L Borman. 1987. Measurements of instantaneous heat flux to metal and ceramic surfaces in a diesel engine. *SAE transactions* 66–81.

[51] Osada, H, H Watanabe, Y Onozawa, K Enya, and N Uchida. 2017. Experimental analysis of heat-loss with different piston wall surface conditions in a heavy-duty diesel engine. In *The proceedings of the international symposium on diagnostics and modeling of combustion in internal combustion engines 2017.9*. The Japan Society of Mechanical Engineers.

[52] Hendricks, T L, D A Splitter, and J B Ghandhi. 2014. Experimental investigation of piston heat transfer under conventional diesel and reactivity-controlled compression ignition combustion regimes. *International Journal of Engine Research* 15(6):684–705.

[53] Kokjohn, S L, R M Hanson, D A Splitter, and R D Reitz. 2011. Fuel reactivity controlled compression ignition (RCCI): a pathway to controlled high-efficiency clean combustion. *International Journal of Engine Research* 12(3):209–226.

[54] Kokjohn, S, R Hanson, D Splitter, J Kaddatz, and R Reitz. 2011. Fuel reactivity controlled compression ignition (rcci) combustion in light-and heavy-duty engines. *SAE International Journal of Engines* 4(1):360–374.

[55] Kokjohn, S, R Reitz, D Splitter, and M Musculus. 2012. Investigation of fuel reactivity stratification for controlling PCI heat-release rates using high-speed chemiluminescence imaging and fuel tracer fluorescence. *SAE International Journal of Engines* 5(2):248–269.

[56] Wurzenberger, J C, R Wanker, and M Schüßler. 2008. Simulation of exhaust gas aftertreatment systems-thermal behavior during different operating conditions. Tech. Rep., SAE Technical Paper.

[57] Papetti, V, P Dimopoulos Eggenschwiler, A Della Torre, G Montenegro, A Onorati, and G Koltsakis. 2019. Heat transfer analysis of catalytic converters during cold starts. Tech. Rep., SAE Technical Paper.

[58] Papetti, V, P Dimopoulos Eggenschwiler, A Della Torre, G Montenegro, A Onorati, A Ortona, and G Koltsakis. 2021. Instationary heat and mass transfer phenomena in additive manufactured open cell polyhedral structures for automotive catalysis. *Chemical Engineering Science* 234:116448.

[59] Arnau, F J, J Martín, P Piqueras, and Á Auñón. 2021. Effect of the exhaust thermal insulation on the engine efficiency and the exhaust temperature under transient conditions. *International Journal of Engine Research* 22(9): 2869–2883.

[60] Yonushonis, T M. 1991. Thick thermal barrier coatings for diesel components. *NASA Lewis Research Center*.

[61] Saad, D, P Saad, L Kamo, M Mekari, W Bryzik, E Schwarz, and J Tasdemir. 2007. Thermal barrier coatings for high output turbocharged diesel engine. *SAE Technical Paper*.

[62] Tricoire, A, B Kjellman, J Wigren, M Vanvolsem, and L Aixala. 2009. Insulated piston heads for diesel engines. *Journal of thermal spray technology* 18(2):217–222.

[63] Uchida, N, and H Osada. 2017. A new piston insulation concept for heavy-duty diesel engines to reduce heat loss from the wall. *SAE International Journal of Engines* 10(5):2565–2574.

[64] Thibblin, A, S Kianzad, S Jonsson, and U Olofsson. 2019. Running-in behaviour of thermal barrier coatings in the combustion chamber of a diesel engine. *Proceedings of the Institution of Mechanical Engineers, Part D: Journal of Automobile Engineering*.

[65] Andruskiewicz, P, P Najt, R Durrett, and R Payri. 2018. Assessing the capability of conventional in-cylinder insulation materials in achieving temperature swing engine performance benefits. *International Journal of Engine Research* 19(6):599–612.

[66] Andruskiewicz, P. 2017. Analytical and Experimental Investigation of Temperature-Swing Insulation. Ph.D. thesis, Universitat Politècnica de València.

[67] Thibblin, A, and U Olofsson. 2020. A study of suspension plasma-sprayed insulated pistons evaluated in a heavy-duty diesel engine. *International Journal of Engine Research* 21(6):987–997.

[68] Beardsley, M.B., and Larson H.J. 1992. Thick Thermal Barrier Coatings for Diesel Components. Tech. Rep., DOE/NASA/0332-1, NASA CR-190759.

[69] Beardsley, M Brad. 2008. *Potential use of quasicrystalline materials as thermal barrier coatings for diesel engine components*. Iowa State University.

[70] Beardsley, M B, D Socie, E Redja, and C Berndt. 2006. Thick Thermal Barrier Coatings (TTBCs) for Low Emission, High Efficiency Diesel Engine Components. Tech. Rep., Caterpillar Inc., Peoria, IL.

[71] Moser, Sean. 2021. Coupled Thermal Mechanical Analysis Methodology for Thermal Performance Evaluation and Failure Mode Identification of Thermal Barrier Coatings for Heavy Duty Diesel Engines. Ph.D. thesis, Clemson University.

[72] William, KJ, and EP Warnke. 1975. Constitutive model for the triaxial behavior of concrete international association for bridge and structure engineering proceedings. *Proc. Intl. Assoc. Bridge Structl. Engrs* 19:1–30.

[73] Powell, T, R O'Donnell, M Hoffman, and Z Filipi. 2017. Impact of a yttria-stabilized zirconia thermal barrier coating on HCCI engine combustion, emissions, and efficiency. *Journal of Engineering for Gas Turbines and Power* 139(11).

[74] Buyukkaya, E, and M Cerit. 2007. Thermal analysis of a ceramic coating diesel engine piston using 3-D finite element method. *Surface and coatings technology* 202(2):398–402.

[75] Cerit, M. 2011. Thermo mechanical analysis of a partially ceramic coated piston used in an SI engine. *Surface and coatings Technology* 205(11):3499–3505.

[76] Moridi, A, M Azadi, and GH Farrahi. 2014. Thermo-mechanical stress analysis of thermal barrier coating system considering thickness and roughness effects. *Surface and Coatings Technology* 243:91–99.

[77] Bayata, F, and Cengiz Y. 2021. The analyses of frictional losses and thermal stresses in a diesel engine piston coated with different thicknesses of thermal barrier films using co-simulation method. *International Journal of Engine Research*.

[78] Zhu, D, and R A Miller. 1998. Investigation of thermal high cycle and low cycle fatigue mechanisms of thick thermal barrier coatings. *Materials Science and Engineering: A* 245(2):212–223.

[79] Baldissera, P, and C Delprete. 2019. Finite element thermo-structural methodology for investigating diesel engine pistons with thermal barrier coating. *SAE International Journal of Engines* 12(1):69–78.

[80] Pierz, PM. 1993. Thermal barrier coating development for diesel engine aluminum pistons. *Surface and Coatings Technology* 61(1-3):60–66.

[81] Zhu, D, and R A Miller. 1997. Influence of high cycle thermal loads on thermal fatigue behavior of thick thermal barrier coatings. Tech. Rep., NASA, Cleveland, Ohio.

[82] Killingsworth, N, T Powell, R O'Donnell, Z Filipi, and M Hoffman. 2019. Modeling the Effect of Thermal Barrier Coatings on HCCI Engine Combustion Using CFD Simulations with Conjugate Heat Transfer. *SAE Technical Paper*.

[83] Caputo, S, F Millo, G Cifali, and F C Pesce. 2017. Numerical investigation on the effects of different thermal insulation strategies for a passenger car diesel engine. *SAE International Journal of Engines*.

[84] Yamashita, C., H. Yamashita, A. Kawaguchi, N. Nishikawa, K. Tanaka, K. Fukui, T. Kurauchi, and K. Nakata. 2019. Development of the heat insulation coating by temperature swing for the combustion chamber wall of gasoline engine (in japanese). *JSAE*.

[85] Chérel, J, J Zaccardi, B Bouteiller, and A Allimant. 2020. Experimental assessment of new insulation coatings for lean burn spark-ignited engines. *Oil & Gas Science and Technology–Revue d'IFP Energies nouvelles* 75:11.

[86] Mohr, D, T Shipp, and X Lu. 2019. The thermodynamic design, analysis and test of Cummins' SuperTruck 2 50% brake thermal efficiency engine system. *SAE Technical Paper*.

[87] Watanabe, Kazumasa, Noboru Uchida, Kazuhiro Yokogawa, and Fumihiro Kawaharazuka. 2021. What Are the Barriers Against Brake Thermal Efficiency beyond 55% for HD Diesel Engines? Tech. Rep., SAE Technical Paper.

[88] O'Connor, J, M Borz, D Ruth, J Han, C Paul, A Imren, D Haworth, J Martin, A Boehman, J Li, et al. 2017. Optimization of an advanced combustion strategy towards 55% BTE for the Volvo SuperTruck Program. *SAE International Journal of Engines* 10(3):1217–1227.

[89] Assanis, D N. 1985. A Computer Simulation of The Turbocharged Diesel Engine System.pdf. Ph.D. thesis, MIT.

[90] Miyairi, Y. 1988. Computer Simulation of an LHR DI Diesel Engine.

[91] Gamma Technologies. 2020. GT-SUITE. Westmont, IL.

[92] Richards, K. J., P. K. Senecal, and E. Pomraning. 2021. *CONVERGE 3.0 Manual*. Convergent Science, Madison, WI, USA.

[93] Assanis, D N, and E Badillo. 1987. Transient heat conduction in low-heat-rejection engine combustion chambers. *SAE Transactions* 82–92.

[94] Olmeda, P., X. Margot, P. Quintero, and J. Escalona. 2020. Numerical approach to define a thermodynamically equivalent material for the conjugate heat transfer simulation of very thin coating layers. *International Journal of Heat and Mass Transfer* 162:120377.

[95] Ghandhi, J.B., and G. Koutsakis. 2021. Comment on "Numerical approach to define a thermodynamically equivalent material for the conjugate heat transfer simulation of very thin coating layers" by P. Olmeda, X. Margot, P. Quintero, J. Escalona, International Journal of Heat and Mass Transfer, Vol. 162 (2020) 120377. *International Journal of Heat and Mass Transfer* 173:121190.

[96] Olmeda, P., X. Margot, P. Quintero, and J. Escalona. 2021. Reply to short communication 'Comment on "Numerical approach to define a thermodynamically equivalent material for the conjugate heat transfer simulation of

very thin coating layers" by P. Olmeda, X. Margot, P. Quintero, J. Escalona, International Journal of Heat and Mass Transfer, Vol. 162(2020) 120377 " by Jaal Ghandhi and Georgios Koutsakis. *International Journal of Heat and Mass Transfer* 171:121023.

[97] Begley, M R, and J W Hutchinson. 2017. *The mechanics and reliability of films, multilayers and coatings*. Cambridge University Press.

[98] Clarke, D R, M Oechsner, and N P Padture. 2012. Thermal-barrier coatings for more efficient gas-turbine engines. *MRS bulletin* 37(10):891–898.

[99] Darolia, R. 2013. Thermal barrier coatings technology: critical review, progress update, remaining challenges and prospects. *International Materials Reviews* 58(6):315–348.

[100] Deijkers, J A., M R Begley, and H N.G. Wadley. 2022. Failure mechanisms in model thermal and environmental barrier coating systems. *Journal of the European Ceramic Society* 42(12):5129–5144.

[101] Levi, Carlos G, J W Hutchinson, M Vidal-Sétif, and C A Johnson. 2012. Environmental degradation of thermal-barrier coatings by molten deposits. *MRS bulletin* 37(10):932–941.

[102] Krämer, S, S Faulhaber, M Chambers, D R Clarke, C G Levi, J W Hutchinson, and A G Evans. 2008. Mechanisms of cracking and delamination within thick thermal barrier systems in aero-engines subject to calcium-magnesium-alumino-silicate (CMAS) penetration. *Materials Science and Engineering: A* 490(1-2):26–35.

[103] Begley, M R, and H NG Wadley. 2012. Delamination resistance of thermal barrier coatings containing embedded ductile layers. *Acta Materialia* 60(6-7): 2497–2508.

[104] Sundaram, S, DM Lipkin, CA Johnson, and JW Hutchinson. 2013. The influence of transient thermal gradients and substrate constraint on delamination of thermal barrier coatings. *Journal of Applied Mechanics* 80(1).

[105] Carslaw, H.S., and J.C. Jaeger. 1959. Conduction of Heat in Solids.

[106] Nellis, G, and S Klein. 2009. *Heat Transfer*. Cambridge University Press.

[107] Pipes, L A. 1957. Matrix analysis of heat transfer problems. *Journal of the Franklin Institute* 263(3):195–206.

[108] Churchill, R V, and J W Brown. 2009. *Complex Variables and Applications, 8th edition*. McGraw-Hill.

[109] Overbye, V D, J E Bennethum, OA Uyehara, and PS Myers. 1961. Unsteady heat transfer in engines. *SAE Transactions* 69:461–494.

[110] Broatch, A, P Olmeda, X Margot, and J Gomez-Soriano. 2020. A one-dimensional modeling study on the effect of advanced insulation coatings on internal combustion engine efficiency. *International Journal of Engine Research*.

[111] Stephenson, DG, and GP Mitalas. 1971. Calculation of heat conduction transfer functions for multi-layers slabs. *Air Cond. Engrs. Trans;(United States)* 77.

[112] Hittle, Douglas C. 1981. Calculating building heating and cooling loads using the frequency response of multilayered slabs. Tech. Rep., Construction Engineering Research Lab (ARMY) Champaign-IL.

[113] Kusuda, T. 1969. Thermal response factors for multi-layer structures of various heat conduction systems. In *Ashrae journal*, vol. 11, 64.

[114] Koutsakis, G, G F Nellis, and J B Ghandhi. 2020. Surface temperature of a multi-layer thermal barrier coated wall subject to an unsteady heat flux. *International Journal of Heat and Mass Transfer* 155.

[115] Hittle, D C, and R Bishop. 1983. An improved root-finding procedure for use in calculating transient heat flow through multilayered slabs. *International Journal of Heat and Mass Transfer* 26(11):1685–1693.

[116] Koutsakis, G., S. Miles, and J. Ghandhi. 2021. Assessment of in-cylinder thermal barrier coatings over a full vehicle drive cycle. *SAE International*.

[117] Rabiner, Lawrence R, and Bernard Gold. 1975. Theory and application of digital signal processing. *Englewood Cliffs: Prentice-Hall* 63–65.

[118] Gingrich, E, M Tess, V Korivi, and J Ghandhi. 2021. High-output diesel engine heat transfer: Part 1 - comparison between piston heat flux and global energy balance. *International Journal of Engine Research*.

[119] Saputo, J. 2021. Personal communication with Stony Brook University.

[120] Bower, A F. 2009. *Applied mechanics of solids*. CRC press.

[121] Jackson, R W, and M R Begley. 2014. Critical cooling rates to avoid transient-driven cracking in thermal barrier coating (TBC) systems. *International Journal of Solids and Structures* 51(6):1364–1374.

[122] Saputo, J C, G M Smith, H Lee, S Sampath, E Gingrich, and M Tess. 2021. Thermal Swing Evaluation of Thermal Barrier Coatings for Diesel Engines. *Journal of Thermal Spray Technology* 1–15.

[123] Chen, Y, and J A Worden. 2000. Evaluation of microalloyed steel for articulated piston applications in heavy duty diesel engines. *SAE Technical Paper*.

[124] Granta Selector. 2020. ANSYS, Inc.

[125] Goodwin, D. G., R. L. Speth, H. K. Moffat, and Bryan W. Weber. 2018. Cantera: An object-oriented software toolkit for chemical kinetics, thermodynamics, and transport processes. `https://www.cantera.org`. Version 2.4.0.

[126] Ra, Y, and R D Reitz. 2008. A reduced chemical kinetic model for ic engine combustion simulations with primary reference fuels. *Combustion and Flame* 155(4):713–738.

[127] Annand, W J D. 1963. Heat transfer in the cylinders of reciprocating internal combustion engines. *Proceedings of the Institution of Mechanical Engineers* 177(1):973–996.

[128] Borman, G, and K Nishiwaki. 1987. Internal-combustion engine heat transfer. *Progress in Energy and Combustion Science* 13(1):1–46.

[129] Andrie, M J, L Kamo, and A Kamo. 2020. Thermal barrier coatings containing aluminosilicate particles. US Patent App. 16/036,364.

[130] European Commission Horizon 2020. 2020. EAGLE Project. GA No. 724084.

[131] Bouteiller, B, A Allimant, J Zaccardi, and J Cherel. 2019. New Ceramic Thermal Barrier Coatings Development in a Spark-Ignition Engine – Experimental Investigation. In *International Thermal Spray Conference*. Yokohama, Japan: ASM International.

[132] Koutsakis, G, and J B Ghandhi. 2020. An Analytical Approach for Calculating Instantaneous Multilayer-Coated Wall Surface Temperature in an Engine. *SAE International Journal of Advances and Current Practices in Mobility* 2:1303–1313.

[133] Chang, J, O Güralp, Z Filipi, D Assanis, T Kuo, P Najt, and R Rask. 2004. New heat transfer correlation for an HCCI engine derived from measurements of instantaneous surface heat flux. *SAE transactions* 1576–1593.

[134] Koutsakis, G., J. Saputo, E. Gingrich, M. Tess, and J. B. Ghandhi. 2022. Delamination Failure on High-Output Diesel Engine Thermal Barrier Coatings. *SAE International*.

[135] Koutsakis, G, M R Begley, J W Hutchinson, and J B Ghandhi. 2022. Fracture-based Transient Thermo-mechanical Analysis of Reciprocating Engine Thermal Barrier Coatings. *Journal of Engineering Fracture Mechanics* 108568.

[136] DieselNet.com. 2020. Non-road transient cycle standard. `https://dieselnet.com/standards/cycles/nrtc.php`.

[137] Koutsakis, Georgios, and J.B Ghandhi. 2022. Analytical Solution of Unsteady Heat Conduction in Multilayer Internal Combustion Engine Walls. *Applied Thermal Engineering* 118681.

[138] Virtanen, P, R Gommers, T E Oliphant, M Haberland, T Reddy, D Cournapeau, E Burovski, P Peterson, W Weckesser, J Bright, Stéfan J. van der Walt, M Brett, J Wilson, K J Millman, N Mayorov, A R J Nelson, E Jones, R Kern, C J Larson, Eand Carey, İ Polat, Y Feng, E W Moore, J VanderPlas, D Laxalde, J Perktold, R Cimrman, I Henriksen, E A Quintero, C R. Harris, A M Archibald, A H Ribeiro, F Pedregosa, P van Mulbregt, and SciPy 1.0 Contributors. 2020. SciPy 1.0: Fundamental Algorithms for Scientific Computing in Python. *Nature Methods* 17:261–272.

[139] Thain, D, T Tannenbaum, and M Livny. 2005. Distributed computing in practice: the condor experience. *Concurrency - Practice and Experience* 17(2-4): 323–356.

[140] Squire, T H, F S Milos, and G C Hartlieb. 2009. Aerospace materials property database (TPSX). *Journal of Spacecraft and Rockets* 46(3):733–736.

[141] Keribar, R, and T Morel. 1987. Thermal shock calculations in IC engines. *SAE transactions* 130–148.

[142] Kamo, L, M Woods, W Bryzik, and M Mekari. 2000. Thermal barrier coatings for monolithic ceramic low heat rejection diesel engine components. *SAE transactions* 681–690.

[143] Assanis, D N, and E Badillo. 1988. Transient analysis of piston-liner heat transfer in low-heat-rejection diesel engines. *SAE Transactions* 97:295–305.

[144] Babu, A., G. Koutsakis, S. Kokjohn, and M. Andrie. 2022. Experimental and analytical study of temperature swing piston coatings in a medium-duty diesel engine. *SAE Technical Paper*.

[145] Koutsakis, G, and J B Ghandhi. 2022. Optimization of Thermal Barrier Coating Performance and Durability over a Drive Cycle. *International Journal of Engine Research*.

[146] Hutchinson, J W, and Z Suo. 1991. Mixed mode cracking in layered materials. *Advances in applied mechanics* 29:63–191.

[147] Hutchinson, R G, and J W Hutchinson. 2011. Lifetime assessment for thermal barrier coatings: tests for measuring mixed mode delamination toughness. *Journal of the American Ceramic Society* 94:s85–s95.

[148] Audet, C., S. Le Digabel, V. Rochon Montplaisir, and C. Tribes. 2022. The NOMAD project. Software available at `https://www.gerad.ca/nomad/`.